Measurement of light shift ratios with a single trapped $^{138}Ba^{+}$ ion, and prospects for a parity violation experiment

Timo W. Koerber

A dissertation submitted in partial fulfillment of
the requirements for the degree of

Doctor of Philosophy

University of Washington

2003

Program Authorized to Offer Degree: Department of Physics

INFORMATION TO USERS

The quality of this reproduction is dependent upon the quality of the copy submitted. Broken or indistinct print, colored or poor quality illustrations and photographs, print bleed-through, substandard margins, and improper alignment can adversely affect reproduction.

In the unlikely event that the author did not send a complete manuscript and there are missing pages, these will be noted. Also, if unauthorized copyright material had to be removed, a note will indicate the deletion.

ProQuest Information and Learning Company
300 North Zeeb Road
P.O. Box 1346
Ann Arbor, MI 48106-1346

In presenting this dissertation in partial fulfillment of the requirements for the Doctoral degree at the University of Washington, I agree that the Library shall make its copies freely available for inspection. I further agree that extensive copying of this dissertation is allowable only for scholarly purposes, consistent with "fair use" as prescribed in the U.S. Copyright Law. Requests for copying or reproduction of this dissertation may be referred to Bell and Howell Information and Learning, 300 North Zeeb Road, Ann Arbor, MI 48106-1346, to whom the author has granted "the right to reproduce and sell (a) copies of the manuscript in microform and/or (b) printed copies of the manuscript made from microform."

Signature _____

Date 10 / 29 / 2003

University of Washington

Graduate School

This is to certify that I have examined this copy of a doctoral dissertation by

Timo W. Koerber

and have found that it is complete and satisfactory in all respects,
and that any and all revisions required by the final
examining committee have been made.

Chair of Supervisory Committee:

E. Norval Fortson

Reading Committee:

Warren Nagourney

Larry Sorensen

Date: 10/29/2003

University of Washington

Abstract

Measurement of light shift ratios with a single trapped $^{138}Ba^{+}$ ion, and prospects for a parity violation experiment

by Timo W. Koerber

Chair of Supervisory Committee:

Professor E. Norval Fortson
Physics

This thesis describes the development and implementation of a new scheme for observing RF transitions between spin states in a single, trapped Ba^{+} ion. We use optical pumping to place the ion in a selected magnetic sublevel of either the $6S_{1/2}$ ground state or the $5D_{3/2}$ metastable state. The ion is exposed to an RF field, and a spin-sensitive version of the electron shelving method detects the resulting spin state. The precision of this kind of RF spectroscopy is limited only by magnetic-field noise, and with the current apparatus, line widths of about 10 Hz can be achieved.

This scheme is applied to a precision measurement of light shifts (or AC Stark shifts) in Ba^{+}. Zeeman energies are altered by a circularly polarized, off-resonant laser, and the resulting resonance shifts are measured simultaneously in both the $6S_{1/2}$ and $5D_{3/2}$ state. When taking the ratio, light intensity and polarization drop out, and we can determine the ratio of P-D to S-P matrix elements with a precision of $< 0.5\%$, with the evaluation of some systematic effects still pending. Motivation for this work comes from the fact that knowledge of P-D matrix elements is essential

for precisely calculating parity-violating transition amplitudes.

A measurement of the latter with a single ion is the ultimate experimental goal of this project. Such an experiment could enable comparison with Standard Model predictions at the sub-percent level and provide an independent check to a recent parity violation experiment in Cs. The observable in this measurement is a spin-dependent light shift, induced by a parity-violating E1 transition between the S and D states in either Ba^+ or Ra^+. The experiment and its systematic problems are analyzed in this thesis. We also propose an alternative scheme using odd isotopes and the E2-forbidden $F = 0 \leftrightarrow F = 1$ transition, along with an initial investigation of its systematic effects.

TABLE OF CONTENTS

LIST OF FIGURES

LIST OF TABLES

GLOSSARY

Abbreviations

AOM: Acusto-optical modulator

CC: Cupcake

DAQ: Data acquisition

EOM: Electro-optical modulator

GSA: Graduate student annoyance

LED: Light-emitting diode

ND: Neutral density

PNC: Parity nonconservation

RF: Radio-frequency

Symbols

α: Fine-structure constant

a: probability for ion to be pumped to $D_{3/2}$,$m = 1/2$

c: Speed of light

δ_L: detuning of the light from resonance, $\omega_L - \omega_0$

Δ: Light shift

$\Delta_{(n,j,m)}$: Light shift of state $|n, j, m\rangle$

Δ_s: effective scalar light shift in a spin system

Δ_d: effective dipole(vector) light shift in a spin system along $\hat{z}$

Δ_q: zz-component of effective quadrupole(tensor) light shift in a spin system

ε_0: dielectric constant

ϵ: polarization

$\boldsymbol{e}_x, \boldsymbol{e}_y, \boldsymbol{e}_z$: cartesian unit vectors

$\boldsymbol{E}, E$: electric field vector amplitude with $E \equiv |\boldsymbol{E}|$

$\boldsymbol{F}$: Force

Γ: spontaneous decay rate or decay width

$\hbar$: Planck's Constant/2π

$\hat{H}$: Hamiltionian

$\mathbb{I}$: Identity matrix

$\boldsymbol{j}_a$: Angular momentum representation for spin-system a

$\boldsymbol{k}$: wave vector

ν: secular trap frequency

ω: Frequency in angular units

ω_L: frequency of a light field

m: ion mass

ω_0: frequency of an atomic resonance

ω_B: Zeeman splitting

ω_s: size of off-resonant scalar light shift in a spin system(see Eq.6.5)

ω_d: size of off-resonant dipole(vector) light shift in a spin system along $\hat{z}$

ω_q: size of off-resonant zz-component of quadrupole(tensor) light shift in a spin system

$\hat{\rho}$: density operator

ρ_{ij}: density matrix elements

$\Theta, \boldsymbol{\Theta}, \Theta_{ij}$: scalar, vectorial (dipole) and tensor(quadrupolar) part of an interaction acting on a spin state

ACKNOWLEDGMENTS

First of all I thank my loving wife Lydia for her care and understanding during this intense time of writing my thesis, and for the many ways she participated in my work life over these past years. I love you Lydia!

Likewise first of all, I'm thankful to God for giving me this time of study, and for creating the intricate objects of our studies in the first place.

I wish to thank my advisor Norval Fortson for his guidance and support during these last few years. I appreciate his patience, skill and graciousness in correcting my - often - naive ideas, and teaching me by example about sound physical reasoning. I have also learned tremendously from his habit of listening and understanding carefully before making judgements, and admire his profound understanding of a broad variety of subjects.

Thanks to Warren Nagourney for teaching me much about experimental physics, including many clever tricks that he invented over the years. I'm thankful for his willingness to get the experiment back up and running when I was ready to give up, as well for his generosity in and out of the lab.

I thank Jeff Sherman, with whom I have shared the joys and GSA's of ion trapping, and who has helped me much, from carefully reading my thesis to providing me with surprise bagels when I was just about to fall into what Germans call the ten o'clock hole. Not to forget his *cake* that is capable of trapping single CC^+ ions. Nor the 100 angry dwarves he introduced me to.

Also thanks to Claire Cramer, Mark Williams, Matt Swallows, Clark Griffith, Jim Richards, David Rosser, Eryn Cook and Anja Koerber, as well as my reading com-

mittee (Norval Fortson, Larry Sorensen, and Warren Nagourney), all of which have participated in weed-whacking this thesis and providing me with valuable comments and corrections.

Thanks to all my colleagues in the lab over the years, for their friendship and for creating a pleasant lab atmosphere: Matt Swallows, Clark Griffith, Dave Pinegar, Laura Kogler, Masataka Iinuma, Roahn Wynar, Alex Cronin, Mike Romalis, Bruce Warrington, Reina Maruyama, Mike Schacht, Kristi Hendrickson, Jeff Sherman, Amar Andalkar, and Rob Lyman.

Thanks especially to Ethan Clarke for his friendship and helpfulness in the lab. Thanks also to glass-blower enigma Bob Morley for his indispensable help, as well as to the skillful and friendly machine shop and office staff.

Chapter 1

INTRODUCTION

It is the endeavor of every experiment in physics to isolate the objects and phenomena one wants to study. This is never completely possible, because inevitably the environment and the measurement process itself will cause effects that can be confused with, or completely dominate, the phenomena of interest. At the very least the effect we are trying to measure must have some signature that distinguishes it from unwanted effects, and usually the accuracy of a measurement is determined by how well one can perform this distinction.

When it comes to studying matter, a"single particle at rest in space", i.e., a microscopic system that is localized and free of perturbations caused by interactions with its environment, symbolizes this ideal of isolation. A single trapped ion in the laboratory is probably one of the closest realizations of this ideal. The ion is trapped by an oscillating electric field, which only interacts minimally with the ion's internal degrees of freedom. The ion is localized to within a fraction of optical wavelengths, and the experiments can take place in an ultra-high vacuum, where collisions with background gas are negligible. As a result, the energy spectrum of the atom is highly free from perturbations. It therefore comes as no surprise that part of the original motivation to trap single ions was the prospect of doing very accurate spectroscopy, ultimately using the ion as a reference for an atomic clock.

On the other hand, novel techniques had to be developed to efficiently extract useful information from a single ion. Traditionally, atomic physics relies on large

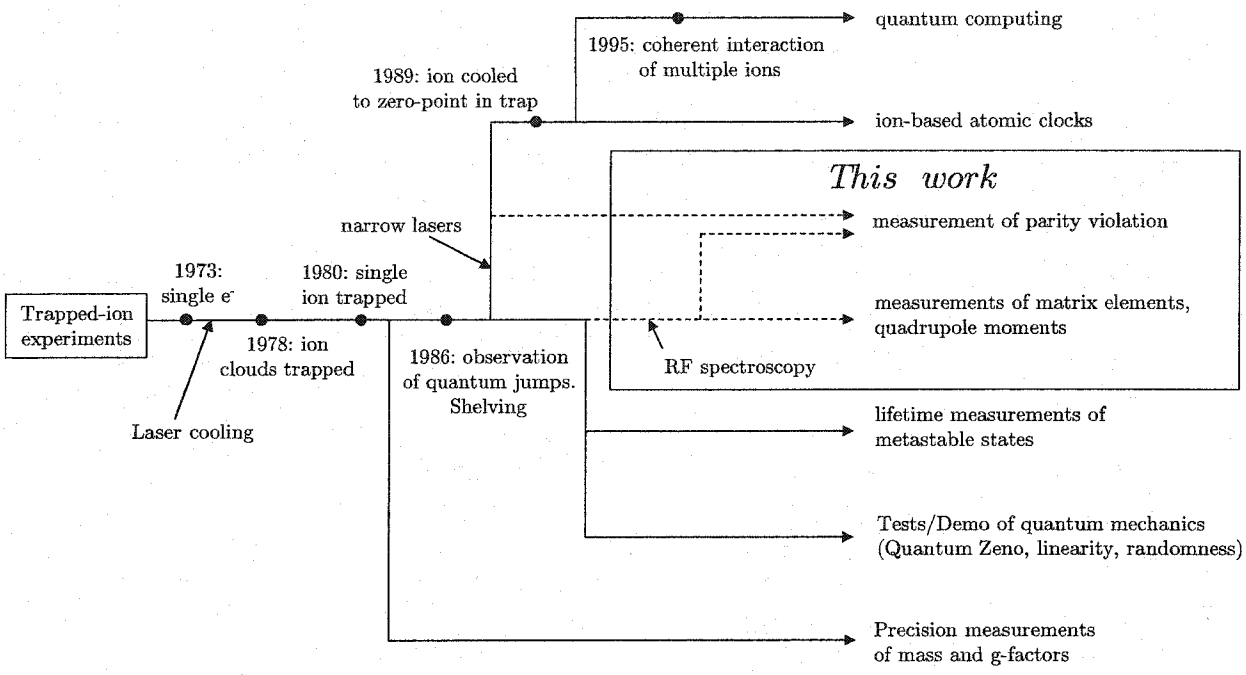

Figure 1.1: Brief overview of ion trap experiments.

samples of atoms to produce measurable quantities. The observation of light absorption by atoms, or the emission of fluorescence light are examples. For a single ion absorption techniques fail, and fluorescence is strong enough only for very fast transitions. However, with a clever amplification scheme dubbed "electron shelving", even very narrow transitions in a single ion can be detected with almost 100 % efficiency. After pioneering experiments on trapping single ions in 1980 [48, 68], several experimental directions have been pursued, as summarized in Figure 1.1. Trapped ions have enabled very precise measurements of atomic masses and g-factors [62], as well as interesting measurements such as the lifetime of metastable states [73]. Because a single ion represents such a well-isolated quantum system, a series of experiments testing and demonstrating quantum mechanics has been performed (e.g.,[32]). Along the original ideas, accurate atomic clocks are being developed [52], and presently their suitability for the construction of a large-scale quantum computer is being in-

vestigated [36]. Progress in many of these fields was also based on the development of narrow and stable laser sources that are able to interact coherently with the ion and take advantage of the narrow line widths achievable with trapped ions.

This thesis describes an experiment that extends single-ion spectroscopy to the Zeeman levels of the ion. With a combination of optical pumping techniques and electron shelving it is possible to precisely set and detect the spin state of a single ion, without having to optically resolve the Zeeman splitting. We can then directly interact with the spin of the ion by using extremely narrow and precisely tunable RF pulses, and measure very small energy differences.

As indicated in Figure 1.1, this method of RF spectroscopy opens up opportunities for new atomic precision experiments. The original motivation for its development is the possibility of measuring parity nonconservation (PNC) with a single trapped ion, as proposed by my advisor Norval Fortson [23] in 1993.

PNC experiments are a probe into the electroweak interaction, which is described by the standard model of particle physics. By testing whether the standard model gives the correct predictions of PNC, such experiments could reveal the existence of new physics such as supersymmetry, or additional Z_0 bosons.

Electroweak studies are carried out in high-energy experiments and in atomic PNC experiments, and deliver complementary results. To date only one atomic experiment, the Boulder experiment on Cesium [66, 19], has enabled comparison with theory at the sub-1% level, and the apparent 2.5σ deviation from the standard model has caused a great deal of upheaval in the physics community. Since then, previously overlooked corrections have been included in the calculations, and the deviation has disappeared for now. Still, an independent, similarly precise and accurate atomic experiment is much needed to provide a confirmation or challenge of the Boulder experiment.

With the proposed ion PNC experiment, measuring a small energy shift in the Zeeman levels allows us to determine, in the end, the weak charge of the ion nucleus, and it seems plausible to measure the effect to better than 1%, thus providing the

needed alternative PNC measurement.

This experiment is very difficult technically, and a long-term project in scope. The ability to perform precise RF spectroscopy is an important building block, but the main challenge lies in the tight requirements for components like the PNC laser or the localization of the ion, necessary to suppress systematic errors sufficiently. The original proposal envisioned trapping an even isotope of barium or radium, but recently it became clear that the atomic structure of odd isotopes may enable measurement schemes with less severe systematic problems and make construction of a good experiment simpler. In this work we provide initial ideas and a first analysis of such an alternate experiment.

More immediately, RF spectroscopy enables some new atomic structure experiments. For example, if we measure shifts of Zeeman levels caused by off-resonant light, we can obtain ratios of atomic matrix elements to high precision. These matrix elements can be compared to theory, and are essential for an accurate calculation of parity violation. In this thesis we describe such a measurement to better than 0.5% precision, but work is left to be done on characterizing some of the systematic effects of this experiment.

This thesis is organized as follows: In Chapter 2 the theory of light shifts, as they occur throughout this work, is developed. First we focus on simple two-level systems, and then generalize to more complicated level structures. Chapter 3 focuses on theoretical background that is related to ion trap physics. In particular, we review the idea of RF traps, quantum jumps and the existence of dark states, as well as laser cooling. We conclude this chapter with a discussion of the RF-interaction with a spin system. In Chapter 4 we describe the experimental apparatus used to trap an ion and to perform RF experiments. We briefly describe some of the more important experimental components, as well as give quantitative details. Chapter 5 explains the experimental procedure followed to obtain spin resonances with a single ion, along with some numerical computations and sample data that demonstrates

RF spectroscopy in two atomic states of Ba^+, $6S_{1/2}$ and $5D_{3/2}$. Chapter 6 describes the measurement of ratios of light shifts using RF spectroscopy. We calculate the expected light shifts by using approximate, theoretical matrix elements, enumerate the dominant systematic effects, and describe the measurement sequence. Finally, the results to-date for the ratio measurement are presented. The next two chapters focus on review, evaluation and new ideas concerning a single ion PNC experiment. We start in Chapter 7 by introducing atomic PNC experiments. Then, we review the original proposal of a PNC experiment with even isotopes. We give the size of the observable shift with PNC matrix elements recently recalculated, and list the anticipated systematic effects, and compare the performance of Ba^+ and Ra^+ in such an experiment. In Chapter 8 we explain some new ideas using odd barium or radium isotopes for a PNC measurement, including an initial discussion of systematic effects and a possible scheme for RF spectroscopy in the resulting spin-1 systems. Finally, Chapter 9 describes some other future directions for our experiment. We briefly analyze a measurement of quadrupole moments in Ba^+, and point out the possibility of an attractive optical clock when using odd isotopes.

Chapter 2

LIGHT SHIFTS

Many of the measurements in this thesis have, in one way or another, to do with light shifts, which are effects of light on the energy levels in atoms. The present experiment measures shifts caused by off-resonant light, and extracts transition matrix elements from these measurements. Likewise, the PNC scheme relies on shifts caused by light that is resonant with atomic levels. Therefore a survey of the light shifts in atoms is presented here in some detail. First we explore the topic qualitatively, followed by a more quantitative treatment and the examination of some important limiting cases.

2.1 Introduction

Light shifts appear in different regimes and can be visualized and treated with correspondingly different pictures. The most important distinction to make is the one between off-resonant shifts and light shifts caused by resonant light. For a two-level system, the relevant quantities that determine these two regimes are the Rabi frequency Ω, which describes the strength of the coupling between atom and light field, the decay rate Γ of the upper state, and the detuning of the light field from the atomic resonance $\delta = \omega_L - \omega_0$, where ω_L is the frequency of the light field and ω_0 is the atomic resonance frequency.

In the case $\delta \gg \Omega$, the light field is off-resonant. Real transitions between levels are practically absent, and the light field does not mix levels appreciably. As a result, the original atomic states retain their integrity, which means they approximately remain

eigenstates of the atom. Equivalently, the energy structure of the atomic levels does not change. The only obvious effect is a shift of all levels that are connected to other atomic levels via the off-resonant light field.

For a two-level atom, light below resonance will cause the levels to shift apart from each other, while light above resonance will decrease the level resonance. The magnitude of the shifts hereby is proportional to the square of the field that causes Ω. One can liken this shift to the potential energy of a classical dipole moment, induced in an atom by an oscillating electric field. The induced dipole moment acquires a frequency-dependent potential energy in the electric field of the light. For light below the resonance frequency of the dipole, it adiabatically follows the electric field and the two oscillate in phase, lowering the dipole's potential energy. For light above resonance, their oscillation is 180° out of phase and a higher potential energy results. Since we need the electric field to first induce the dipole moment and then again to interact with it, the potential energy is quadratic in the electric field. In fact, such light shifts are also called "dynamic Stark shifts" and are an AC-version of quadratic Stark shifts, in which the atom responds with its dynamic rather than static polarizability to the external field.

In a photon picture these shifts can be understood as stimulated radiative corrections to the energy levels of the atom, involving the absorption and emission of a photon from the incident light field. This correction involves, to lowest order, two processes of stimulated photon creation/annihilation and is therefore quadratic in E, which is consistent with the classical picture. For extremely intense fields, higher-order terms can become significant, leading to a non-linear response of the atom to the light intensity (hyperpolarizability). From the point of view of the light, the forward-scattered field is phase-shifted relative to the incident field by these processes. Such a phase change, when summing over many atoms in a medium, is the origin of the index of refraction of this medium. More details can be found in [11, p.114f].

The case $\Omega \gg \delta, \Omega \gg \Gamma$ leads to resonant level shifts and is considerably more

subtle, affording no classical analogue. Now the light field and the atom are strongly coupled and there is more or less complete Rabi-flopping between the levels connected by the light; the stationary states are now superpositions of the unperturbed atomic eigenstates. The new eigenstates are found by diagonalizing the interaction Hamiltonian. If one is only interested in the composition of the resulting eigenstates, this procedure is sufficient. However, if one wants to understand the energy structure and the resulting possible transitions, one has to include the quantum states of the light field since it is now strongly coupled to the atom. The corresponding picture is that of the "dressed atom", in which the basis states of the system are product states of photon number states and the unperturbed atomic states. As we will see, an infinite periodic ladder of basis states results. The light-atom coupling will now mix those basis states and create a ladder of new eigenstates. For this new ladder, transitions between adjacent ladder elements are allowed and more complicated spectra result. One example is the two additional lines that appear to the spectrum of a two-level system which together with the original resonance make up the so-called Mollow resonance triplet [43], as will be discussed later in more detail.

Generalizing this from a two-level system to light shifts that occur in atomic states with sublevels is not straight-forward. It involves finding the new eigenstates and eigenvalues of the complete interaction Hamiltonian. For two multiplets this problem can be decomposed in terms of effective Hamiltonians that only act among the sublevels of each state.

In the following we will treat off-resonant and near-resonant light shifts quantitatively, considering first simple two-state systems and then generalizing to situations where multiple levels are involved.

2.2 Semiclassical treatment of light-matter interaction

Even though the most generalized treatment of light shifts will require treating the light as a quantized field, we will often work in a semiclassical framework where we describe the atom as a quantum system and the light field as a classical field that acts as a perturbation to the Hamiltonian $\hat{H}_0$ of the atom, where the hat denotes operators. The latter is defined by

$$\hat{H}_0 = \hbar \sum_i \omega_i |i\rangle\langle i| \tag{2.1}$$

where the sum is over all atomic states and $|i\rangle$ are the eigenstates of $\hat{H}_0$ in the Schroedinger picture, with ω_i denoting the corresponding energies.

2.2.1 Density matrix and interaction

A unified treatment of coherent interactions, such as a monochromatic light field, and incoherent interactions, such as spontaneous decay, is possible with the density operator formalism [42]. The density operator, written in terms of the atomic eigenstates, is given by

$$\hat{\rho} = \sum_{ij} \rho_{ij} |i\rangle\langle j| \tag{2.2}$$

Because $\hat{\rho}$ is composed of Schroedinger states, its off-diagonal elements are explicitly time-dependent. The time evolution of $\hat{\rho}$ is given by the Liouville equation

$$\frac{d\hat{\rho}}{dt} = -\frac{i}{\hbar}[\hat{H}_0, \hat{\rho}] + \mathcal{L}_{\text{decay}} \tag{2.3}$$

which is equivalent to Schroedinger's equation except for the term $\mathcal{L}_{\text{decay}}$, which describes incoherent processes. We will ignore this term in the following description because it is negligibly small for all light shifts we consider here.

If there is an additional interaction, the total Hamiltonian $\hat{H}$ is given by

$$\hat{H} = \hat{H}_0 + \hat{H}_{\text{int}} \tag{2.4}$$

In our case this interaction is due to a monochromatic light field, which we write as

$$\boldsymbol{E}(\boldsymbol{r},t) = \boldsymbol{E}_0 \cos(\omega_L t + \boldsymbol{k}\cdot\boldsymbol{r} + \phi) \tag{2.5}$$

It will be convenient to split this field into two (unphysical) parts

$$\boldsymbol{E}(\boldsymbol{r},t) = \boldsymbol{E}^{(-)}(\boldsymbol{r},t) + \boldsymbol{E}^{(+)}(\boldsymbol{r},t) \tag{2.6}$$

with

$$\boldsymbol{E}^{(\pm)}(\boldsymbol{r},t) = \frac{1}{2}\boldsymbol{E}_0 e^{\pm i(\omega_L t + \boldsymbol{k}\cdot\boldsymbol{r} + \phi)} \tag{2.7}$$

In general, the interaction Hamiltonian can be written as:

$$\hat{H}_{\text{int}} = \sum_{ij}(\frac{\hbar}{2}\Omega_{ij}e^{-i\omega_L t} + \frac{\hbar}{2}\Omega_{ij}^{*}e^{i\omega_L t})|j\rangle\langle i| \tag{2.8}$$

where Ω_{ij} and Ω_{ij}^{*} are transition matrix elements corresponding to the spatial parts of $\boldsymbol{E}^{(-)}(\boldsymbol{r},t)$ and $\boldsymbol{E}^{(+)}(\boldsymbol{r},t)$, respectively. The first term contains an exponential that on resonance will cancel the exponential from the Schroedinger states and will therefore have a strong effect on the evolution of $\hat{\rho}$. However, for near-resonant light the second, "counter-rotating" term leads to a rapidly oscillating term that can be neglected because its effect on the evolution of $\hat{\rho}$ is much smaller than that of the "co-rotating" term. Doing so is called the rotating wave approximation (RWA) and will be assumed from hereon. In essence, only the field $\boldsymbol{E}^{(-)}(\boldsymbol{r},t)$, which by itself is not a physical field, contributes to the interaction. We can write

$$\boldsymbol{E}^{(-)}(\boldsymbol{r},t) = \frac{1}{2}\boldsymbol{E}(\boldsymbol{r})e^{-i\omega_L t} \text{ with} \tag{2.9}$$

$$\boldsymbol{E}(\boldsymbol{r}) = \boldsymbol{E}_0 e^{-i\boldsymbol{k}\cdot\boldsymbol{r} - i\phi} \tag{2.10}$$

In general, the electrical part of the interaction energy depends on the integral of the charge density of the electron wave function and the spatial part of the electric field. However, for optical transitions the wavelength of the field is large compared to the size of the electron's wave function and therefore its spatial variation is small. We can

thus expand the interaction around $\boldsymbol{r} = 0$ in terms of the field, yielding the multipole expansion (see [33] and App.A.3)

$$W = q\Phi(0) - \boldsymbol{d}\cdot\boldsymbol{E}(0) - \frac{1}{2}\sum_{ij} Q_{ij}\,\partial_i E_j(\boldsymbol{r})|_{\boldsymbol{r}=0} + \ldots \tag{2.11}$$

with

$$d_i = ex_i \tag{2.12}$$

$$Q_{ij} = e(x_i x_j - \frac{1}{3}r^2\delta_{ij}) \tag{2.13}$$

There is a corresponding expansion for the magnetic multipoles which we don't consider here. The sum (2.11) is made of scalar products of two cartesian tensors, with growing rank. Because $|\frac{1}{E}\frac{dE}{dx}|a_0 \ll 1$, where a_0 is the size of an atom, the terms get progressively smaller. In an atom (or ion) the first term averages to zero, and the second term is the electric dipole term, corresponding to an E1 transition. The third term gives rise to an electric quadrupole (E2) transition. If we pick the E1 term here, we can write with these definitions

$$\Omega_{ij} = \frac{1}{\hbar}\langle j|\boldsymbol{E}_0\cdot\hat{\boldsymbol{d}}|i\rangle, \tag{2.14}$$

where Ω_{ij} are the transition matrix elements caused by the light field expressed in frequency units, also called Rabi frequencies.

It is convenient to eliminate the explicit time dependence of $\hat{H}_{\rm int}$ by a transformation into a frame that is corotating with ω_L. This is not an approximation and can be done with an appropriately chosen unitary transformation $\mathcal{U}$. The operators transform according to

$$\hat{\tilde{\rho}} = \mathcal{U}\hat{\rho}\mathcal{U}^\dagger \tag{2.15}$$

$$\hat{\mathcal{H}} = \mathcal{U}\hat{H}\mathcal{U}^\dagger - i\hbar\mathcal{U}\frac{d\mathcal{U}^\dagger}{dt} \tag{2.16}$$

Observable populations are independent of this transformation. The transformation does make the resulting eigenstates have energy differences that are shifted by ω_L relative to their difference in the lab frame.

2.2.2 Application to a two-state system

We can now use this formalism to examine the simplest of all cases, a two-state system without decay, made up of the states $|a\rangle$ and $|b\rangle$. Using the full formalism is overkill in this simple case and more elegant ways of writing and solving this problem exist, such as likening it to a spin resonance experiment (see Section 3.5), but this illustrates how a general case would be treated. Written in matrix form, the corresponding quantities from the last section become:

$$\hat{H}_0 = \hbar \begin{pmatrix} -\omega_0/2 & 0 \\ 0 & \omega_0/2 \end{pmatrix}, \Psi = \begin{pmatrix} a \\ b \end{pmatrix} \tag{2.17}$$

$$\hat{H}_{\text{int}} = \frac{\hbar}{2} \begin{pmatrix} 0 & \Omega e^{i\omega_L t} \\ \Omega e^{-i\omega_L t} & 0 \end{pmatrix} \tag{2.18}$$

$$\Omega = \frac{eE_0}{\hbar} \langle b|\hat{r}|a\rangle \tag{2.19}$$

After transforming into a rotating frame using

$$\mathcal{U} = \begin{pmatrix} e^{-i\omega_L t/2} & 0 \\ 0 & e^{i\omega_L t/2} \end{pmatrix} \tag{2.20}$$

we end up with a transformed total Hamiltonian

$$\mathcal{H} = \frac{\hbar}{2} \begin{pmatrix} -\delta & \Omega \\ \Omega & \delta \end{pmatrix} \tag{2.21}$$

Besides removing the time dependence of the interaction, the transformation also shifts the energies of the transformed states $|\tilde{a}\rangle$ and $|\tilde{b}\rangle$ by $+\omega_L/2$ and $-\omega_L/2$, respectively, corresponding to the exponentials in Eq.(2.20). To recover the energies of the states in the lab frame, one has to first apply the reverse transformation.

Insights about the dynamics of this system can be gained by working in the basis $\{|\tilde{a}\rangle, |\tilde{b}\rangle\}$. According to Eq.(2.3) this Hamiltonian leads to the following equations of

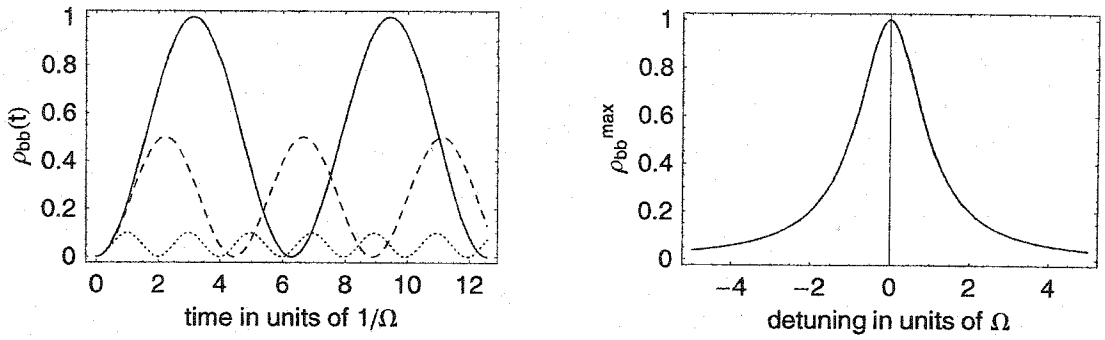

Figure 2.1: Left graph shows $\rho_{bb}(t)$ for $\delta = 0$ (solid), $\delta = \Omega$ (dashed) and $\delta = 3\Omega$ (dotted). The right graph shows the maximum value of ρ_{bb} as a function of detuning.

motion for the transformed elements of the density matrix operator $\hat{\tilde{\rho}}$ in that basis:

$$\begin{aligned}
\tilde{\rho}'_{aa}(t) &= -\frac{i}{2}\Omega[\tilde{\rho}_{ab}(t) - \tilde{\rho}_{ba}(t)] \\
\tilde{\rho}'_{ab}(t) &= \frac{i}{2}\Omega[\tilde{\rho}_{bb}(t) - \tilde{\rho}_{aa}(t)] + 2i\delta\tilde{\rho}_{ab}(t) \\
\tilde{\rho}'_{ba}(t) &= \frac{i}{2}\Omega[\tilde{\rho}_{aa}(t) - \tilde{\rho}_{bb}(t)] - 2i\delta\tilde{\rho}_{ba}(t) \\
\tilde{\rho}'_{bb}(t) &= \frac{i}{2}\Omega[\tilde{\rho}_{ab}(t) - \tilde{\rho}_{ba}(t)]
\end{aligned} \tag{2.22}$$

These are coupled first-order equations, also called Bloch equations. If n is the number of atomic states, there are n^2 Bloch equations. Generally one can solve these equations numerically, but this case is simple enough for analytical solutions to be found. For the initial conditions

$$\tilde{\rho}(0) = \begin{pmatrix} 1 & 0 \\ 0 & 0 \end{pmatrix} \tag{2.23}$$

the excited-state population $\tilde{\rho}_{bb}(t)$ is given by

$$\tilde{\rho}_{bb}(t) = \frac{\Omega^2}{\tilde{\Omega}^2}\sin^2\frac{\tilde{\Omega}t}{2} \tag{2.24}$$

$$\tilde{\Omega}^2 = \Omega^2 + \delta^2, \tag{2.25}$$

where $\tilde{\Omega}$ is sometimes called the generalized Rabi frequency. We see that in this

basis, the light field causes the population to oscillate between the two states with a frequency $\tilde{\Omega}$ and an amplitude $\frac{\Omega^2}{\tilde{\Omega}^2}$. The oscillation is complete on resonance, and becomes smaller (and faster) as the detuning δ is increased.

2.3 Off-resonant shifts in a two-state system

Now we look at the same system, but use its stationary states as a basis. As before, the Hamiltonian in a coordinate system rotating with the light field ω_L is calculated in Eq.(2.21) is given by

$$\mathcal{H} = \frac{\hbar}{2}\begin{pmatrix} -\delta & \Omega \\ \Omega & \delta \end{pmatrix} \tag{2.26}$$

Solving the eigenvalue problem gives the following results:

$$E_{\tilde{1},\tilde{2}} = \pm\frac{\hbar}{2}\tilde{\Omega} \tag{2.27}$$

$$\begin{aligned} |\tilde{1}\rangle &= \cos\theta|\tilde{a}\rangle + \sin\theta|\tilde{b}\rangle \\ |\tilde{2}\rangle &= -\sin\theta|\tilde{a}\rangle + \cos\theta|\tilde{b}\rangle \end{aligned} \tag{2.28}$$

$$\text{with } \tan 2\theta = -\frac{\Omega}{\delta} \text{ and } \tilde{\Omega}^2 = \Omega^2 + \delta^2$$

$\{|\tilde{1}\rangle, |\tilde{2}\rangle\}$ are linear combinations of the original states and form a stationary, coupled basis. The angle θ parameterizes the degree of state mixing, and $\sin^2\theta$ gives the probability that the system is found in the admixed state. We can see that in the off-resonant limit $\delta \gg \Omega$, $\mathcal{H}$ is almost diagonal and $\sin\theta \approx \frac{\Omega}{2\delta}$, $\cos\theta \approx 1$, which means that the levels are not mixed appreciably. In this limit the probability to find the system in the admixed state is given by

$$\sin^2\theta \cong \frac{\Omega^2}{4\delta^2}, \tag{2.29}$$

decreasing quadratically in δ. It then makes sense to associate the two energies Eq.(2.27) with the original levels $|\tilde{a}\rangle$ and $|\tilde{b}\rangle$. Then, accounting for the transformation into the rotating frame (see Section 2.2.2), we can write the energies for the states

$|a\rangle$ and $|b\rangle$ as

$$E_a = \frac{\hbar}{2}(-\omega_L + \tilde{\Omega}) \approx -\frac{\hbar}{2}\omega_0 + \frac{\hbar\Omega^2}{4\delta}$$
$$E_b = \frac{\hbar}{2}(+\omega_L - \tilde{\Omega}) \approx +\frac{\hbar}{2}\omega_0 - \frac{\hbar\Omega^2}{4\delta} \tag{2.30}$$

The magnitude of the off-resonant light shift (in frequency units) experienced by each level is therefore

$$\Delta = \frac{\Omega^2}{4\delta} \tag{2.31}$$

Eqs.(2.30) also show that for light detuned *below* resonance the levels are shifted *apart* from each other, and for light detuned *above* resonance the levels are shifted *towards* each other.

All of this assumes the rotating wave approximation. As the detuning is made larger and approaches a sizeable fraction of ω_0, this approximation ceases to be valid since now both terms in Eq.(2.8) contribute significantly to the dynamics of the system, and for accurate results we have to take both parts into account: The detuning $\delta = \omega_L - \omega_0$ then becomes comparable to that of the counter-rotating wave, $\delta^c = -\omega_L - \omega_0$.

An interesting effect can result from the counter-rotating term: Ordinarily one can't observe light shifts with the field that causes them. Instead its presence creates new states and energies that can then be observed by a second field. One exception is the case where the counter-rotating part of a field causes an observable shift. The two terms in Eq.(2.8) act like two independent fields, where the off-resonant field shifts the resonance, and the near-resonant field can be used to observe this shift, for example by performing some form of spectroscopy. This small energy shift between the two levels is sometimes called the Bloch-Siegert shift. According to Eq.(2.30) and for $\omega_L = \omega_0$, $\delta^c = -2\omega_0$, the levels are shifted apart, with the shift for each level given by

$$\Delta^{\mathrm{BS}} = \frac{\Omega^2}{4\delta^c} = \frac{\Omega^2}{8\omega_0}. \tag{2.32}$$

For optical transitions, the shift $\frac{\Omega^2}{8\omega_0}$ is not appreciable, but for transition frequencies in the RF or lower it can become important.

2.4 Near-resonant shifts for a two-level system

If we consider a more general case where Ω is not necessarily small compared to δ, the present description runs into ambiguities: On resonance, do the levels get shifted by $+\Omega$ or $-\Omega$? Or does both happen simultaneously? Then there would be four states in the system, rather than the original two.

To resolve these issues and to capture all the features of an atom in a light field that is on or close to resonance and not dominated by spontaneous decay ($\Omega \gg \delta, \Gamma$), we have to include the quantized light field in our description rather than just treating it as a classical wave. The picture that emerges is that of the "dressed atom". It is presented in [11] in detail and we will summarize some relevant parts here.

2.4.1 Dressed states

We pick the simplest case of a single radiation mode in a coherent state at frequency ω_L, and a two-level system as before. Now $\hat{H}_0$ is made up of two parts, one for the atom and one for the light:

$$\hat{H}_A = \hbar\omega_0 |b\rangle\langle b| \tag{2.33}$$

$$\hat{H}_L = \hbar\omega_L (a_L^\dagger a_L + \frac{1}{2}), \tag{2.34}$$

where $a_L^\dagger$ and a_L are photon creation and annihilation operators. The eigenstates of $\hat{H}_0 = \hat{H}_A + \hat{H}_L$ are now labelled by two quantum numbers: the number N of photons in the mode, and the atomic quantum number a or b. The result is an infinite ladder of eigenstates. One can identify manifolds consisting of states $|a, N+1\rangle$ and $|b, N\rangle$; the manifolds themselves are separated by ω_L (see Figure 2.2). In the electric dipole approximation and neglecting all spatial orientation, $\hat{H}_{int} = -\hat{d}\hat{E}$, and the operators

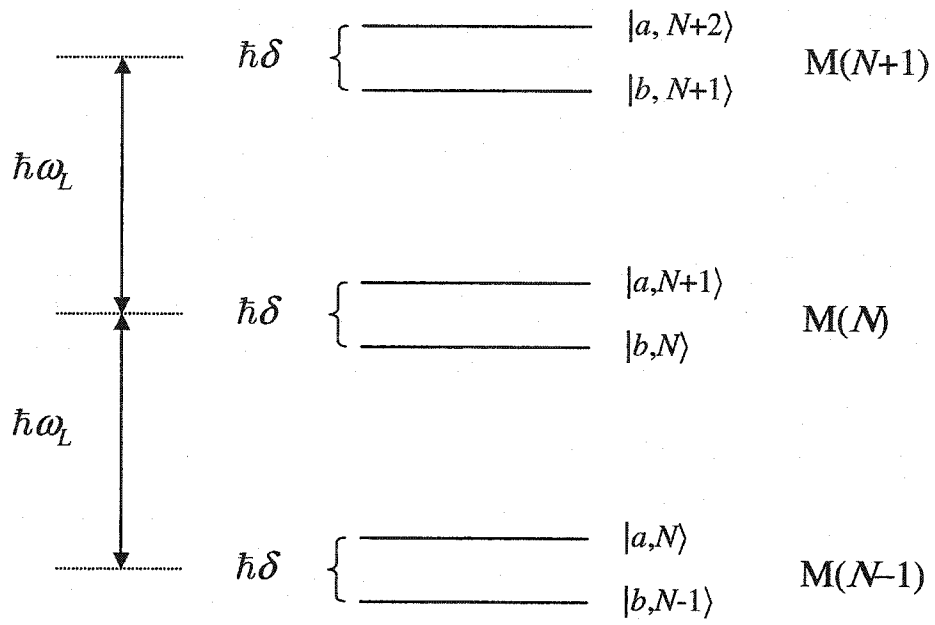

Figure 2.2: Uncoupled dressed levels of a two-level system and a single radiation mode. M(N) refers to the manifolds, labelled by photon number N.

for field and atom are given by

$$\hat{E} = \sqrt{\frac{\hbar\omega_L}{2\varepsilon V}}(a_L + a_L^\dagger) \tag{2.35}$$

$$\hat{d} = d_{ab}(\mathcal{S}_+ + \mathcal{S}_-), \tag{2.36}$$

$$\mathcal{S}_+ = |b\rangle\langle a| \quad , \quad \mathcal{S}_- = |a\rangle\langle b| \tag{2.37}$$

where V is the mode volume of the field. Thus $\hat{H}_{\text{int}}$ can be written as

$$\hat{H}_{\text{int}} = -\hat{d}\hat{E} \tag{2.38}$$

$$= d_{ab}g(\mathcal{S}_+ a + \mathcal{S}_- a^\dagger + \mathcal{S}_+ a^\dagger + \mathcal{S}_- a) \tag{2.39}$$

$$\text{with} \qquad g = \sqrt{\frac{\hbar\omega_L}{2\varepsilon V}} \tag{2.40}$$

The first two terms of $\hat{H}_{\text{int}}$ couple the states $|a, N+1\rangle$ and $|b, N\rangle$. For $\delta = 0$, this is a resonant process for which the corresponding exponentials cancel. The last two terms cause off-resonant effects and omitting them amounts to the RWA in this fully

quantized description. The resonant coupling can then be written as

$$\langle b, N|\hat{H}_{int}|a, N+1\rangle = d_{ab}g\sqrt{N+1} \tag{2.41}$$

In the laser mode approximation ($\langle N\rangle \gg \Delta N \gg 1$, where ΔN is the spread of photon number states of the light field), $\sqrt{N+1}$ can be replaced by the average $\sqrt{\langle N\rangle}$ and the coupling can be expressed in terms of the (classical) electric field since $E_0 = 2g\sqrt{\langle N\rangle}$:

$$\langle b, N|\hat{H}_{int}|a, N+1\rangle = \frac{1}{2}E_0 d_{ab} = \frac{1}{2}\hbar\Omega \tag{2.42}$$

The resulting total Hamiltonian, written in matrix form with the basis $\{|b, N\rangle, |a, N+1\rangle\}$ immediately looks identical to (2.26):

$$\mathcal{H} = \frac{\hbar}{2}\begin{pmatrix} -\delta & \Omega \\ \Omega & \delta \end{pmatrix} \tag{2.43}$$

The eigenvalues and vectors are then given by Eqs.(2.27,2.28):

$$E_{1,2} = \frac{\hbar}{2}(-\delta \pm \tilde{\Omega}) \tag{2.44}$$

$$\begin{aligned} |1, N\rangle &= \cos\theta|a, N+1\rangle + \sin\theta|b, N\rangle \\ |2, N\rangle &= -\sin\theta|a, N+1\rangle + \cos\theta|b, N\rangle \\ \tan 2\theta &= -\frac{\Omega}{\delta}, \end{aligned} \tag{2.45}$$

where $|1, N\rangle$ are superposition states made from states in the manifold M(N).

In the laser mode approximation the coupling Ω is approximately independent of N. Therefore the coupled manifolds around N, two of which are shown in Figure (2.3), all have the same energy splitting, and form a regular ladder just as the uncoupled state do. And since only neighboring manifolds can have allowed transitions between them, Figure (2.3) gives, for all practical purposes, a complete picture of the situation. Conversely, we could still use the previous formalism which neglected the light field to find the new eigenstates and energies. But we have to realize that really a ladder

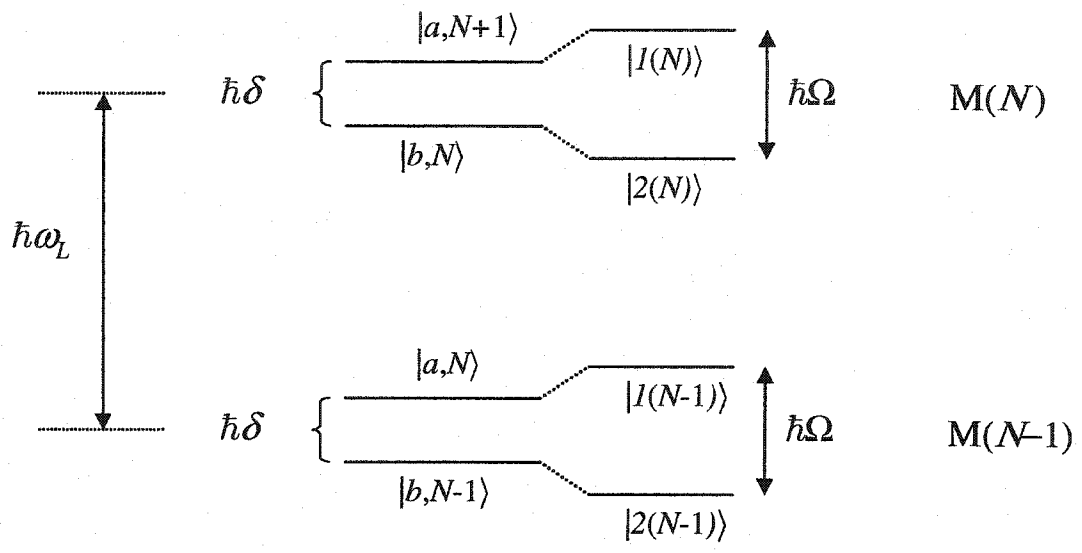

Figure 2.3: Coupled dressed levels of a two-level system and a single radiation mode.

of those states exist between which, in general, transitions are possible that didn't exist before.

For the uncoupled states (i.e., if we assume that $\hat{H}_{int} = 0$), the only transitions that can be excited by a probe laser (one that is weak enough not to perturb the system it is probing) are $|a, N\rangle \longleftrightarrow |b, N\rangle$ between adjacent manifolds. This is because the selection rules require a change in the atomic quantum number *and* $\Delta N = 0$. The latter rule is observed because the probe laser has a different mode and thus can't change N. When just looking at the atomic quantum number, all these transitions are degenerate and collapse into the familiar transition $|a\rangle \longleftrightarrow |b\rangle$, resonant at ω_0. On the other hand, with the light field at ω_0 interacting with the atom, four transitions are allowed between the coupled states. We can read off the resonance frequencies

from Figure 2.3 and find

Transition	resonant at
$\|1,N\rangle \longleftrightarrow \|1,N-1\rangle$	ω_0
$\|2,N\rangle \longleftrightarrow \|2,N-1\rangle$	ω_0
$\|1,N\rangle \longleftrightarrow \|2,N-1\rangle$	$\omega_0+\Omega$
$\|2,N\rangle \longleftrightarrow \|1,N-1\rangle$	$\omega_0-\Omega$

(2.46)

The process of spontaneous emission is also complicated by this additional structure; corresponding to the transitions (2.46) there is now a three-peaked fluorescence spectrum, which is also called the Mollow triplet [43]. Spontaneous emission can be interpreted as a cascading process down the ladder, in which photons from the laser mode are converted into scattered photons.

If the light is far detuned, the states $|1,N\rangle$,$|2,N\rangle$ approach the uncoupled states. They still have a slightly different energy than the uncoupled states, where the energy shift is the off-resonant light shift calculated before. Still, even off-resonant light introduces additional features that are not described by just looking at the atom: The slight admixtures into the main states lead to the existence of transition amplitudes between, for example, state $|a,N\rangle$ (which has an admixture of $|b,N-1\rangle$) and $|a,N-1\rangle$. These amplitudes are therefore resonant at the laser frequency. The levels from which these transitions appear to occur from (when ignoring the dressed-state ladder) are also called *virtual levels*. However, in the dressed (complete) picture these are as real as any other levels. Spontaneous decay from these virtual levels are the physical origin of light scattering processes. Rayleigh scattering, for example, is spontaneous emission into the light-perturbed ground state (so that $\omega_{\rm sc}=\omega_L$ and the scattering is elastic) when the light is tuned far *below* resonance. The inelastic analog is called Raman scattering, and is labelled Stokes Raman scattering or anti-Stokes Raman scattering, depending on whether $\omega_{\rm sc}$ is smaller or larger than ω_L.

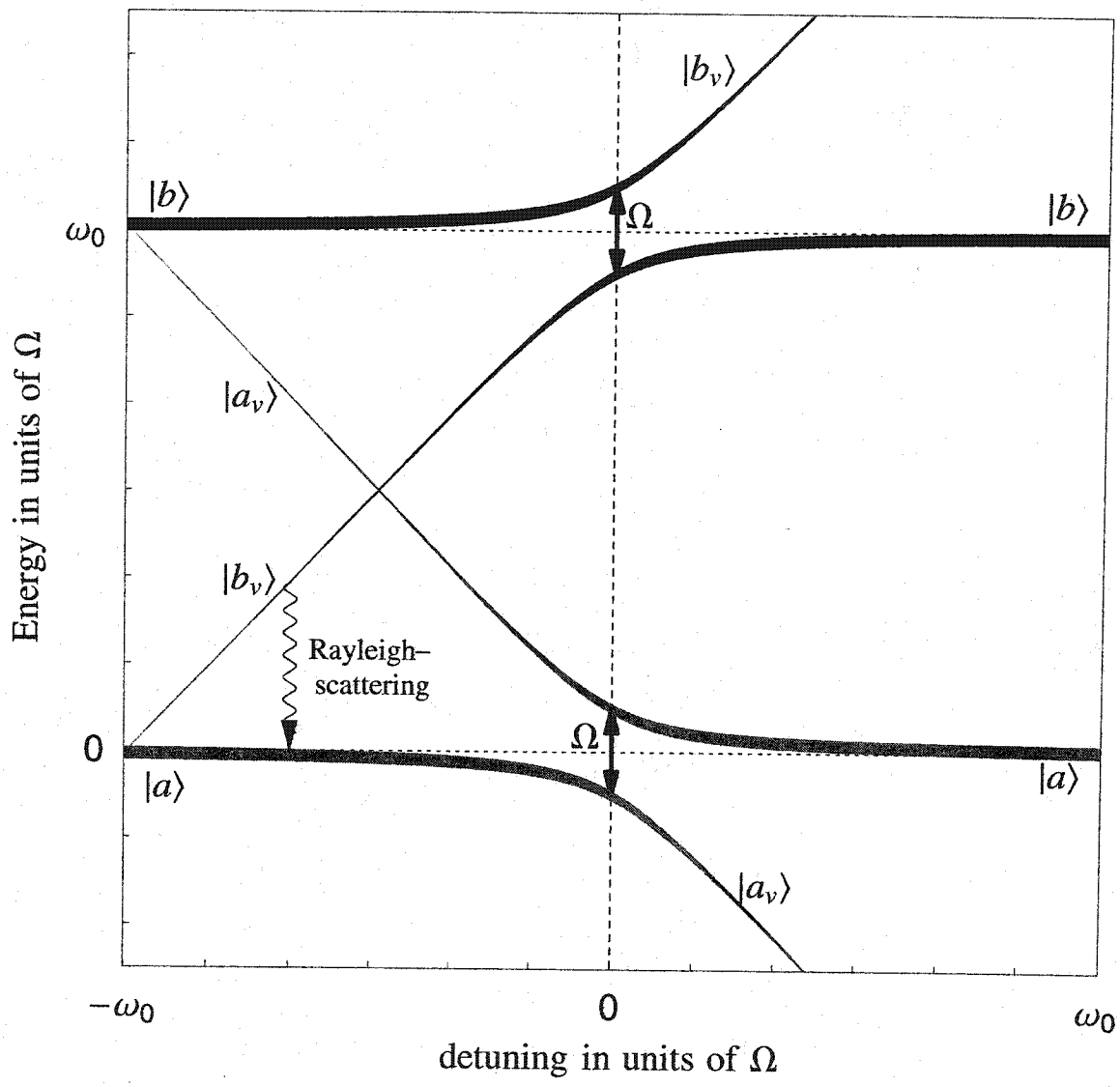

Figure 2.4: Energy levels of a two-level atom in a light field with detuning δ from resonance ω_0. Thickness of the lines indicate the degree to which the correspondingly labelled state $|a\rangle$ or $|b\rangle$ is mixed into the level (see Eq.(2.47)). For this graph we chose $\omega_0/\Omega = 6$, but for a typical optical transition, $\omega_0 \gg \Omega$. Characteristic for the region of strong mixing is an anti-crossing of the involved levels.

2.4.2 A visualization for dressed levels

We now try to visualize the dressed atom levels in a way that retains as much compatibility as possible with a bare atomic level diagram, showing their dependence on the frequency of the light field. For large detunings this can be done by drawing the atomic levels that belong to two adjacent manifolds with the same photon number, $|a, N\rangle$ and $|b, N\rangle$, ignoring the small admixture that they have. The other two levels, $|a, N+1\rangle$ and $|b, N-1\rangle$, would be irrelevant were it not for their small admixtures, $\epsilon|b, N\rangle$ and $\epsilon|a, N\rangle$ respectively. These admixtures, displaced from the "main" $|a, N\rangle$ and $|b, N\rangle$ by ω_L, represent the virtual levels. Therefore we define:

$$\begin{aligned} |a\rangle &\equiv |a, N\rangle + \epsilon|b, N-1\rangle \\ |b\rangle &\equiv |b, N\rangle + \epsilon|a, N+1\rangle \\ |a_v\rangle &\equiv \epsilon|a, N\rangle + |b, N-1\rangle \\ |b_v\rangle &\equiv \epsilon|b, N\rangle + |a, N+1\rangle \end{aligned} \tag{2.47}$$

In the region of strong mixing ($\delta \lesssim \Omega$) these state designations lose their meaning and we would have to call the states $|1,(N-1)\rangle$,$|2,(N-1)\rangle$,$|1,(N)\rangle$,$|2,(N)\rangle$ as in the previous section. Figure 2.4 shows the resulting picture. One could also say that the states $|a\rangle$ and $|b_v\rangle$ are the *same* states when only looking at the atomic part. They are distinguished only by one more or less photon in the light field. The same is true for $|b\rangle$ and $|a_v\rangle$. Even though these are pairwise identical states, transitions between them now can occur because of their slight admixture and their energy separation of ω_L.

When making the light more and more resonant, the mixture of states gets more and more balanced and their energy approaches that of the original $|a\rangle$ and $|b\rangle$ states, up to $\pm\frac{1}{2}\Omega$. On resonance they contain an even mixture of $|a\rangle$ and $|b\rangle$. On the other side of the resonance, with this notation, virtual and real levels reverse roles and the previously "virtual" levels approach the unperturbed energy of the original states.

Also shown in the graph is a visualization of off-resonant scattering from a virtual

level.

2.4.3 Adiabatic state transfer

In the PNC measurement we are utilizing the large shifts of $\Delta = \pm\Omega/2$ by using resonant light. One problem one has to solve is to make sure that an atom initially prepared in a given atomic state ($6S_{1/2}$, for example) will remain in that state after the PNC measurement is finished, so that we can do a spin state analysis on that state. It is not obvious that this will happen because the light field turned on during the PNC interaction will strongly mix the two states it is resonantly connecting (in the case of Ba^+, $6S_{1/2}$ and $5D_{3/2}$). In fact, if one would suddenly turn on resonant light in our two-level system prepared in the ground state, the atom would evolve according to

$$|\Psi(t)\rangle = \cos\Omega t|a\rangle + \sin\Omega t|b\rangle, \tag{2.48}$$

ignoring the photon labels. When turning off the light, the ion is, in general, left in a superposition state of $|a\rangle$ and $|b\rangle$ instead of state $|a\rangle$ alone. In order to prevent this, one could start the light with large negative detuning and by slowly decreasing the detuning "move" the system adiabatically along state $|a\rangle$ into resonance. After driving some RF transition the process could be reversed and the atom would end up in $|a\rangle$ where it had started. In fact, if we were to end the process by making δ positive, we would end up with the virtual state of $|a_v\rangle$, which is equivalent to $|b\rangle$. We would have essentially caused a population inversion, and the procedure would be called adiabatic rapid passage [42]. Since it is the ratio δ/Ω that determines the x coordinate in Figure 2.4, there is an alternative, and more practical way of achieving the same goal: instead of changing the detuning one can slowly ramp up (and down) the laser intensity, provided that the laser is detuned somewhat from resonance.

2.5 Generalization to multiplets

2.5.1 Near-resonant shifts for two multiplets with degenerate sublevels

In a real atom, the two levels $|a\rangle$ and $|b\rangle$ often contain multiple sublevels that have energy separations small compared to Ω and are therefore all part of the resonant interaction. In general this means there will be mixing of multiple levels and finding the shifted energies amounts to solving an eigenvalue problem. Again the couplings between sublevels $|a, m\rangle$ and $|b, n\rangle$ can be written in terms of a $n \times m$ matrix version of the Rabi-frequency, $\mathbf{\Omega}$, with elements

$$\Omega_{nm} = \frac{1}{\hbar}\langle b, n|\boldsymbol{E} \cdot \hat{\boldsymbol{d}}|a, m\rangle. \tag{2.49}$$

In the state vector $\Psi = (\boldsymbol{a}, \boldsymbol{b})^T$, $\boldsymbol{a}$ and $\boldsymbol{b}$ are now m and n column vectors, and the Hamiltonian Eq.(2.43) is generalized to the $(m+n) \times (m+n)$ matrix

$$\mathcal{H} = \frac{\hbar}{2}\begin{pmatrix} -\delta\,\mathbb{I}_{m\times m} & \mathbf{\Omega}^\dagger \\ \mathbf{\Omega} & \delta\,\mathbb{I}_{n\times n,} \end{pmatrix} \tag{2.50}$$

where $\mathbb{I}$ is the identity matrix. Diagonalizing this Hamiltonian will give the new eigenstates and eigenvectors of the system. We can then relabel the states to include photon states and can draw two manifolds of such states, if we are interested in a dressed-state picture.

In general, diagonalizing $\mathcal{H}$ can be hard and its solutions don't lend themselves to a very intuitive interpretation. But by rewriting the problem in terms of eigenvalue problems that pertain to each level individually, we can gain more insight into the structure of the resulting light shifts. The following has been described in more detail in [55].

If the usual eigenvalue equation is written in its squared form,

$$\mathcal{H}^2|\Psi\rangle = \lambda^2|\Psi\rangle \tag{2.51}$$

the problem is reduced to a block-diagonal structure since

$$\mathcal{H}^2 = \frac{\hbar^2}{4}\begin{pmatrix} \delta^2\,\mathbb{I}_{m\times m} + \boldsymbol{\Omega}^\dagger\boldsymbol{\Omega} & 0 \\ 0 & \delta^2\,\mathbb{I}_{n\times n} + \boldsymbol{\Omega}\boldsymbol{\Omega}^\dagger \end{pmatrix} \tag{2.52}$$

As a result, the eigenvalue equation can be decoupled into equations involving only $\boldsymbol{a}$ or $\boldsymbol{b}$:

$$\mathcal{H}^2|\Psi\rangle = \lambda^2\begin{pmatrix}\boldsymbol{a}\\ \boldsymbol{b}\end{pmatrix} = \frac{\hbar^2}{4}\begin{pmatrix}(\delta^2\,\mathbb{I}_{n\times n} + \boldsymbol{\Omega}^\dagger\boldsymbol{\Omega})\boldsymbol{a}\\ (\delta^2\,\mathbb{I}_{m\times m} + \boldsymbol{\Omega}\boldsymbol{\Omega}^\dagger)\boldsymbol{b}\end{pmatrix} \tag{2.53}$$

These two equations are themselves eigenvalue problems of an $m \times m$ matrix $\boldsymbol{\Omega}^\dagger\boldsymbol{\Omega}$, and an $n \times n$ matrix $\boldsymbol{\Omega}\boldsymbol{\Omega}^\dagger$. Written in terms of eigenvalues

$$\lambda^* = \frac{4}{\hbar^2}\lambda^2 - \delta^2 \tag{2.54}$$

these eigenvalue equations simply read

$$(\boldsymbol{\Omega}^\dagger\boldsymbol{\Omega})\boldsymbol{a} = \lambda^*\boldsymbol{a} \tag{2.55}$$

$$(\boldsymbol{\Omega}\boldsymbol{\Omega}^\dagger)\boldsymbol{b} = \lambda^*\boldsymbol{b} \tag{2.56}$$

where $\boldsymbol{a}$ and $\boldsymbol{b}$ are eigenvectors corresponding to the eigenvalues λ^*. $\boldsymbol{\Omega}^\dagger\boldsymbol{\Omega}$ can be considered the near-resonant "effective" Hamiltonian: It acts only within one multiplet, yet captures the effect of the interaction with the other multiplet. Unlike the off-resonant effective Hamiltonian that we will introduce later, its eigenvalues don't directly give the light shifts; instead, Eq.(2.54) must be used.

Using this formalism, the following properties of the eigenvalues and eigenvectors of $\mathcal{H}$ can be proven [55, p.161ff]:

1. λ^* is positive and real.

2. For each non-zero eigenvalue λ^* there are two eigenvalues and two corresponding eigenvectors of H:

$$\lambda_\pm = \pm\tfrac{\hbar}{2}\sqrt{\lambda^* + \delta^2} \tag{2.57}$$

$$\Psi_\pm = \begin{pmatrix} \boldsymbol{a} \\ \boldsymbol{b}_\pm \end{pmatrix} \quad \text{with} \tag{2.58}$$

$$\boldsymbol{b}_\pm = \tfrac{\boldsymbol{\Omega}^\dagger}{\frac{2}{\hbar}\lambda_\pm + \delta}\boldsymbol{a} \tag{2.59}$$

The eigenvalue equations (2.55,2.56) have the same non-zero eigenvalues λ^*.

3. For each $\lambda^* = 0$ in the eigenvalue equation Eq.(2.55) for $\boldsymbol{a}$, there is one eigenvector of the form

$$\Psi = \begin{pmatrix} a \\ 0 \end{pmatrix} \tag{2.60}$$

with $\lambda = 0$ and $\boldsymbol{\Omega a} = 0$. In the same way, for each $\lambda^* = 0$ in Eq.(2.56) for b, there is one eigenvector $\Psi = (\boldsymbol{0}, \boldsymbol{b})^T$ with $\lambda = 0$ and $\boldsymbol{\Omega}^\dagger \boldsymbol{b} = 0$.

There are several causes for the existence of zero eigenvalues: If $m \neq n$ (pick for concreteness the case $m > n$), the matrix $\boldsymbol{\Omega}^\dagger\boldsymbol{\Omega}$ that applies to level a will have a null space of $m-n$ and correspondingly there will be that many zero eigenvalues. The remaining n eigenvalues are identical to those of $\boldsymbol{\Omega}\boldsymbol{\Omega}^\dagger$ and can yield additional zeros, for example if some sublevels are completely uncoupled. The eigenstates a or b corresponding to a zero eigenvalue will in general be superpositions of the original, unperturbed sublevels, depending on the solutions of Eqs.(2.55,2.56). The corresponding states (2.60) are "uncoupled" in the sense that they only contain states from one manifold. Because $\lambda = 0$ for these states, they do not experience a light shift. These are also the same states that become "dark states" when spontaneous decay is present, because excitation out of these states is absent (see Section 3.3).

Note that the required $n + m$ eigenstates of the total Hamiltonian come out correctly: There are $2n$ eigenstates from the n shared eigenvalues of the two effective Hamiltonians, and $m - n$ states from the level with the greater multiplicity, which adds up to $m + n$.

2.5.2 *Near-resonant shifts for two multiplets with Zeeman splitting*

When magnetic fields are splitting the components of the multiplets, the problem cannot in general be broken down with the formalism of effective Hamiltonians. In particular, the result (3) is no longer valid and there are no longer completely uncoupled states. In fact, this effect allows us to prevent pumping into dark $5D_{3/2}$ states when the ion is in the fluorescence cycle by applying a sufficiently strong magnetic field (see Section 3.3). Of course there can still be "trivial" dark states by applying an interaction $\mathbf{\Omega}$ that leaves some sublevels uncoupled — which is done in the experiment when optically pumping into magnetic sublevels of $6S_{1/2}$ and $5D_{3/2}$ with circularly polarized light.

In the presence of a magnetic field $\boldsymbol{B}$, Hamiltonian Eq.(2.50) takes on the generalized form

$$\mathcal{H} = \begin{pmatrix} -\frac{\hbar\delta}{2}\mathbb{I}_{m\times m} + \boldsymbol{J_a}\cdot\boldsymbol{B} & \frac{\hbar}{2}\mathbf{\Omega} \\ \frac{\hbar}{2}\mathbf{\Omega}^\dagger & \frac{\hbar\delta}{2}\mathbb{I}_{n\times n} + \boldsymbol{J_b}\cdot\boldsymbol{B} \end{pmatrix} \tag{2.61}$$

where $\boldsymbol{J_{a,b}}$ is the appropriate representation of the angular momentum operator for levels $\boldsymbol{a}, \boldsymbol{b}$. As before, diagonalizing this Hamiltonian will lead to the complete solution of the problem. In two limiting situations simplifications can be made:

1. $\omega_B \gg \Omega$, where Ω is the size of the couplings of $\mathbf{\Omega}$ the order of magnitude of $\sqrt{\lambda^*}$. In this case the magnetic splitting is much larger than the light shifts and only one pair of sublevels is strongly coupled for a given detuning δ; the Zeeman splitting removes any other states much further than Ω. The two coupled states can be described like the two-state system in Section 2.4. Off-resonant shifts of the two coupled states to the remaining states can then be treated as a further perturbation.

2. $\Omega \gg \omega_B$

   If the light shifts are much larger than the Zeeman splitting, the sublevels are

near-degenerate from the point of view of the incident light so that the transitions are driven with couplings Ω that don't depend on slightly different detunings due to the Zeeman splittings. The eigenvalues λ are then approximately the same as without the magnetic field. We can rewrite Eq.(2.61) as

$$(\lambda - \delta)\boldsymbol{a} = \left(\frac{\hbar^2}{4}\Omega^\dagger \frac{1}{\lambda + \frac{\hbar}{2}\delta - \boldsymbol{J_a}\cdot\boldsymbol{B}}\Omega + \boldsymbol{J_a}\cdot\boldsymbol{B}\right)\boldsymbol{a} \tag{2.62}$$

$$(\lambda - \delta)\boldsymbol{b} = \left(\frac{\hbar^2}{4}\Omega \frac{1}{\lambda - \frac{\hbar}{2}\delta - \boldsymbol{J_b}\cdot\boldsymbol{B}}\Omega^\dagger + \boldsymbol{J_b}\cdot\boldsymbol{B}\right)\boldsymbol{b} \tag{2.63}$$

where λ are the eigenvalues of $\mathcal{H}$. This is a complicated equation because the eigenvalues λ are appearing on both sides of the equation. However, for $\Omega \gg \omega_B$ and nonzero eigenvalues λ, which are of order Ω, the magnetic interaction in the denominator of Eq.(2.62) can be neglected. On resonance the equation is reduced to

$$\lambda\boldsymbol{a} = \left(\frac{\hbar^2}{4}\frac{\Omega^\dagger\Omega}{\lambda} + \boldsymbol{J_a}\cdot\boldsymbol{B}\right)\boldsymbol{a} \tag{2.64}$$

$$\lambda\boldsymbol{b} = \left(\frac{\hbar^2}{4}\frac{\Omega\Omega^\dagger}{\lambda} + \boldsymbol{J_b}\cdot\boldsymbol{B}\right)\boldsymbol{b} \tag{2.65}$$

This is still a complicated equation, but it can be interpreted in a useful way: The energies of the levels are given by the sum of the effective Hamiltonian (up to a factor $\lambda \simeq \sqrt{\lambda^*}$) and the interaction due to the magnetic field.

2.5.3 Example

To visualize what happens to a multilevel system with and without degeneracy, we pick a 1×2 level system as depicted in Figure (2.5), and find the eigenvalues and eigenvectors of the complete Hamiltonian. If we draw the energy levels in the same fashion as in Figure (2.4), the diagrams of Figure (2.6) emerge. Both graphs show the energies of the states and their virtual counterparts as a function of light detuning.

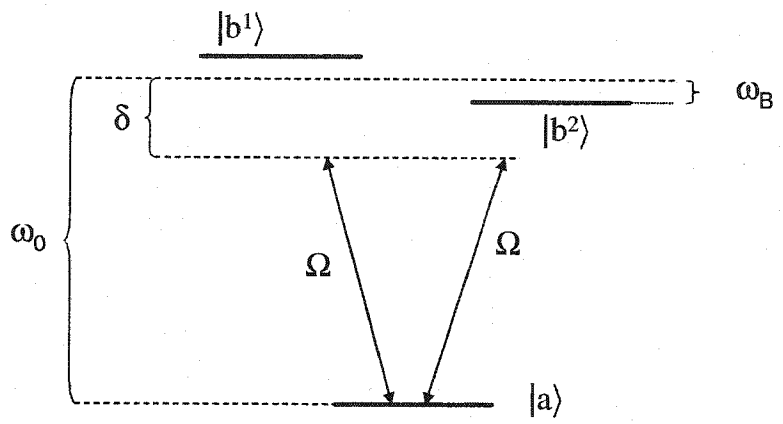

Figure 2.5: 2×1 system with Zeeman splitting and identical coupling Ω to each level, detuned by δ from resonance ω_0.

The upper graph corresponds to the (near) degenerate case where $\Omega \gg \omega_B$, and the region of strong mixing involves all three levels. As a calculation of the eigenvectors shows, the three states on resonance are

$$|1\rangle = \frac{1}{2}(|b^1\rangle + |b^2\rangle) + \frac{1}{\sqrt{2}}|a\rangle \tag{2.66}$$

$$|2\rangle = \frac{1}{\sqrt{2}}(-|b^1\rangle + |b^2\rangle) \tag{2.67}$$

$$|3\rangle = \frac{1}{2}(|b^1\rangle + |b^2\rangle) - \frac{1}{\sqrt{2}}|a\rangle \tag{2.68}$$

with eigenvectors $\lambda_{1/3} = \pm\Omega/\sqrt{2}$, $\lambda_2 \simeq 0$. This agrees with the prediction from Section 2.5.1 that there is one zero eigenvalue (difference in level multiplicity), where the corresponding eigenvector is a superposition of only one upper states, and there is no mixing with the lower state. As mentioned before, $|2\rangle$ is also called a dark resonance, or dark coherence, as there is no coupling from it to $|a\rangle$. A graphical indication of this seems to be the level anti-crossing $|1\rangle$,$|3\rangle$ with a sandwiched state $|2\rangle$.

For the opposite case where $\Omega \ll \omega_B$, only one of the upper levels is strongly mixed with the lower one, depending on the detuning. Each resonance (at $\omega_0 \pm \omega_B$)

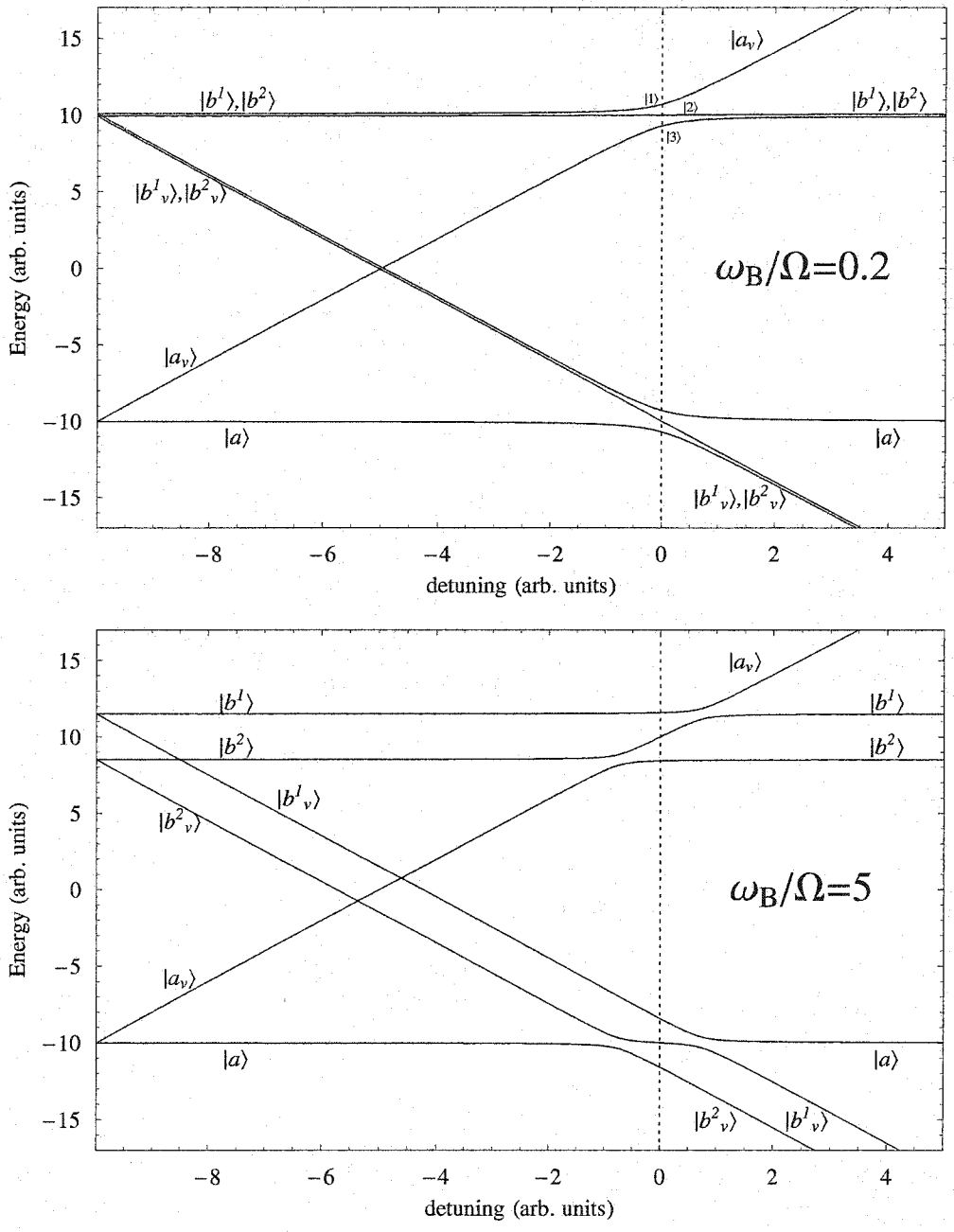

Figure 2.6: The graphs show the energy levels and virtual levels of the three-level system from Figure 2.5 as a function of detuning δ. For the upper graph, $\omega_B = 0.2\Omega$ while for the lower graph, $\omega_B = 5\Omega$.

behaves like a two-level resonance with the third state untouched. This leads to two separate level anti-crossings.

2.5.4 Off-resonant shifts with multiplets

Lastly we return to off-resonant shifts, but use the formalism just developed to describe multi-level atoms. For two multiplets, the problem starts identically to that involving near-resonant shifts. The Hamiltonian is given by Eq.(2.50), and the new energies for the lower levels of the system are given by eigenvalue equation (2.54):

$$\lambda^2 = \frac{\hbar}{2}\left(\lambda^* + \delta^2\right) \tag{2.69}$$

where λ^* denotes the eigenvalues of $\mathbf{\Omega}^\dagger\mathbf{\Omega}$. This equation is the multiplet version of Eq.(2.27). Therefore, in the limit where the detuning δ is much larger than the eigenvalues of the effective Hamiltonian, we can adopt approximation Eq.(2.30) to write for the light shifted energies

$$\lambda = \frac{\hbar}{4\delta}\lambda^* \tag{2.70}$$

The shifted energies can also be considered solutions to the eigenvalue equation of an "effective Hamiltonian" H_{eff}:

$$H_{\text{eff}} = \frac{\hbar}{4\delta}\mathbf{\Omega}^\dagger\mathbf{\Omega} \tag{2.71}$$

This description is useful because it contains all effects of the interaction, yet only applies to one multiplet. Later we will see that this enables us to consider, e.g. the light fields as acting like an "effective magnetic field", which simplifies analysis and intuitive understanding of their effects. It also shows the surprising fact that while an off-resonant light shift doesn't mix states from different multiplets strongly, it can still completely mix states belonging to the *same* multiplet.

In a system where $\mathbf{\Omega}^\dagger\mathbf{\Omega}$ is already diagonal, we can simply write

$$\Delta_m = \frac{1}{4\delta}(\mathbf{\Omega}^\dagger\mathbf{\Omega})_{mm} \tag{2.72}$$

For an atom with many levels, the same light field can lead to couplings of each level to a number of other ones. Also, the counter-rotating terms must be included since the field will always be far off-resonant for some level pairs. The full expression for the light shifts of a state γ with angular momentum j is therefore given by

$$\Delta_{\gamma m} = \frac{1}{4} \sum_{\gamma', \pm\omega_L} \frac{\left[\mathbf{\Omega}^\dagger(\gamma, \gamma')\mathbf{\Omega}(\gamma, \gamma')\right]_{mm}}{\omega_\gamma - \omega_{\gamma'} \pm \omega_L} \tag{2.73}$$

Explicitly, the shift looks like this:

$$\Delta_{\gamma m} = \frac{e^2 E^2}{4\hbar^2} \sum_{\gamma', m', \pm\omega_L} \frac{|\langle \gamma, jm | \hat{\boldsymbol{\varepsilon}} \cdot \boldsymbol{r} | \gamma, j'm' \rangle|^2}{\omega_\gamma - \omega_{\gamma'} \pm \omega_L} \tag{2.74}$$

where $\frac{e^2E^2}{4\hbar^2}$ can also be written in terms of the light intensity:

$$\frac{e^2 E^2}{4\hbar^2} = \frac{2\pi}{\hbar} \alpha I \quad \text{with} \tag{2.75}$$

$$\alpha = \frac{e^2}{4\pi\varepsilon_0 \hbar c} \tag{2.76}$$

$$I = \frac{1}{2} c \varepsilon_0 E^2 \tag{2.77}$$

2.5.5 Multipole structure of light shifts

We have seen that both off-resonant and near-resonant light shifts in multiplets can be written in terms of an effective interaction that contains $\mathbf{\Omega}^\dagger\mathbf{\Omega}$. The structure of the resulting light shifts (i.e. how the various sublevels of a multiplet are affected) is determined by the geometry of the field(s) that cause them. To see this dependence, we can expand H_{eff} in terms of tensor objects that interact with corresponding multipole moments of the electron spin. These tensor objects (scalar, vector, quadrupole,...) contain the geometry of the fields. This is analogous to the way one expands the energy of a charge distribution into its multipole moments interacting with various gradients of the electric field. But unlike that case, spin space is finite, and a finite number of angular momentum multipole moments span this space. $\mathbf{\Omega}^\dagger\mathbf{\Omega}$ is a $(2m+1) \times (2m+1)$ Cartesian tensor, and to match this number of independent

components, we need $2m+1$ spherical multipoles [53, p.234]. The expansion can thus be written as

$$\Omega^\dagger\Omega = \sum_{k=0}^{n}\sum_{q=-k}^{k} \Theta_q^{(k)} j_q^{(k)} \tag{2.78}$$

where n is the number of spin states, and $j_q^{(k)} = Y_q^{(k)}(\boldsymbol{j})$ (see [53, p.234]) are spherical tensors made from angular momentum operator $\boldsymbol{j}$, given in its appropriate representation. Mostly, only the first three multipoles are relevant. These can also be written in terms of Cartesian irreducible tensors:

$$\Omega^\dagger\Omega = \Theta\,\mathbb{I}_{n\times n} + \boldsymbol{\Theta}\cdot\boldsymbol{j} + \sum_{il}\Theta_{il} j_{il} + \ldots \tag{2.79}$$

The objects $\Theta, \boldsymbol{\Theta}, \Theta_{il}$ parameterize the effect of the light fields into that of a scalar, vector, and (quadrupole) tensor interaction. They will be calculated in terms of the light field(s) for specific cases in Section 7. In general, though, the tensor objects $\Theta, \boldsymbol{\Theta}, \Theta_{il}$ are made by forming tensor products of the field and derivative vectors. On this basis multipoles can sometimes be ruled out without any calculations: For example, for single field causing an E1 transition, there are only two vectors $\boldsymbol{E}$ available (one from $\boldsymbol{\Omega}$ and one from $\boldsymbol{\Omega}^\dagger$). These can at the most form a scalar (dot product), a vector (cross product) and a quadrupole tensor (direct product). Therefore a quadrupole shift is the highest possible multipole shift in this case. Often the polarization of the field will impose further restrictions.

The advantage of the multipole expansion is the characteristic behavior of the various multipoles: The scalar part can't distinguish between different sublevels and will lead to a collective shift of all of them. The vector part looks identical to that of a magnetic field interacting with a spin and is often dubbed "effective magnetic field". The quadrupole part, at least its diagonal elements, leads to shifts that depend on m^2.

Chapter 3

THEORETICAL BACKGROUND FOR THE EXPERIMENTAL METHODS

This chapter reviews some more theoretical building blocks associated with this experiment. First we review the physics of RF ion traps and motivate the simple description of the RF field creating a harmonic "pseudopotential". We then understand the shelving method as a way of detecting the quantum state of a single ion — the foundation for almost all ion trap experiments. We describe the process of laser cooling that is used to minimize the kinetic energy of the ion and confine it in the Lamb-Dicke regime, where the ion's localization is much better than an optical wavelength, so that Doppler effects vanish. Finally, we develop the theory of RF interactions with the spin levels of an atom. We treat the simple two-level system, and then generalize to ladders with an arbitrary number of spin states. We then apply this generalization to the four-level system that the $5D_{3/2}$ state presents.

3.1 Ion traps

In this section we discuss the basic properties of the RF trap used in the experiment. The purpose of the trap is to confine the ion motion in all directions and to localize it to an area much smaller than the wavelength of visible light.

If we intend to only use electric fields for trapping, we may write down a simple potential for evaluation:

$$\Phi(x, y, z, t) = \frac{U}{2}(c_x x^2 + c_y y^2 + c_z z^2) \tag{3.1}$$

If all coefficients were positive, this potential would represent a harmonic potential in all three directions:

$$\boldsymbol{F} = -e\boldsymbol{\nabla}\Phi = -eU \begin{pmatrix} c_x x \\ c_y y \\ c_z z \end{pmatrix}, \tag{3.2}$$

assuming a particle with charge $+e$. However, the potential has to fulfill Laplace's equation $\nabla^2\Phi(x, y, z, t) = 0$, which leads to the condition

$$c_x + c_y + c_z = 0, \tag{3.3}$$

making at least one of the coefficients negative. This is an example of Earnshaw's theorem, according to which it is not possible to confine a charge with static electric forces alone. One solution to this problem consists of using an additional magnetic field, which makes confinement possible. A major type of ion traps, the *Penning trap*, uses this idea. For our purposes, however, the magnetic field needs to be independently controllable, which makes a Penning trap unsuitable. Surprisingly, if we make the potential in Eq.(3.1) oscillatory,

$$U(t) = U \cos \omega_{\mathrm{RF}} t + V, \tag{3.4}$$

we can achieve confinement, in the sense of bounded solutions for the resulting equations of motion.

Intuitively, this behavior can be understood in the following way: Suppose the ion starts off with some initial velocity and position away from the RF center of the trap ($x = y = z = 0$), and we pick a direction i and a half-period of the potential for which the force $F_i = qU(t)c_i x_i$ is repulsive. As a result, the ion will be pushed further away from the trap center. During the following half-cycle the ion experiences an attractive force. But since now the ion is further away from the center of the trap, the average of this force is larger than the average of the repulsive force. The net result is that averaged over one cycle of the oscillating potential, the ion experiences

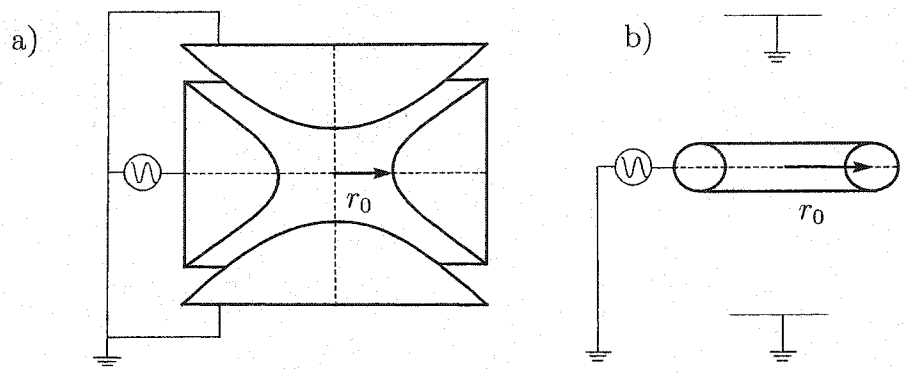

Figure 3.1: a) cross-section of an ideal Paul trap consisting of hyperbolic ring and endcaps. b) simplified ring trap without endcaps, used in this experiment.

an *attractive* force. This is independent of the sign of c_i, but does depend on the ion not traversing more than a fraction of the trap area during one period of oscillation[1]. The ion motion can then be described in terms of a slower, approximately harmonic motion, the *secular* motion, and a fast, small-amplitude motion with the frequency of the oscillating potential, the *micromotion.*

To obtain a more quantitative understanding trapped ion physics, we discuss its classical equations of motion. We consider an ideal Paul trap, which is depicted in Figure 3.1a. It consists mainly of a central ring with a hyperbolic cross-section, and two endcaps which are hyperboloids of revolution. This geometry traces the equipotential surfaces of the simple quadrupole potential of Eq.(3.1) for $c_x = c_y = -1/2c_z$, and will therefore reproduce this potential, given by

$$\Phi(x, y, z, t) = \frac{U \cos \omega_{\mathrm{RF}} t}{2r_0^2}(x^2 + y^2 - 2z^2). \tag{3.5}$$

[1]An alternative physical explanation for confinement is this: When averaging over one period of the RF, the forces on an ion due to the *oscillating* electric field are the same as those on an electric dipole that is anti-parallel to the same *static* field. Since such a dipole seeks locations of minimum field, so does the ion. And since there is such a minimum at the trap center, confinement results

In this experiment we use a simplified geometry in which the endcaps are removed and replaced by distant ground planes (see Figure 3.1b). Also, we use a simple ring with a cross-section that is approximately circular. The resulting potential will deviate from the ideal quadrupole form of Eq.(3.5), but close to the RF center of the trap it still approximates a quadrupole potential. This is so because any expansion around a minimum or maximum of a potential will be quadratic to lowest order. Since a single ion is confined to a space much smaller than the trap dimension, it essentially sees an ideal quadrupole potential. The other consequence of this geometry is smaller gradients of the potential for a given voltage on the ring, as compared to the ideal case. Because of this the trapping strength is weakened, which can be expressed as a "voltage loss factor" f_{loss}. The dependence of this factor on the particular trap geometry has been studied quantitatively in [72].

The potential Eq.(3.5) gives three uncoupled equations of motion that are identical in structure. Because of its cylindrical symmetry, the equations in the x and y directions are identical.

$$\ddot{z} = -\frac{2e}{m}\frac{U}{r_0^2}(\cos\omega_{\text{RF}}t)z \tag{3.6}$$

$$\ddot{x} = \frac{e}{m}\frac{U}{r_0^2}(\cos\omega_{\text{RF}}t)x \tag{3.7}$$

where e/m is the charge-to-mass ratio of the ion, and r_0 is the ring radius as shown in Figure 3.1. These differential equation can all be transformed to the standard form of the Mathieu equation

$$\frac{d^2x_i}{d\xi^2} + [a_i - 2q_i\cos(2\xi)]x_i = 0 \tag{3.8}$$

by substituting

$$\xi = \frac{\omega_{\text{RF}}t}{2}, a_z = -2a_x = -\frac{8qU}{mr_0^2\omega_{\text{RF}}^2}, q_z = -2q_x = -\frac{4qV}{mr_0^2\omega_{\text{RF}}^2}. \tag{3.9}$$

Solutions are given [26] by

$$x_i(\xi) = Ae^{i\beta_i\xi}\sum_{n=-\infty}^{\infty} C_{2n}e^{i2n\xi} + Be^{-i\beta_i\xi}\sum_{n=-\infty}^{\infty} C_{2n}e^{-i2n\xi} \tag{3.10}$$

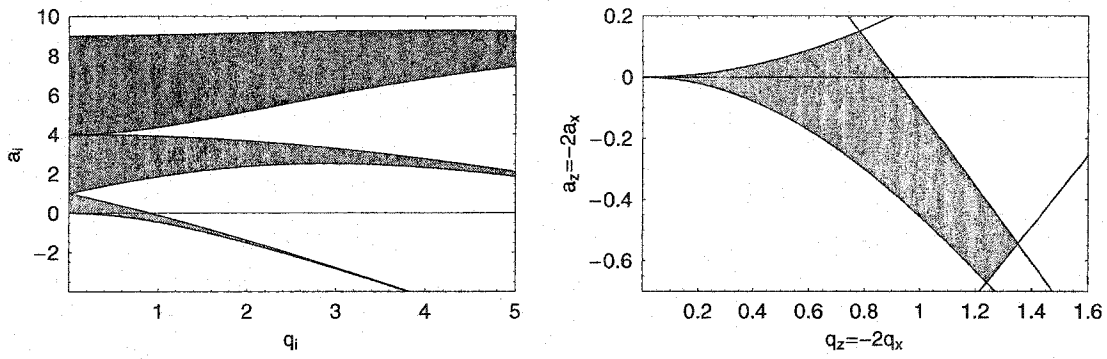

Figure 3.2: Left graph shows the regions where the characteristic exponent $\beta_i(a_i, q_i)$ is real-valued and the ion trajectory is stable in dimension i. The regions are bounded by integer values of β_i. Right graph shows the region where β_i is real in all three dimensions.

where β_i, also called the characteristic exponent, and the coefficients C_{2n} are functions of trap parameters a_i and b_i. A and B are constants that depend on initial conditions. The solution will be bounded if the characteristic exponent is real-valued and non-integer. In order to express β_i in terms of the trap parameters, we plug Eq.(3.10) into (3.8) to get the recursion relation

$$\begin{aligned} C_{2n+2} - D_{2n}C_{2n} + C_{2n-2} &= 0 \\ D_{2n} &= (a_i - (2n+\beta_i)^2)/q_i \end{aligned} \tag{3.11}$$

With its help we can express the characteristic exponent as the continued fraction [40]

$$\beta_i(a_i, q_i)^2 = a_i - q_i \left(\frac{1}{D_0 - \frac{1}{D_2 - \frac{1}{\cdots}}} + \frac{1}{D_0 - \frac{1}{D_{-2} - \frac{1}{\cdots}}} \right) \tag{3.12}$$

To obtain a numerical value for β_i, the continued fraction can be truncated after the desired accuracy is achieved. We can now plot a "stability diagram" that shows the regions in parameter space (a_i, q_i) where β_i is real-valued. Such a diagram is shown in Figure (3.2a). The regions are bounded by integer values of β_i. If we superimpose such graphs for x, y and z, we can find joint regions where the motion is stable in all

three dimensions. The lowest of these regions is the one almost all traps operate in, and it is displayed in Figure 3.2b. It is characterized by all characteristic exponents fulfilling $0 \leq \beta_i \leq 1$.

For $a_i, q_i^2 \ll 1$, which corresponds to the previously mentioned condition that the ion doesn't move significantly during one RF period, the coefficients C_{2n} fall off rapidly with growing n, and we can find a simple solution for the ion trajectory by assuming that $C_{\pm 4} \simeq 0$. Then, from Eq.(3.12) we find

$$\beta_i \simeq \sqrt{a_i + \frac{q_i^2}{2}} \tag{3.13}$$

and with initial conditions $A = B$ we get

$$x_i(t) \simeq 2AC_0 \cos(\frac{\beta_i}{2}\omega_{\mathrm{RF}}t)[1 - \frac{q_i}{2}\cos(\omega_{\mathrm{RF}}t)] \tag{3.14}$$

The ion motion is seen to consist mainly of a harmonic motion around the trap center at frequency

$$\nu_i = \frac{\beta_i}{2}\omega_{\mathrm{RF}}, \tag{3.15}$$

also called the secular frequency. Furthermore, there are small excursions at the RF driving frequency that are a factor of $q_i/2$ smaller in amplitude than the secular motion.

If we average Eq.(3.14) over one period of the RF field, only the simple harmonic motion with the secular frequency ν_i remains. This motion also can be considered the consequence of a time-averaged "pseudopotential"

$$\Phi_{\mathrm{pseud}} = \frac{1}{2}m\sum_{i=i}^{3}\nu_i^2 x_i^2 \tag{3.16}$$

that is created by the oscillating RF electric field [26].

The approximate well-depth of this potential can be found by substituting for x_i the largest distance for which the trapping potential is still confining. Due to the strong anharmonicities in the ring traps used here, this distance is typically only about

one-tenth of the dimensions of the trap, which leads to typical trapping well-depths of 1 eV.

For this work a classical description of the ion motion is sufficient. A full quantum treatment is presented for example in [40].

3.2 Quantum jumps and Shelving

The statistical descriptions of the interaction of the ion with light by a density matrix is sufficient for describing its average and stationary properties, such as transition rates or energy shifts. However, with a single ion we routinely experience a dynamical feature that is conceptually foreign to such a description, namely the observation of quantum jumps.

It is interesting to gain some historical perspective here. For the first 50 years of quantum mechanics it was generally believed impossible to observe single quantum systems. As late as 1952, Schrödinger wrote [50]

> "...we never experiment with just one electron or atom or (small) molecule. In thought experiments we sometimes do; this invariably entails ridiculous consequences."

This statement was challenged by a proposal by Dehmelt [14], who succeeded in 1973 to trap a single electron in a Penning trap. Dehmelt also proposed to trap single ions, motivated by the promise of high-resolution optical spectroscopy that could become possible with the narrow transitions and long observation times that an isolated particle affords. However, even if all technical problems like Doppler broadening and laser issues were resolved, fundamentally the spectral width of atomic lines cannot be smaller than the rate at which photons are scattered from the corresponding transition. On the other hand, the direct observation of fewer and fewer scattered photons becomes practically impossible when only observing a single particle. Dehmelt's idea was to indirectly observe such weak transitions, using "quantum jumps" in a single

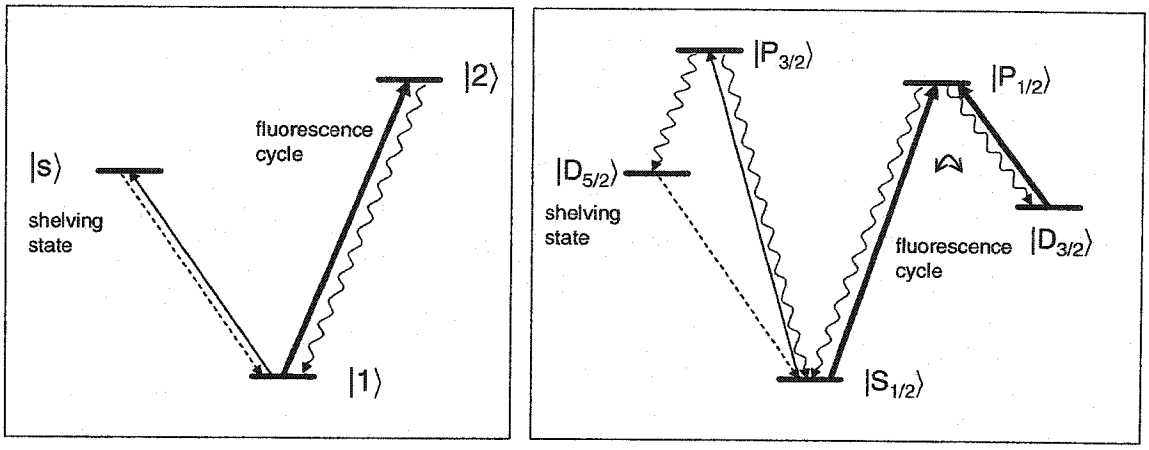

Figure 3.3: The left figure shows the simplest system for the occurrence of quantum jumps, where the lifetimes of the states are $\tau_s \gg \tau_2$. Many photons are scattered when the atom is in the $|1\rangle \leftrightarrow |2\rangle$ fluorescence cycle. When the atom makes a transition to the shelving state, the fluorescence stops until a transition back to $|1\rangle$ is made. The right figure shows the atomic system for Ba^+. The fluorescence cycle consists of three levels, and the shelving level is driven indirectly.

quantum system. In general terms, consider a level structure as shown in Figure 3.3, where we drive a strong (dipole) transition between ground state $|1\rangle$ and excited state $|2\rangle$. If we drive this transition, we can observe a large rate $1/\tau_2$ of fluorescence photons, and we say that the atom is in the fluorescence cycle. In addition, there is a state $|s\rangle$, which we call a *shelving state* if there is no strong decay channel from or to any of the states in the fluorescence cycle. If we drive this transition with a second laser, Dehmelt expected the following behavior: If a transition to $|s\rangle$ is made, the atom will remain there for a time long compared to τ_2. During this time no light can be scattered on the strong transition and an extended "dark" period occurs. Then, by spontaneous or induced emission, the atom "jumps" back to $|1\rangle$ and can once more produce fluorescence. Therefore, by observing the discrete changes in the ion fluorescence, one can induce whether the extremely weak transition to $|s\rangle$ has been occurring. One could also describe this indirect observation method as an "amplifica-

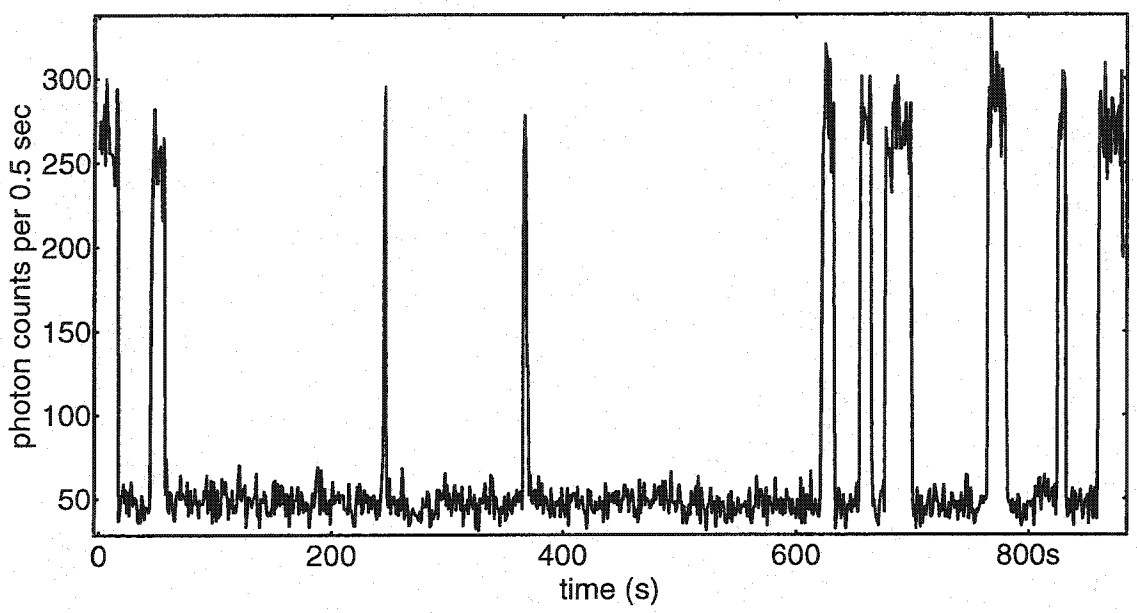

Figure 3.4: Fluorescence signal from a single Ba^+ ion when the transitions are continuously driven as shown in Figure 3.3. The shelving transition rate, $|S_{1/2}\rangle \rightarrow |P_{3/2}\rangle$ was about 0.2 Hz while the lifetime of the shelving state is about 35 s.

tion scheme": One microscopic transition (from $|1\rangle$ to $|s\rangle$) leads to a macroscopically observable change in fluorescence. By observing or not observing this fluorescence one can infer whether the ion is in the quantum state $|s\rangle$ or not. On the other hand, this would not work with an ensemble, as there the random nature of transitions would lead to a constant fluorescence intensity. The latter could easily be calculated with the traditional ensemble approach, while there was no theoretical description to describe quantum jumps of an individual system.

Ten years after this proposal, such quantum jumps were first observed in single-ion experiments [47, 54, 2]. We show such an observation, as is now routinely made when trapping single Ba^+ ions, in Figure 3.4.

It is fair to say that the observation of quantum jumps had considerable implications for both experimental and theoretical atomic physics. Experimentally it has enabled several new fields to emerge. Dehmelt's original scheme has been pursued by

a number of groups to build an atomic clock based on a single ion [52, 64], and to date such clocks, based on optical transitions, challenge the accuracy and precision of traditional atomic-beam fountain clocks. Shelving was used to measure extremely long lifetimes of metastable states [73], and has enabled studies of entangled states and quantum computing with single ions [10, 40]. Lastly, it is at the core of RF spectroscopy as pursued here, and therefore prerequisite for efforts like the proposed PNC experiment with a single ion [23]. Immediately, we use quantum jumps as a first diagnostic to count the number of ions in the trap; see Section 5.1.1 for more details.

Theoretically, the observation of quantum jumps has stimulated the construction of theoretical methods that can describe the evolution of individual quantum systems conditioned on a particular observation of the trace they leave in the environment as a result of a decay. The basic idea is to include the quantized radiation field in the description and to discriminate between density operators corresponding to different numbers of emitted photons. The individual density operators then describe the *conditional* evolution of the system, depending on the measurement or null-measurement of photons. These formalisms have been named quantum jump, Monte Carlo wave function, or quantum-trajectory methods, and are reviewed in [50, 6].

3.3 Dark states

In this section we consider several issues that have to do with "dark states" of the ion, where it is no longer able to produce fluorescence light despite the presence of lasers. In our ion experiments two kinds of dark states are relevant and will be investigated in more detail: dark states in Zeeman levels, and dark states due to coherence of atomic levels in the presence of two laser fields. The part of the Ba^+ spectrum we are concerned with in the following are the three levels $6S_{1/2}$, $6P_{1/2}$, and $5D_{3/2}$ with resonance frequencies ω_b and ω_r (see. Figure 3.3) driven by a blue and a red laser that may be detuned by δ_b and δ_r, respectively. To see the ion, we observe its fluorescence

on the $6P_{1/2} \rightarrow 6S_{1/2}$ transition. Since the ion can decay into the metastable $5D_{3/2}$ state, the red laser is used to "repump" the ions and keep them in the fluorescence cycle.

3.3.1 Dark states in Zeeman levels

Consider driving a transition between two degenerate multiplets j_i and j_f, where the upper state j_f is responsible for fluorescence. If one of the lower m-levels is not coupled by the laser field, the ion will remain in this state and cease to fluoresce once it decays into the state. This process is usually called optical pumping [30], and is used intentionally to prepare the ion in an angular momentum eigenstate. More generally, it is possible that a *superposition* of m-levels is decoupled from the light field. This is because for superpositions, we add the individual transition amplitudes, and the different amplitudes may cancel. When the ion decays into this superposition, and the superposition is not destroyed, fluorescence ceases as before. This process is called "coherent population trapping "(CPT) [4].

About the possibility of optical pumping and population trapping we can make the following statements [4]: For $j_f = j_i + 1$ neither optical pumping nor CPT is possible. For $j_f = j_i - 1$ there will always be either two uncoupled states or two uncoupled superposition states. For $j_f = j_i$ there is one uncoupled state; for integer $j_f = j_i$ there is also the possibility of one superposition state.

In Ba^+, the case $j_f = j_i - 1$ occurs between the $5D_{3/2}$ and $6P_{1/2}$ levels. Even if we connect all $5D_{3/2}$ levels to $6P_{1/2}$ (with linearly polarized light driving $\Delta m = \pm 1$ transitions), there wouldn't be sustained absorption and emission because the ion would quickly decay into a dark superposition state. Because this transition is needed for ion detection, we need a way to destabilize superposition states. Two ways exist to do this: With an applied magnetic field we lift the degeneracy of the sublevels and cause superposition states to evolve into states that are coupled again. Another way of understanding the existence and destruction of superposition states is this:

Degeneracy means that the evolution of states looks the same irrespective of the orientation of the quantization axis. We therefore are free to choose the quantization axis along the polarization of the applied light field. Along this axis, only $\Delta m = 0$ transitions are driven and the ion will decay into the uncoupled outer spin levels of $5D_{3/2}$. Turning on a magnetic field with an axis that is not parallel to the quantization axis will mix spin levels, causing the population to rise in the coupled $m = \pm 1/2$ levels. The larger the magnetic field, the faster this mixing occurs, and roughly, the excitation rate out of $6P_{1/2}$ is given by the Zeeman frequency caused by the magnetic field. We can also understand this behavior when examining eigenvalues and eigenvectors of the coupling Hamiltonian, as done in Section 2.5.1. In practice the minimum magnetic fields required to provide sufficiently fast mixing are on the order of 1 Gauss.

If we desire to work with much lower magnetic fields, a second method can also be used to destabilize superposition states. Since the composition of the dark superpositions are functions of the light polarization, changing the polarization will cause a different superposition to be dark. In order to "arrive" at the new dark superposition, the ion will have to go through some absorption/fluorescence cycles. Then, if we modulate the polarization sufficiently quickly, we can keep the ion continuously fluorescing as it is kept from ever settling into a dark superposition. This may have to be done in a parity experiment where low magnetic fields are desirable.

3.3.2 Dark states in atomic levels

Even if we succeed in preventing CPT from occurring, there can still be dark superposition states of different *atomic* levels. These "dark resonances" are most commonly encountered in a Λ-type system like that formed by the three states in Ba^+ [60, 51]. To see this, we neglect the multiplet structure for now, and find the steady-state solutions of the Bloch equations for such a system, assuming monochromatic lasers. In Figure 3.5 we show the steady-state population for $6P_{1/2}$ as a function of the blue laser frequency, for various detunings of the red laser. The spontaneous decay rates

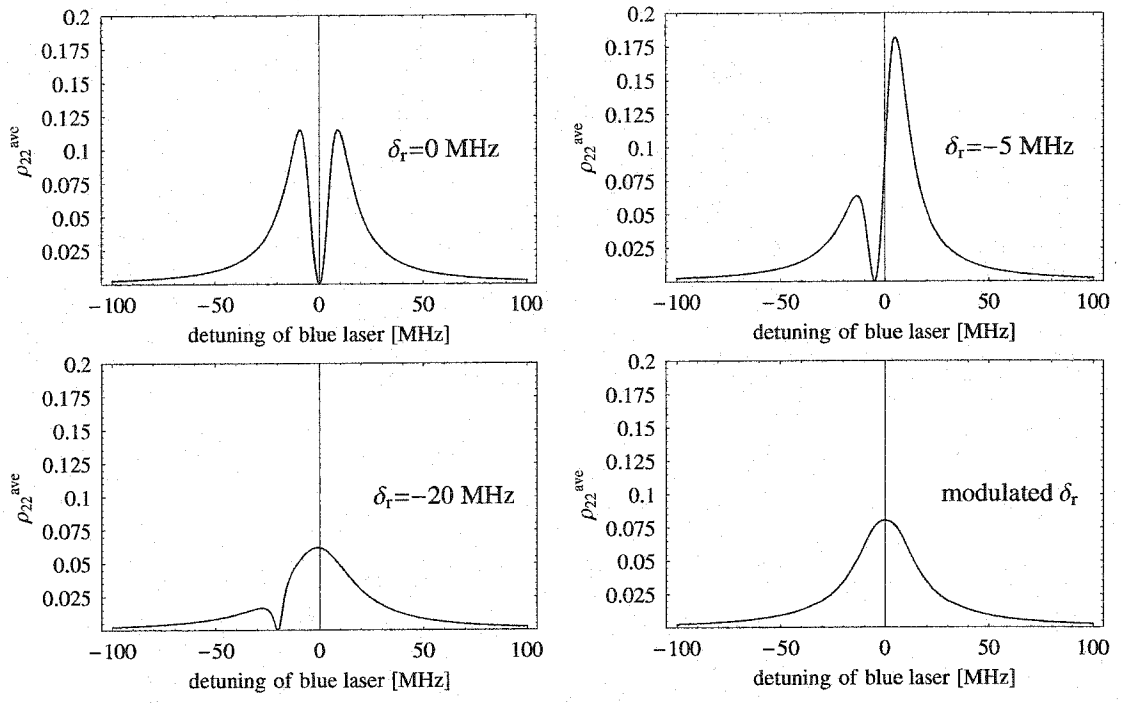

Figure 3.5: Steady-state population for $6P_{1/2}$ as a function of the blue laser frequency, for various detunings of the red laser. The spontaneous decay rates are chosen to be $\Gamma_r = 5\,\mathrm{MHz}$, $\Gamma_b = 15\,\mathrm{MHz}$, and both Rabi frequencies are $\Omega_r = \Omega_b = 10\,\mathrm{MHz}$. The last graph shows the resulting resonance when the red laser frequency is modulated with a bandwidth of 100 MHz.

in this model are chosen to be $\Gamma_r = 5\,\mathrm{MHz}$, $\Gamma_b = 15\,\mathrm{MHz}$, and both Rabi frequencies are $\Omega_r = \Omega_b = 10\,\mathrm{MHz}$. We see that for the condition $\delta_r = \delta_b$ the population ρ_{22} vanishes and fluorescence would cease. The complicated line shape can be avoided by intentionally broadening one or both lasers. Since the blue laser is used for cooling, we choose to broaden the red laser. Experimentally we achieve this by modulating the laser frequency within a 100-MHz band. We can simulate this by averaging over many resonance line shapes with different red detuning. When doing this, we find that the original Lorentzian line shape is recovered. The modulation effectively smears out the coherent effects and makes the $6S_{1/2} \leftrightarrow 6P_{1/2}$ transition appear like a simple two-state

resonance.

Even though the single-photon amplitudes to $6P_{1/2}$ vanish for $\delta_r = \delta_b$, this is also the condition for a two-photon resonance between $6S_{1/2}$ and $5D_{3/2}$. This is also called a Raman resonance and can be used to create coherent transitions by "circumventing" the short-lived state $6P_{1/2}$.

3.4 Laser cooling of a trapped particle

The physics of laser cooling of trapped particles depends on three characteristic frequencies [58], along with the three ratios that can be formed from these quantities:

1. The spontaneous transition rate Γ.

2. The recoil energy due to absorption or emission of a photon, expressed in frequency units: $\epsilon = \frac{\hbar k^2}{2m}$, where m is the ion mass, and $k = \omega/c$.

3. the secular frequency ν.

The ratio ν/Γ is used to distinguish two different trapping/cooling regimes: If $\nu/\Gamma \ll 1$, the orbital period in the trap is much larger than the lifetime of the excited state. As a result, an absorption-emission process takes place at almost constant velocity, and we can essentially neglect the influence of the harmonic trap potential on the cooling process. Laser cooling theory for free atoms can be used in this case, which is often called the *heavy-particle limit*, or the *weak confinement limit*. A further distinction here is based upon the ratio $\xi = \epsilon/\Gamma$. If the recoil frequency is small compared to the line width, any observationally significant changes in the ion velocity are the result of *many* absorption-emission processes. The individual contribution to the atom's momentum are small, and we can describe momentum transfer to the atom as a *continuous* process. Then a suitable description is a semi-classical approach where the quantum nature of the field is ignored, except for implicitly acknowledging it

by the inclusion of spontaneous emission. This approach will be sufficient for our purposes and is described in more detail below. In the opposite case, where ξ is no longer small, the problem must be solved fully quantum-mechanically.

In the limit $\nu/\Gamma \gg 1$ the emission process takes place over an extended portion of the particle orbit. Here the frequency sidebands at multiples of ν due to the ion motion are resolved. The trap has now strong effects on the cooling process and will be described quantum-mechanically, where the quantum number n describes the vibrational level of the atom in the trap. Now the atom can change its kinetic energy essentially only in quanta of $\hbar\nu$. Absorption of a photon at sideband frequencies corresponds to a change in n, and tuning a laser to a lower sideband results in a decrease of n upon absorption. The *strong-confinement regime* [3] also implies the smallness of a third ratio, $\eta^2 = \epsilon/\nu$, called the Lamb-Dicke parameter. When η is small, then most of the time, the subsequent photon emission will not change n (see Section 3.4.2). In this limit so-called sideband cooling is possible that can cool the trapped particle to the vibrational zero-point in the trap [67]. In the *strong confinement* limit the Lamb-Dicke limit leads to a suppression of spontaneous emission that changes n and therefore minimizes diffusive ion heating. In the *weak confinement limit* our experiment is operating in, the Lamb-Dicke limit is also operative. Here, though, the broad transitions involve different changes of the vibrational number n simultaneously [45], and the net effect is that the cooling process becomes very similar to Doppler cooling of a free particle, irrespective of η.

3.4.1 Laser cooling of a free particle

As we have seen, in the *weak confinement limit* we are operating in, it is sufficient to understand laser cooling of a free particle. Here we consider the effect of a laser, detuned from resonance, on the motion of the particle. We assume that in the approximation $\xi \ll 1$, we can write a classical "light-pressure" force on the atom that is due to the absorption of photons. It is given by the photon momentum times the

absorption rate $\Gamma\rho_{ee}$, where ρ_{ee} is the excited-state probability [40]

$$\rho_{ee} = \frac{s/2}{1+s+(2\delta_{\text{eff}}/\Gamma)^2} \tag{3.17}$$

$$F = \hbar k \Gamma \rho_{ee}, \tag{3.18}$$

where $s = 2\Omega^2/\Gamma^2$ is the saturation parameter, and the effective detuning is $\delta_{\text{eff}} = \delta - kv$, the laser detuning minus the Doppler shift. For small velocities the force can be expanded in v:

$$F \sim F_0(1+\kappa v), \tag{3.19}$$

where F_0 is a velocity-independent radiation-induced force and

$$\kappa = \frac{8k\delta/\Gamma^2}{1+s+(2\delta/\Gamma)^2} \tag{3.20}$$

is a damping coefficient that will provide viscous drag if δ is negative. The cooling rate is then

$$\dot{E}_c = \langle Fv \rangle = F_0(\langle v \rangle + \kappa \langle v^2 \rangle), \tag{3.21}$$

where the first term vanishes for trapped particles since there $\langle v \rangle = 0$. On the other hand, photon emission also imparts a recoil momentum to the ion. Since the emission pattern is symmetric, the average momentum change is zero, but the momentum shows diffusion, $\langle p^2 \rangle \neq 0$. Considered as a random walk in momentum space, the average momentum gain is given by the square root of the number $N = \Gamma\rho_{ee}t$ of momentum recoils, $\sqrt{\langle p^2 \rangle} = \xi\hbar k\sqrt{N}$, where ξ is a geometrical factor that accounts for the fact that emission takes place in all directions while we only consider the momentum diffusion along one axis. It takes the value $\xi = 2/5$ [58] for dipole radiation. From this, a heating rate can be calculated:

$$\dot{E}_{\text{em}} = \frac{1}{2m}\frac{d}{dt}\langle p^2 \rangle \tag{3.22}$$

Absorption also gives rise to the same diffusion term, but since here momentum is only exchanged along the axis of the laser beam, the geometrical factor becomes $\xi_{\text{abs}} = 1$. Both contribute to the heating rate $\dot{E}_h = \dot{E}_{\text{abs}} + \dot{E}_{\text{em}}$.

The terminal kinetic energy of the atom is reached when $\dot{E}_c = \dot{E}_h$, and is given by [40]. It is minimized for $\delta = -\Gamma\sqrt{1+s}/2$ and gives

$$E_{\min} = k_B T_{\min} = \frac{\hbar\Gamma\sqrt{1+s}}{4}(1+\xi) \sim \hbar\Gamma/2 \tag{3.23}$$

One difference between a free and a trapped particle is that for a free particle three sets of counter-propagating lasers are necessary to provide cooling for *all* particle velocities. For a trapped particle, one laser is sufficient provided that it is oriented so that its electric field has a component along each of the trap's principal axes.

3.4.2 Absence of Doppler-broadening in the Lamb-Dicke regime

One of the most striking advantages of trapped particles is the absence of the first-order Doppler effect, provided that the particle is trapped in the Lamb-Dicke regime. To see this we here examine here how $\eta \ll 1$ alters the effect of the ion motion on the absorption and emission frequencies.

Quantum mechanically, the Doppler effect is a result of momentum and energy conservation during photon absorption and emission [15]. The recoil momentum transferred to/from the atom leads to a change in the kinetic energy of the atom which is mirrored by a corresponding change in the photon's energy. This change in the photon's energy is proportional to the velocity of the atom, which leads to the normal expression for the Doppler shift. To see this, we demand relativistic energy and momentum conservation during and absorption process:

$$\hbar\omega' = \sqrt{p_f^2c^2 + (m_0c^2 + E_f)^2} - \sqrt{p_i^2c^2 + (m_0c^2 + E_i)^2} \tag{3.24}$$

$$p_f = p_i + \hbar k \tag{3.25}$$

With $p_i = mv_i$, $m = \gamma m_0$, $\hbar\omega_0 = E_f - E_i$ we find after making appropriate approximations:

$$\omega' = \omega_0 + kv_i - \omega_0\frac{v_i^2}{2c^2} + \frac{\hbar\omega_0^2}{2mc^2} + ... \tag{3.26}$$

The second term is the first-order Doppler shift, the third term represents the second-order Doppler shift while the last term is independent of atom velocity and called the recoil shift.

This derivation assumes that the photon momentum and thereby its recoil energy is absorbed by the atom. This is now not necessarily true. We have seen that in a trap, the atom can absorb energy only in quanta of the vibrational quantum number, $\hbar\nu$. If we now assume the Lamb-Dicke regime where the recoil energy is much smaller than $\hbar\nu$, energy conservation makes the change of n very unlikely and most of the time *no recoil energy* is transferred to or from the atom. Momentum conservation is still obeyed because in those cases the momentum is transferred *to the macroscopic trap itself*, leading to negligible energy transfer and $\omega' = \omega_0$, irrespective of the atom's velocity. The photon energy is unchanged and the Doppler effect should essentially vanish[2]. Explicitly we can see this by setting $p_f = p_i$ in Eq.(3.24). After approximating we then get

$$\omega' = \omega_0 - \omega_0 \frac{v_i^2}{2c^2} + ... \tag{3.27}$$

Indeed, the Doppler effect and the recoil shift vanish. Interestingly, the second-order Doppler effect persists and thus reveals itself as a purely relativistic effect.

This phenomenon was originally discovered by Dicke in 1953 [15], when he modelled the collisional confinement of atoms/molecules in a gas by a particle in a box. He found that when the dimensions of the box become smaller than the wavelength of the light, it can no longer be assumed that the recoil is absorbed by the individual atom, and a similar situation as with the Lamb-Dicke regime ensues, which can lead to the so-called *Dicke-narrowing* of Doppler-broadened atomic lines.

It is no surprise, then, that the Lamb-Dicke parameter can also be written in

---

[2] A related phenomenon is the Mössbauer effect where absorption of γ rays by nuclei happens without recoil effects when the nuclei are part of a crystalline structure below the Debye temperature. In that case the crystal as a whole absorbs the recoil momentum.

terms of the spatial extent of the ion motion:

$$\eta^2 = \frac{\epsilon}{\nu} = \left(\frac{\pi x_0}{\lambda}\right)^2, \tag{3.28}$$

where $x_0 = \sqrt{2\hbar/m\nu}$ is the size of the oscillator ground-state wave function [58]. Thus, whenever a particle is confined to a region smaller than a wavelength of light, then the first-order Doppler shift of this light vanishes when absorbed or emitted by the atom.

3.5 Spin dynamics

Since we are dealing with and driving transitions within magnetic sublevels, in other words manipulating the orientation of angular-momentum states, we have to learn about the physics of such systems. In particular we have to generalize the well-known $j = 1/2$ system to systems with higher j. Experimentally we encounter three-level systems like the ground state $6S_{1/2}$(F=1) in $^{137}Ba^+$, and four-level systems, notably the $5D_{3/2}$ state in $^{138}Ba^+$.

There are two approaches to find the more general solutions to the equations of motion. One is to use the density matrix formalism from Section 2.2.2, and then solve the differential equations, in general numerically. When we do this we can include higher-order multipole shifts of the levels (for example those produced by light fields), decay processes and more. For the special case of resonant interactions with only vector-like splittings, we can use the representations of spin rotation to find an analytic solution for arbitrary spin. To motivate this and to show the correspondence between a "spin picture" and a "state picture," it is instructive to first study the behavior of a classical model of our spin-RF interaction: A classical spin (i.e. something with angular momentum and a magnetic moment) exposed to an oscillating magnetic field.

3.5.1 *Classical spin flips in a rotating frame, and correspondence to j=1/2*

The spin $\hbar\boldsymbol{j}$, considered here as a classical vector, has associated with it a magnetic moment $\boldsymbol{\mu} = \gamma\hbar\boldsymbol{j}$, where γ is the gyromagnetic ratio. In the presence of a static field $\boldsymbol{B}_0$ it will experience a torque, causing it to precess around the magnetic field with a frequency $\omega_0 = |\gamma \boldsymbol{B}_0|$:

$$\hbar\frac{d\boldsymbol{j}}{dt} = \boldsymbol{\mu} \times \boldsymbol{B}_0 = \gamma\hbar\boldsymbol{j} \times \boldsymbol{B}_0 \tag{3.29}$$

Let us assume that initially, $\boldsymbol{j}$ points in the direction of $\boldsymbol{B}_0$. In addition, we also apply a rotating magnetic field $\boldsymbol{B}$ that is perpendicular to the static field and rotates with frequency $-\omega$. Now we look at the situation from a coordinate system corotating with $\boldsymbol{B}$. First we substitute the derivative in a rotating frame, $d_t = \partial_t - \boldsymbol{\omega}\times$, to write

$$\hbar\frac{d\boldsymbol{j}}{dt} = \gamma\hbar\boldsymbol{j} \times \boldsymbol{B}_{\text{eff}} \tag{3.30}$$

with $\boldsymbol{B}_{\text{eff}} = \boldsymbol{B}_0 - \boldsymbol{\omega}/\gamma$. The spin now sees this effective field instead of $\boldsymbol{B}_0$, and also a static field $\boldsymbol{B}$, and it will precess about the total magnetic field $\boldsymbol{B}_{\text{total}} = \boldsymbol{B}_{\text{eff}} + \boldsymbol{B}$. To be more specific, assume $\boldsymbol{B_0} = B_0\boldsymbol{e}_z$ and $\boldsymbol{B} = B\boldsymbol{e}_y$. Then the total field becomes

$$B_{\text{total}} = \sqrt{\left(B_0 - \frac{\omega}{\gamma}\right)^2 + B^2} \tag{3.31}$$

and the precession frequency $\tilde{\Omega} = \gamma B_{\text{total}}$ can be written as

$$\tilde{\Omega} = \sqrt{(\omega_0 - \omega)^2 + \Omega^2} \tag{3.32}$$

where $\Omega = \gamma B$ is called the Rabi frequency. For $\omega = \gamma B_0 = \omega_0$ (resonance condition) the effective field vanishes and the spin precesses around B, with Rabi frequency Ω.

The suggestive naming makes the equivalence to a two-level system clear:

- The precession frequency ω_0 corresponds to the energy difference between the two levels.

- The interaction B is a rotating magnetic field, where only one sense of ω can lead to the resonance condition. Were ω reversed, it would make the effective field bigger and the spin would continue to precess around *it*. In the state picture this corresponds to the rotating wave approximation where a sinusoidal field is split into a co-rotating and counter-rotating part, and only the co-rotating part has a significant impact on the evolution of the system.

- The transformation to the rotating frame corresponds to the unitary transformation Eq.(2.20); it removes fast time dependence from the problem.

- Finally, in both cases the Rabi frequency characterizes the energy of the interaction.

- On resonance the spin precesses about the y axis, making full flips with respect to the original B field, corresponding to the complete population exchange that happens for a two-state system on resonance.

3.5.2 Dynamics for $j > 1/2$

If we calculate the *projection* of the spin onto the z-axis, we recover the same evolutions of populations as Eq.(2.24). We will do this here in a way that can be generalized to arbitrary quantum mechanical spin systems, that is systems with arbitrary j. If our spin starts out in the state $|jm\rangle$ at $t_0 = 0$, and rotates around the y axis, the resulting state after a time t has been rotated by an angle $\beta = \Omega t$. The resulting state can be obtained by applying the corresponding rotation operator:

$$|\Psi(\beta)\rangle = e^{\frac{-2i\hat{j}_y\beta}{\hbar}}|jm\rangle \tag{3.33}$$

Projecting this onto some the z axis, gives m' projections

$$d^{(j)}_{m'm}(\beta) = \langle jm'|\Psi(\beta)\rangle \tag{3.34}$$

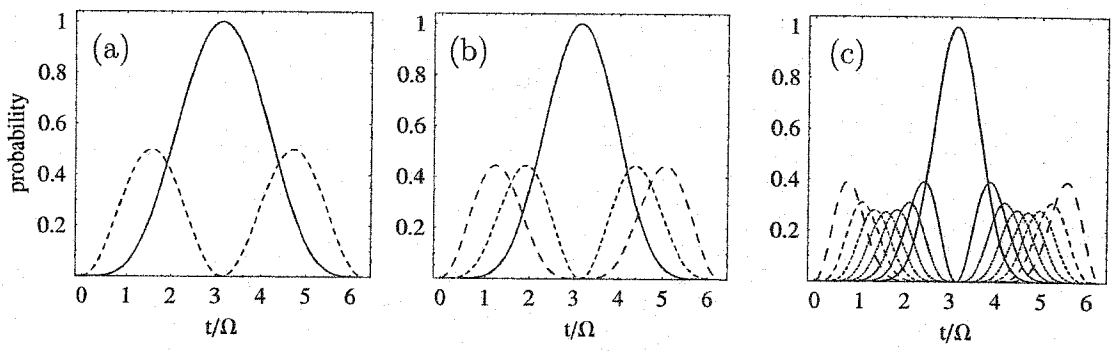

Figure 3.6: Excited-state population evolutions for (a) three-level, (b) four-level, (c) nine-level system, with the population initially ($t = 0$) being in the lowest (ground) spin state, which is not shown. The finer the dashing, the higher the m-level.

The matrix $d^{(j)}(\beta)$ is the representation of the $\hat{y}$ rotation operator for spin j. It can be worked out for various j using the representations of j_y; for $j = 1/2$ this is just, up to a factor 2, the Pauli matrix σ_y, and gives

$$d^{(1/2)}(\beta) = \begin{pmatrix} \cos\beta & -\sin\beta \\ \sin\beta & \cos\beta \end{pmatrix} \tag{3.35}$$

For initial conditions $p_{(m=-1/2)} = 1$ we find the excited-state population $p = d^{(1/2)}_{-\frac{1}{2}\frac{1}{2}}(\beta) = \sin^2\beta$, as expected. $d^{(j)}_{m'm}(\beta)$ can be obtained for any j by Wigner's formula [53, p.223], which can be derived using an oscillator model of angular momentum.

For a four-level system, we have explicitly

$$d^{(3/2)}(\beta) = \begin{pmatrix} \cos\beta^3 & -\sqrt{3}\cos\beta^2\,\sin\beta & \sqrt{3}\,\cos\beta\sin\beta^2 & -\sin\beta^3 \\ \sqrt{3}\cos\beta^2\,\sin\beta & \frac{\cos\beta+3\,\cos(3\beta)}{4} & \frac{\sin\beta-3\,\sin(3\beta)}{4} & \sqrt{3}\,\cos\beta\sin\beta^2 \\ \sqrt{3}\,\cos\beta\sin\beta^2 & \frac{-\sin\beta+3\,\sin(3\beta)}{4} & \frac{\cos\beta+3\,\cos(3\beta)}{4} & -\sqrt{3}\cos\beta^2\,\sin\beta \\ \sin\beta^3 & \sqrt{3}\,\cos\beta\sin\beta^2 & \sqrt{3}\cos\beta^2\,\sin\beta & \cos\beta^3 \end{pmatrix} \tag{3.36}$$

We will use this representation when modelling the observed spin resonance in the $5D_{3/2}$ state (see chapter 5). As we can see, the resulting populations become more

complicated for higher j, gaining frequency terms with multiples of Ω. However complicated, the spin flip is periodic and so is the evolution of the population. To demonstrate this, we plot in Figure 3.6 the excited-state populations for a three, four, and nine-state system (the latter corresponds to $j = 4$) when the spin starts out in the lowest m level.

Confusion can arise about the meaning of the Rabi frequency when there are more than two spin levels present: If we follow the definition of the Rabi frequency from Section 2.2.1, it is just the interaction matrix element times the driving field. Following the definitions in this section, the interaction Hamiltonian between two spin levels $\langle j, m'|$ and $|j, m\rangle$ with $m' - m = 1$ due to a magnetic RF field oscillating perpendicular to the quantization axis

$$B(t) = B\cos\omega t \tag{3.37}$$

is given by

$$H_{\text{int}} = \frac{\hbar}{2}\Omega \tag{3.38}$$

with Rabi frequency Ω

$$\begin{aligned} \Omega_{m'\leftrightarrow m} &= \frac{1}{\hbar}\langle j, m'|g_{(j,l,s)}\mu_B B\hat{j_+}|j, m\rangle \\ &= g\mu_B B\sqrt{(j-m)(j+m+1)} \end{aligned} \tag{3.39}$$

and the Landé g-factor

$$g \equiv g_{(j,l,s)} = 1 + \frac{j(j+1) + s(s+1) - l(l+1)}{2j(j+1)} \tag{3.40}$$

For a two-level system this coupling $\Omega_{\frac{1}{2}\leftrightarrow-\frac{1}{2}} = g\mu_B B$ is the *same* as the energy (or frequency) difference between the levels due to a static field of the same size, which is the original definition of the Rabi frequency and comes naturally out of a classical treatment. This is no longer true for systems with more than two levels, as can be seen in Figure 3.7. In fact, according to Eq.(3.39) there is a different "Rabi"-frequency between each pair of levels; yet it still makes sense to speak of *one* Rabi

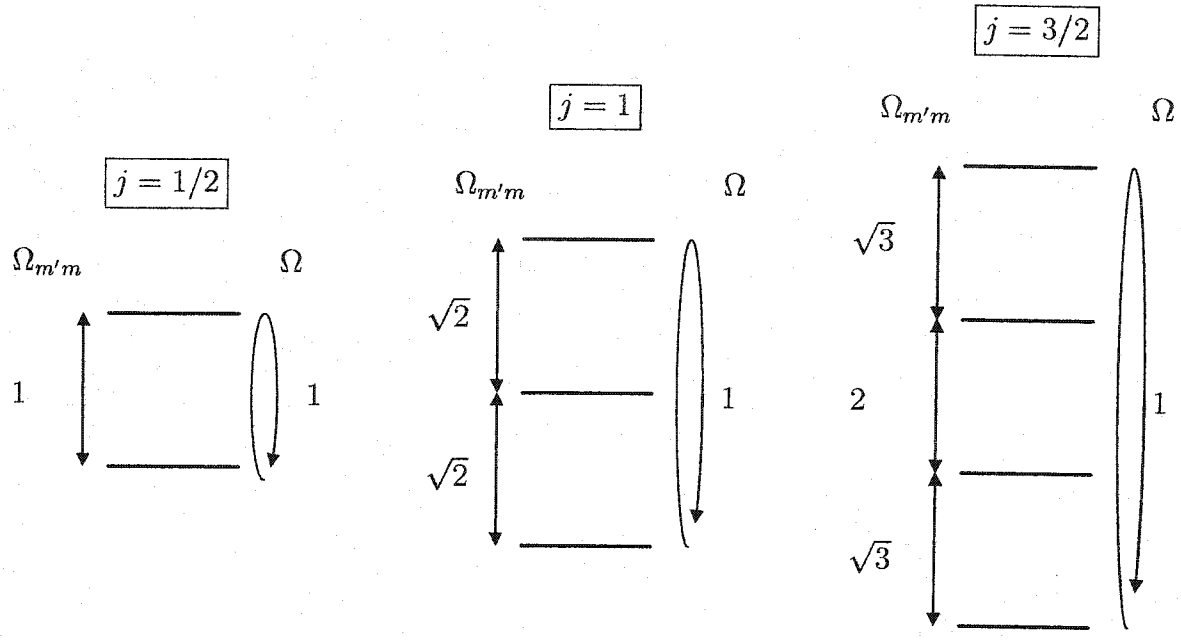

Figure 3.7: Comparison of the spin-flop Rabi frequency Ω, and the individual couplings $\Omega^j_{m'm}$, in units of $g\mu_B B$. Only for $j = 1/2$ do the two different concepts coincide.

frequency, the one that determines when the spin, on resonance, will return to its original orientation. We will therefore always denote the m subscripts when referring to an individual coupling for a multi-state ladder. We note that for our relevant states,

$$ {}^{S}\Omega_{\frac{1}{2}\leftrightarrow-\frac{1}{2}} = 2\mu_B B \tag{3.41} $$

$$ {}^{D}\Omega_{\frac{1}{2}\leftrightarrow-\frac{1}{2}} = \frac{8}{5}\mu_B B \tag{3.42} $$

$$ {}^{D}\Omega_{\frac{3}{2}\leftrightarrow\frac{1}{2}} = \frac{4\sqrt{3}}{5}\mu_B B. \tag{3.43} $$

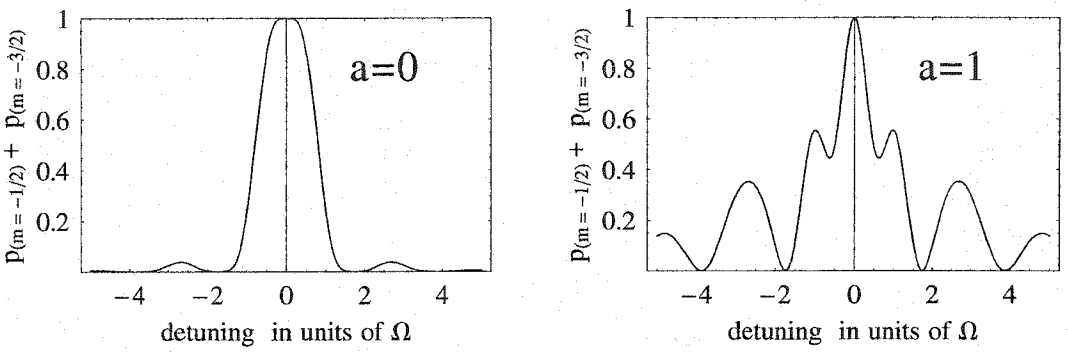

Figure 3.8: RF resonance profile for the D-state resonance, for the extreme initial conditions $a = 0$ and $a = 1$.

3.5.3 Spin resonance in the case $j = 3/2$

Here we examine features of case $j = 3/2$ in more detail, since it appears experimentally in the $5D_{3/2}$ state. Before applying the RF magnetic field, we use optical pumping to prepare the ion in a (speaking in ensemble language) statistical mixture of $m = 1/2$ and $m = 3/2$ state. Then, after driving a spin flip transition, we measure the combined population in the $m = -1/2$ and $m = -3/2$ states, as is explained in greater detail in Section 5.2. The resonance line shape becomes dependent on the initial conditions given by the statistical mixture. We can describe the mixture by a parameter a that represents the probability for the ion to be pumped into the $m = 1/2$ level. Then, by calculating populations for a π-pulse for different RF detunings, we can calculate the line shape depending on the choice of a. As we can see in Figure 3.8, where the limiting cases $a = 0$ and $a = 1$ are plotted, the line shape depends quite sensitively on a. We can thus imagine inferring the initial condition a from a fit to an experimental line shape. We perform such fits in Section 6.2.1 in an attempt to characterize a systematic problem associated with measuring off-resonant light shifts in the D-state.

Next we generalize the D-state RF transitions to the case where the energies

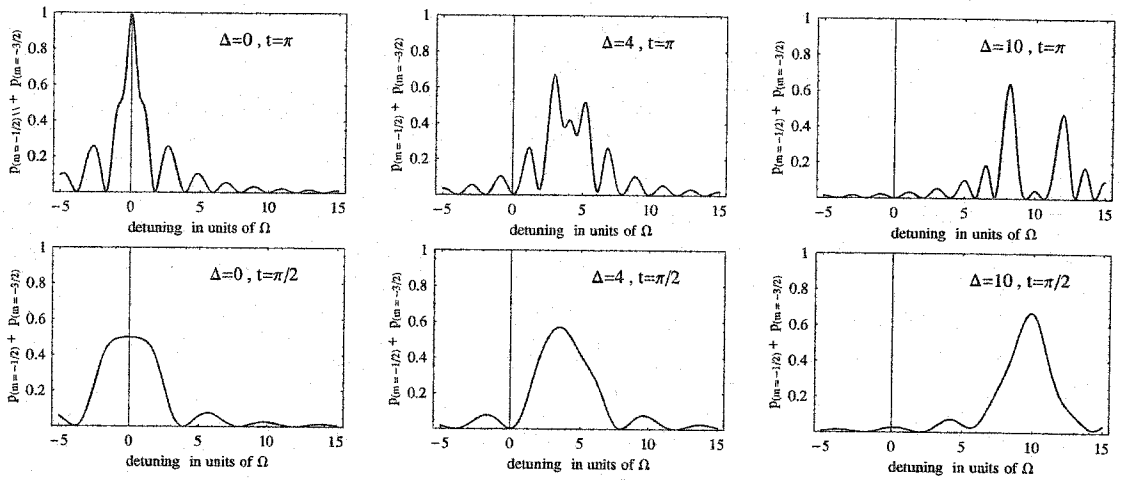

Figure 3.9: D-state RF resonance profile in the presence of light shifts. The upper graphs show the line shapes for a D-state $\pi - pulse$, while the lower graphs are $\pi/2$-pulses that become π-pulses for the isolated two-state system $m = 1/2 \leftrightarrow m = -1/2$.

between any two levels may be different. This is a situation encountered, for example, when measuring off-resonant light shifts. For this case we have to resort to the Bloch equations introduced in Section 2.2.1. The time-independent Hamiltonian for the D-state will then be

$$\mathcal{H} = \frac{\hbar}{2}\begin{pmatrix} \Delta_{3/2} & \sqrt{3}\Omega & 0 & 0 \\ \sqrt{3}\Omega & \Delta_{1/2}+\delta & 2\Omega & 0 \\ 0 & 2\Omega & \Delta_{-1/2}+2\delta & \sqrt{3}\Omega \\ 0 & 0 & \sqrt{3}\Omega & \Delta_{-3/2}+3\delta \end{pmatrix} \tag{3.44}$$

The shifts Δ_m are induced by an off-resonant laser, and depend on its wavelength, intensity and polarization, and are calculated in Section 6.1.1. For concreteness we pick a case we have also examined experimentally. For λ =632 nm and circularly polarized light, we find that $\Delta_{3/2} - \Delta_{1/2} = 1.33\Delta$ and $\Delta_{-1/2} - \Delta_{-3/2} = 0.65\Delta$, where $\Delta = \Delta_{1/2} - \Delta_{-1/2}$ is the shift between the innermost m-levels that we want to measure. Also, we choose the initial condition $a = 0.7$, a value often obtained in the experiments. With this we can find the π-pulse resonance line shape for various

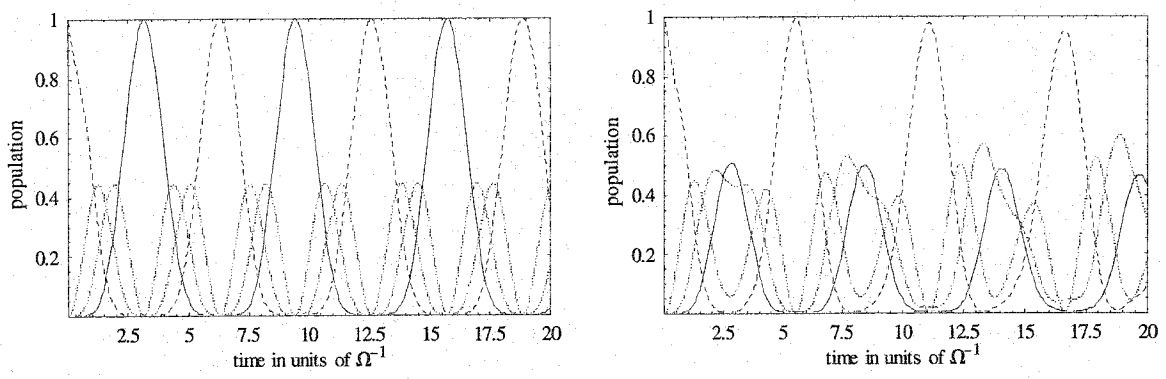

Figure 3.10: Left graph shows the time evolution of the for D-levels when the ion starts out in $m = 3/2$ (solid line). The $m = \pm 1/2$ populations are represented by dotted lines and the $m = -3/2$ population is shown as a dashed line. In the left graph no light shift is present; in the right graph, $\Delta = \Omega$, and the evolutions are no longer periodic.

values of Δ by numerically solving the Bloch equations. The result can be found in the upper graphs of Figure 3.9. For $\Delta \simeq \Omega$ (middle upper graph) the line shape is quite complex, and for $\Delta > \Omega$ (right upper graph) we find a two-peaked structure that is centered around the shift Δ. We can understand this line shape through an interesting mingling of the two definitions for the Rabi frequency given in the previous section: As Δ is made larger, the levels behave more and more like separate two-level systems, and for $\Delta \gg \Omega$ the RF can only drive one level pair resonantly for a given frequency. We then effectively measure the resonance of the innermost m-levels as they act more and more like an isolated system. The coupling $\Omega^D_{\frac{1}{2}\leftrightarrow-\frac{1}{2}} = 2g\mu_B B$ acts now as the Rabi frequency, in the sense that the RF exposure time $t = \pi/\Omega^D_{\frac{1}{2}\leftrightarrow-\frac{1}{2}}$ leads to a spin-flip in this system. Since $\Omega^D_{\frac{1}{2}\leftrightarrow-\frac{1}{2}}$ is twice as large as the Rabi frequency for the $j = 3/2$ system, we thus drive 2π-pulses, which lead to a two-peaked spectrum as on resonance the spin is returned to its origin. Therefore, in order to obtain a single resonance at the location Δ by driving a π-pulse, we have to cut the exposure time in half. This is demonstrated in the lower graphs of Figure 3.9. The amplitude of

these resonances for $\Delta \gg \Omega$ (which is the usual experimental condition) is just given by a. This tells us that optical pumping must be done in such a way as to produce a reasonably large value of a.

Lastly, out of curiosity, we examine the time-evolution of the populations when the energy differences become different from each other. We plot in Figure 3.10 the evolutions for the case $\Delta = \Omega$. The most striking feature is that the evolution ceases to be periodic. This shows that now the classical picture of a rotating spin breaks down. As Δ is made larger, the time-evolution reduces to a simple sinusoidal oscillation between two levels if the RF frequency is resonant with any of the level pairs. The periodicity of such level structures have been studied systematically in [56].

Chapter 4

APPARATUS

This chapter gives a detailed description of the ion trap apparatus currently in use. A schematic diagram of the current setup is shown in Figure 4.1. The ion is trapped in a ring trap enclosed in an ultra-high vacuum housing which is magnetically shielded. The ion is excited to the $6P_{1/2}$ state with a blue laser at 493 nm, and its blue fluorescence is observed. Ion fluorescence is detected with a photo multiplier and evaluated with a data acquisition system. The blue laser is red-detuned from resonance and cools the ion. In addition, a red laser at 650 nm is used to prevent pumping into the $5D_{3/2}$ metastable state. The blue laser starts out as an infrared laser that is frequency-doubled in an enhancement cavity. Both laser sources are external-cavity diode lasers that are frequency-stabilized using opto-galvanic spectroscopy. Their polarization and intensity are controlled with shutters, movable neutral density filters, and AOM and EOMs, before they are combined with a dichroic mirror and focused onto the trap center. Counterpropagating to these two beams is a laser that causes off-resonant light shifts. It is produced by either a dye or an argon ion laser on a different optical table and transported to the trap via a single-mode fiber. This light is stabilized in intensity and usually circularly polarized. Furthermore, there is a Ba^+ discharge lamp that supplies light at 455 nm to drive the $6S_{1/2}$ to $6P_{3/2}$ transition, as well as an LED producing light around 615 nm used to quench the metastable $5D_{5/2}$ state.

In the following, the important parts of this apparatus will be described in greater detail.

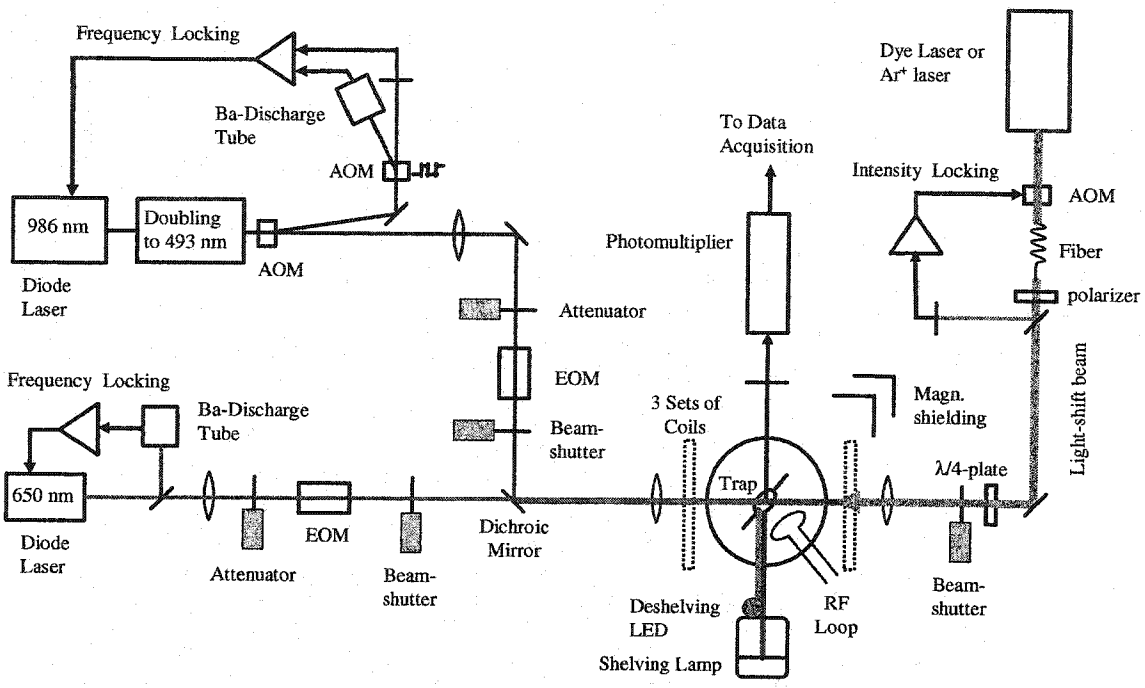

Figure 4.1: Apparatus diagram

4.1 *Ion trap assembly*

Most of our experiments have been carried out with the trap depicted in Figure 4.2. Care has been taken not to use magnetic materials, in order to prevent fluctuating fields and large field gradients. The trap itself is made out of twisted tantalum wire ($\varnothing\,0.2\,\mathrm{mm}$), where a ring ($\varnothing\,0.75\,\mathrm{mm}$) has been formed by separation of the two wires. The RF loop is made from the same wire, while the compensation electrodes and support leads for the electron filament are made from thicker tantalum wire. All elements are spotwelded to the tungsten feedthroughs.

The ovens are small tubes made from rolled and spotwelded tantalum foil, closed off on one side and attached to two tantalum support leads, one at the closed end and one at the middle of the tube. That way the back part of the tube acts as an oven while the cooler front part acts as an aperture to limit the solid angle of the

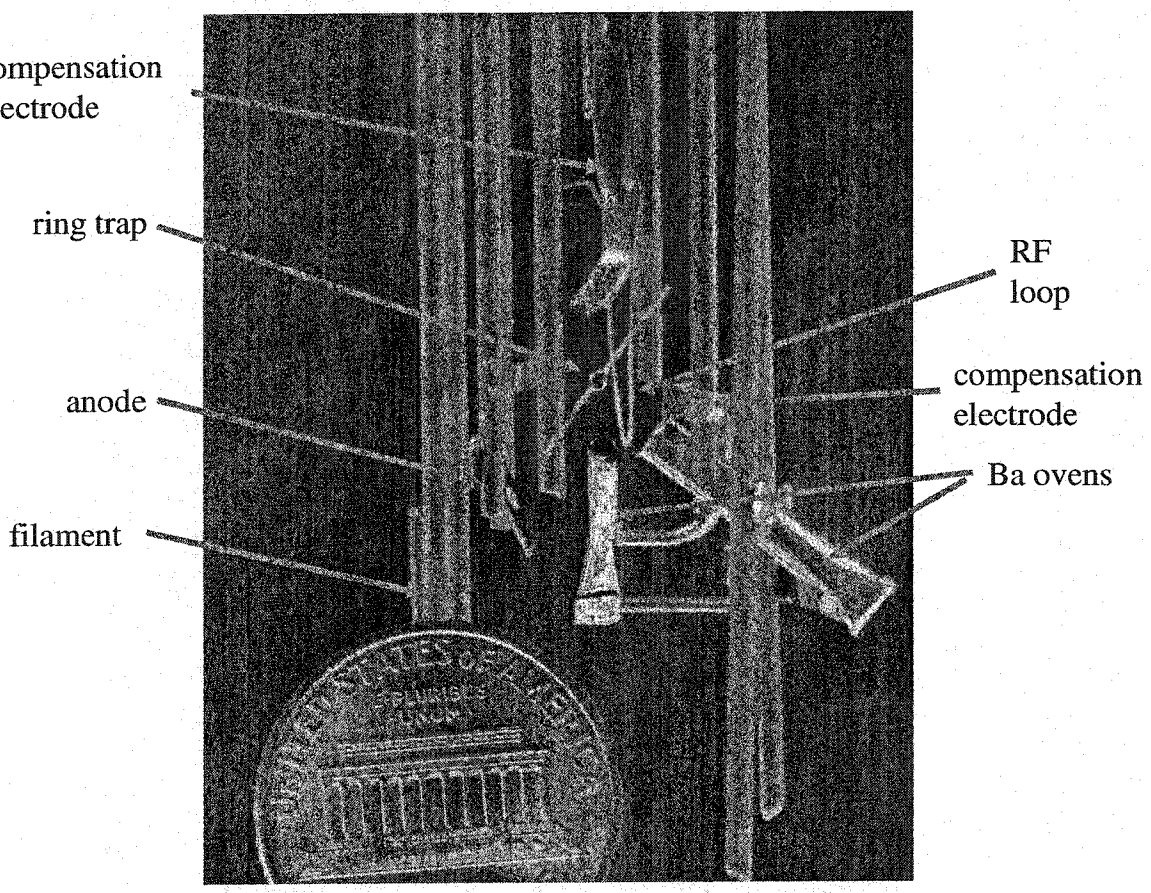

Figure 4.2: Picture of the non-magnetic trap. The trap ring, compensation plates and ovens are made out of tantalum, the feedthroughs and the filament are tungsten.

barium atomic beam. Prior to final assembly the ovens are filled with metallic barium and tested in an evaporator chamber. A glass plate in front of the oven will make deposited barium visible and helps in determining appropriate current settings, as well as checking whether the solid angle is acceptable. The latter is a concern because of the danger of coating the vacuum windows with barium, as well as causing electrical shorts in the trap. We assemble two ovens to have some redundancy in case one oven fails.

An electron beam intersects with the barium atoms at the site of the trap to produce barium ions. The beam is created with a negatively biased filament and a grounded anode with a pinhole.

After the trap system is fully assembled (Figure 4.2), it is cleaned in an ultrasonic cleaner with acetone and deionized water. The ovens are filled with metallic barium immediately prior to mounting the system in the vacuum chamber and evacuation. This is because metallic barium oxidizes very quickly, and the small chunks of the metal we cut (with a knife) to fill the ovens have a "lifetime" of only about 5 minutes when exposed to air. The chunks are cut in advance and stored under an argon atmosphere. The vacuum chamber is shown in Figure 4.3 is made from standard ultrahigh vacuum parts and contains a 20 l/s ion pump, as well as an ion gauge. To reach an ultra-high vacuum, we bake the chamber at 350 °C for about three days. The final pressure achieved with the internal ion pump after bake-out is usually around 5×10^{-11} Torr.

4.2 RF-systems

4.2.1 Trap RF

There are two RF systems present: One for creating the trapping potential and one to drive RF transitions between spin states. The trapping RF system uses an oscillator at 10 MHz, followed by a 10-Watt amplifier, producing a maximum RF voltage of

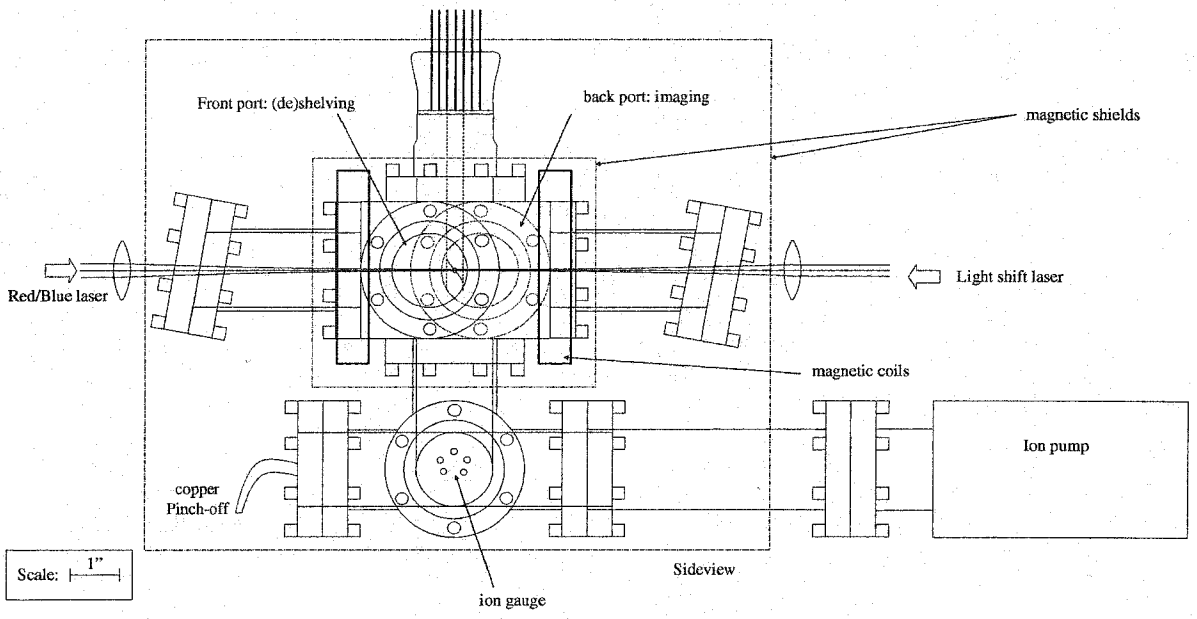

Figure 4.3: Sideview drawing of vacuum enclosure, including the two layers of magnetic shielding.

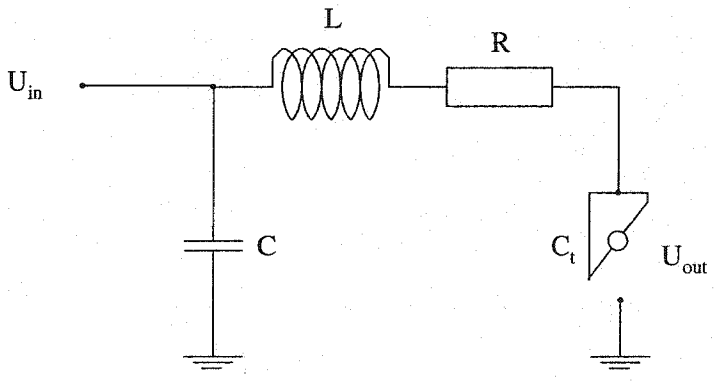

Figure 4.4: Resonant circuit, designed to achieve high RF trap voltages.

20 V peak across a 50 Ω resistor. However, in order to make a sufficiently stiff trap with secular frequencies on the order of MHz, we need several hundred volts. This is achieved with a resonant step-up circuit as shown in Figure 4.4. The capacitor C is much larger than the capacitance of the trap to ground, C_t, and the resonance frequency is given by $\omega_r \simeq \sqrt{1/LC_t}$. R is the distributed resistance of the coil L. On resonance $Z_C + Z_{C_t} + Z_L = 0$ and the impedance of the circuit is given by $Z_{\text{res}} = Z_C - \frac{Z_C^2}{R}$, and impedance matching is achieved when $\text{Re}(Z_{\text{res}}) = (C^2\omega^2 R)^{-1} = 50\,\Omega$. On resonance the step-up ratio $U_{\text{out}}/U_{\text{in}} \simeq C/C_t$. This ratio is large when the trap capacity is small and C large, which implies a small resistance R through the impedance matching condition. Typical values for the step-up ratio are $U_{\text{out}}/U_{\text{in}} \simeq 50$, so that we achieve around 1000 V RF voltage at the trap.

4.2.2 RF system for driving spin flips

The RF magnetic field needed for manipulating the spin states in the S and D states was generated with a half-loop (R=2.5 mm) of tantalum wire that is oriented to create a magnetic field approximately perpendicular to the static B-field. The trap lies at the center of this half-loop, about 1 mm away from its plane, to allow laser access to the ion trap. The loop is connected to ground via a 50 Ω load and driven by a Wavetek programmable waveform synthesizer. Pulsing the RF on and off is accomplished with a mixer (conversion loss ∼ 6 dB) with its IF input controlled by a gate signal generated by a counter on the data acquisition board. With this system, square RF pulses with pulse lengths from 1 μs to about 1 s can be produced. Between the synthesizer and the mixer we inserted a 22 dB attenuator to be able to produce the desired magnetic fields with synthesizer voltage settings of about U_{pulse}=1 V_{p-p}. From this setup we would expect a 1 V_{p-p} sine signal to produce a 0.4 mA current in the half-loop which will produce a magnetic field of about $B = \frac{\mu_0 I}{4R} = 0.5$ mG. According to Eq.(3.42)

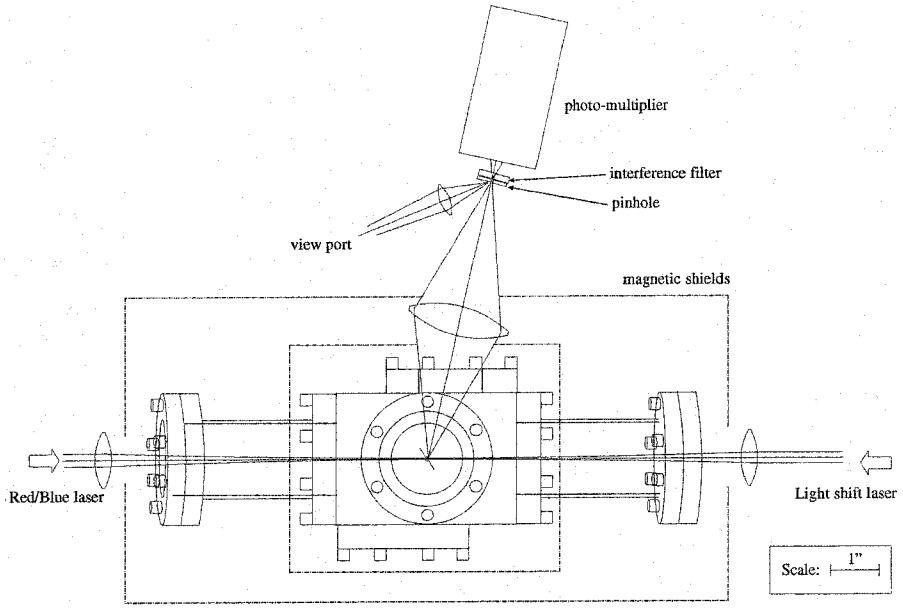

Figure 4.5: Imaging system, consisting of a photo-multiplier tube and a lens that images the ion fluorescence onto a pinhole.

this will produce, for example, a Rabi frequency between the innermost D-levels of

$$({}^{D}\Omega_{\frac{1}{2}\leftrightarrow-\frac{1}{2}})/U_{\text{pulse}} = 1100\,\text{Hz}/\text{V}_{\text{p-p}} \tag{4.1}$$

4.3 Imaging system

The ion fluorescence is monitored through one of the horizontal ports of the chamber with a photo multiplier (see Figure 4.5). With a camera lens the trap center is imaged onto a small pinhole ($\varnothing \sim 0.1\,\text{mm}$), which can also be viewed with a microscope eye piece. Between pinhole and photomultiplier the light passes through an interference filter (bandwidth 5 nm) that suppresses light that is not at 493 nm. The photomultiplier signals are shaped and counted by the data acquisition system. If we assume that the fluorescence emission is isotropic, for a saturated transition we would expect a count rate of $R_c = \frac{1}{2} f \Gamma \frac{\Omega_{\text{solid}}}{4\pi} q_e q_0$, where $f = 0.78$ is the fractional decay rate from

$6P_{1/2}$ to $6S_{1/2}$, Γ =125 MHz the decay rate from $6P_{1/2}$, $\frac{\Omega_{\text{solid}}}{4\pi}$ the fractional solid angle of detection, q_e the quantum efficiency of the detector, and q_0 a loss factor due to reflection and absorption at optical surfaces, filters etc. The fractional solid angle is given by the numerical aperture of the imaging lens:

$$\frac{\Omega_{\text{solid}}}{4\pi} = \frac{1}{2}(1 - \sqrt{1 - \text{NA}^2}) \tag{4.2}$$

For our system with NA=0.2, with the typical quantum efficiency of 10 % for our photomultiplier, and a loss factor $q_0 = 0.4$ (mainly due to the interference filter), we would expect a count rate of about 20000 counts/s. Experimentally we only observe at most 1200 counts/s. We attribute this to an aging photomultiplier with diminished quantum efficiency, but have never independently tested this hypothesis. A count rate of >800 counts/s is adequate for our experiment so far since the speed of our measurements currently is limited by other processes, mainly, the RF exposure time, shelving and deshelving time (for explanation for these terms see next chapter). However, in the long run the experiment will benefit from higher count rates, and the reason for the low rates should be established.

Initial alignment of the imaging system can be done with a bright light that enters the front port in the direction of the photo multiplier. When the focus is set correctly, the trap will cast a sharp shadow onto the plane of the pinhole, which can be monitored through the microscope eyepiece. Then the pinhole can be centered visually in the shadow of the trap. This procedure is good enough to see some ion fluorescence, after which the ion signal itself is used for optimization.

4.4 Initial loading procedures

To make sure that the ovens are producing a beam of barium atoms, we turn the trap into an electron emitter by electrically heating and biasing the ring negatively. The electron current is monitored and adjusted to be a few nanoamperes. Then the ovens are heated to produce a beam of barium atoms. When atoms are deposited on

the trap ring, the emission current increases dramatically because of the lower work function of barium compared to tantalum. This way we ensure that barium atoms are produced and hitting the trap. The initial laser beam alignment is done by first steering the beam so that it is partially blocked by the trap ring. By watching the transmitted beam when steering the beam we can perform a knife-edge test and set the focus. Then we move the beam horizontally until it hits the opposite side of the ring, and center it using the mean of the two micrometer settings. We do the same for the vertical direction and iteratively repeat this procedure until it has converged.

When all optical elements are aligned and the red and blue laser are locked to the correct frequencies and linearly polarized, and after turning on a static magnetic field, we can attempt to trap ions. Initially, we use high trap RF voltages and an oven temperature setting that has proven to deposit barium atoms on the trap. The filament is heated to produce an electron current of $\sim 50\mu A$. These settings will produce ions at a high rate and causes a small ion cloud to be trapped. Fluorescence from this cloud can relatively easily be detected, and subsequently the alignment is optimized as the cloud size is made progressively smaller. In the end filament and oven settings are made low enough as to only produce one ion every few seconds. If the geometry is such that background from the filament is not too large, we can see the creation of a trapped ion in real-time as the fluorescence signal will change discretely.

4.5 Blue Laser stabilization

The blue laser has a short-time stability (up to several minutes) that is sufficient to remain in resonance with the $6S_{1/2}$ to $6P_{1/2}$ transition, but requires long-term frequency stabilization. For this purpose we use optogalvanic spectroscopy with a barium discharge lamp. It relies on the fact that resonant light slightly increases the ionization rate of Ba^+ and thus increases the discharge current through the lamp.

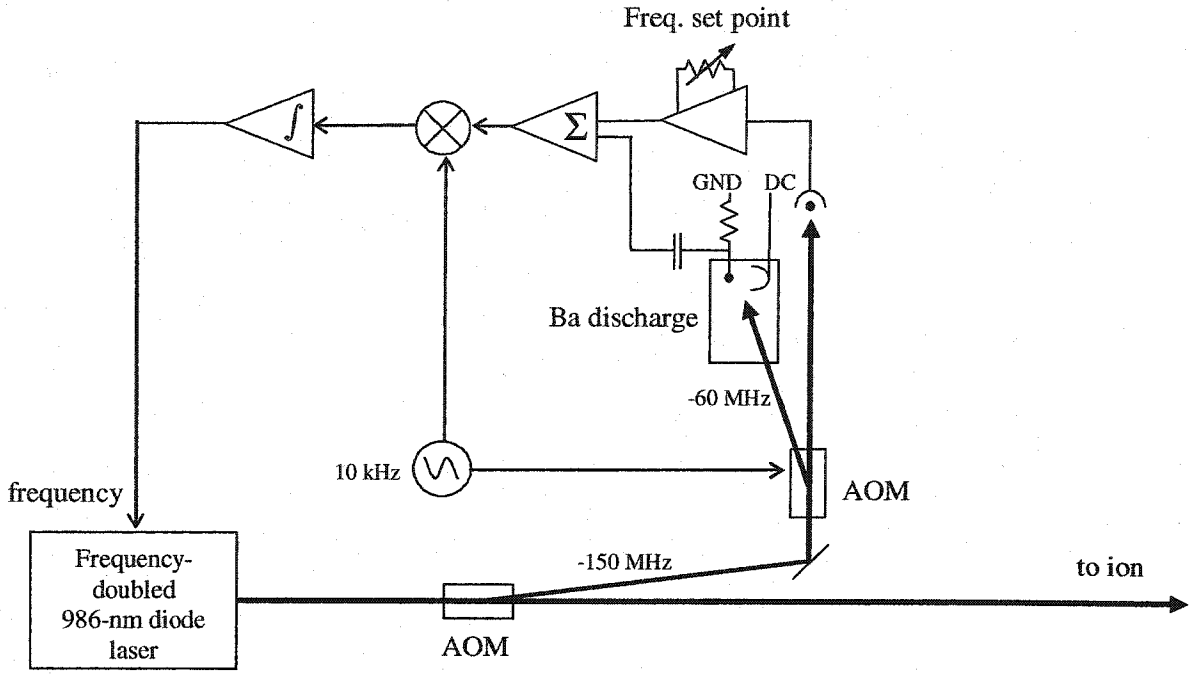

Figure 4.6: Block diagram for blue laser frequency stabilization.

The current due to this laser interaction is much smaller than the background current and has to be isolated with some kind of phase-sensitive detection.

The locking scheme for the blue laser is shown in Figure 4.6. Light from the doubling cavity goes through an AOM, and the unshifted (zeroth order) beam is used for ion trapping. The first-order beam is shifted down in frequency by about 150 MHz and is sent though a second AOM, which shifts the light down by another 60 MHz before it is directed onto the barium discharge. This way, when the laser is tuned to the correct frequency (about 10 MHz below resonance), the light used for locking will be at the side of the opto-galvanic resonance, which is Doppler-broadened to about 1 GHz. We can then subtract a constant offset from the opto-galvanic resonance and use the resulting signal as the error signal for feedback to the laser. We choose the offset so that the error signal will be zero for the correct laser frequency. The flaw of this scheme is that the zero-point for the error signal is dependent on the amplitude

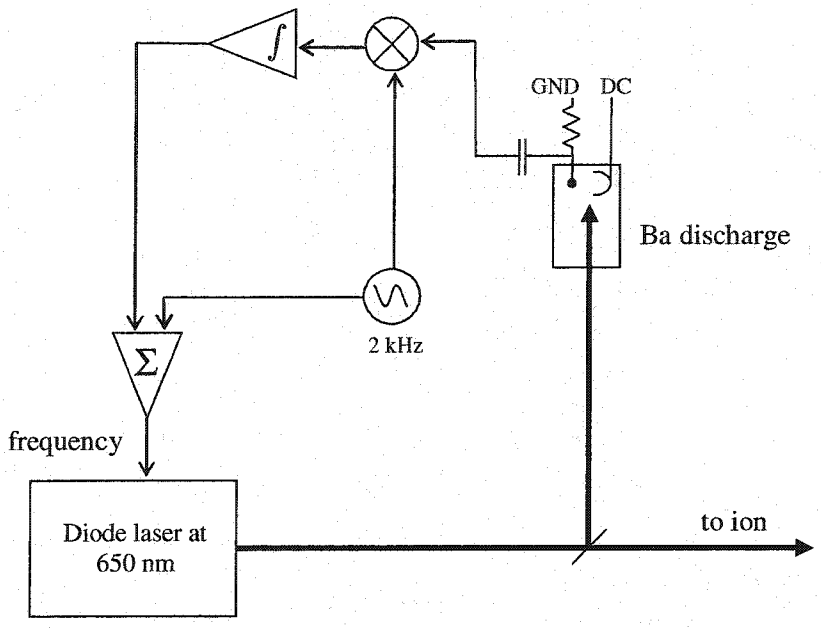

Figure 4.7: Block diagram for red laser frequency stabilization.

of the opto-galvanic resonance which in turn depends mainly on the intensity of the laser. We remedy this by making the offset proportional to the intensity also. Thus experimentally the offset is produced by a photodiode monitoring the laser intensity (the zeroth order beam coming out of the second AOM), and an adjustable gain effectively changes the zero-point of the error signal and thus the lock point for the laser frequency. To obtain good signal-to-noise, we port the measurement to AC and use phase-sensitive detection. We do this by modulating the second AOM at around 10 kHz. Then, the *sum* of modulated photodiode signal and ionization current signal (both converted to voltages) are sent to a lock-in amplifier. Since the two are exactly of opposite phase, this corresponds to a subtraction at DC. The output of the lock-in amplifier is integrated with a large time constant ($\simeq$100 s) and fed back to the piezo frequency control of the laser.

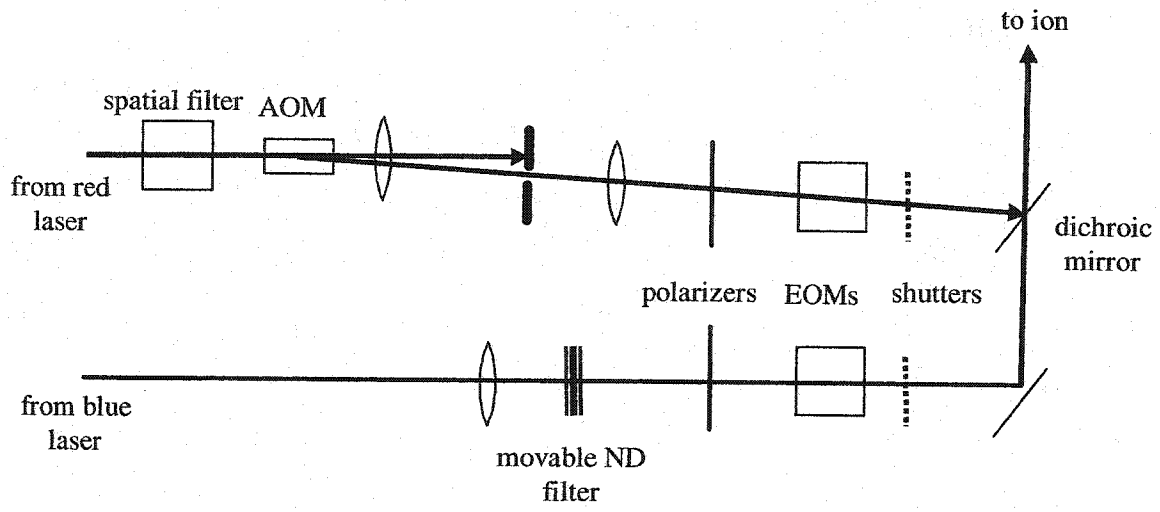

Figure 4.8: Polarization and intensity control of red and blue lasers.

4.6 *Red laser stabilization*

The red laser is naturally modulated in frequency to destroy any dark coherences and simplify spectroscopy, as we have seen in Section 3.3. We can thus use this modulation (deviation is about 100 MHz) to produce an error signal around the peak of the opto-galvanic line. We do this by simply shining the modulated light onto a discharge lamp and detecting the ionization current with a phase-sensitive detector (see Figure 4.7). On one side of the resonance the opto-galvanic signal is in phase with the modulation, producing a positive signal, while on the other side they have opposite phase, leading to a negative signal. On resonance and far away from resonance the signal is zero. The resulting signal is essentially the derivative of the opto-galvanic resonance, which looks like a dispersion-shaped signal.

4.7 *Polarization and intensity control*

For optical pumping and spin state detection we need to have the capability of making either beam circularly or linearly polarized. For this we use an EOM with its fast axis

rotated by 45^o relative to the light polarization which is fixed with a linear polarizer. The EOMs are driven by a high-voltage amplifier and a circuit that can switch quickly between two high-voltage settings, depending on a TTL signal from the computer. We set the voltage for circular polarization by minimizing the ion fluorescence; for perfect circularly polarized light no fluorescence is observable as one of the ion's spin states is completely uncoupled.

Furthermore, for spin state detection we need to attenuate the beams by about a factor of 50000. Initially this was done for both lasers with a neutral density filter that could be moved in and out of the beam with a stepper motor. This has the disadvantages that it is relatively slow (a few ms), that the attenuation is fixed, and that the stepper motor is a potential noise source for magnetic fields. Therefore an AOM attenuator has been installed, but only for the red beam so far. The idea is to simply use the first-order beam of an AOM and to block all other orders. The first-order beam can then be conveniently turned on or off, or attenuated at will by varying the RF power to the AOM. The problem here is light scattering in the crystal and the bad beam shape from the diode laser, both of which lead to an imperfect separation of the different orders coming out of the AOM. With a spatial filter before and after the AOM we achieve an attenuation factor of 50000-100000. One has to deal with the fact that the first-order beam is shifted in frequency. For the red laser the AOM operates at 50 MHz, but since the laser is broadened to about twice that, part of the laser spectrum is still resonant with the ion. For the blue laser we would simply have to change the frequency lock-point to compensate for the additional frequency shift.

Lastly, there is the need to completely shut off the laser beams. We use mechanical shutters made from small stepper motors for this purpose.

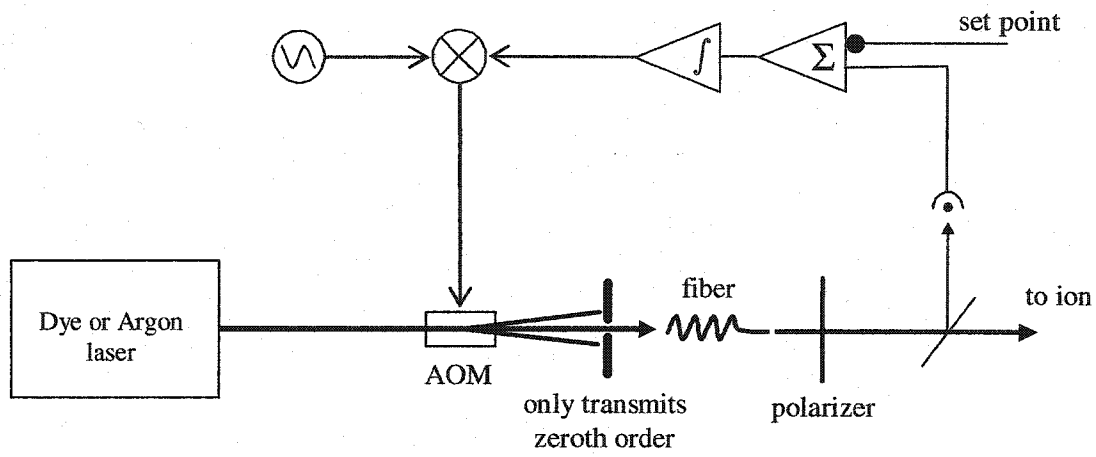

Figure 4.9: Block diagram for light shift laser intensity stabilization. Using a mixer, an RF source (50 MHz) is modulated by a feedback circuit to vary the RF power to the AOM.

4.8 Light shift laser

4.8.1 Intensity stabilization

The light that causes off-resonant light shift has to be stable in spatial pointing, polarization and intensity during the measurement time of many hours. Any fluctuations will lead to a broadening of the light shifted resonances, which should be avoided if we want to achieve good measurement precision. The light is produced either with a dye laser, or comes directly from an argon ion laser. In either case, pointing, polarization and intensity noise have to be taken care of. By coupling light through a single-mode fiber, any pointing noise is converted to intensity noise at the fiber output. Likewise, a linear polarizer after the fiber converts polarization noise to intensity noise. Then we use the following scheme to stabilize the laser intensity to better than 1 %. We monitor the light intensity with a photo detector, and subtract an offset to obtain an error signal. The latter controls the RF power sent to an AOM installed upstream of the fiber, which is aligned to only accept the zeroth order beam. By increasing RF power to the AOM we cause more light power to appear as higher-order beams,

and the power of the 0^{th} order to decrease accordingly. Depending on wavelength and alignment, the AOM can remove up to about 70 % of the laser power. Thus the feedback will regulate the laser intensity to maintain a constant intensity as monitored by the photo diode. It proved important to mount the AOM upstream of the fiber because otherwise it introduces additional steering noise due to thermal effects.

4.8.2 Measurement of the spot size at the ion

The light shift laser is assumed to be Gaussian in cross-section, so that the intensity of the beam profile at the focal point can be described by

$$I(x,y) = I_0 e^{-\frac{2(x^2+y^2)}{\omega_0^2}} \tag{4.3}$$

Its spot size ω_0 was measured by two different methods. First, by moving the beam until it hits a side of the trap ring one can obtain a measure of its spot size. Assuming that the trap clips the beam vertically, the fraction of unblocked intensity for $x = \omega_0/2$ is $\int_{-\infty}^{-\omega_0/2} I(x,y)dx \simeq 84\%$. Finding this point and moving the beam horizontally until $\int_{-\infty}^{\omega_0/2} I(x,y)dx \simeq 16\%$ are blocked, corresponds to a beam translation of ω_0, which can be measured with a micrometer mount. The result of this measurement is about $\omega_0 = 21\,\mu$m.

Alternatively, and more precisely albeit more tediously, we can measure the size of the light shift as we move the beam profile across the ion. The resulting light shifts should trace out Eq.(4.3) and allow ω_0 to be determined. Figure 4.10 shows such a measurement for the 514 nm light shift laser when adjusted to approximately the tightest focus. The spot size was determined to be $\omega_0 = 18(1)\,\mu$m, which corresponds to a confocal parameter (distance from the focus where spot size has increased by $\sqrt{2}$) of $z_0 = \frac{\pi\omega_0^2}{\lambda} = 2\,$mm.

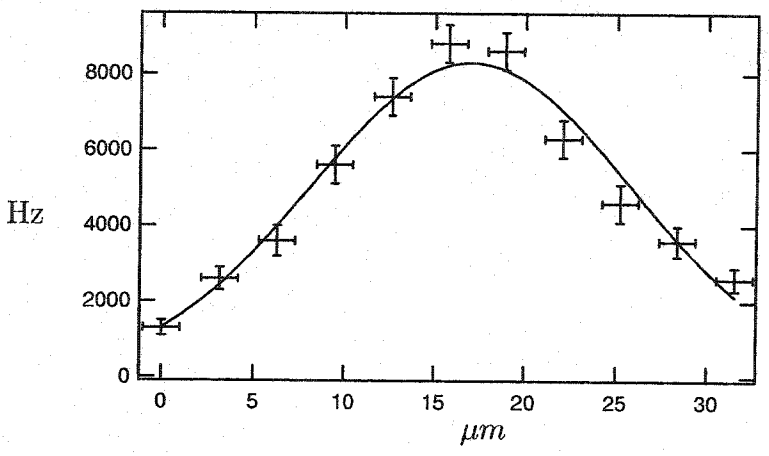

Figure 4.10: Graph shows light shift of the D state as a function of the focus location of the 514 nm light shift laser. The fit is to a Gaussian beam profile and yields the spot size $\omega_0 = 18(1)\,\mu$m.

4.9 Data Acquisition

The data acquisition was done with a National Instruments (NI) DAQ card (6025E) on a PC running Igor Pro with an NI extension. The computer had control over laser shutters, laser polarization, blue laser power and frequency, the shelving and deshelving lamps, as well as the RF synthesizer. Igor Pro was programmed to execute an experimental step every 50 ms. Ion fluorescence was counted asynchronously by the DAQ card and an ion count stored in a buffer every 50 ms.

4.10 Magnetic field issues

Magnetic field change in the laboratory are on the order of a few milligauss and thus broaden Zeeman resonances to a few kHz. Magnetic shielding is therefore necessary in order to achieve smaller line widths. For useful RF measurements a magnetic shielding factor of a few hundred is necessary; for a PNC experiment the shielding would have to be better by another factor of 100. We therefore constructed two layers of magnetic shielding around the vacuum enclosure (see Figure 4.3). Due to spatial

constraints we had to violate several design rules for good shields, such as the absence of sharp corners and the size of holes in the shields (see [59]); nevertheless, the axial shielding factor of the freshly annealed shields was measured to be about 2000. We suspect that the process of repeated installation and disassembly of the shields has degraded this shielding factor, though. Also, the presence of the strong magnetic coils inside the shields (see below) saturates the inner shields, leading to a reduction of the shielding factor. The shields are degaussed occasionally to relax any magnetic tension.

The coils are driven by a home-made stabilized current supply. It has a fractional long-term stability (1 day) of at least 10^{-5} as measured by a precision resistor and a highly stable voltage source. There are two additional, orthogonal single coils installed that allow us to change the magnetic field direction, but they have rarely been used so far.

4.11 History

I conclude this chapter with a brief recent history of people and equipment involved in the barium ion trap efforts at the University of Washington.

For the first year I worked with the ion trap apparatus that Kristi Hendrickson and Mike Schacht had built to do first investigations into a PNC experiment (see [55, 31]. They performed lifetime measurements, and were the first to observe a light shifted Zeeman resonance in the $5D_{3/2}$ state, as well as E2 transitions with a laser at $2.05\,\mu$m. They had two trap systems, one of which had a built-in mirror to perform initial test with an ion in a standing wave, as planned for a PNC experiment.

At the same time there was a barium trap set up in Warren Nagourney's lab which was used in the 90's for several interesting experiments (see, for example, [71, 73]. Warren Nagourney constructed this apparatus and the laser systems, and Justin Torgerson, a post-doc at the time, had just finished constructing a new doubling

system to produce light at 493 nm. In 2000 it was then decided to continue with this apparatus, combining the available resources and experience. Parts of Mike Schacht and Kristi Hendrickson's apparatus were incorporated (like magnetic shields for the ion pump), and the goal for my work became further investigation of RF spectroscopy for a potential PNC measurement (mainly achieving narrow line widths and doing a precise light shift measurement) as well as a measurement of quadrupole moments, as proposed by Warren Nagourney (see Section 9.2 for more details). I mainly worked on implementing fast shelving and deshelving and an overall fast measurement cycle, installing magnetic shields, observing RF resonances of $6S_{1/2}$, and finally designing a new, non-magnetic trap. In 2002 I was joined by colleague Jeff Sherman, who will carry on the current light shift/quadrupole measurement, and is preparing to trap odd barium isotopes for further progress toward a PNC measurement, and possibly, other experiments. Very recently, post-doc Anna Markhotok also joined this effort.

Chapter 5

RF SPECTROSCOPY WITH BA^+

The original motivation for pursuing this ion-trap experiment was a new approach to an atomic PNC measurement conceived by my advisor [23], where the PNC observable is a spin-dependent light shift. Its effect is to alter the Zeeman resonance frequency of spin levels, and is described in detail in Chapter 7. This observable could be measured by doing the analog of RF spectroscopy in the single ion: If we can prepare the ion in a specific spin state, drive a transition that on resonance will change this spin state, and then detect the resulting spin state, we could measure this PNC observable. This technique has two main advantages compared to spectroscopy using optical transitions. First, the fractional frequency stability would be extremely challenging to achieve with lasers since the observable shift in Ba^+ is at most 0.5 Hz. Second, the observable is a shift in the *resonance* frequency between two spin-levels, which means that common-mode shifts of the levels are discriminated against when using RF spectroscopy. This feature can be used effectively to reduce noise and systematic effects in the experiment.

Later it was realized that RF spectroscopy with a single ion might be useful in other experiments, too. We can use it to measure ratios of matrix elements, as we will see in Chapter 6. Also, there are new ideas for its application that involve the measurement of quadrupole moments, an important topic in the ion-clock field (see Chapter 9).

This chapter is concerned with the ground work for these experiments: the realization and study of RF spectroscopy with a single Ba^+ ion. We will go through all the necessary building blocks and conclude with some experiments demonstrating its

capabilities and limitations. The following sections focus on the overall description of the necessary building blocks for RF spectroscopy. More technical details about the trap system, lasers, etc. can be found in Chapter 4, and more theoretical background about ion trapping is found in Chapter 3.

5.1 Trapping an ion

We use a small Paul ring trap for its easy optical access and for the ability to heat and clean the trap surfaces. The trap and adjacent elements are enclosed in an ultra-high vacuum chamber that is magnetically shielded. We employ the following loading procedure: The Barium is stored in a small cylindrical oven that has one open end aimed at the trap. By electrically heating the oven, a small Ba atomic beam is created, which intersects with an electron beam at the trap. Impact ionization takes place, and resulting ions are confined by the trap potential. In order to detect the ion, we use its fluorescence from $6P_{1/2}$ to $6S_{1/2}$ when illuminating it with a focused beam at 493.5 nm (blue[1]). This laser is detuned from the resonance by about half the line width of the transition to achieve optimal Doppler cooling in the unresolved-sideband regime, as described in Section 3.4. A second, repump laser at 650 nm (red) is necessary to prevent the ion from getting stuck in the metastable $5D_{3/2}$ state, to which it can also decay from $6P_{1/2}$; see Figure 5.1. Also, as we have seen in Section 3.3, we need to destabilize the dark states in the $5D_{3/2}$ state, which is done here with a static magnetic field. Both lasers copropagate along the magnetic field, which enables them to drive $\Delta m = \pm 1$ transitions. Then, with both lasers on and linearly polarized, there are no uncoupled states, and the ion emits spontaneous radiation at both blue and red colors. Also, care has to be taken that the lasers are not detuned by an equal amount from the $6P_{1/2}$ resonance, because in that case we would get Raman transitions from

[1]Traditionally this wavelength has been called "blue" in this lab, and "green" in other labs trapping Ba^+, such as the Innsbruck lab. The truth is that 493 nm is just in between these two primary colors and therefore is best described as *turquoise*.

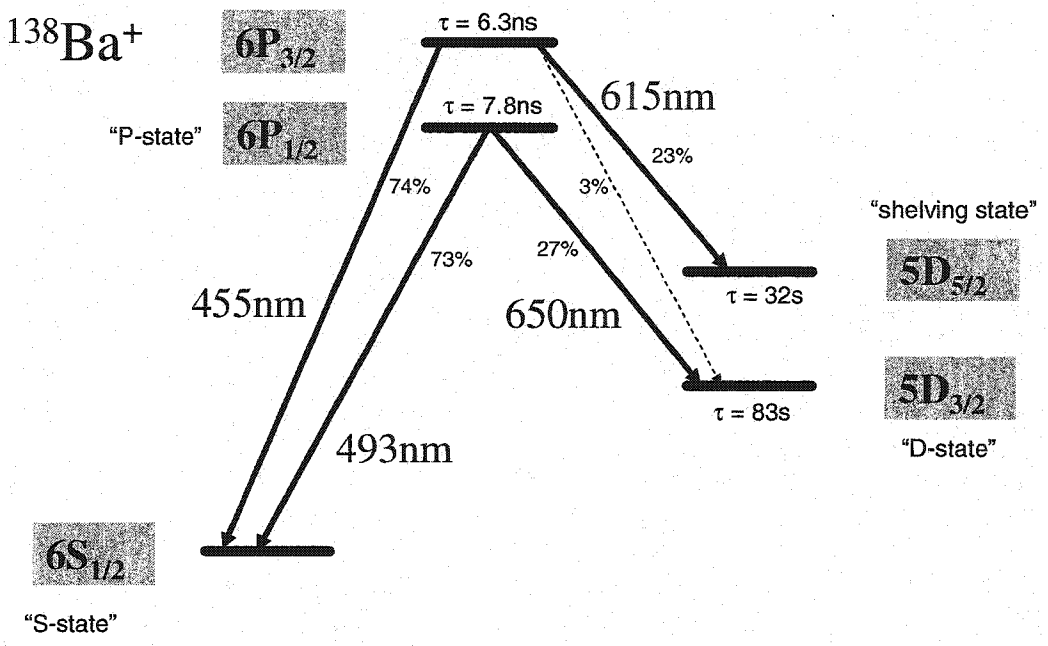

Figure 5.1: Level diagram of $^{138}Ba^+$, showing the dipole decay channel for the relevant states. Also shown are lifetimes and branching ratios.

$6S_{1/2}$ to $5D_{3/2}$ and no fluorescence from $6P_{1/2}$ could be seen (see Section 3.3). To prevent this problem altogether, we modulate the red laser frequency over a band of 100 MHz, which destroys any coherences and always leads to fluorescence. The fluorescence is recorded by a photomultiplier that discriminates against other light sources by imaging the ion onto a pinhole, and by using a narrowband interference filter at the blue wavelength.

5.1.1 Quality control: Is it really a single?

With elements in place, we see around 1000 counts/sec from the photomultiplier, with a background of about 60 counts/sec. Unambiguous proof for the presence an ion (or ions) is the fact that the *blue* fluorescence signal vanishes when turning off the *red* laser. This can only be explained by an ion getting stuck in the metastable $5D_{3/2}$ level. However, this indication is only of limited use when it comes to finding the

number of ions trapped. Usually, this number is small: first, because the oven and electron beam settings are such that the creation of an ion at the trap is not a likely event, and second because, once fluorescence is detected, we stop the ion creation. In addition, when using a weak trapping potential, the trap is simply not capable of holding more than a few ions. Coulomb repulsion will force excess ions out to regions where the pseudopotential approximation is not valid anymore, and the excessive RF heating and lack of laser cooling leads to rapid ion loss.

Still, it is common to trap one to five ions simultaneously. In the case of multiple ions, the fluorescence signal will usually be higher than for one ion, but sometimes the enhanced micromotion due to inter-ion repulsion will weaken the signal, making it an unreliable measure for the number of ions[2]. Furthermore, one first needs a calibration of the signal strength of a single ion. A much better method is the use of quantum jumps using the "shelving state" $5D_{5/2}$. With red and blue lasers on, we turn on a lamp that excites the ion(s) to the $6P_{3/2}$ state. This makes $5D_{5/2}$ an uncoupled state and the ion will eventually decay into it. This is evidenced by the cease of fluorescence light. At the point the "shelving lamp" is turned off. The ion(s) will then spontaneously decay back to $6S_{1/2}$, at which point they are again able to take part in the fluorescence cycle. With a lifetime of 35 seconds, it is easy to see the ions come back individually to the ground state by monitoring sudden changes (usually increases) in the fluorescence count rate. Then, by counting the number of steps, we can count the number of ions in the trap. Figure 5.2 shows such a process in which six ions were found to be present. There are several ways to end up with a single ion. One way is to simply turn of the RF trap potential and repeat the loading process. Another way is to turn off one of the lasers for a while. Without cooling, RF heating [61] will eventually make all ions leave the trap. Often, after waiting for a minute or so, the last ion will still be there, because its heating rates are much slower.

---

[2]Another indicator are the counting statistics: for multiple ions there is noise in the counting signal that significantly exceeds the amount expected from shot noise.

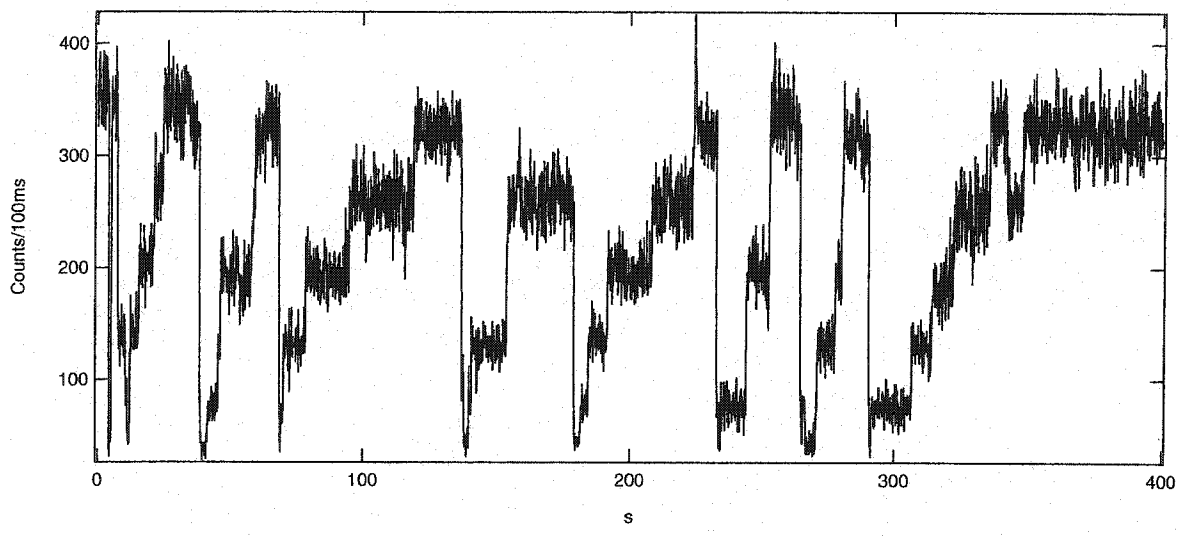

Figure 5.2: Fluorescence signal with red and blue lasers on. Periodically the shelving lamp is turned on, upon which all ions rapidly decay into the dark $5D_{5/2}$ (sharp drops in the count rate). The step-wise increase in the count rate is due to several ions independently decaying from $5D_{5/2}$. Six discrete count rate levels can be identified, probably corresponding to six ions in the trap.

5.2 Spin state preparation

With a single, trapped and cooled ion, we can now proceed to the next step, which is to prepare the ion in a definite spin state. With the $5D_{5/2}$ already used for shelving, two stable levels remain that can be used for this purpose: The $6S_{1/2}$ state, in the following simply named "S-state", and the $5D_{3/2}$ "D-state". We will want to be able to do RF spectroscopy in both states, since RF measurements in each level (and in both levels simultaneously) enable useful experiments. For the S-state, we can uncouple one of the two spin levels by making the blue laser circularly polarized. No matter where the ion starts out, it has to eventually decay to the uncoupled state, which we take to be $m = 1/2$. This is evidenced, again, by a drop in the ion fluorescence. Since polarization and alignment to the magnetic field axis are not perfect, the decoupling is incomplete; more accurately, the transition rate out of $m = 1/2$ is reduced as

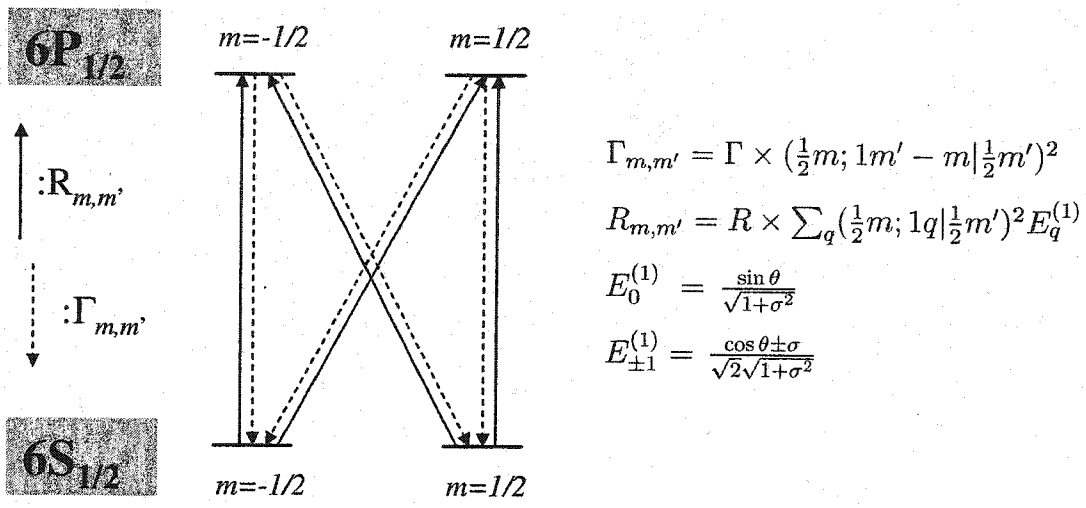

Figure 5.3: Decay and excitation rates for a rate equation model that predicts steady-state populations in the S-state. $E_q^{(1)}$ are the spherical components of the electric field.

compared to those out of the other states, such as $m = -1/2$ and the D-states. It is instructive to set up a rate equation model for this system. If we assume that the red laser is approximately linearly polarized, the D levels don't have to be included in the model. For the two S and P levels, we have for the populations

$$\dot{s}_m(t) = \sum_{m'} [\Gamma_{m,m'} p_{m'}(t) - R_{m,m'} s_m(t)] \tag{5.1}$$

$$\dot{p}_m(t) = \sum_{m'} [-\Gamma_{m,m'} p_m(t) + R_{m,m'} s_{m'}(t)] . \tag{5.2}$$

With the definitions of Figure 5.3 we can find the equilibrium solutions by setting the time derivatives to zero. We also take the limit where $\Gamma \to \infty$, which means that the decay rates are much larger than the laser excitation rates. This is not a good approximation, but will simplify the result without altering it much. If we consider an electric field with polarization σ (defined in App. A.5) whose axis of propagation

is tilted by an angle θ, we find for the steady-state population of $m = 1/2$:

$$s_{1/2}(t \to \infty) = \frac{1}{2} + \frac{2\sigma \cos\theta}{3 + 2\sigma^2 - \cos(2\theta)} \tag{5.3}$$

We can see that the population $s_{1/2}(t \to \infty)$, which is 1 for $\sigma = 1, \theta = 0$, degrades linearly with σ and quadratically with misalignment. Experimentally $\sigma > 0.95$ are readily achievable, which means we can effectively pump into specific spin levels.

For the D-state we have to do the reverse and set the red laser to circular polarization, leaving the blue laser linearly polarized. The difference is that now, in general, *two* levels in the D-state are uncoupled. Therefore, it is not obvious which state the ion will decay into. A preparation of the $m = 3/2$ level is possible by tilting the propagation axis of the red laser. This enables us to drive $\Delta m = 0$ transitions, which couples the $m = 1/2$ state only and leaves the $m = 3/2$ state as the only uncoupled state in the system. If there is no quadrupole shift present, all levels have the same energy separation and it doesn't matter which state the ion is in when doing RF spectroscopy. Unfortunately, in a measurement of light shifts, the only useful state is $m = 1/2$, as will be discussed further in Section 3.5.3. To understand how the probability for pumping to $m = 1/2$ (in the future referred to as the parameter a) depends on polarization and alignment, we can solve a similar rate equation model for the D-state. The solution is shown in Figure 5.4. We see that a drops sharply when increasing θ, as expected. When the polarization is also imperfect, this drop is mitigated. Even with pure Zeeman splitting, a has observable consequences because it changes the shape of the resulting resonance, an effect we are studying in Section 3.5.3. Experimentally we observe the maximum value to be $a \simeq 0.8$.

For the D-state there is also an alternative geometry: With the polarization of the red laser along B, only $\Delta m = 0$ transitions are driven, which leaves the outer two m-levels uncoupled. Such a geometry will be helpful in a measurement of the quadrupole moment of the D-state (see Section 9.2).

For both S and D stats, with pumping rates on the order of MHz, the pumping

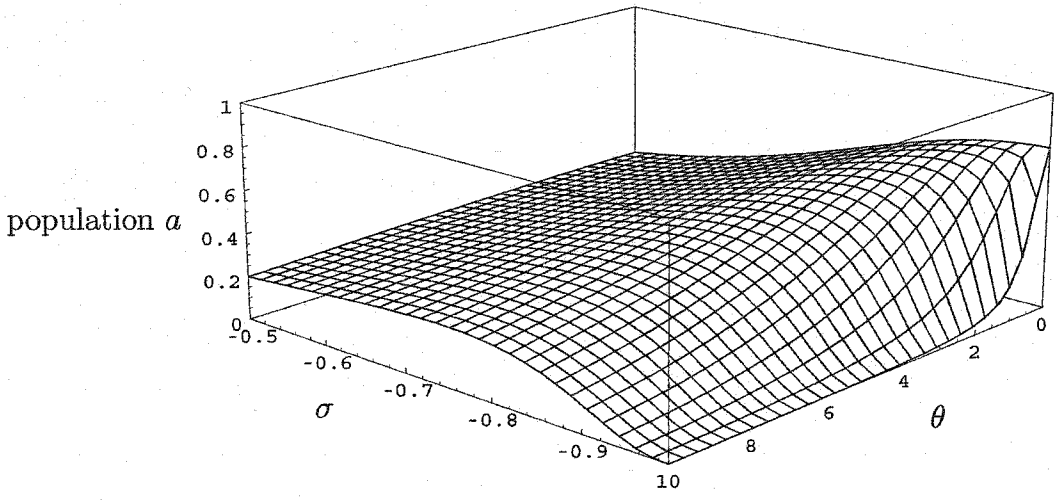

Figure 5.4: Steady-state probability a to be in the $5D_{3/2}$,$m = 1/2$ state, after pumping with a red laser with polarization σ and misalignment θ. A large probability is desired for measuring light shifts in the $5D_{3/2}$ state. This occurs naturally unless the polarization is very *good* and the misalignment is sufficiently large.

process happens as quickly as we can reliably set the polarization to be circularly polarized. After that we turn off both lasers to set the stage for RF spin flips. In each case care must be taken to turn off the circularly polarized laser *first.* Otherwise the ion will, after being pumped out of the desired spin state by spurious polarization (which even for good circular polarization happens with a kHz-like frequency), decay into the wrong atomic level.

5.3 RF-transitions and Spin-state detection

Now that the ion is prepared in the $m = 1/2$ state, or at least in a set of sublevels, we can drive a spin-flip transition. For this purpose there is a small half-loop of wire built into the apparatus. It oriented to produce an oscillating field perpendicular to the static magnetic field when driven with an RF source. The latter is a waveform generator that allows us to control amplitude and frequency with a computer, which also uses a mixer to apply RF pulses of well-defined duration. As we have seen in

Section 3.3, we need a minimum static field of about 1 Gauss, which produces MHz-sized resonance frequencies. The ratio of resonance frequencies $R_0 = \omega_0^S/\omega_0^D$ is just the ratio of g-factors, 2.5 in our case, without relativistic corrections.

5.3.1 S-State

It is fairly easy to see that in order to observe RF resonances with a single ion, we need some variation of the shelving technique discussed in Section 3.2: The only observable quantity from the ion is its fluorescence, and many fluorescence photons are needed to produce a detectable signal. If we were to somehow excite the spin states selectively so that only one state would yield fluorescence, we would only get on the order of 1 photon before the spin information is destroyed by this spontaneous emission.

The question then arises of how to get the ion into the shelving state in a spin-dependent way. The most direct and effective way would be to use a laser at 1.76 μm to drive a transition from $6S_{1/2}$ to $5D_{5/2}$ by way of an optical π-pulse. It would be possible, with some work, to access the individual spin levels independently with such a laser, but for PNC experiments much smaller energy splittings are desirable. Instead, with the right Clebsch-Gordan chemistry, it happens that transition out of one spin state is exactly twice as fast as the other when using a circularly polarized 1.76 μm laser. We can thus drive π-pulse for one spin state, which for the other spin state is a 2π-pulse and returns it to the $6S_{1/2}$ state. This requires driving a coherent transition, implying that $\Omega \gg \Gamma$, where Ω is the (optical) Rabi frequency and Γ the laser line width. Even though we have a color-center laser that is in principle capable of driving such a transition, the project has not yet been undertaken. Instead, we use a more indirect, two-step method. First we apply a blue laser pulse that has the same circular polarization as the light used for state preparation. If the spin state has not changed since state preparation, this pulse will have no effect on the ion. From $m = -1/2$, however, the ion can be excited to the $6P_{1/2}$ level and has a *chance* to decay into the D-state. This is desired, because then we have encoded the *spin*

state information into *atomic state information*, namely, a change in spin state has resulted in a change from S to D state. Since the ion can also decay back into S, this correlation is not perfect.

In the second step, we don't have to worry about addressing spin-states anymore. We simply have to determine whether the ion is in the S or in the D state. This can be accomplished with shelving: A pulse from the shelving lamp will promote the ion into $6P_{3/2}$, if it was still the $6S_{1/2}$ state; the ion in the $5D_{3/2}$ state will not be affected by the shelving pulse. From $6P_{3/2}$ it will eventually decay into the $5D_{5/2}$ state. Note that we also lose information in this process since the ion has a chance of about 15 % of decaying into the $5D_{3/2}$ state instead.

Now we can finally turn on the red and blue lasers, both linearly polarized, to observe fluorescence. If the ion is shelved, we don't observe fluorescence; if the ion was in the $5D_{3/2}$ state, fluorescence takes place.

If we analyze this scheme closer, we find that its first step is fairly inefficient: The $6P_{1/2}$ branching ratio favors a decay back into the $6S_{1/2}$ state; there is a 73% chance that the ion will decay back to $6S_{1/2}$. If that happens, there is a 2/3 chance that the ion will decay back to the spin state it came from, and the ion can try for the D-state again. Eventually the ion either ends up in the D-state or $m = 1/2$ state. All said, there is a theoretical 40 % probability that an ion in $m = -1/2$ will be transferred to the $5D_{3/2}$ state. Add to this imperfect shelving and we would expect a maximum *shelving contrast* (i.e. difference in shelving probabilities for $m = 1/2$ vs. $m = -1/2$) of 34 %.

A practical issue comes from imperfect circular polarization of the blue laser during the probe pulse. If it is on for too long, it will excite the ion out of the $6S_{1/2}$ state irrespective of the spin state, and the ion will end up in the D-state. Too short a time will not cause any excitation, as is illustrated in Figure 5.5, where we solve the rate equations in their time-dependent form. We can see that at some defined time the probability *difference* to be in the D-state is maximal (right graph). It turns out that

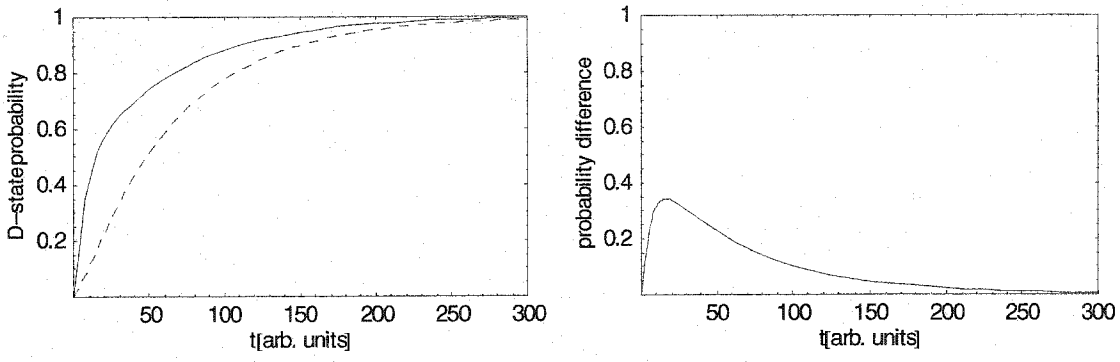

Figure 5.5: The left graph shows the rise in D-state population when the ion starts out in $m = -1/2$ (solid) and $m = 1/2$ (dashed). The right graph shows the difference in these probabilities. The optimal probe time is given by the maximum of this difference.

in the experiment, this optimal time is smaller than 0.01 ms and too short to access with the mechanical shutters we use. We therefore attenuate the light by a factor of about 10^4 before pulsing the laser on; this brings the optimal time up to a manageable few milliseconds. One idea to improve the probability that the ion ends up in the $5D_{3/2}$ state would be to simply have the (weak) blue laser and the RF on at the same time. Then, on resonance, the D-state would be the only uncoupled state and the ion would certainly end up there. If the RF is not on resonance, only spurious polarization would take the ion out of the $m = 1/2$ state. But even a weak blue laser will produce light shifts that can be much larger than the precision of our RF measurement, and due to frequency drifts of the laser such shifts are not predictable. A compromise solution is currently implemented. It consists of simply repeating the pattern of RF pulse and blue probe pulse. That way, we give the ion a number of chances to decay into the $5D_{3/2}$ state. When doing this, we can't speak of coherently driving the RF transition anymore because of the spontaneous decay back to the $6S_{1/2}$ state. As a result, the resonance profiles obtained with this method don't show coherent features such as additional "Rabi-sidebands". But it is possible to enhance the correlation

$m = 1/2 \rightarrow 5D_{3/2}$ state considerably, as we show in Section 5.5.

5.3.2 Spin resonance in the D state

Optical pumping leaves the ion in either the $m = 1/2$ or $m = 3/2$ state (collectively called subset) enabling us to do RF-spectroscopy in the D-state. As before, a is the probability for the ion to be pumped into the $m = 1/2$ state. An RF π-pulse will then cause the ion to be in $m = -1/2$ with probability a and in $m = -3/2$ with probability $1 - a$. To detect this change from one subset to the other, we can do the reverse of the S state detection: we apply a pulse of circularly polarized red light, which excites the ion when the transition to the other subset has been made. Now the P-state branching ratio leads to a high probability that, once the ion is pumped out of the D-state, it will decay into the S-state. Thus the correlation between spin information and state change is fairly high: Theoretically, it is 94% for the $m = -3/2$ state and 81% for the $m = -1/2$. The extreme m-level has a higher probability of ending up in the S-state because an excitation takes it to the $P, m = -1/2$ level. From there it has a higher probability of decaying back into the subset it came from, compared with the $D, m = -1/2$ and its corresponding $P, m = +1/2$ excited state. In practice, these correlations depend on laser parameters such as misalignment and pulse length. For future reference we will call the ratio of correlations b, theoretically given by $b = 94\%/81\% = 1.16$. After this first step everything is identical to the S resonance; we use shelving to determine whether the ion was in the S or D state. For the D-state resonance, the maximum achievable shelving contrast is then 77 %.

Note that if the RF is on resonance, the ion should have a high probability of being in S and thus to get shelved. For the S-resonance the situation is reversed and we would expect a *small* shelving probability if spin-flips are driven.

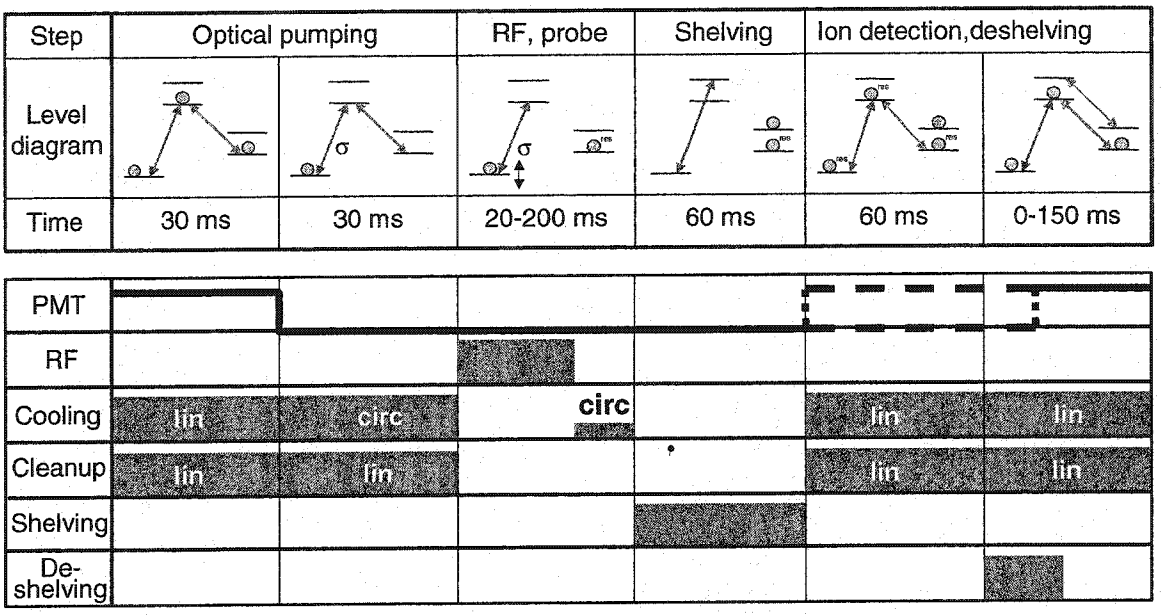

Figure 5.6: Sequence of steps when performing RF spectroscopy in the S-state.

5.4 *The sequence and some sample data*

The question arises of how to best make a reliable judgement about the absence or presence of ion fluorescence, given that there is also a background count rate present. It seems most reasonable to set the count threshold so that it is an equal number of standard deviations removed from the background counts and from the ion counts. If N is the number of collected photons when the ion fluoresces, and f is the fraction of N that is due to background counts, the optimal threshold setting is then $\frac{fN}{\sqrt{f}+1}$. The safety margin s, in units of standard deviations (either from N or from fN), is given by $s = \sqrt{N}\frac{1-f}{\sqrt{f}+1}$. Thus in order to have a safety margin of three standard deviations, sufficient for our purposes, we need to count $N = 20$ photons when the ion fluoresces. This assumes a noise/signal factor of $f = 0.1$. Since we collect about 1000 photons/s, the detection process ideally takes about 20 ms. In reality we count for about 50 ms, and there is also some overhead associated with data collection. If the ion is found to be shelved, it needs to be forced out of the shelving state ("deshelved") since left

alone it would stay there for $\sim 30s$. This is done with a bright orange LED that has some light power at 615 nm, which drives the $5D_{5/2} \leftrightarrow 6P_{3/2}$ transition.

Repeating this sequence of state preparation, RF transitions, and spin-state detection, we will obtain a *shelving probability*, which is correlated with the spin state of the ion after the RF interaction. We can thus find shelving probabilities for various RF frequencies around a spin resonance and trace out the resonance profile, usually with the goal of determining the line center with maximum precision. For a summary of this procedure, along with some information about the timing in our current measurement sequence, see Figure 5.6. In order to build up statistics for all frequencies simultaneously, we cycle through frequencies rather than finding probabilities sequentially.

When recording RF resonances, several parameters have to be set: The RF-amplitude determines the RF Rabi frequency and therefore the RF-induced line width of the transition. If our goal is to minimize this line width, we will tend to choose lower and lower Rabi frequencies. Correspondingly the RF pulse length has to be adjusted to keep the product Ωt constant and still drive a π-pulse. On the other hand, during the measurement time of a resonance, which is on the order of tens of minutes to hours, the magnetic field drifts around and effectively induces a line width broadening Γ_B; see Section 5.7 for more details. If we make Ω smaller than this line width, we lose shelving contrast because then the magnetic broadening "smears out" the resonance. We therefore most often choose a Rabi frequency that causes a line width comparable to the line broadening. The ratio Ω/Γ_B also determines the line shape of the transition. While the line shape for $\Omega \gg \Gamma_B$ is given by the coherent RF transition, for the opposite case it is determined by the type of noise the B-field exhibits. Experimentally a Gaussian describes this line shape very well. For $\Omega \sim \Gamma_B$ the line shape is a convolution of a Gaussian and the coherent line shape, but will in practice be approximated with a Gaussian.

Other parameters involve the number and spacing of the frequency bins, and the

number of runs N through all bins, which determines the statistical accuracy of the resulting shelving probabilities. The latter is given by Poisson statistics as

$$\delta p = \sqrt{\frac{\bar{p}(1-\bar{p})}{N}} \tag{5.4}$$

5.5 *RF spectroscopy in the S-state*

An example of RF spectroscopy in the S-state, when driving a single π-pulse, is given in Figure 5.7. The error bars for the individual shelving probabilities is given by Eq.(5.4). For this measurement the magnetic broadening was not dominant, and the most appropriate model is given by the two-state resonance profile given in Section 2.2.2. We can see that the shelving contrast is about 25 %, which is among the best we achieved, but falls short of the theoretical maximum of 34 %. We attribute this mainly to imperfect optical pumping and probing, but don't understand completely why we couldn't achieve a contrast closer to the maximum, or why the shelving contrast is in general somewhat unreliable for the S-state resonances. The imperfections in polarization and alignment should still allow for a better contrast. On the other hand, the blue laser is narrow and might partially resolve the Zeeman splitting and/or frequency sidebands due to micromotion. This could lead to more complicated pumping/probing behavior that should be studied in more detail.

To prove that spinflips are really taking place, we can capture their time-evolution by recording shelving probabilities for different RF pulse lengths while the RF frequency is unchanged and on resonance. Such a measurement is shown in Figure 5.8. The shelving contrasts of Figure 5.7 and Figure 5.8 are comparable, but their offset differs significantly. This is due to a difference in exposure times for the probe pulse, which, if on for too long, will cause all shelving probabilities to approach zero, as we have seen in the previous section.

Figure 5.9 demonstrates the increase in shelving probability when we repeat the sequence of RF-spin flip and probing. In this case five repetitions were performed

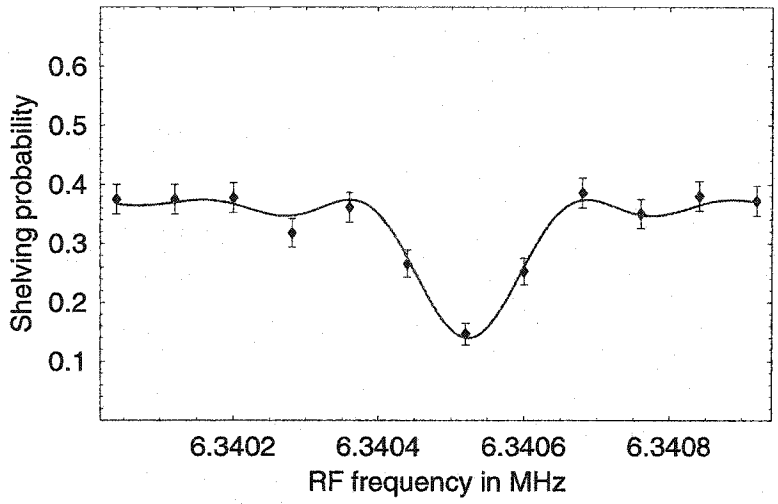

Figure 5.7: Shelving probability as a function of RF frequency with the RF frequency timed to produce a π-pulse on resonance. The fit is the coherent line shape for a two-level system calculated in Section 2.2.2, with scale/offset factors as free parameters. Data: scan030311-ion104-3.

before shelving. There are no longer coherent features in this line shape, and with magnetic field drifts comparable to the Rabi frequency, a Gaussian is the most appropriate fit function.

5.6 RF measurements in the D-state

In the D-state the shelving contrast is inherently higher, and our measurements sometimes approach the theoretical limit of 77 %. An example can be seen in Figure 5.10, where a transition with very large Rabi frequencies was driven. This makes all magnetic broadening irrelevant even for long measurement times, and we can record the line shape of a coherently driven transition, capturing all details of the line shape by recording a large number of frequency bins. The line shape is described by a combination of Wigner functions, or by solving the appropriate Bloch equation, as discussed in Section 3.5.3. Now the line shape becomes dependent on the initial condition a, as well as the readout parameter b that accounts for the fact that the shelving probabil-

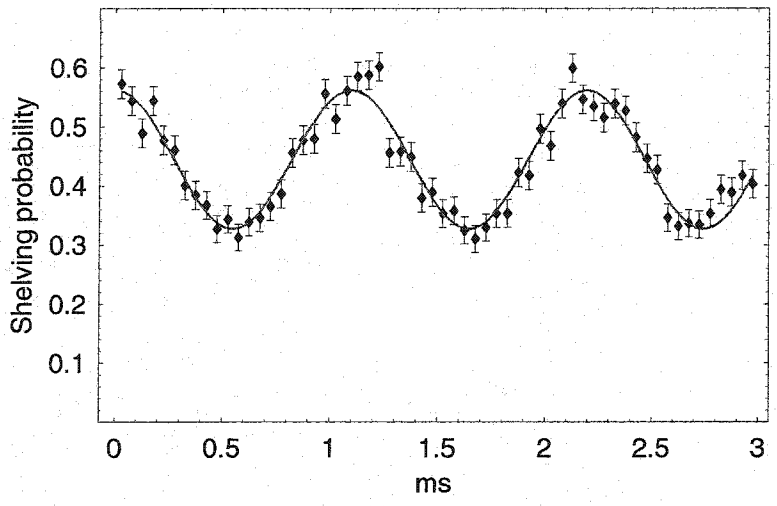

Figure 5.8: Shelving probability for RF spectroscopy in the S-state as a function of RF exposure time for a fixed, resonant RF frequency. The fit is a sinusoidal population oscillation with scale/offset factors as free parameters. Data: scan030310-ion104-1.

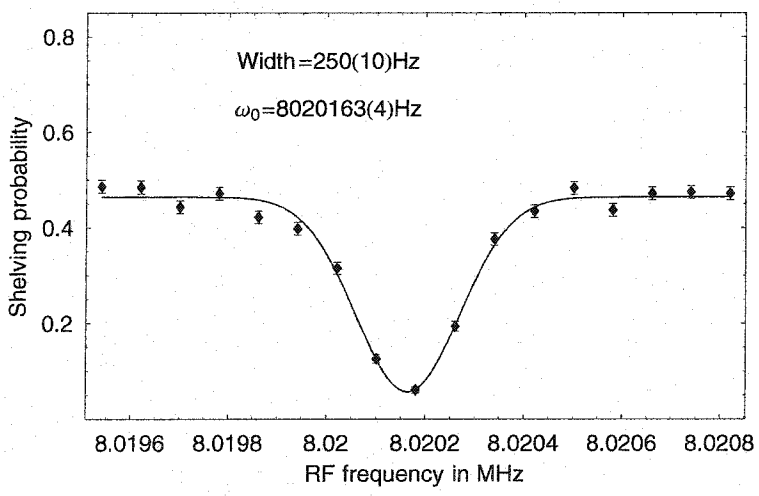

Figure 5.9: Shelving probability for RF spectroscopy in the S-state, as a function of RF frequency with RF frequency and probe beam pulsed repeatedly, as described in Section 5.3.1, yielding larger shelving contrasts. The data is fitted with a Gaussian. Data: scan020807-ion044-1.

ities from $D, m = 1/2$ and $D, m = 3/2$ are different. The two graphs in Figure 5.10 have been recorded at different times with unavoidably different conditions of laser alignment and polarization. As a result, different line shapes emerge, and the initial condition a can be determined by a fit to the line shape.

The coherent behavior can also be seen in the time domain, as shown in Figure 5.11. Again the fit is to the Bloch equations with a and b as free parameters. In Figure 5.11 the Rabi-oscillation time is short compared with the coherence time of the RF transition, which is effectively given by the inverse of the magnetically induced line width. This means that many complete Rabi oscillations will occur before decoherence from the magnetic field leads to an averaging over populations and an effective damping of the oscillations. Only slight damping occurs in Figure 5.12 after 40 ms; in the measurement in Figure 5.13, the magnetic noise is much larger and quick damping takes place after a few milliseconds.

Lastly, we test our ability to understand resonance line shapes for the complicated case of Figure 3.9 where we drive a coherent transition in the presence of an off-resonant light shift on the order of Ω. The data in Figure 5.14 was recorded with circularly polarized light at 632 nm focused onto the ion. We model this data with solutions to the Bloch equations that include the effects of the off-resonant light, as explained in more detail in Chapter 2. The fit describes the major features of the line shape correctly, but falls short of a complete description of the line shape. This is because the model includes untested assumptions about polarization and alignment of the light, and broadening due to intensity fluctuations of the light shift laser are not taken into account.

5.7 Magnetic field drifts and precision of spectroscopy

Ultimately the achievable line widths are only limited by the RF observation time, which in turn is limited by the lifetime of the atomic states we are interested in. For

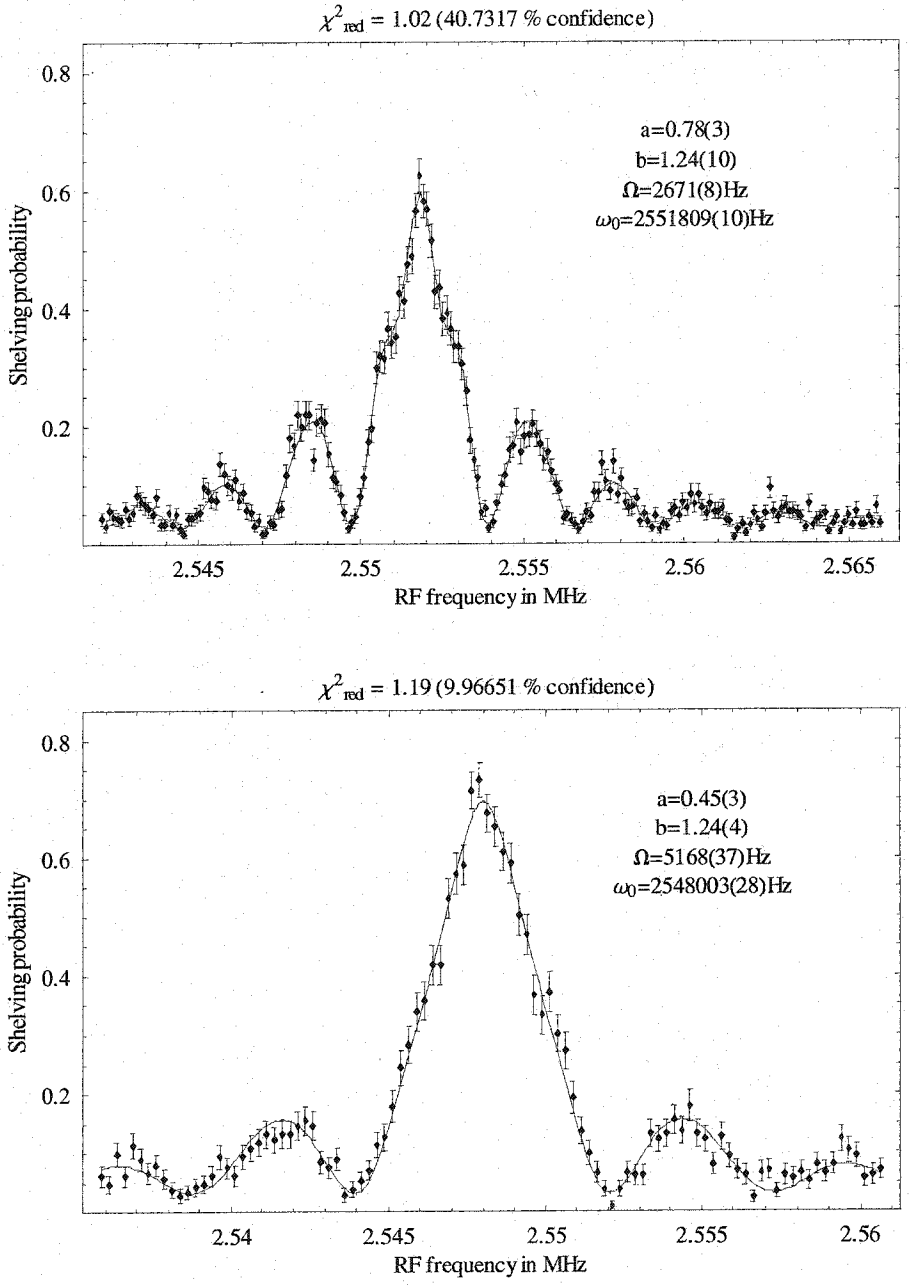

Figure 5.10: Coherent line shape for the D-state without any light shifts present. The fits are a solution to the Bloch equation with a, b, ω_0, Ω and scale/offset factors as free parameters. The two graphs are taken with different red laser alignment when optically pumping, leading to different initial conditions a and therefore to different line shapes. Data: scan030318-ion104-2, scan030804-ion104-1.

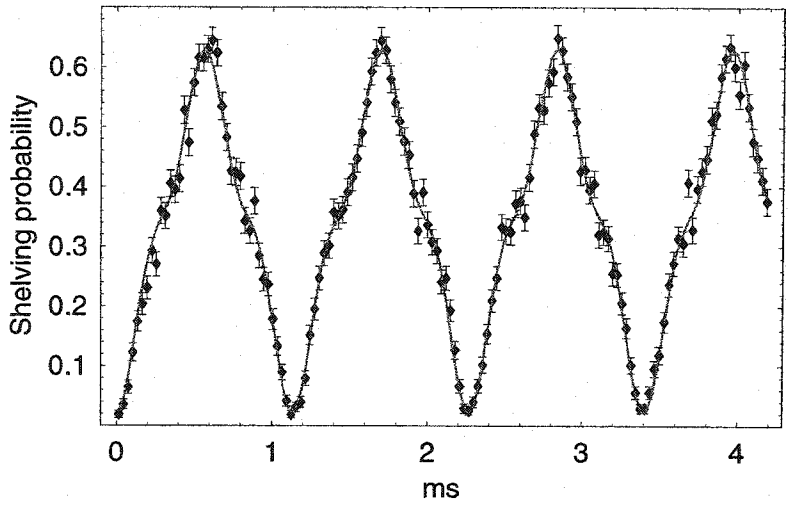

Figure 5.11: Shelving probability as a function of RF exposure time for a fixed, resonant RF frequency. The fit is a solution to the Bloch equation with free parameters a, b, and scale/offset factors. Data: scan030304-ion104-1.

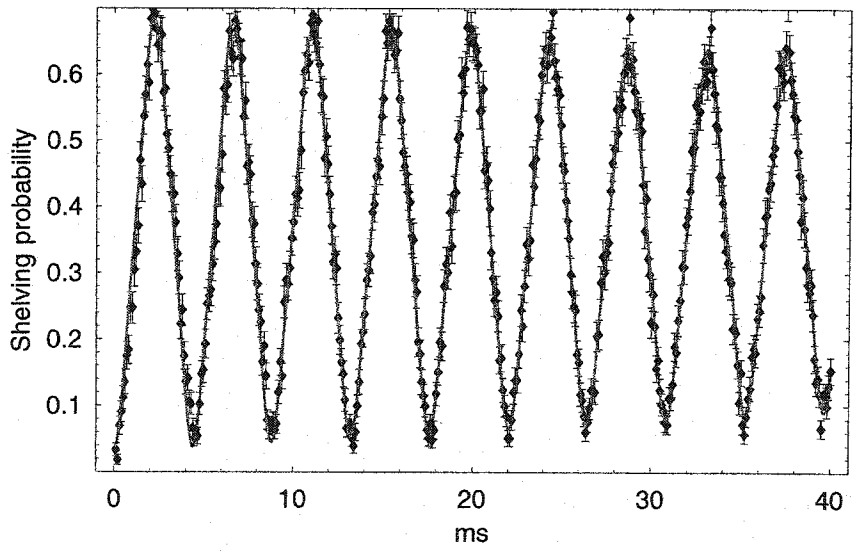

Figure 5.12: Shelving probability as a function of RF exposure time for a fixed, resonant RF frequency. The fit is a solution to the Bloch equation with free parameters a, b, and scale/offset factors. We can see that many oscillations take place, with a slight decay in the amplitude. Data: scan030317-ion104-1.

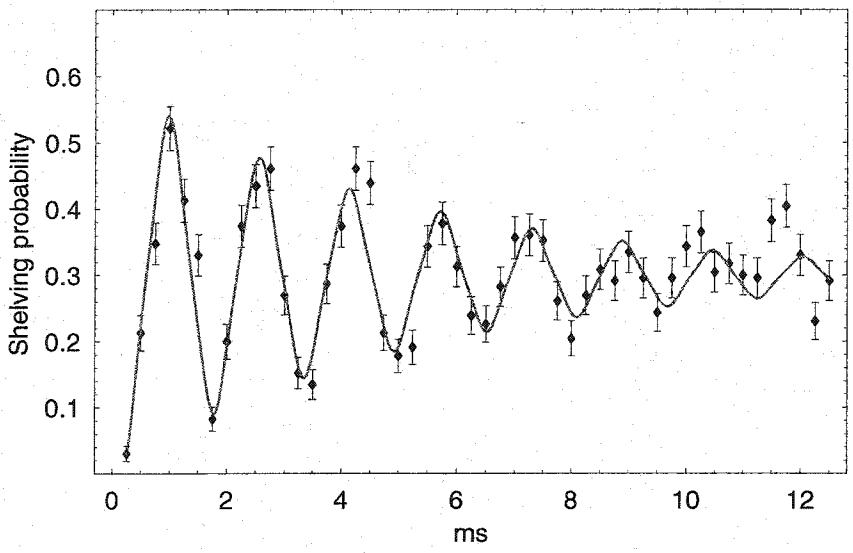

Figure 5.13: Shelving probability as a function of RF exposure time for a fixed, resonant RF frequency. The fit is a solution to the Bloch equation with free parameters a, b, and scale/offset factors. We can see decoherence due to the strong magnetic field noise in this measurement. Data: scan030626-ion104-6.

the $5D_{3/2}$ state, with a lifetime of $\tau \simeq 80\,\mathrm{s}$, this should lead to a line width of about $\Gamma = (2\pi\tau)^{-1} = 2\,\mathrm{mHz}$. Since the precision of the resonance frequency scales linearly with the line width (and only as the square root of the measurement time), achieving narrow lines is of prime importance for any precision experiment.

The one (and seemingly *only*) limiting factor so far has been magnetic field noise, which moves the resonance around during a measurement and leads to a broadening of the line. Fluctuations of the ambient magnetic field in the lab are on the order of a few milligauss, leading line widths of several kHz (see the initial measurements in [55]). Installation of magnetic shielding around the trap vacuum chamber reduced this line width by about a factor of five to ten, falling short of the expectation of line widths on the order of 1 Hz, expected by measuring the shielding factor of the shields. Suspicion arose that the source of magnetic field noise might come in part from locations very close to the ion, especially after we could not find correlations between

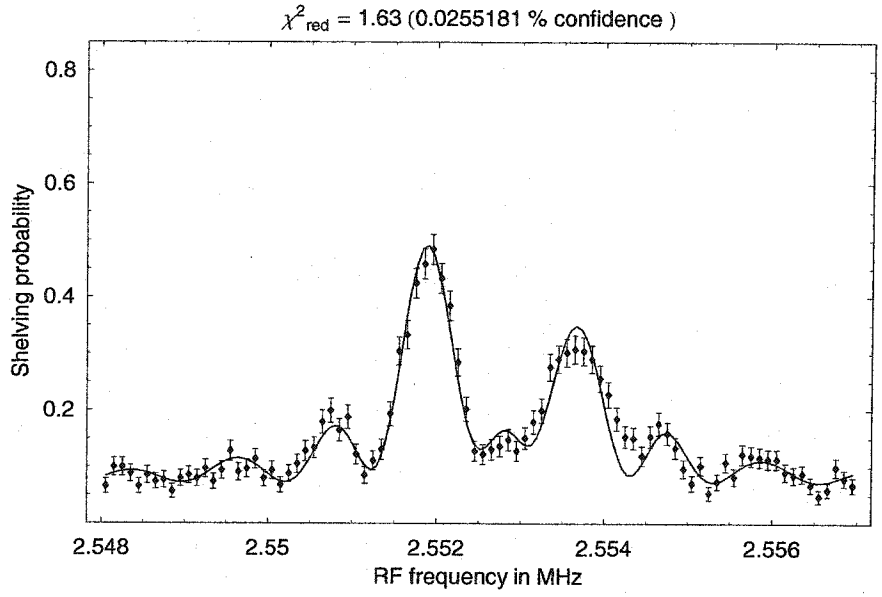

Figure 5.14: D-state coherent resonance in the presence of a light shift $\Delta \simeq \Omega$. The fit is a solution to the Bloch equation with a, b, ω_0, Δ and scale/offset factors as free parameters. The fit captures the main features of this complicated line shape, but makes untested assumptions (e.g. about light polarization) which lead to errors in the model. Data: scan030403-ion104-6.

the measured field changes in the lab and changes in the resonance frequency of the ion. It became clear that the residual noise was mainly a slow (on the order of tens of minutes) drift of the magnetic field, because the short-term line widths achievable were much better than the line widths achieved in a measurement lasting several hours. This is demonstrated in graph 5.16, where we continuously took resonance data for about 16 hours, and then found the resonance frequencies for 20-minute intervals. The dependence of the resonance on time shows the typical time constant and size of these drifts. The main suspect for these drifts became magnetic materials deposited very close to the ion, mainly by the ion loading process (see Chapter 4 for more details). After building a new, non-magnetic trap system, we found that the drifts were much reduced, allowing at times line widths on the order of 10 Hz, as seen in Figure 5.15. Much better line widths would require a more stable current source for the magnetic coils that create the static magnetic field. However, even now we experience large fluctuations at times whose cause is not understood. For example, both graphs Figure 5.12 and Figure 5.13 have been recorded under seemingly similar circumstances with the new, non-magnetic trap, yet the magnetic noise differs by at least a factor of 20. These periods of large fluctuations so far have been intermittent and lasted for a relatively short time. In their absence the short-term stability (1 hour) is about 10 Hz, and the long-term stability (1 month) is about 300 Hz, as we can see from comparing resonances taken over a three-week period in Table 6.16.

5.8 The g-factor ratio and off-resonant effects

The ratio of resonance frequencies $R_0 = \omega_0^S/\omega_0^D$ is just the ratio of g-factors, 2.5 in our case, without relativistic corrections. The g-factor ratio has been measured with an ion cloud in a Penning trap [37] and was found to be $R_0 = 2.505220(2)$. We spent considerable time trying to reproduce this value, and found systematically *lower* values. We also found that the ratio decreased as the trap RF amplitude was

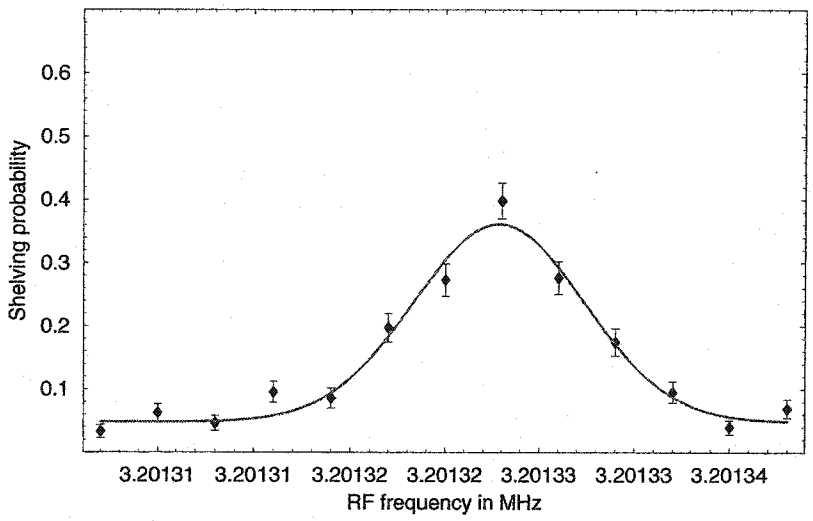

Figure 5.15: Graphs shows a narrow D-state resonance with a line width of 10 Hz, where the error of the line center is 0.4 Hz.

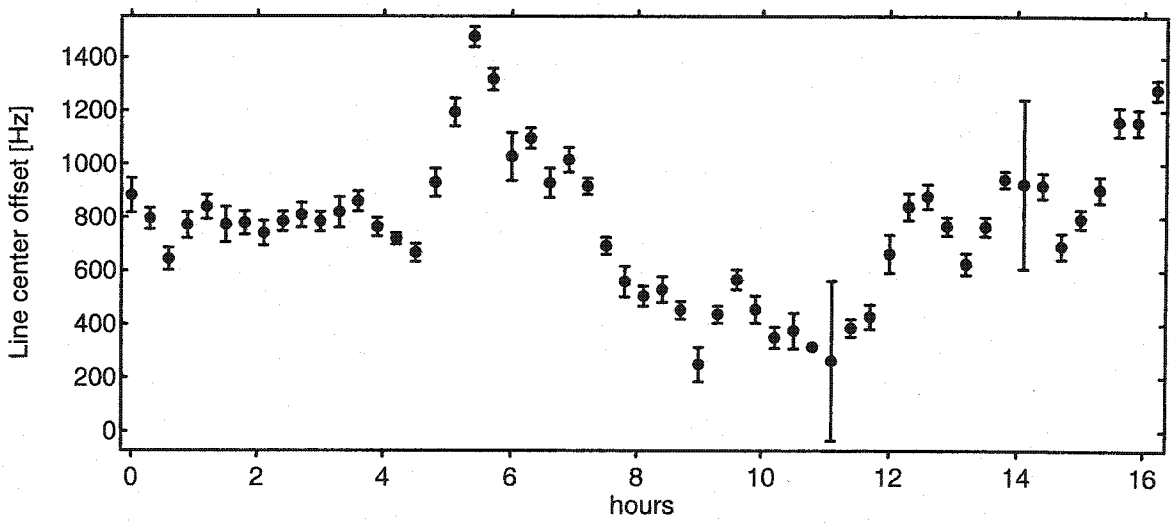

Figure 5.16: Graphs shows the D-state resonance as a function of time, obtained by bunching shelving results into 20-min chunks and fitting to Gaussians. The error bars are derived from the Gaussian fits. Zero corresponds to a resonance frequency of 3.2 MHz. Data: scan030402-ion104-1.

Table 5.1: Some S/D ratio measurements for different trap RF powers and resonance frequencies.

RF	Data	S-res.[Hz]	D-res.[Hz]	Ratio	diff. to [37]
2W	030314-ion104-5	6381877(24)	2547755(7)	2.504901(12)	-0.000318
1W	030311-ion104-1	6340522(7)	2531105(7)	2.505041(7)	-0.000178
0.8W	030313-ion104-1	12375745(20)	4939907(4)	2.505259(5)	+0.000039
1.9W	030314-ion104-1	12376323(14)	4939902(9)	2.505378(5)	+0.000158
3W	030313-ion104-2	12376350(200)	4939737(14)	2.505468(43)	+0.000248

increased (see Table 5.1). We hypothesize that this systematic error in the ratio is due to off-resonant shifts caused by the trap RF frequency at 10 MHz. Even though ideally there are no ac *currents* at the site of the ion, asymmetries in the geometry of the leads etc. make residual currents unavoidable. At the typical resonance frequencies given by the static magnetic field, $\omega_0^S \simeq 6\,\mathrm{MHz}$ and $\omega_0^D \simeq 2.5\,\mathrm{MHz}$. This makes the trap RF frequency have a positive detuning relative to the S-state resonance. Therefore we would expect the m-levels to be shifted towards each other, making ω_0^S systematically smaller. On the other hand, ω_0^D should experience no such shift since the shifts due to two adjacent m-levels cancel. Therefore we would expect the ratio S/D to decrease, with the decrease getting larger for stronger trap RF fields.

To test this hypothesis, we roughly doubled the static magnetic field so that the S-resonance became about 12 MHz. Now the detuning due to the trap RF is negative, and we should expect a systematically *larger* ratio. As Table 5.1 shows, this is indeed the case.

For light shift measurements where we are interested in the *difference* of S-resonances and D-resonances, this shift should not be a problem. However, the shift in the S-state was on the order of hundreds of Hz; in an ultimate PNC experiment, line broadening though a time-dependence of this effect has to be considered.

Chapter 6

MEASUREMENT OF THE RATIO OF MATRIX ELEMENTS IN BA^+

Most atomic physics measurements can, in one way or another, be expressed in terms of matrix elements between atomic states. Examples of such atomic properties include lifetimes of atomic states, polarizabilities, hyperfine structure, or branching ratios. Then, these experimentally determined matrix elements can be compared against calculated values to help advance our theoretical understanding of atoms. Finally, if we trust both calculations and experiment, a discrepancy between them might point to phenomena undiscovered so far. An example of this is parity violation in atoms, where the standard model predictions can be tested by way of a comparison of calculations and experimental values for PNC matrix elements. For the planned experiment in Ba^+ and Ra^+, this comparison involves the S-D PNC matrix elements. Unfortunately, their calculation involves knowledge of the P-D matrix elements, which are hard to calculate precisely, and have also not been measured to more than a few percent accuracy. However, a recent paper about such calculations [19] has this to say about the accuracy of PNC S-D amplitudes in Cs, Fr, Ba^+ and Ra^+:

> "We have shown that by using a hybrid mixed-states-sum-over-states approach the accuracy of the calculations of PNC s-d amplitudes could compete with that of Cs 6s-7s if $p_{1/2}$-$d_{3/2}$ E1 amplitudes are measured to high accuracy."

With the current measurement of light shift ratios we intend to contribute such a high-accuracy measurement of the P-D matrix elements in Ba^+. The experiment also

proves the concept of using RF spectroscopy with a single ion for precision measurement, as envisioned for a PNC experiment.

The idea of this experiment is to measure a change of the Zeeman resonance frequency caused by the light shift from an off-resonance laser.

As we have seen in Section 2.5.4, a light field with intensity I and polarization $\hat{\varepsilon}$ causes light shifts in an atomic level γ given by

$$\Delta_{\gamma m} = \frac{2\pi}{\hbar}\alpha I \sum_{\gamma', m', \pm\omega_L} \frac{|\langle \gamma, jm|\boldsymbol{\epsilon}\cdot\hat{\boldsymbol{r}}|\gamma, j'm'\rangle|^2}{\omega_\gamma - \omega_{\gamma'} \pm \omega_L} \tag{6.1}$$

where α is the fine structure constant, and ω_L is the frequency of the light. If we knew ω_L, I and ϵ of the applied light, we could use a measurement of Zeeman resonance shifts to determine the corresponding sum of matrix elements. While the frequency ω_L is readily measured, it is exceedingly difficult to determine the intensity at the site of the ion. However, if we measure the shift in a second atomic state caused by the same off-resonant light, the field intensity I cancels in the ratio. If, in addition, the shift is measured between the same sets of magnetic substates, we will see that all remaining dependencies of the ratio are of second order in the polarization error and misalignment with respect to the magnetic field.

In Ba^+ we have two such states available, $6S_{1/2}$ and $5D_{3/2}$, and are set up to measure Zeeman resonances between $m = 1/2$ and $m = -1/2$ spin states. With circularly polarized light we can induce a differential light shift that will change the Zeeman resonance of these states. The light shifts are due to the off-resonant coupling to higher atomic states, as shown in Figure 6.1. By measuring the shift in both states simultaneously, a ratio of these light shifts is measured. The precisely measurable quantity is a ratio of sums of matrix elements, which doesn't sound too useful at first glance. However, only a few matrix elements contribute significantly to the light shift, and the effect of the smaller terms can be calculated. Also, because we can perform this measurement for different wavelengths, we can enhance sensitivity to different matrix elements in the sum. For example, when choosing a wavelength that is close

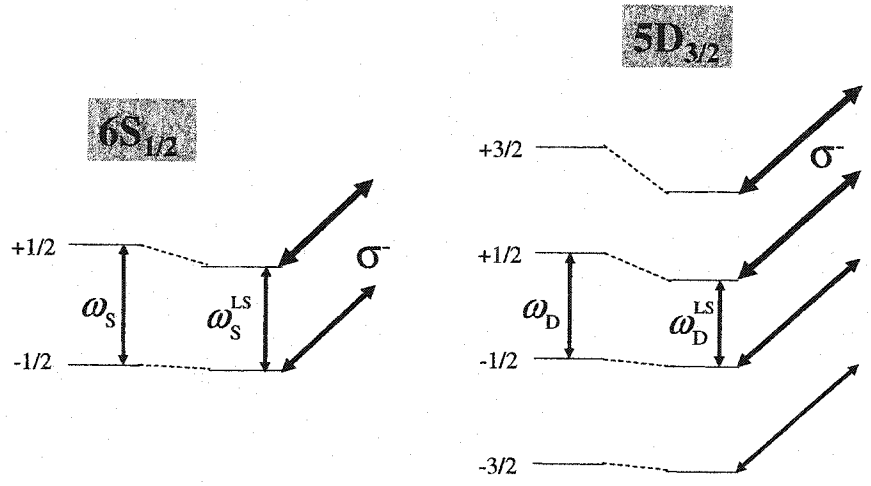

Figure 6.1: Zeeman resonances in both $6S_{1/2}$ and $5D_{3/2}$ are altered by circularly polarized, off-resonant light. The observable of the measurement is then the ratio $R = \frac{\omega_S^{LS} - \omega_S}{\omega_D^{LS} - \omega_D}$.

to the P-D resonances, the Zeeman shifts in the D-state are mainly caused by P-D matrix elements, so that all additional effects can be treated as known corrections. Choosing a shorter wavelength will emphasize the D-F matrix elements more and allow their determination. Since the S-P matrix elements are well-known, a ratio measurement is sufficient to obtain the desired D-P matrix elements.

6.1 Light shift calculation and extraction of matrix elements

6.1.1 Calculation

We have seen in Section 2.5.4 that it is possible to capture the effects of off-resonant light on an atomic state in terms of an effective Hamiltonian H_{eff}. As a result, the spin levels evolve according to the Hamiltionian

$$H = H_0 + H_{\text{eff}}, \tag{6.2}$$

where $H_0 = g\mu_B B_0 \hat{j}_z$ is the static magnetic field causing the initial Zeeman splitting and defining the quantization axis.

We will now express H_{eff} in terms of the atomic structure and the applied light field. We start with the expression for the light shifts of a state $|\gamma, j\rangle$ due to its off-resonant interaction to a multiplet $|\gamma', j'\rangle$, Eq.(2.71):

$$H_{\text{eff}} = \frac{\hbar}{4\delta_{\gamma\gamma'}} \mathbf{\Omega}^\dagger \mathbf{\Omega} \tag{6.3}$$

With the help of the vector structure formalism and including the counter-rotating term and the interaction to multiple states j', we can write this expression as (comp. [55, p.353])

$$H_{\text{eff}} = \frac{\hbar}{4} \sum_{\gamma', \pm\omega_L} \frac{|\langle\gamma'||d||\gamma\rangle|^2}{\omega_{\gamma\gamma'} \pm \omega_L} \left[s(j,j') \boldsymbol{E}^* \cdot \boldsymbol{E} + id(j,j') (\boldsymbol{E}^* \times \boldsymbol{E}) \cdot \hat{\boldsymbol{j}} + q(j,j') \hat{j}_{ik} (E_i^* E_k) \right] \tag{6.4}$$

where $s(j,j'), d(j,j'), q(j,j')$ are the coefficients for the scalar, vector (dipole), and tensor (quadrupole) parts of the Hamiltonian. The vector structure in Eq.(6.4) itself is characteristic of an interaction $\mathbf{\Omega_1}^\dagger \mathbf{\Omega_2}$ where both Ω's are dipole interactions, such as in the present case. The coefficients, however, are unique to the angular momentum of the two multiplets, j, j'. They have been calculated explicitly in [55] (see Table 6.1) for the combinations relevant to the analysis of the light shifts of $6S_{1/2}$ and $5D_{3/2}$.

The sum over states γ' in Eq.(6.4) has to be performed over all states with dipole coupling to state γ, and can be thought of as weighted by the energy difference to state γ. For an accurate calculation, a large number of states, and in general contributions from core excitations, have to be included. It depends on the frequency of the off-resonant light which ones are the dominant couplings, but for visible light we can identify the two 6P states as providing the dominant couplings for the $6S_{1/2}$ state, and the 6P and 4F levels for the $5D_{3/2}$ state. These couplings account for over 95 % of the observed light shifts.

The corresponding dipole matrix elements for these transitions can be found in Table B.4. Together with the energies of the states (see Table B.2) we then have

Table 6.1: Multipole coefficients from [55]

j, j'	$s(j,j')$	$d(j,j')$	$q(j,j')$
1/2,1/2	1/6	1/3	0
1/2,3/2	1/6	−1/6	0
3/2,1/2	1/12	1/12	−1/12
3/2,3/2	1/12	1/30	1/15
3/2,5/2	1/12	−1/20	−1/60

all necessary elements to numerically calculate light shifts. Furthermore the vector structure allows us to examine their dependence on the field geometry. We can rewrite Eq.(6.4) as

$$H_{\text{eff}} = \hbar \left[\omega_s \epsilon^* \cdot \epsilon + i\omega_d (\epsilon^* \times \epsilon) \cdot \hat{\boldsymbol{j}} + \omega_q \hat{j}_{ik} (\epsilon_i^* \epsilon_k) \right] \tag{6.5}$$

where the coefficients $\omega_s, \omega_d, \omega_q$ now have units of frequency and include the sum in Eq.(6.4) as well as the corresponding multipole factors. They depend explicitly on the frequency and intensity of the applied off-resonant light.

6.1.2 Ideal geometry

The scalar part of H_{eff} will lead to a common-mode shift of all sublevels. While this shift will be important in the parity experiment, it is not observable here since we are only measuring frequency differences between spin states. We can therefore neglect this part of the interaction. The vector interaction ω_d *will* create a differential shift between spin states and can be thought of as an effective magnetic field; it acts in the same way as a magnetic field with direction

$$\boldsymbol{\sigma} = i\epsilon^* \times \epsilon \tag{6.6}$$

To maximize the effect (and to minimize systematic effects, as we will see), $\boldsymbol{\sigma}$ should lie along the external magnetic field, so that the two fields can be added directly. We

can also see from Eq.(6.6) that the polarization must have imaginary components or else $\boldsymbol{\sigma} = 0$. So, to obtain $\boldsymbol{\sigma} = \boldsymbol{e}_z$, we require $\boldsymbol{\epsilon} = \frac{1}{\sqrt{2}}(1, i, 0)$. This corresponds to completely circularly polarized light travelling along $\boldsymbol{B}$, and the differential shift of adjacent spin levels is simply given by $\Delta = \omega_d$.

With the vector interaction alone, the ratio of light shifts would be a very robust quantity because alignment imperfections affect both light shifts in the same manner, cancelling in the ratio (except for effects that become important if the two fields become comparable in size and misaligned, as discussed in Section 6.2. For the $5D_{3/2}$ state there is an additional quadrupole interaction, however. For the $\boldsymbol{\epsilon}$ given above, the quadrupole part of H_{eff} is given by $\omega_q \hat{j}_{zz}$, which is diagonal with the diagonal elements $(-\omega_q, \omega_q, \omega_q, -\omega_q)$. This leads to a shift of the innermost levels with respect to the outermost ones, but doesn't produce a shift of the innermost levels with respect to each other. Therefore, if we choose to measure the shift of the innermost energy difference, the quadrupole shift doesn't contribute and we avoid an increased sensitivity of the ratio to the alignment.

To summarize, the field geometry described by $\boldsymbol{\epsilon} = \frac{1}{\sqrt{2}}(1, i, 0)$ can be considered as optimal, and it is well-motivated to measure the ratio of the $m = -1/2 \leftrightarrow m = 1/2$ shifts in the S and D state.

6.1.3 Wavelength dependence of the light shifts

Using the ideal field geometry, we can calculate the numerical values of the light shifts and plot them against the wavelength of the applied off-resonant light, which will help to motivate the choice of a particular wavelength for the ratio measurement. Even though we can use the equations derived in the previous section to calculate light shifts, a more convenient form – valid for the ideal geometry – comes from Eq.(2.74), written here for the case of circularly polarized light, using the Wigner-

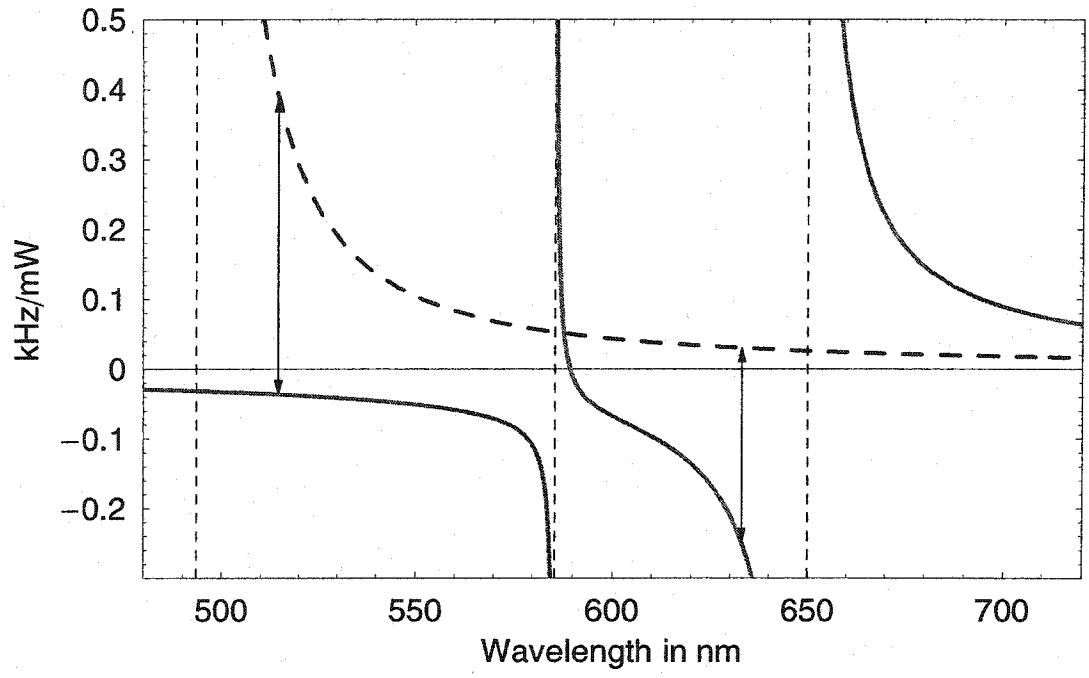

Figure 6.2: Calculated shifts of the resonance frequency of the $m = -1/2 \leftrightarrow m = 1/2$ transition in $6S_{1/2}$ (dashed line) and $5D_{3/2}$ (solid line) for circularly polarized light with $\boldsymbol{k} \| \boldsymbol{B}$, in Hz/mW for light focused onto a 50-μm spot size . The shifts are plotted as a function of wavelength of the applied light. Also shown are resonances at 493 nm,585 nm and 650 nm in vertical dashed lines. The two locations where data has been taken are indicated by two sets of arrows at 514.6 nm and 632.8 nm.

Eckart theorem:

$$\Delta_{jm} = \frac{e^2 E^2}{4\hbar^2} \sum_{\gamma', m', \pm\omega_L} \frac{|\langle \gamma' j' m' || r^{(0)} || \gamma j m \rangle|^2}{\omega_\gamma - \omega_{\gamma'} \pm \omega_L} \frac{|(jm, 11|j'm')|^2}{2j'+1}, \tag{6.7}$$

where $\Delta_{jm}/(2\pi)$ is the light shift of state $|\gamma, jm\rangle$ in units of s^{-1}.

We can use this to calculate the differential light shifts between the $m = \pm 1/2$ D and S states in Ba^+ when using circularly polarized light. Figure 6.2 shows a graph showing such shifts as a function of the wavelength of the applied light. All dominant couplings ($7P_{1/2}$, $7P_{3/2}$, $8P_{1/2}$, $8P_{3/2}$, $4F_{5/2}$) and a few more have been included in this calculation. The shifts become large in the vicinity of an atomic resonance, and the corresponding matrix element dominates the sum Eq.(6.7) because of its small

energy denominator. Furthermore, they change sign when going from the red to the blue side of the resonance, as expected.

Another interesting feature involves the S-state shift. The shifts due to $6P_{1/2}$ and $6P_{3/2}$ would exactly cancel were it not for the fine structure splitting (and small relativistic corrections that cause the radial integrals to differ slightly, see Table B.4). This can also be seen by the fact that for detunings much larger than the fine structure splitting, the shift decreases $\propto \frac{1}{\delta^2}$ instead of inversely to the detuning. The reason for this behavior is that the interaction really is an electric dipole operator coupling to orbital angular momentum states. In the case of $6S_{1/2}$ there is only one such state $(l = 0, m_l = 0)$ coupling to one other state $(l = 1, m = 1)$. The dipole operator doesn't know about the spin of the electron (it commutes with it), and the only difference between the $m = -1/2$ and the $m = +1/2$ state *is* the orientation of the electron spin. Therefore, if we sum over all couplings of the 6P fine structure components (neglecting the different energy denominators), we recover the "raw" coupling to the $(l = 1, m = 1)$ state which can't be different for the two ground state m-levels.

Several issues have to be weighted when choosing a particular wavelength for a ratio measurement.

For the best signal-to-noise in the experiment, it is beneficial to have the shift in the S-state be larger than the D-state shift because the former is harder to measure, mainly because of the smaller shelving contrast and the larger line width due to magnetic fluctuations. There is no problem with a ratio where the S-shift is much larger than the D-shift, as long as the imbalance doesn't make the S-shift comparable to the Zeeman splitting.

As mentioned in the introduction, this ratio measurement is useful because it yields information about matrix elements involving the D-state, which are challenging to calculate. Both the coupling to the 6P states and the coupling to the 4F state are interesting, and it would be most beneficial to acquire data that allows both couplings to be deduced. To this end, Figure 6.3 details the contributions to the D-state light

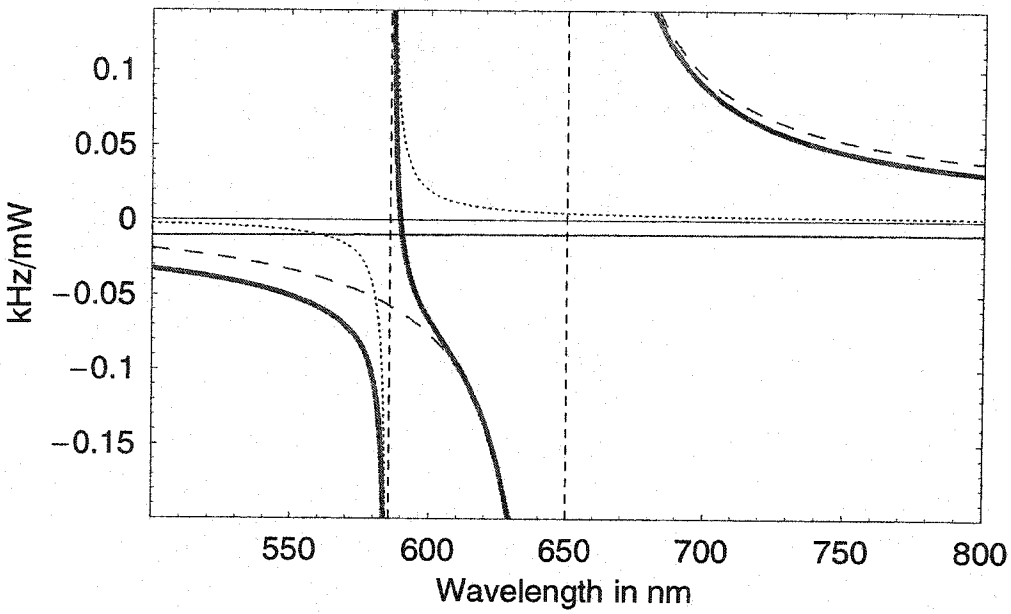

Figure 6.3: Calculated shifts of the resonance frequency of the $m = -1/2 \leftrightarrow m = 1/2$ transition in $5D_{3/2}$ for an ideal geometry, as a function of wavelength of the applied light. The three thin curves show the contributions of the three dominant couplings separately: dotted line = $6P_{3/2}$, dashed line= $6P_{1/2}$, solid line = $4F_{5/2}$. The thick line shows the sum and thereby, to within 95 %, the total light shift.

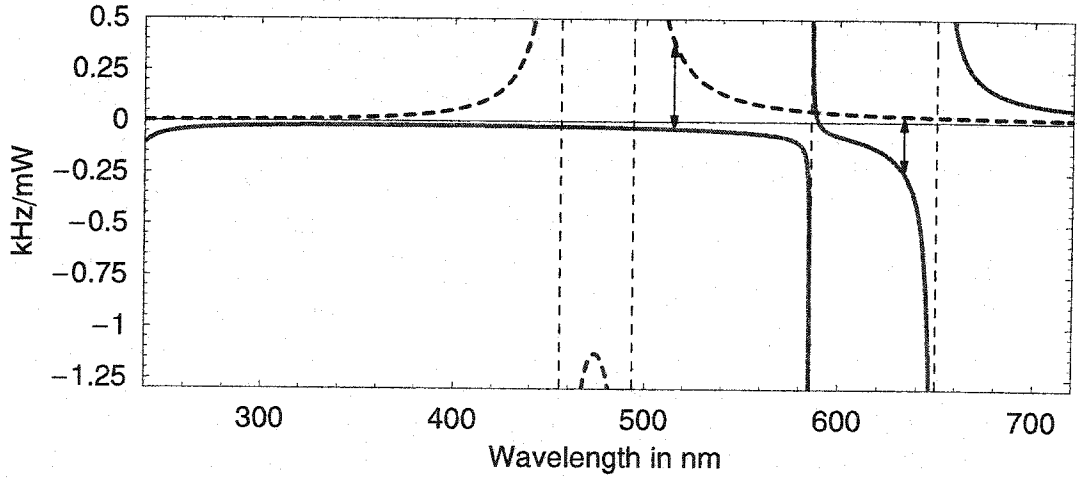

Figure 6.4: Same graph as Figure 6.2, but for an extended wavelength range.

shift. We can see that, since the 4F state is so far off-resonant ($\lambda_{\text{res}} = 232\,\text{nm}$, see Figure 6.4), it contributes a value to the light shift that is essentially constant over the wavelength range considered. If we take data at a wavelength close to the 6P resonances, the 6P contributions will far outweigh the 4F background and the 6P couplings can be determined. Then, with a measurement that is more sensitive to the 4F coupling and knowledge about the 6P matrix elements we can extract the 4F coupling.

The light source most conveniently available is an argon laser, which can be used directly with one of its laser lines. So far we have used the strong line at 514.6 nm to precisely determine a ratio that has a significant 4F contribution; another interesting line would be the blue 476 nm line. It would emphasize the 4F coupling even more while yielding a very large S-shift (about 1.2 kHz/mW). Misalignment systematics involving this S shift may become more difficult due to its size, though.

The other laser configuration available is the argon laser pumping a dye laser, which allows us to move to a wide range of places in Figure 6.2. We have taken some data at 633 nm, which is dominated by the 6P coupling. It is much harder, though, to achieve the same precision as with 514.6 nm ratio, as described in Section 6.3.2.

6.2 Systematic effects in the ratio measurement

6.2.1 Line shape effects in the D state resonance

As we have seen in Section 3.5.3, as long as the Rabi frequency is much smaller than the frequency difference of the shifted D levels, the innermost D levels behave much like an isolated two-level system, because the outer two levels are off-resonant. They still do, however, have a small effect on the evolution of the system, which manifests itself in a modification of the two-level resonance line shape. Since the two outermost resonances ($\pm 1/2 \leftrightarrow \pm 3/2$) are light-shifted by a different amount, their presence leads to an asymmetry of the central resonance. Finally, because the resonance data

is fitted with a gaussian model, this asymmetry can lead to a wrong estimate of the line center and thus to a systematic error of the light shift ratio.

To anticipate the size of this effect, we can produce simulated data that uses the same parameters as the actual experimental data, i.e the same ratio δ/Ω and the same initial conditions in the D state. Then a comparison between a Gaussian fit of the simulation and the known light shift will give an estimate of the effect.

To obtain the experimental parameters, we record a D resonance with a large RF amplitude, so that the coherent character of the RF transition dominates the line shape of the transition. No light shift is applied during this measurement. Such data, recorded in between light shift ratio runs, is shown in Figure 6.5. Solving the four-state Bloch equations (see Section 3.5.3), we obtain a model with the following free parameters: pulse area $A = \Omega t_{\text{pulse}}$, the initial conditions a, readout parameter b (defined in Section 5.3.2), and offset and x and y scaling factors. This model yields very good agreement with the resonance data, and the free parameters can be determined. The RF pulse length t_{pulse} was set to 0.400 ms, which yields a Rabi frequency of Ω =1270(60) Hz[1]. The RF transition was driven with V_{RF}=3.2 V RF into a 50 Ω load. This gives the experimental Rabi frequency (and RF-line width) calibration for the light shift data

$$\Omega/V_{\text{RF}} = 835(20)\,\text{Hz/V} \tag{6.8}$$

During data taking we didn't observe a significant change in the product $V_{\text{RF}} \times t_{\text{pulse}}$ required to produce a resonance like Figure 6.5. This justifies assuming that during data taking no major change in the geometry or electronics of the RF system took place and Eq.(6.8) is approximately valid for the data taken.

Armed with these parameters, we can now simulate the effect of the off-resonant outer levels on light-shifted resonances. To illustrate this effect, see Figure 6.6. Here, the simulated line shapes for a few ratios Δ/Ω are plotted for the experimentally

[1]These frequencies have to be multiplied by 2π in order to obtain angular frequencies

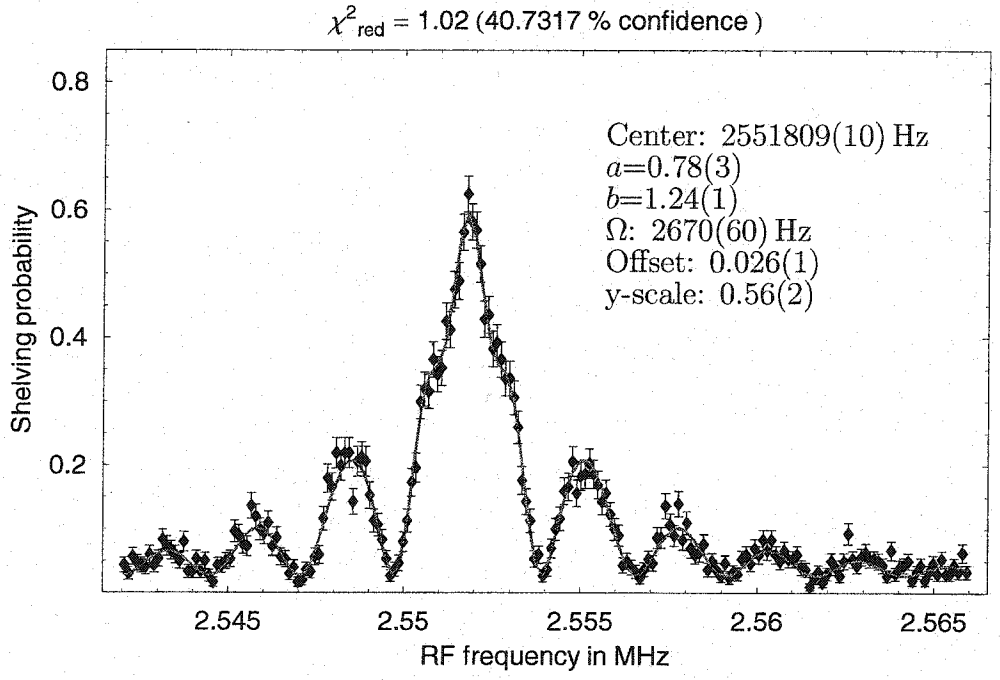

Figure 6.5: Numerical solutions of the Bloch equation, fitted to resonance data (scan030804-ion104-1), give detailed information about the parameters of the transition. The fit results are given in the graph. Of most interest are the initial condition of the D state, a, and the Rabi frequency.

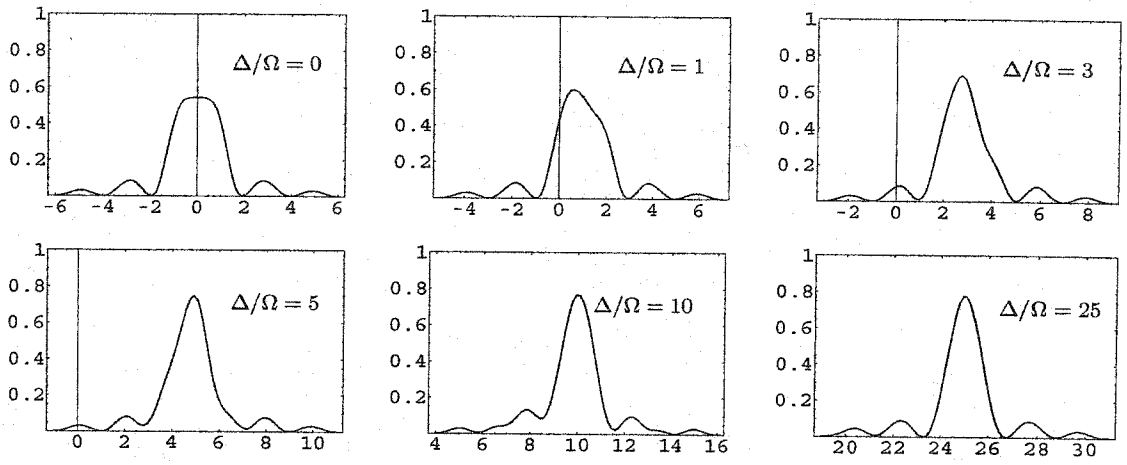

Figure 6.6: Numerical solutions of the Bloch equation shows line shape of the $m = -1/2 \longleftrightarrow m = 1/2$ transition in $6S_{1/2}$ for various ratios Δ/Ω. The x-axes are in units of δ/Ω, and the y-axes show the ideal shelving probability. The free parameters reflect the experimentally observed initial condition a=0.78.

obtained value of $a = 0.78$. We can see that the line shape approximates that of a simple two-level system as the light shift is made larger, but even for $\Delta/\Omega = 10$ the line shape looks slightly asymmetric.

To get a measure of this effect on the line center as estimated by gaussian fits, we generate a series of these graphs and compare fit results to the actual light shift, which we know exactly in this simulation. The asymmetry causes in all cases an estimate of the line center that is lower than the correct value, which would tend to make the ratio systematically larger. The numerical results, plotted in terms of relative error in the line center as a function of the ratio Δ/Ω, is given in Figure 6.7. For light shift ratios taken with a large light shift (10 kHz) and small Rabi frequencies (160 Hz) the ratio Δ/Ω is about 60 and the error is close to 0.2 %. To test whether we indeed see these predicted systematic shifts, we recorded two interleaved, identical light-shifted D resonances at the center of the light shift intensity (to be as insensitive as possible to most other systematic effects that rely on a gradient in the light shift

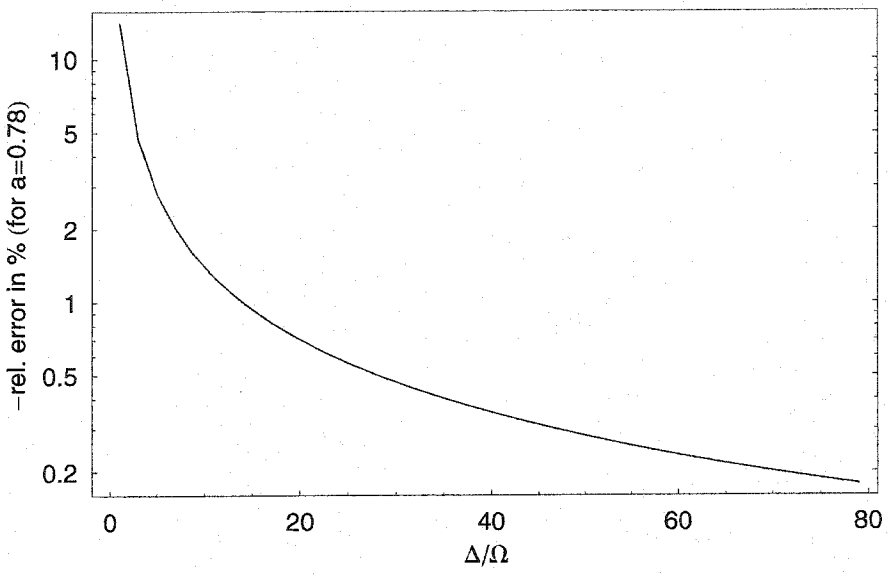

Figure 6.7: Relative error in line center estimation when fitting Gaussians to resonances with varying ratios Δ/Ω, calculated for a=0.78 and b=1.24.

intensity). The only difference between them is the RF amplitude. In scan030811-ion104-1 we compared D-scans with a ratio $\Omega/\delta = 62$ and 13, respectively. The light shifts agreed within the statistical error, +0.3(0.4) %, even though we would expect a -1 % deviation from Figure (6.7). We do not understand at this time why these line shape effects are not observed. Maybe a fortuitous cancellation occurs between this effect and other systematic shifts that depend on the RF amplitude. More systematic tests need to be done.

6.2.2 Systematic ion displacement

If there is some mechanism that shifts the average location of the ion while the measurement is done, it poses a potential systematic problem if this shift is different during measurements of the S states vs. the D states. This is because then the ion may see a systematically different light intensity. The effect on the ratio of any such ion shift is stronger if the ion is located off to the side of the light shift beam instead of

being centered. To test for these systematics, we can record light shift ratios with the ion in various locations relative to the gaussian beam. It may also be instructive to study displacement effects for the S and D states individually. For the S state this can be done by comparing two light shifted S resonances with different RF amplitudes. If there is any difference, it must be attributed to displacement effects. For the D state, the RF amplitude also affects the line shape, making this diagnostic more difficult to interpret.

For a Gaussian beam as defined in Eq.(4.3), the maximum gradient is at the location $x = \omega_0/2$ and is given by $dI(x)/dx = 2I_0/(\sqrt{e}\omega_0)$. This gives a maximum relative intensity change of

$$\frac{dI(x)/dx}{I_0} = \frac{2}{\sqrt{e}\omega_0} \tag{6.9}$$

This relative intensity change directly translates into a comparable relative systematic error in the ratio measurement. Centering the ion in the Gaussian beam is done by (roughly) measuring light shifts in various locations (see Section 4.8.2), and choosing the location that corresponds to the maximal light shift. We then say that the ion is nominally centered. If we can experimentally determine the maximum to within a relative error p, the ion might still be off to the side as much as $x = \omega_0\sqrt{-\log(1-p)/2}$ (corresponds to $1\,\sigma$). Compared with the maximum gradient, the gradient corresponding to this position is reduced by a factor

$$f_{\mathrm{red}} = \sqrt{2e}(1-p)\sqrt{-\ln(1-p)} \tag{6.10}$$

The spot size of the beam was measured in Sec.4.8.2 to be ω_0=18(1) μm. This then corresponds to an error of $\frac{dI(x)/dx}{I_0}$=6.7 %/μm in the ratio measurement at the point of maximum gradient. If we can find the maximum to within 5 %, this error is multiplied for a nominally centered ion by a reduction factor $f_{\mathrm{red}} = 0.5$.

The following mechanisms were identified to potentially cause this harmful effect:

1. The RF magnetic field[2] through the trap ring will also induce an RF electric

[2]unless explicitly stated, any RF field mentioned in this list refers to the weak spin-flip RF field

field. It is conceivable that this field acts as an additional trapping potential and shifts the average ion position. This effect would depend both on frequency and on amplitude of the RF, which are different in S and D state. If such a shift is sizeable, it could lead to a systematic shift in the ratio. We estimate the amplitude of the electric field gradient as $(dE/dx)_B = \omega B/(2\pi)$, where ω is the drive frequency. For a B-field of 1 mG and ω=6 MHz this is about $(dE/dx)_B$ =0.1 V/m^2.

Then we assume that this gradient causes a pseudopotential, just like the electric field gradient produced by the drive RF does. In the pseudopotential approximation, the harmonic force on the ion is given by

$$F = -\frac{d\Phi_{\text{pseudo}}}{dx} = -m\nu^2 x \tag{6.11}$$

$$= m\beta^2\frac{\omega^2}{4}x = a\,m\frac{\omega^2}{4}x = -e\frac{U}{r_0^2}x, \tag{6.12}$$

where Eqs.(3.9,3.15) have been used, and β and a are as defined in Section 3.1. On the other hand, the size of the gradient of the electric field that produces this force is given by (see Eq.(3.1))

$$(dE/dx) = \frac{d^2\Phi}{dx^2} = \frac{U}{r_0^2} \tag{6.13}$$

and therefore, with the E-field gradient due to the magnetic field,

$$F = -e(dE/dx)_B x \tag{6.14}$$

If we assume that the trap center of the additional trap potential is misplaced from the main trap potential by a distance on the order of the trap size, we conclude that the force due to this additional pseudopotential at the size of the (real) trap center is F=10^{-23} N. To compensate for this force, the ion position in the main trap potential has to move by x =10^{-7} μm, far too little to produce a systematic change in intensity.

2. The RF field could induce RF power into the trap ring, causing it to slightly heat and move around, taking the ion with it. To estimate this effect, we assume that the oscillating magnetic field induces a current in the trap ring. Together with the conductivity of tantalum, after taking into account ring dimensions and the skin-depth at 10 MHz, we find the dissipated electrical power. Then, with the mass and heat capacity of the ring we can find the heat rate of the ring due to induction. The needed physical properties of tantalum at room temperature are: Conductivity σ =7.5 $\mathrm{m}^{-1}\Omega^{-1}$, density ρ =16 $\mathrm{g/cm}^3$, and specific heat capacity c_p =0.14 J/(gK). The trap ring has a radius R =0.375 mm and the radius of the tantalum wire is r =0.1 mm.

   With these numbers we find that the skin depth is $\delta = \sqrt{\frac{2\varepsilon_0 c^2}{\sigma\omega}}$ =0.06 mm. The dissipated power is $P = \frac{\sigma A}{L}U^2$. With cross-section $A \simeq 2\pi\delta r$, $L = 2\pi R$, and $U = B\omega\pi R^2$ we find that P =9×10^{-10} W. An RF pulse lasting for one second will therefore cause a temperature change of $\Delta T = \frac{Pt}{mc_p}$ =5×10^{-6} °C. Let us further assume that the temperature of the trap assembly during a data run fluctuates by only 1 mK, and that all line broadening of the light shifted resonances (on the order of 5 kHz in the S-state resonance as seen in the following section) would come from these small mK-sized temperature changes. Then a systematic temperature effect would still be three orders of magnitude smaller and on the order of a few Hz, and therefore too small to be relevant.

3. Rectification of RF. Even though the RF is ac-coupled into the trap one could imagine there to be some rectification effect in the RF circuitry that provides the RF trapping field. If the trap as a whole would acquire a dc voltage, the secular frequencies would be altered, but the ion position would only change if there are other static electric fields present. To consider a worst-case scenario in which a rectification would directly affect the ion position, we imagine there be a potential difference across the dimension of the trap, equal in magnitude

to the applied RF voltage. Typical RF-voltages are about 20 mV, which would give an electric field of 2.5 V/m over the trap dimensions. This corresponds to a force F=4×10^{-19} N on the ion, causing an ion displacement of about 1 nm. This, too, is small enough to be neglected.

6.2.3 Systematic magnetic field changes

Errors in the ratio would also emerge if there is a magnetic field change that is correlated with the presence of the light shift laser. In this case the frequency difference between shifted and unshifted resonances will be altered. This could happen, for example, if the shutter that controls the light shift laser produces a different magnetic field in the off vs. on position. If the field systematically changes between S-state measurements and a D-state measurements, but remains the same for presence and absence of the light shift laser, the ratio is not changed.

6.2.4 Misalignment systematics

Here we examine the impact that imperfect beam alignment of the light shift laser — imperfect polarization and failure to be parallel to the static magnetic field — will have on the ratio. M. Schacht has done such an analysis [55], giving order-of-magnitude approximations of the expected effects. Here we calculate the error expressions more explicitly, also correcting some typos in his calculation.

We start with the ideal geometry and introduce small perturbations in the polarization and alignment of the light. If we assume that there is a small angle α between the magnetic field and the $\boldsymbol{k}$ vector, and furthermore introduce a small relative phase between ϵ_x and ϵ_y that makes the light slightly elliptically polarized, we can write the polarization as

$$\epsilon = \frac{1}{\sqrt{2}} \begin{pmatrix} \cos\alpha \\ ie^{i\delta} \\ \sin\alpha \end{pmatrix} \tag{6.15}$$

This gives an effective magnetic field the form $\boldsymbol{\sigma} = (-\cos\delta\,\sin\alpha, 0, \cos\delta\,\cos\alpha)$, which is no longer parallel to the external magnetic field. The two fields must be added vectorially, and the new quantization axis and energies will be given by the resulting field. The energies will in general be *smaller* than without the misalignment, by a factor that depends on the relative size of the effective field with respect to the magnetic field. Since this size is different for S and D state, this misalignment effect doesn't cancel in the ratio and leads to a systematic shift. Fortunately, as long as the effective field is much smaller than the magnetic field, the effect is quadratic in the misalignment angle α. This is explicitly calculated by writing down the perturbed Hamiltonian, that now contains off-diagonal elements:

$$H(\alpha,\delta) = \begin{pmatrix} \frac{-3\,B0}{2} - \frac{3\,d\,\cos(\alpha)\,\cos(\delta)}{2} & \frac{-\sqrt{3}\,d\,\cos(\delta)\,\sin(\alpha)}{2} & 0 & 0 \\ \frac{-\sqrt{3}\,d\,\cos(\delta)\,\sin(\alpha)}{2} & \frac{-B0}{2} - \frac{d\,\cos(\alpha)\,\cos(\delta)}{2} & -d\,\cos(\delta)\,\sin(\alpha) & 0 \\ 0 & -d\,\cos(\delta)\,\sin(\alpha) & \frac{B0}{2} + \frac{d\,\cos(\alpha)\,\cos(\delta)}{2} & \frac{-\sqrt{3}\,d\,\cos(\delta)\,\sin(\alpha)}{2} \\ 0 & 0 & \frac{-\sqrt{3}\,d\,\cos(\delta)\,\sin(\alpha)}{2} & \frac{3\,B0}{2} + \frac{3\,d\,\cos(\alpha)\,\cos(\delta)}{2} \end{pmatrix} \tag{6.16}$$

Diagonalizing this matrix, we find for the shift of adjacent m-levels

$$\Delta_{\mathrm{d}} = \sqrt{B^2 + \omega_d \cos\delta(2B\cos\alpha + \omega_d\cos\delta)} - B \tag{6.17}$$

For $\omega_d \ll B$ we can expand this around $\omega_d = 0$ to get

$$\Delta_{\mathrm{d}} = -\cos\alpha\,\cos\delta\,\omega_d + \frac{\omega_d^2}{2B}(\cos\delta\,\sin\alpha)^2 + O[\omega_d^3] \tag{6.18}$$

The same procedure can be applied to the quadrupole part of the interaction. Ideally, the quadrupole part vanishes, but due to the misalignment off-diagonal elements appear in the Hamiltonian. Since here almost all of the off-diagonal elements become non-zero, a diagonalization is much harder. With the approximations $\cos\alpha = 1, (\sin\alpha)^2 = \sin\delta\,\sin\alpha = 0$ we can diagonalize $H(\alpha,\delta)$ and find an expansion solution for the quadrupole shift:

$$\Delta_{\mathrm{q}} = \frac{3}{4}\frac{\omega_q^2}{B}(\sin^2\delta - 2\sin^2\alpha) + O[\omega_q^3] \tag{6.19}$$

Since both the dipole and quadrupole errors are assumed to be small, it is a good approximation to solve for the two shifts separately in a perturbative manner, and then add them to get the total light shift: $\Delta^D = \Delta^D_{\rm d} + \Delta^D_{\rm q}$ and $\Delta^S = \Delta^S_{\rm d}$.

For the measurement at 514 nm we get an S-light shift of about 100 kHz with $\omega_B = 6\,\text{MHz}$, while the D-light shift is about 10 kHz with $\omega_B = 2.5\,\text{MHz}$. This means the second-order alignment error in the shift will be larger in the S-state by a factor of about 40, and we can ignore the second-order errors of the D-shift. This allows us to write the light shift ratio as

$$R_{\rm pert} = \frac{\Delta^S}{\Delta^D} = \frac{\cos\alpha\,\cos\delta\,\omega^S_{\rm d} + \cos\delta^2\,\sin\alpha^2\,(\omega^S_{\rm d})^2/(2\omega^S_B)}{\cos\alpha\,\cos\delta\,\omega^D_{\rm d}} \tag{6.20}$$

$R_{\rm pert}$ deviates from the ideal ratio $R = \omega_{\rm d,S}/\omega_{\rm d,D}$ by the factor $R_{\rm pert} = f_{\rm pert} R$

$$f_{\rm pert} \simeq 1 + \frac{\omega^S_{\rm d}}{2\omega^S_B}(\sin^2\alpha) \tag{6.21}$$

This means that for a misalignment of $\alpha = 20°$ the ratio error reaches only about 0.1 %, and small misalignment doesn't appear to be a significant problem in the ratio measurement.

6.3 Light shift ratio data

6.3.1 Setup and procedure

The measurement sequence for all light shift data is shown in Figure 6.8. We interleave four RF resonance experiments, two for the D-state and two for the S-state. The two S-state measurements are identical, except that the light shift laser is absent during one and is turned on during the RF interaction for the other. The same is true for the two D-state resonances, and in addition for the light-shifted D-state resonance we cut the RF pulse time in half, as discussed in Section 3.5.3. The interleave has the advantage that slow magnetic field drifts (slower than the time it takes to cycle through the four resonances) appear in all resonances and should cancel when taking frequency differences.

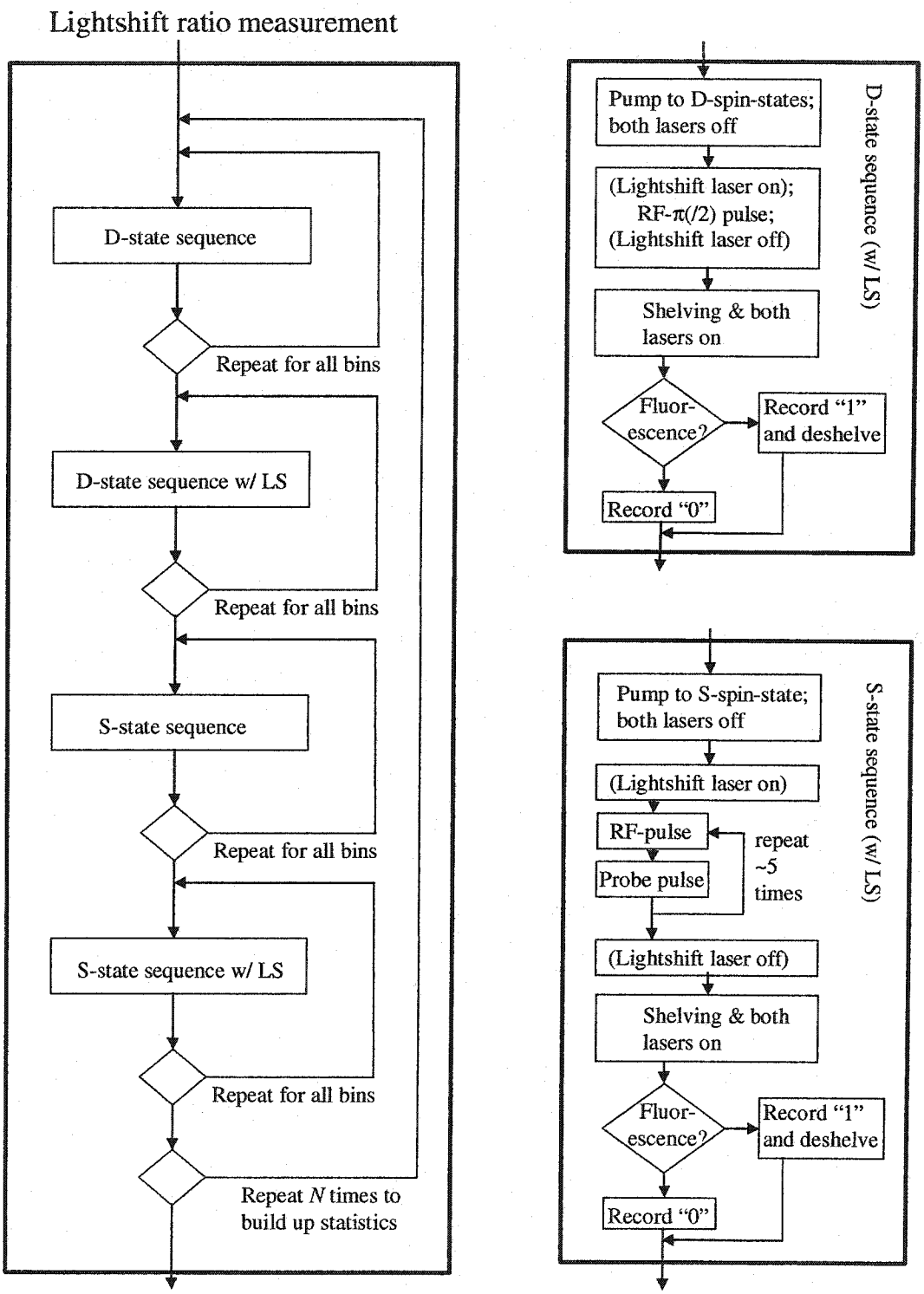

Figure 6.8: Flowchart for light shift ratio measurement

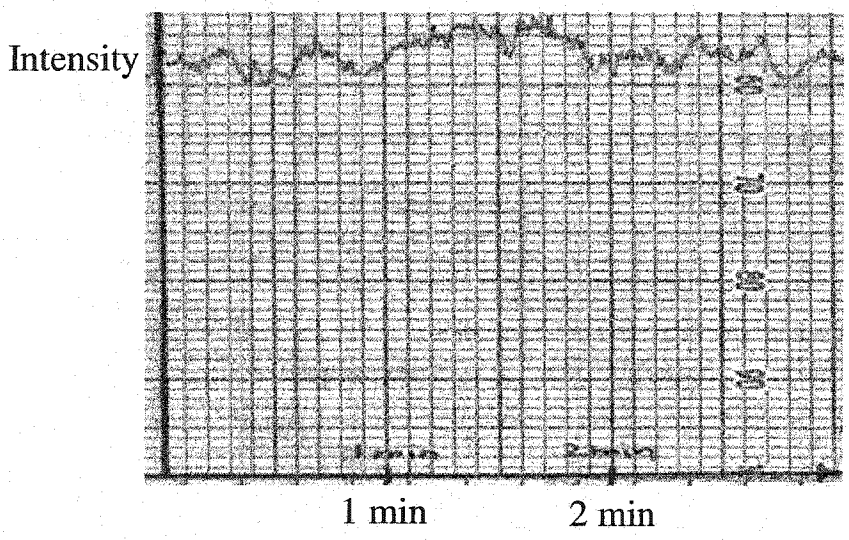

Figure 6.9: Intensity fluctuations of a stabilized light shift laser, partially blocked at its waist by the trap.

A ratio of light shifts was then extracted in the following way: The resonance data sets were individually analyzed by fitting a Gaussian to them and obtaining the line center and standard error of the line center. This gives the shifted and unshifted resonances for S and D states, $\omega^S, \omega^D, \omega^S_{\rm LS}, \omega^D_{\rm LS}$. The ratio R is then given by

$$R = \frac{\omega^S_{\rm LS} - \omega^S}{\omega^D_{\rm LS} - \omega^D} \tag{6.22}$$

So far measurements of the ratio of light shifts have been performed briefly at 632 nm using a dye laser pumped by an argon laser, and then mainly at 514 nm using the argon laser directly. In both cases the light was fiber-coupled and intensity-stabilized as described in Chapter 4, circularly polarized and focused onto the ion. Much time was spent producing light that is not only intensity-stabilized, but also highly stable spatially. This is because unless the ion is perfectly centered in the Gaussian beam, spatial fluctuations of 1 μm cause intensity fluctuations of $\sim$ 5%. Since we use a single-mode fiber, the light coming out of the fiber should be free from steering noise. On the other hand, our optical table is not vibrationally isolated from the laboratory,

and the trap itself is only supported by two thin wires (see picture 4.2). To test the spatial stability of the trap with respect to the beam, we steered the beam so that it was partially blocked at its waist by the trap. Then we recorded the transmitted intensity with a photodetector while the light was intensity-stabilized. A typical result, performed with light from the dye-laser, can be seen in Figure 6.9. The intensity fluctuates by about 15 % over a few minutes. Part of this fluctuation turned out to be steering noise induced by the AOM, which is used for intensity stabilization and was mounted *after* the fiber initially. After moving it to a location *before* the fiber, the fluctuations were reduced to about 5 % over a few minutes. Later we show how this steering noise is reflected in broadening of the light shifted resonances. It would be good to eliminate the remaining source(s) of steering noise to take full advantage of the intensity stabilization which works to better than 1 % accuracy currently.

Another problem was the changing birefringence in our fiber, which led to a changing polarization coming out of the fiber. This translated to sometimes close to 100 % intensity fluctuations after the linear polarizer, which obviously is very disruptive to the measurement. An interlock interrupted data taking when a constant intensity couldn't be maintained anymore, and manual adjustments had to be done in such a case. The installation of polarization-preserving fiber should fix this problem in the future.

6.3.2 Ratio at 632 nm

Initially work was done using a dye-laser which we ran without single-mode selectivity or frequency control. The light from the dye laser was filtered with an interference filter (bandwidth 3 nm) and its wavelength was measured with a wavemeter to be 632 nm, but we did not do frequent checks to ensure the stability of this wavelength over time. As we have seen, for this wavelength the S-shift is fairly small (around 15 Hz/mW for a beam focused to 50 μm) and large intensities are needed to make this shift precisely measurable. This is especially true since the achievable line widths

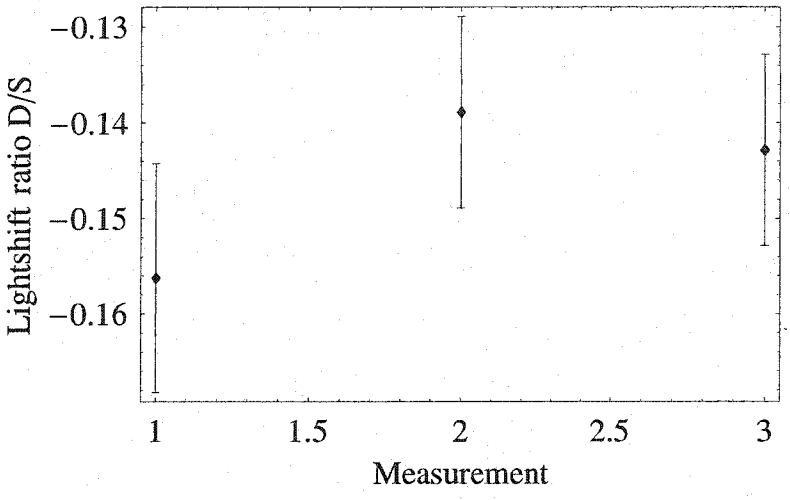

Figure 6.10: Ratio measurement at 632 nm

for S-resonances are about 2.5 times larger than the D-resonances due to the larger susceptibility to magnetic noise. Due to problems with our pump laser, we were only able to get about 25 mW of usable power, which translated into ratio measurements precise to only about 10 % and thus not useful for an extraction of matrix elements (see Figure 6.10).

6.3.3 Ratio at 514 nm

Most of the data has been taken using an argon laser in single line mode at 514.68 nm. This wavelength lends itself to an easier measurement since here the S-state shift is naturally large, and sufficient laser power is available. We typically produced shifts in the S-state of 50-100 kHz and correspondingly 5-10 kHz shifts in the D-state. This enabled much more precise determination of the ratio, as can be seen in Table 6.16. The precision of most individual ratio measurements was between 0.2 % and 0.5 %. The precision is limited by the line width of the light-shifted resonances, which in turn are limited by the stability of the light intensity at the site of the ion. We can see from Table 6.16 that the line widths-to-shift ratios are mostly 3-10 %, which seems

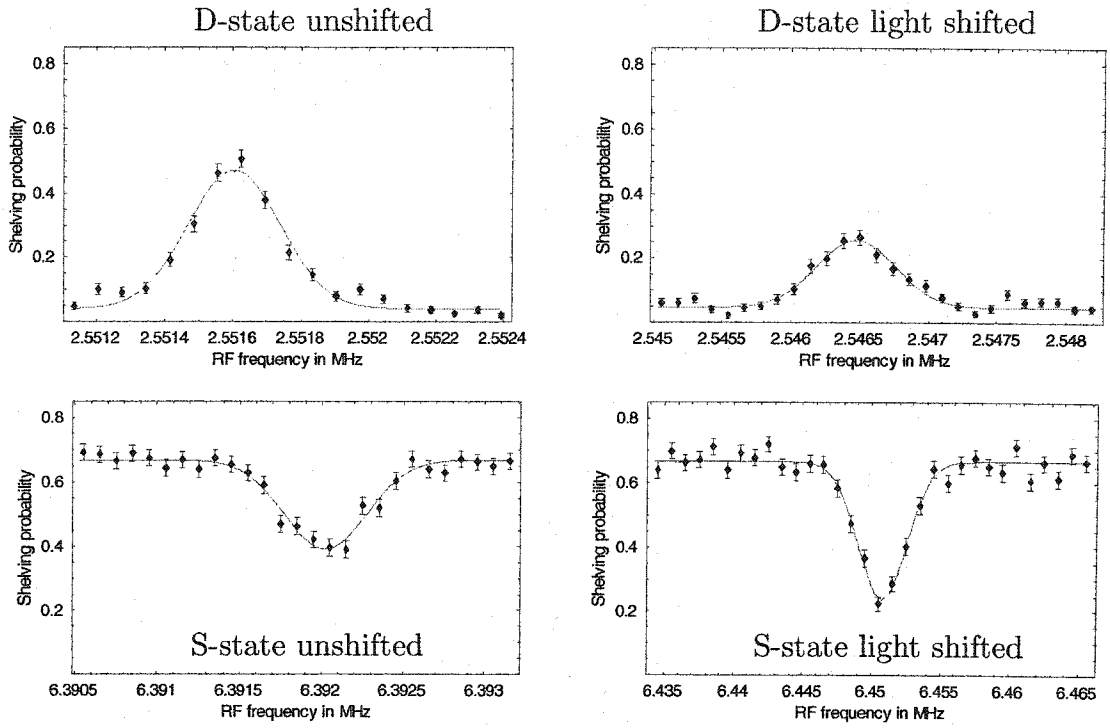

Figure 6.11: Sample light shift ratio data (scan030714-ion104-3) at λ =514.678(3) nm. Gaussian fits to the data yields a ratio of the light shifts R(S/D)=-11.45(6).

to indicate that the intensity fluctuates by about that amount during a light shift measurement.

A typical data set obtained in these measurements, from which the data in Table 6.16 is derived, is shown in Figure 6.11. We started with an old laser tube, with which we completed 12 ratio measurements. All of these measurements were taken with the ion nominally centered in the laser beam. We varied mainly the laser intensity and the axial position of the ion relative to the laser, leading to different absolute light shifts, but presumably to the same light shift ratio. We also altered the quality of circular polarization significantly for one measurement, and this, too, shouldn't affect the ratio significantly. The resulting ratio data is summarized in Figure 6.12, were we plot the ratios against the absolute D-shifts. The ratios are indeed consistent with a

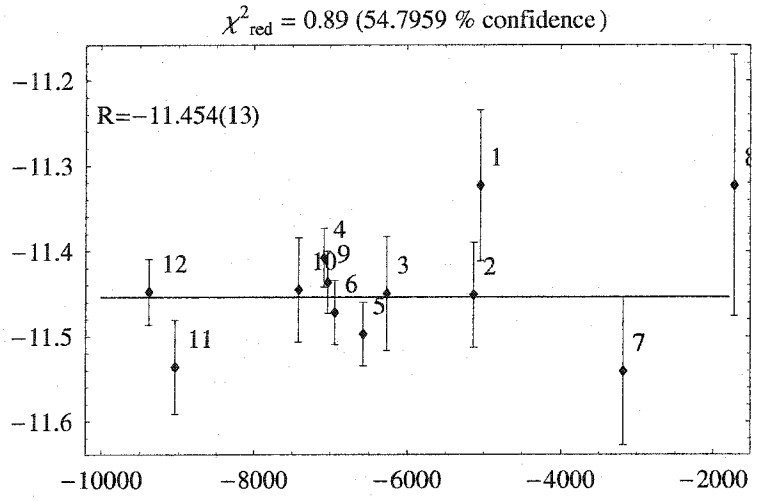

Figure 6.12: Light shift ratio data taken with the old argon ion laser, as a function of the light shift in the D-state. The number labels correspond to the run number in Table.6.16. All data has been taken with the ion nominally centered in the laser beam. The different sizes of light shifts are a result of different light powers and laser waist sizes. The data is consistent with a constant value, giving a ratio R=-11.454(13).

constant value, which from linear regression is given by $R = -11.454(13)$.

After these measurements the old argon laser failed and was replaced with newer Coherent Innova 400 argon laser. The data taken so far with the new laser are plotted in Figure 6.13. All data has been taken with the same laser intensity and axial ion position, but with the ion at different positions relative to the beam center. The ion position for each data point is indicated in Table 6.16. Two issues can be identified. First, the data is not very consistent with a constant value. There seems to be some systematic effect associated with the ion seeing a spatial light gradient. In fact, when we only plot the data that correspond to the ion being off on *one* side of the laser (see Figure 6.14), we find a trend toward lower ratios. The result for misplacement off to the *other* direction is not conclusive yet, but does seem to fit with a constant value fairly well (see Figure 6.15). More data has to be taken to understand the ratio dependence on the ion location, and to explain such dependencies by one of the

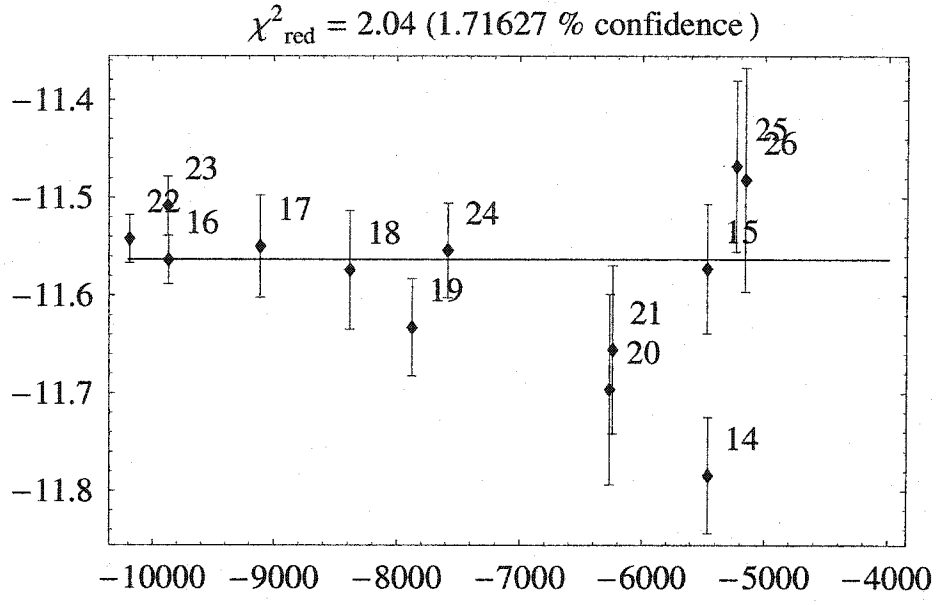

Figure 6.13: Light shift ratio data taken with the new argon ion laser, as a function of the light shift in the D-state. The number labels correspond to the run number in Table.6.16. All data has been taken with the same laser intensity and axial ion position, but with the ion at different positions relative to the beam center. The data is not consistent with a constant value. Considering only the data points corresponding to a nominally centered ion, we do get a constant ratio value: $R = -11.543(12)$.

models discussed.

The other issue is more mysterious: If we only look at the center data taken with the new argon laser (data sets #16, #17, #22, #23), we find that these data points are consistent with a constant value, but that value is given by $R = -11.542(12)$. This deviates from the mean value for the old argon laser by 0.09, or 0.75 %, exceeding the statistical error of the mean values by 7σ. The two theories for this discrepancy so far have been the following: If somehow the two argon lasers would have a light frequency difference of 100 GHz, the difference in ratios would be accounted for, following our calculation of the effect from Section 6.1.1. However, measurements with a wavemeter show that the frequencies coincide to better than 10 GHz. The other explanation would be the effect of the broad pedestal of spontaneous emission from the argon

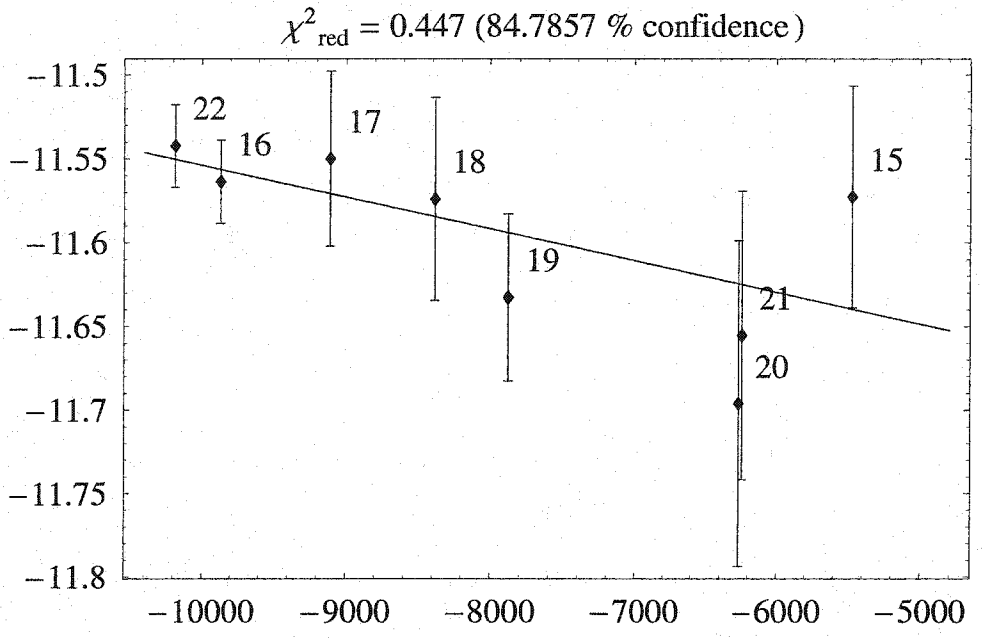

Figure 6.14: Subset of points from Figure 6.13 that correspond to the ion being progressively misplaces from the beam center in one horizontal direction, and linear fit.

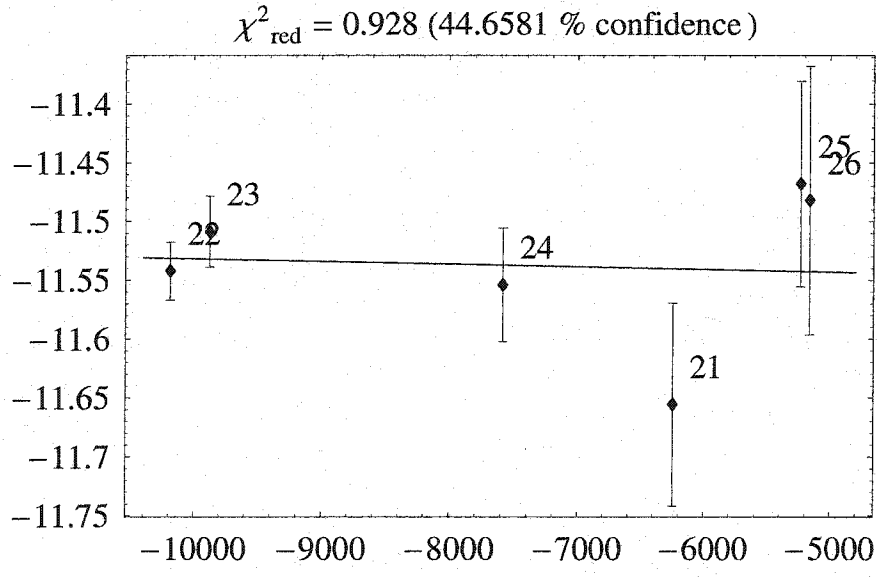

Figure 6.15: Subset of points from Figure 6.13 that correspond to the ion being progressively misplaces from the beam center in the other horizontal direction, and linear fit.

	General			D				DLS				S			
#	File	ion position	N	RF-V.	Linecenter	LW	Bins	RF-V.	Linecenter	LW	Bins	RF-V.	Linecenter	LW	Bins
1	030713-ion104-4	center (σ=0.98)	64	0.4	2551672 (14)	292	20	0.8	2546624 (30)	728	28	0.13	6392182 (34)	547	27
2	030714-ion104-3	center	345	0.4	2551604 (10)	320	20	0.8	2546472 (24)	673	28	0.13	6392022 (14)	591	27
3	030716-ion104-1	center	326	0.4	2551568 (10)	222	20	0.4	2545302 (14)	430	34	0.13	6391946 (11)	345	27
4	030716-ion104-4	center	306	0.4	2551707 (10)	232	20	0.4	2544623 (11)	383	34	0.13	6392238 (11)	456	27
5	030716-ion104-5	center (σ=0.7)	222	0.4	2551701 (7)	212	20	0.4	2545129 (16)	444	34	0.13	6392221 (16)	425	27
6	030719-ion104-2	center (σ=0.98)	144	0.4	2551697 (14)	254	20	0.4	2544760 (11)	385	26	0.13	6392234 (16)	398	20
7	030719-ion104-3	center	409	0.4	2551637 (20)	262	20	0.4	2548454 (12)	377	26	0.13	6392135 (11)	450	20
8	030720-ion104-1	center	214	0.4	2551697 (21)	277	20	0.4	2549964 (10)	410	40	0.13	6392242 (18)	480	20
9	030720-ion104-3	center	301	0.4	2551728 (19)	273	20	0.4	2544695 (8)	424	26	0.13	6392272 (13)	442	20
10	030721-ion104-1	center	26	0.4	2551454 (16)	266	20	0.8	2544039 (33)	686	26	0.13	6391756 (21)	284	20
11	030722-ion104-2	center	43	0.4	2551580 (25)	300	17	0.8	2542535 (32)	900	26	0.13	6392086 (37)	520	25
12	030723-ion104-1	center	130	0.4	2551755 (21)	358	17	0.8	2542366 (17)	885	26	0.13	6392388 (19)	515	25
13	030723-ion104-3	side	29	0.4	2551660 (22)	237	17	0.4	2546864 (25)	615	29	0.13	6392172 (31)	508	25
14	030729-ion104-1	side (new Ag+)	118	0.4	2551697 (14)	253	17	0.4	2546236 (20)	515	23	0.13	6392371 (15)	355	25
15	030729-ion104-3	side	174	0.4	2551813 (20)	320	17	0.4	2546344 (19)	511	23	0.13	6392505 (15)	405	25
16	030730-ion104-3	center	142	0.2	2551678 (12)	300	23	0.2	2541808 (13)	342	25	0.13	6392267 (25)	545	25
17	030730-ion104-5	(x;y)=(219/60)	106	0.2	2551790 (12)	223	23	0.2	2542681 (26)	480	25	0.13	6392496 (14)	345	25
18	030731-ion104-2	(x;y)=(218/60)	79	0.2	2551769 (15)	177	23	0.4	2543385 (31)	818	28	0.13	6392378 (21)	431	25
19	030801-ion104-2	(x;y)=(218/60)	101	0.2	2551715 (14)	206	23	0.2	2543838 (20)	498	20	0.13	6392295 (27)	690	25
20	030801-ion104-4	(x;y)=(217/60)	69	0.2	2551755 (15)	303	23	0.2	2545487 (36)	537	26	0.13	6392357 (24)	411	25
21	030801-ion104-5	(x;y)=(217/60)	98	0.2	2551618 (9)	262	23	0.2	2545375 (36)	718	26	0.13	6392063 (15)	495	25
22	030804-ion104-4	center	84	0.2	2551868 (16)	254	23	0.2	2541681 (11)	240	25	0.13	6392673 (19)	471	25
23	030805-ion104-3	(x,y)=(222/60)	104	0.2	2551642 (14)	248	23	0.2	2541767 (13)	330	25	0.13	6392171 (27)	595	25
24	030805-ion104-7	(x,y)=)223/60)	144	0.2	2551630 (12)	220	23	0.2	2544043 (17)	389	25	0.13	6392118 (13)	403	25
25	030806-ion104-2	(x,y)=(224/60)	112	0.2	2551643 (17)	240	23	0.2	2546409 (20)	433	25	0.13	6392131 (19)	456	25
26	030806-ion104-3	(x,y)=(224/60)	96	0.2	2551658 (13)	348	23	0.2	2546498 (24)	435	25	0.13	6392125 (33)	576	25

	SLS					Analysis									
#	RF-Vol	Linecenter		LW	Bins	D-shift	rel.	LW D/LS	S-shift	rel.	LW S/LS	RATIO	ERROR	rel
1	1.1	6449341	(240)	5155	32	-5048 (33)	0.7 %	14.4 %	57159 (242)	0.4 %	9.0 %	**-11.323**	**0.0884**	0.8 %
2	1.1	6450790	(102)	4125	32	-5132 (26)	0.5 %	13.1 %	58768 (103)	0.2 %	7.0 %	**-11.451**	**0.0614**	0.5 %
3	1.1	6463690	(370)	6122	32	-6266 (17)	0.3 %	6.9 %	71744 (370)	0.5 %	8.5 %	**-11.45**	**0.0669**	0.6 %
4	1.1	6473051	(175)	5964	32	-7084 (15)	0.2 %	5.4 %	80813 (175)	0.2 %	7.4 %	**-11.408**	**0.0344**	0.3 %
5	1.1	6467781	(139)	4223	32	-6572 (17)	0.3 %	6.8 %	75560 (140)	0.2 %	5.6 %	**-11.497**	**0.0372**	0.3 %
6	1.0	6471815	(160)	4077	24	-6937 (18)	0.3 %	5.5 %	79581 (161)	0.2 %	5.1 %	**-11.472**	**0.0375**	0.3 %
7	0.6	6428870	(57)	3009	24	-3183 (23)	0.7 %	11.8 %	36735 (58)	0.2 %	8.2 %	**-11.541**	**0.0865**	0.7 %
8	0.3	6411865	(24)	1213	24	-1733 (23)	1.3 %	23.7 %	19623 (30)	0.2 %	6.2 %	**-11.323**	**0.153**	1.4 %
9	1.0	6472706	(95)	4236	24	-7033 (21)	0.3 %	6.0 %	80434 (96)	0.1 %	5.3 %	**-11.437**	**0.0362**	0.3 %
10	1.0	6476623	(167)	3339	24	-7415 (37)	0.5 %	9.3 %	84867 (168)	0.2 %	3.9 %	**-11.445**	**0.061**	0.5 %
11	1.0	6496429	(167)	4800	24	-9045 (41)	0.4 %	10.0 %	104343 (171)	0.2 %	4.6 %	**-11.536**	**0.0551**	0.5 %
12	1.0	6499871	(187)	5460	24	-9389 (27)	0.3 %	9.4 %	107483 (188)	0.2 %	5.1 %	**-11.448**	**0.0385**	0.3 %
13	0.8	6446261	(369)	5027	30	-4796 (33)	0.7 %	12.8 %	54089 (370)	0.7 %	9.3 %	**-11.278**	**0.11**	1.0 %
14	0.8	6456725	(152)	3974	30	-5461 (24)	0.4 %	9.4 %	64354 (153)	0.2 %	6.2 %	**-11.784**	**0.0596**	0.5 %
15	0.8	6455796	(170)	5175	30	-5469 (28)	0.5 %	9.3 %	63291 (171)	0.3 %	8.2 %	**-11.573**	**0.0662**	0.6 %
16	0.7	6506400	(132)	3422	30	-9870 (18)	0.2 %	3.5 %	114133 (134)	0.1 %	3.0 %	**-11.564**	**0.0248**	0.2 %
17	1.6	6497704	(340)	7842	30	-9109 (29)	0.3 %	5.3 %	105208 (340)	0.3 %	7.5 %	**-11.55**	**0.0521**	0.5 %
18	1.6	6489414	(314)	10550	30	-8384 (34)	0.4 %	9.8 %	97036 (315)	0.3 %	10.9 %	**-11.574**	**0.0606**	0.5 %
19	1.5	6483926	(269)	7633	30	-7877 (24)	0.3 %	6.3 %	91631 (270)	0.3 %	8.3 %	**-11.633**	**0.0498**	0.4 %
20	1.5	6465669	(406)	6949	30	-6268 (39)	0.6 %	8.6 %	73312 (407)	0.6 %	9.5 %	**-11.696**	**0.0975**	0.8 %
21	1.5	6464828	(320)	10369	30	-6243 (37)	0.6 %	11.5 %	72765 (320)	0.4 %	14.2 %	**-11.655**	**0.0862**	0.7 %
22	0.7	6510253	(111)	3034	32	-10187 (19)	0.2 %	2.4 %	117580 (113)	0.1 %	2.6 %	**-11.542**	**0.0246**	0.2 %
23	0.7	6505818	(200)	4462	32	-9875 (19)	0.2 %	3.3 %	113647 (202)	0.2 %	3.9 %	**-11.509**	**0.0302**	0.3 %
24	1.2	6479778	(278)	6950	32	-7587 (21)	0.3 %	5.1 %	87660 (278)	0.3 %	7.9 %	**-11.554**	**0.0485**	0.4 %
25	1.0	6452154	(345)	7398	32	-5234 (26)	0.5 %	8.3 %	60023 (346)	0.6 %	12.3 %	**-11.468**	**0.0876**	0.8 %
26	1.0	6451372	(499)	6977	32	-5160 (27)	0.5 %	8.4 %	59247 (500)	0.8 %	11.8 %	**-11.482**	**0.1144**	1.0 %

Figure 6.16: Light shift ratio data at 514 nm taken so far.

laser. A small fraction of this light will be coupled into the fiber and will get focused onto the ion. A difference in such spurious light between the old and new laser may explain the different ratios. The fluorescence pedestal would be mostly light with a shorter wavelength than 493 nm, which would make the S-shift and therefore the ratio *smaller*. Tests are currently underway to see whether, with the new laser, such effects can be isolated. Even if no effect is found, we cannot go back to the old tube to test for this effect there, so we may never find a definite answer as to what caused this difference. In that case more thorough systematic tests have to be made to ensure that the data taken with the new argon laser are well-understood.

We also tested for systematic field changes induced by the shutter that controls the light shift laser. We did this by recording interleaved resonances with the shutter in either position, but without the presence of the light shift laser. No shift was detected in this diagnostic measurement, and we conclude that the shutter is not causing problems.

Chapter 7

PARITY VIOLATION WITH A SINGLE ION

7.1 Introduction

7.1.1 What is parity violation?

Parity is the operation of space reflection, where all spatial coordinates are reversed through the origin. Alternatively, space reflection is just the product of a mirror reflection and a rotation around an axis perpendicular to the mirror plane. Since all of known physics is invariant under rotations (isotropy of space), we can think of the parity operation also as a mirror reflection, which is often easier to imagine.

Macroscopic objects that are defined by two or more vectors can have chirality due to geometry, i.e. we can speak about left-handed and right-handed versions of these objects; a parity operation transforms one into the other.

A physical law conserves parity if it retains its form under a parity operation. Equivalently, parity is conserved if left and right cannot be defined by doing a physical experiment[1]. Parity violation arises when it is not the geometrical arrangement of objects, but the *interaction itself* that distinguishes one orientation of physical space from the other.

This means the following for experimental observables in parity-conserving interactions: If the observables are chiral vector quantities, that chirality must be due to the geometric chirality in the experiment; such is the case, for example, in optical rotation by chiral molecules. If the observables are *scalar* (i.e. transition rates, energy shifts), they must be P-even, because otherwise a mirror version of an experiment

[1]but rather must be defined by convention, i.e. by reference to some chiral object.

would give different results than the experiment itself. We could then define left and right by reference to a physical experiment alone, and parity would be violated. This leads, as Bouchiat&Bouchiat state in a good overview of atomic parity violation [8], to a golden rule for the search for parity violation: find a P-odd (pseudo)scalar observable that is built from the fields and vectors used in the experiment; any non-zero value constitutes parity violation.

Quantum-mechanically, this means that parity is violated if any pseudoscalar matrix elements are nonzero. The usual parity selection rules for the electromagnetic interaction are preventing exactly this from happening.

Until the 1950's it was assumed that parity is conserved in all physical processes. In 1956, however, Lee and Yang [39] pointed out that no evidence existed for parity to be conserved in the weak interaction. Their work was motivated by a quest to understand the observation that two elementary particles (τ, θ), while sharing all properties (mass, charge,...), decay into two different final states of opposite parity. Lee and Yang pointed out that if parity were violated, τ and θ could in fact be one and the same particle. They proposed an experiment to test parity conservation by observing the emission direction of electrons in the β decay of polarized nuclei. In 1957 such an experiment was performed with ^{60}Co nuclei [70] and parity violation was observed experimentally for the first time.

However, it was thought that the weak interaction was only mediated by the W^+ and W^- bosons, both of which change the identity of the involved particles, and to first order such weak interactions would be absent in stable atoms. But the electroweak theory introduced in the early 1960s predicted a neutral mediator, the Z_0 boson, which was directly detected in 1983 at CERN. This neutral-current interaction does not only lead to coupling between nucleons in stable atoms, but also has an effect on the electrons, as they have a finite probability for being in the nucleus and exchanging Z_0 bosons with quarks. Like its charged counterparts, Z_0 is a pseudovector particle, which means that part of the resulting Hamiltonian that describes this interaction is

pseudoscalar, and the atomic Hamiltonian no longer has definite parity. This means that the eigenstates of the atom constituents are no longer parity eigenstates: In particular, electron wave functions acquire admixtures of opposite parity states. This leads to the manifestation of parity violation through the breakdown of parity selection rules.

7.1.2 Testing the Standard Model

The Standard Model is the currently accepted theory that describes all known particles, and the electromagnetic, weak and strong force in a unified way. While it has so far passed all experimental tests, there is some consensus that it probably is not the ultimate description of nature. Most importantly it cannot be extended to include a consistent description of gravity. Also, for a truly fundamental theory there are too many free parameters that have to be determined experimentally, and there is no explanation for the gauge hierarchy problem (the large energy difference between electro-weak and grand unification).

Alternative models, such as supersymmetry , may be better descriptions of nature, but also have predictable consequences that must be tested experimentally. These predictions come either in the form of new, heavy particles, or new possible interactions leading to extended radiative corrections[49]. A new particle, such as a heavy Z boson, could be found directly, i.e. in a resonant process in high-energy collisions, but require the accelerator energies to match its mass. The lower mass limit on new gauge bosons today is given by a Tevatron experiment to about 600 GeV[12]. Theories don't predict the masses of these new particles, but do suggest mass scales on the order of 1 TeV, maybe making them accessible to future, very-large-scale high-energy experiments.

An alternative way to look for the same "new physics" is surprisingly found in low-energy atomic physics. At atomic energy scales around 1 eV the electromagnetic interaction dominates and determines the gross properties of atoms. The weak inter-

action is still present, however, as a far off-resonant process in which virtual Z_0 bosons are exchanged among the nucleons and between nucleonic quarks and electrons.

The relative influence of the weak interaction on the wave functions of bound electrons can be estimated by comparing two amplitudes: The amplitude for photon exchange between electron and proton in the atom, and the amplitude for Z_0 exchange between electron and quarks. The ratio of the amplitudes is given by the ratio of the corresponding propagators. Since the electromagnetic and weak coupling constants are comparable, it is sufficient to consider the energy denominator of the propagators. In general, a boson propagator is $\propto \frac{1}{(pc)^2-(Mc^2)^2}$. The photon is massless, and its momentum in an exchange over atomic dimensions a_0 is given by the uncertainty relation as $p = \frac{\hbar}{a_0}$. We can express a_0 in terms of the atomic binding energy $E_b \simeq \frac{e^2}{a_0}$ and find that $pc \simeq \frac{E_b}{\alpha} \simeq 10^3\,\mathrm{eV}$, where α is the fine structure constant. For the Z_0 boson the momentum is small compared to its mass (in energy units) and can be neglected, and its propagator is given with $M_{Z_0}c^2 \simeq 10^{11}\,\mathrm{eV}$. This means that the weak force in this situation is weaker than the electromagnetic force by a factor of 10^{-16}. Relativistic enhancements in heavy atoms [8] increase this number considerably, but the weak effects are still very small, about 10^{11} times smaller than the electromagnetic interaction in atoms like Cs or Ba^+. Assuming the same coupling, effects from new bosons would be smaller yet by a factor $(M_{Z_0}/M_{Z_{\mathrm{new}}})^2$.

On the other hand, the weak interaction violates parity while the strong and EM interactions don't. Thus, measuring a parity-violating effect in atoms can only be explained by the weak interaction, and new physics appears directly as a deviation of the weak interaction from standard model predictions. For example, measuring parity violation and finding agreement with the standard model to 1 % would exclude new bosons with a mass <1 TeV, which is already better than the capabilities of current high-energy experiments.

The usual point of contact between a PNC experiment and particle physics is the weak nuclear charge, Q_W, which plays the same role for the weak interaction as the

electric charge for the electromagnetic interaction. With the help of the accurately measured mass of the Z_0 boson ($90.187 \pm 0.007\,\mathrm{GeV}$) and the weak-mixing angle θ_W, the standard model can predict Q_W for a given atomic nucleus. A parity violation experiment in conjunction with atomic theory can supply an experimental value for Q_W, which can then be compared against theoretical predictions.

7.2 Atomic PNC experiments

All atomic PNC experiments to date have measured the transition rate between two states for which there is a PNC-induced electric dipole matrix element *and* an electromagnetically allowed transition element [13], which is naturally much larger than the PNC matrix element. In this way, there will be an interference term that is *linear* in the parity-violating amplitude. In terms of Rabi-frequencies the transition rate R is proportional to

$$R \propto |\Omega^{PNC} + \Omega^{\mathrm{allowed}}|^2 = |\Omega^{PNC}|^2 + |\Omega^{\mathrm{allowed}}|^2 + 2\mathrm{Re}(\Omega^{\dagger PNC}\Omega^{\mathrm{allowed}}) \qquad (7.1)$$

The last term is the pseudoscalar interference term that is measured in all experiments. The first term can be neglected because it depends quadratically on the small PNC amplitude. The second term dominates the transition rate, and must be distinguished from the interference term. This is done mainly by using the parity violating signature of the interference term, which makes it behave differently under various sign reversals than the allowed, parity-conserving term. There is a trade-off when choosing the size of the ratio $\Omega^{\mathrm{allowed}}/\Omega^{PNC}$. For a small ratio, the relative size of the interference term is large, which minimizes systematic effects. On the other hand, the absolute size of the rate becomes small, and the experiment will become limited by statistics. So far all experiments have chosen either an M1 amplitude or a Stark-induced E1 amplitude as interference partner. Currently, the most precise PNC experiment comes from a Stark-interference measurement in Cs by a group in Boulder [66]. In this experiment, the transition rate between the $6S_{1/2}$ and $7S_{1/2}$ states in an external electric and

Table 7.1: Completed atomic PNC experiments to date, along with experimental and, where available, theoretical precision. Taken from [13, p.10].

Element	Method	Group	Exp. Precision	Theor. Precision
Cs	Stark-	Colorado[69]	0.35%	0.5%[1, 21]
	interference	Paris[9]	12%	
Tl		Berkeley[17]	19%	3%[20]
Tl	optical	Seattle[63]	1%	3%[20]
	rotation	Oxford[22]	3%	
Pb		Seattle[41]	1%	8%
		Oxford	3%	
Bi (876 nm)		Oxford	2%	11%
		Seattle	16%	
Bi (648 nm)		Oxford	9%	>50%
		Moscow	23%	
		Novosibirsk	13%, 13%	

magnetic field is observed in an atomic Cs beam, and a small pseudoscalar dependence $\propto \boldsymbol{k} \cdot \boldsymbol{\sigma}_L \times \boldsymbol{B}$ of the absorption cross-section constitutes the PNC signal. Here $\boldsymbol{k}$ is the propagation direction of the light, and $\boldsymbol{\sigma_L}$ its polarization. The precision of this experiment was 0.35 %. Since Cs has only one outer electron outside a closed, not very polarizable shell, atomic theory is very precise, and has enabled a comparison with the standard model at the sub-1% level. Initially a departure from the standard model at the 2.5σ level was indicated, but over the last five years the theoretical calculations have been amended and corrected multiple times, and at this point there seems to be good agreement with the standard model.

In experiments in Seattle and elsewhere, experiments with thallium, lead and bismuth atomic vapors have been performed, and the observable was a dependence of optical rotation on a pseudoscalar quantity like $\boldsymbol{k} \cdot \boldsymbol{\sigma}_L$. The most precise of these was a 1%-optical rotation measurement in thallium, done in our lab in 1995. But for thallium atomic theory is only accurate to about 3%. For reference, Table 7.1, taken from A. Cronin's thesis [13], summarizes all atomic PNC experiments completed so far, along with experimental method and achieved accuracies.

An entirely new method for measuring PNC was suggested by Norval Fortson in 1993, involving an E2 interference with a single, trapped barium ion between its $6S_{1/2}$ and $5D_{3/2}$ states. Ba^+ is isoelectronic to Cs and has similarly precise atomic theory [27, 19], which makes this experiment a candidate for a precise, independent check of the Boulder results. This experiment will be reviewed in detail here as it has been the original motivation for this work, and still is, probably in a modified form, the ultimate experimental goal.

7.3 Idea of PNC with a single ion: An overview

As we have seen, all experiments so far measure, in one way or another, transition rates. Another way to measure matrix elements is by the light shift they induce in the

coupled levels. Here we have the choice between driving the transition on resonance or detuned from resonance. For the latter case the shifts are quadratic in the Rabi frequency Ω and fall of with $1/\delta$. A better situation is achieved with on-resonant shifts; here the shifts are maximal and are *linear* in Ω. However, it turns out that we still need an interference partner, even one with a much larger amplitude than the PNC amplitude.

If there were an absence of such an interaction, the resonant condition would be impossibly hard to achieve because Ω would be solely due to PNC and therefore very small (on the order of Hz); any laser would have to be much more stable than that or else the light shift would depend sensitively on the laser frequency (only for $\delta \ll \Omega$ does the light shift become independent of δ). The additional interaction provides a large Ω, and therefore lowers the laser requirements dramatically. Also, it turns out that the interference term can provide a vector spin interaction, which can then be measured directly by doing RF spectroscopy.

In the remainder of this section we summarize the idea of using such a light shift approach to measure PNC with a single ion, followed by a more detailed treatment, focused on understanding and calculating the PNC observable, and the systematic problems. The experiment originally was proposed in [23] for even isotopes. It could be carried out with $^{138}Ba^{+}$ or $^{226}Ra^{+}$, and the discussion could apply equally well to both species. However, for simplicity we give state designations only for Ba^{+} in the following sections. The last part of this chapter then deals with comparison of radium and barium. PNC with odd isotopes is discussed in Chapter 8.

The original scheme of detecting PNC in $^{138}Ba^{+}$ is to drive a transition between $6S_{1/2}$ and $5D_{3/2}$. This transition is strictly forbidden by parity selection rules, but takes place to the extent parity is violated by a small admixture of opposite parity states to the main atomic states, in this case mainly the admixture of $P_{1/2}$ states to the ground state. The allowed quadrupole transition amplitude between the same two states serves as an interference partner. A quadrupole amplitude is roughly a factor

10^{-4} smaller than an allowed electric dipole amplitude. Since the dipole transition is only allowed because of parity violation, it is suppressed by about a factor of 10^{-11}. Thus the ratio of the matrix elements is of order $\langle E2\rangle/\langle E1^{\mathrm{PNC}}\rangle = 10^7$. This turns out to be too large in a single running wave because of systematic errors from the large quadrupole amplitude. More flexibility in controlling this ratio is afforded by using two separate, but coherent beams in standing-wave configurations. With the ion at the antinode of one beam and at the node of the other, the PNC and quadrupole transitions can essentially be controlled independently. For the following, we assume that $\boldsymbol{E}'$ is a large field that drives the PNC amplitude, and $\boldsymbol{E}''$ a much smaller field phased independently to drive the quadrupole amplitude. As we will see later, the dipole light shift Δ_d^{PNC} due to these fields can be written in terms of an effective magnetic field as

$$\boldsymbol{\Theta}_{\mathrm{pnc}} \propto (2(\boldsymbol{E}'\cdot\boldsymbol{\nabla})\boldsymbol{E}'' + \boldsymbol{E}'\times(\boldsymbol{\nabla}\times\boldsymbol{E}'')) \tag{7.2}$$

in the large optical field limit (the shift due to the quadrupole coupling alone is much greater than the laser line width) that will be obtained in the experiment. The parity-violating character of this interaction can be seen by the fact that $\boldsymbol{\Theta}_{\mathrm{pnc}}$ transforms like a polar vector, unlike genuine magnetic fields which are axial vectors. This leads to a light shift Δ_d^{PNC} with pseudoscalar character. The behavior under a phase shift of the optical fields serves to distinguish $\boldsymbol{\Theta}_{\mathrm{pnc}}$ from non-PNC shifts. For example, the sense of this shift will be reversed, without in principle inducing any other changes, when the sign of either $\boldsymbol{E}'$ or $\boldsymbol{E}''$ is reversed through a 180° optical phase shift. The interference between the quadrupole and PNC-induced dipole amplitudes yields a differential light shift of the ground state spin levels of $\sim 0.25\,\mathrm{Hz}$ for an electric field of $E' = |\boldsymbol{E}'| = 10000\,\mathrm{V/cm}$. It seems plausible to measure this shift to sub-percent precision in a matter of days, if line broadening can be avoided.

A major advantage of using the change in spin resonance frequency for measuring the PNC light shift is that the light shift of the ground state due to the quadrupole field alone is a *scalar* shift Δ_s^Q and does not affect the energy splitting of the sub-

states. Therefore, amplitude fluctuations in E'' do not directly interfere with the PNC measurement. The field E'' can be made much smaller than E' to reduce systematic effects associated with misalignments of the quadrupole field, as long as Δ_s^Q remains much greater than the line width of the 2.05 μm laser source, so that the light shift remains insensitive to the laser frequency (see Eq.(2.57)). For example, $E''/E' = 10^{-2}$ would generate $\Delta_s^Q/2\pi \cong 50$ kHz, common to each $m_s = \pm\frac{1}{2}$ substate of the $6S$ level.

In the following sections we examine some of these issues in more detail.

7.4 The PNC Hamiltonian

As we have seen, the weak interaction violates parity and imparts an admixture of opposite-parity states into the wavefunction of the electron. This admixture leads to subtle effects in the behavior of the electron, notably the presence of small transition amplitudes that are strictly forbidden by parity selection rules. Measuring these amplitudes is the task of atomic PNC experiments.

The parity-violating part of the electron-nucleus interaction Hamiltonian $H_{\rm PNC} = A_e V_N + V_e A_N = H_1 + H_{2a}$ consists of the product of electron axial vector current and nucleon vector currents $H_1 = A_e V_N$, and the product of electron vector current and nucleon axial vector currents $H_{2a} = V_e A_N$ [34].

If we only retain the part that operates on the electrons, H_1 can be written in the limit of a non-relativistic nucleus as

$$H_1 = \frac{G_w}{2\sqrt{2}} \gamma_5 Q_w \rho(r), \tag{7.3}$$

where Q_W is the weak nuclear charge

$$Q_W = -N + Z(1 - 4\sin^2\theta_W), \tag{7.4}$$

G_w the weak coupling constant, $\rho(r)$ the neutron and proton density functions (assumed to be equal), and γ_5 a Dirac matrix. From the standpoint of the electron, $\rho(r)$ is essentially a delta function, only non-zero for nuclear dimensions.

H_1 is independent of nuclear spin and a scalar in the electronic variables and thus unable to change the angular momentum of the electron. H_{2a} is the nuclear-spin dependent part of the coupling, and can change electron angular momentum. A third coupling, H_{2b} comes from the electromagnetic coupling of the electron to the nuclear anapole moment, which is a parity-violating toroidal magnetic moment discussed, for example, in [8]. Since the two spin-dependent effects are identical in structure, one can't experimentally distinguish between them. H_{2a} results only from unbalanced nucleon spin, and hence should be $\sim H_1/Q$, where Q is the number of nuclei. It is further reduced because for the electron vector current, $|1 - 4\sin^2\theta|$ is small. This latter reduction does not appear in H_{2b}, which makes it the dominant source of spin-dependent PNC effects. In heavy atoms (Cs, Ba^+), the combined spin-dependent effect $H_2 = H_{2a} + H_{2b}$ is a few percent of the spin-independent effect.

It is clear from this discussion that in even isotopes only H_1 exists, while in odd isotopes both H_1 and H_2 are present. To distinguish between them we can, for example, repeat the same PNC measurement between two level pairs with different total angular momentum F. H_1 and H_2 have different dependences on F, and the two separate contributions can be determined. One could also choose a pair of states for which there is *only* a spin-dependent PNC coupling. It was suggested [25], for example, to use the $S_{1/2}$-$D_{5/2}$ transition in an odd Ra^+ or Ba^+ isotope, and measure the forbidden E1 amplitude between these states. Since for this transition $\Delta J = 2$ and the E1 transition can only change J by unity, the PNC amplitude has to provide another $\Delta J = 1$, which disqualifies the spin-independent part. Perhaps the best approach would be to measure the spin-dependent part by a direct microwave transition between different F sublevels in the $6S_{1/2}$ state.

7.5 *E1 PNC matrix element*

As a consequence of $H_{\rm PNC}$, electric dipole transitions between states of the same nominal parity become possible. Anticipating calculations with hyperfine structure, we can write the dipole transition element between such two states $|J'I'F'M'_F\rangle \equiv |\gamma'\rangle$ and $|JIFM_F\rangle \equiv |\gamma\rangle$ as [34]

$$\langle\gamma'|er_q^{(1)}|\gamma\rangle = \sum_n \frac{\langle\gamma'|er_q^{(1)}|n\rangle\langle n|H_{\rm PNC}|\gamma\rangle}{W_n - W} + \sum_n \frac{\langle\gamma'|H_{\rm PNC}|n\rangle\langle n|er_q^{(1)}|\gamma\rangle}{W_n - W'} \tag{7.5}$$

where $|n\rangle$=$|nj_nm_n\rangle|Im_I\rangle$ is an intermediary state of opposite parity to both initial and final state, and $H_{\rm PNC} = H_1 + H_2$. The denominators are the energy differences between the states of opposite parity that are mixed by $H_{\rm PNC}$. To relate this amplitude to PNC matrix elements conventionally used, we write it in its reduced form

$$\langle\gamma'|er_q^{(1)}|\gamma\rangle = \frac{(F'M'_F|1q;FM_F)}{\sqrt{2F'+1}} \times \langle\gamma'||er^{(1)}, H_{\rm PNC}||\gamma\rangle \tag{7.6}$$

For the even isotopes under consideration here, the spin-dependent Hamiltonian vanishes, and we can proceed with only considering H_1. Since it commutes with nuclear spin, we can write the reduced matrix elements in the j basis according to Eq.(A.2):

$$\langle\gamma'||er^{(1)}, H_1||\gamma\rangle = (-1)^{J+I+F'+1}\sqrt{(2F+1)(2F'+1)}\begin{Bmatrix} J & F & I \\ F' & J' & 1 \end{Bmatrix} \times \langle\gamma'j'||er^{(1)}, H_1||\gamma j\rangle \tag{7.7}$$

with

$$\langle\gamma'j'||er^{(1)}, H_1||\gamma j\rangle = \left(\sum_n \frac{\langle\gamma'j'||er^{(1)}||nj_n\rangle\langle nj_n||H_1||\gamma j\rangle}{W_n - W} + \sum_n \frac{\langle\gamma'j'||H_1||nj_n\rangle\langle nj_n||er^{(1)}||\gamma j\rangle}{W_n - W'}\right) \tag{7.8}$$

If there is no nuclear spin altogether, we can simply write

$$\langle\gamma'j'm'_j|er_q^{(1)}|\gamma jm_j\rangle = \frac{(j'm'_j|1q;jm_j)}{\sqrt{2j'+1}} \times \langle\gamma'j'||er^{(1)}, H_1||\gamma j\rangle \tag{7.9}$$

The PNC reduced matrix element $\langle \gamma' j' || e r^{(1)}, H_1 || \gamma j \rangle$ can now be related to the spin-independent PNC matrix element $\mathcal{E}_{\rm PNC}$, which is conventionally defined by $\mathcal{E}_{\rm pnc} = \langle \gamma' j' \tfrac{1}{2} | ez | \gamma j \tfrac{1}{2} \rangle$ for $j, j' = \frac{1}{2}$. This convention also seems to hold for our case ($j' = \frac{3}{2}$) [19], but it is not clear whether there is a convention for arbitrary j.

The spin-dependent matrix element can also be written in terms of a reduced matrix element [25], but now this element is dependent on I and F, and will not be considered here.

For further analysis we write this PNC-enabled dipole transition between two states $|\gamma' j'\rangle$ and $|\gamma j\rangle$ ($I = 0$) in terms of a Rabi frequency $\mathbf{\Omega}'$ with elements

$$\Omega'_{m'm} = \frac{1}{\hbar} \langle \gamma' j' || e r^{(1)}, H_1 || \gamma j \rangle \times \sum_q \frac{(j' m'_j | 1q; j m_j) E'^{(1)}_q}{\sqrt{2j'+1}} \tag{7.10}$$

The electric field here is the spherical vector (see App.A.3) corresponding to the field $\boldsymbol{E}$ as defined in Eq.(2.9). Lastly, we write Eq.(7.10) in terms of cartesian field coordinates as

$$\Omega''_{m'm} = \frac{1}{\hbar} \langle E2 \rangle f(\boldsymbol{E})_{m'm}, \tag{7.11}$$

where $\boldsymbol{f}$ is a cartesian tensor that captures the geometrical structure of the interaction.

7.6 E2 matrix element

The E2 coupling $\mathbf{\Omega}''$ can be written as

$$\Omega''_{m'm} = \langle j' m' | \frac{1}{2} \sum_{ij} \partial_i E''_j(\boldsymbol{r})|_{r=0} | jm \rangle, \tag{7.12}$$

evaluated at $\boldsymbol{r} = 0$. For a running or standing wave we have, respectively,

$$E''_j(\boldsymbol{r}) = E''_j e^{-i\boldsymbol{k}\cdot\boldsymbol{r} - i\phi} \quad \Rightarrow \quad \partial_i E''_j(\boldsymbol{r})|_{r=0} = -ik_i e^{-i\phi} E''_j \tag{7.13}$$

$$E''_j(\boldsymbol{r}) \equiv E''_j e^{-i\phi} \sin(\boldsymbol{k}\cdot\boldsymbol{r}) \quad \Rightarrow \quad \partial_i E''_j(\boldsymbol{r})|_{r=0} = -ik_i e^{-i\phi} E''_j \tag{7.14}$$

Alternatively, we can write $\Omega''_{m'm}$ in spherical form,

$$\Omega''_{m'm} = \frac{1}{\hbar}\langle \gamma' j' || e r^{(2)} || \gamma j \rangle \times \sum_q \frac{(j' m'_j | 2q; j m_j) \nabla E^{(2)}_q}{\sqrt{2j'+1}}, \tag{7.15}$$

with the spherical tensors $\nabla E^{(2)}_q$ defined in Eq.(A.23).

Lastly, we also write Eq.(7.15) in terms of cartesian field coordinates as

$$\Omega''_{m'm} = \frac{1}{\hbar}\langle E2 \rangle f(\boldsymbol{\nabla E})_{m'm}, \tag{7.16}$$

7.7 PNC observable

The two interactions $\boldsymbol{\Omega}'$ and $\boldsymbol{\Omega}''$ add coherently, and we can write

$$\boldsymbol{\Omega} = \boldsymbol{\Omega}' + \boldsymbol{\Omega}''. \tag{7.17}$$

Light shifts are given in terms of the effective interaction $\boldsymbol{\Omega}^\dagger \boldsymbol{\Omega}$, which for the $6S_{1/2}$ state is a 2×2 matrix and can therefore (see Section 2.5.5) be expanded into a scalar and vectorial part:

$$\boldsymbol{\Omega}^\dagger \boldsymbol{\Omega} = \Theta \, \mathbb{I}_{2\times 2} + \boldsymbol{\Theta} \cdot \boldsymbol{j} \tag{7.18}$$

On the other hand, we can write $\boldsymbol{\Omega}^\dagger \boldsymbol{\Omega}$ in terms of $\boldsymbol{\Omega}'$ and $\boldsymbol{\Omega}''$ as

$$\begin{aligned} \boldsymbol{\Omega}^\dagger \boldsymbol{\Omega} &= (\boldsymbol{\Omega}'^\dagger + \boldsymbol{\Omega}''^\dagger)(\boldsymbol{\Omega}' + \boldsymbol{\Omega}'') \\ &\simeq \boldsymbol{\Omega}''^\dagger \boldsymbol{\Omega}'' + (\boldsymbol{\Omega}'^\dagger \boldsymbol{\Omega}'' + \boldsymbol{\Omega}''^\dagger \boldsymbol{\Omega}') \end{aligned} \tag{7.19}$$

The first term is only due to the quadrupole coupling, and is much larger than the second, PNC-interference term; it is on the order of 10s or 100s of kHz. On the other hand, we can choose a geometry that makes the vector component of this interaction zero, and makes it show up only as a scalar shift Δ^Q_s. Then it will not change Zeeman frequencies, and fluctuations of this term will not directly interfere with the PNC measurement. The ideal geometry will, on the other hand, maximize the vector

component of the PNC term to give the largest observable effect, which is on the order of $\Delta_d^{PNC} \sim 0.5\,\mathrm{Hz}$. The experiment takes place in an external magnetic field with a Zeeman splitting ω_B such that $\Delta_s^Q \gg \omega_B \gg \Delta_d^{PNC}$. For a quantization axis defined by the magnetic field, the off-diagonal elements of $(\Omega'^{\dagger}\Omega'' + \Omega''^{\dagger}\Omega')$ correspond to shifts perpendicular to the magnetic field, and are suppressed by $(\Delta_d^{PNC}/\omega_B)$. Only the diagonal elements contribute significantly to an energy change. Under this assumption we can rewrite Eq.(7.19) in a simpler way as

$$\Omega^{\dagger}\Omega \;\rightarrow\; (\Omega^{\dagger}\Omega)_{mm} \simeq (\Omega''^{\dagger}\Omega'')_{mm} + 2\mathrm{Re}(\Omega'^{\dagger}\Omega'')_{mm}, \tag{7.20}$$

Also under this assumption, the on-resonance light-shift without any laser detuning, and for magnetic fields much smaller than the light Rabi frequencies (in our case those from the pure quadrupole term), is given by Eq.(2.57) as

$$\Delta_{(m)} = \frac{1}{2}\sqrt{(\Omega^{\dagger}\Omega)_{mm}} = \frac{1}{2}\sqrt{\Theta_{\mathrm{sc}} + (\boldsymbol{\Theta}\cdot\boldsymbol{j})_{mm}} = \frac{1}{2}\sqrt{\Theta_{\mathrm{sc}} + (\Theta_z j_z)_{mm}} \tag{7.21}$$

The difference in light shifts of the two sublevels is the on-resonance vector light shift (or dipole shift) in the direction of the quantization axis. Because the scalar shift is much larger than the vector shift, we can find a simple expression[2] for the dipole shift:

$$\omega_d = \Delta_{(1/2)} - \Delta_{(-1/2)} = \frac{1}{2}\sqrt{\Theta + \frac{1}{2}\Theta_z} - \frac{1}{2}\sqrt{\Theta - \frac{1}{2}\Theta_z} \simeq \frac{\Theta_z}{4\sqrt{\Theta}} \tag{7.22}$$

This derivation was not as straight-forward as the case of off-resonant light shifts, but it remains true that a dipole shift is given by the vector interaction of the effective Hamiltonian, as expected. In this sense the vector interaction can still be regarded as an effective magnetic field.

7.8 *Vector structure*

To find the geometrical dependence of the multipole light shifts in terms of the vectors that are causing them, one can write down all possible combinations of the vectors ∇,

[2] using $\sqrt{c+a/2} - \sqrt{c-a/2} = \frac{a/2}{\sqrt{c}} + O(\frac{a^3}{c^{5/2}})$

$\boldsymbol{E}'$ and $\boldsymbol{E}''$ that give scalars and vectors, with the constraint that each combination has to be linear in all vectors. Then one can explicitly calculate the coefficients for the combinations by picking simple field orientations and comparing with the interaction written in spherical components. M. Schacht also has developed a more systematic way to calculate the vector structure that doesn't require knowing all possible field combinations a priori. With the help of generalized Pauli matrices σ (see[55, p.211]) we can write

$$\begin{aligned}(\boldsymbol{\Omega}'^{\dagger}\boldsymbol{\Omega}'')_{m_1m_2} &= C\sum_{s,m'}\frac{\langle\frac{1}{2}m_1|1,s;\frac{3}{2}m'\rangle\langle\frac{3}{2}m'|2,s;\frac{1}{2}m_2\rangle}{2\frac{3}{2}+1}E_s^{(1)}E_s^{(2)}\\ \Rightarrow \boldsymbol{\Omega}'^{\dagger}\boldsymbol{\Omega}'' &= C\sum_{i,j,k}\sigma_{ij}\begin{pmatrix}1&3\\2&2\end{pmatrix}\sigma_k\begin{pmatrix}3&1\\2&2\end{pmatrix}\partial_i E''_j E'_k\\ &= C\frac{1}{2\sqrt{10}}\left(2(\boldsymbol{E}'\cdot\boldsymbol{\nabla})\boldsymbol{E}''+\boldsymbol{E}'\times(\boldsymbol{\nabla}\times\boldsymbol{E}'')\right)\cdot\boldsymbol{j}\end{aligned} \tag{7.23}$$

with

$$C=\frac{1}{\hbar^2}\langle 5D_{3/2}||er^{(2)}||6S_{1/2}\rangle\langle 5D_{3/2}||er^{(1)}||6S_{1/2}\rangle\equiv\frac{1}{\hbar^2}\langle E1^{\mathrm{PNC}}\rangle\langle E2\rangle \tag{7.24}$$

As we can see, there is no scalar shift due to this interaction.

On the other hand, for the quadrupole term we get both a scalar and a vector part [38]:

$$\begin{aligned}\boldsymbol{\Omega}''^{\dagger}\boldsymbol{\Omega}'' &= \frac{\langle E2\rangle\langle E2\rangle}{20\hbar^2}(\boldsymbol{\nabla}\times\boldsymbol{E}'')\cdot(\boldsymbol{\nabla}\times\boldsymbol{E}'')\,\mathbb{I}_{2\times2}\\ &+\frac{\langle E2\rangle\langle E2\rangle}{20\hbar^2}\left[2((\boldsymbol{\nabla}\times\boldsymbol{E}'')\cdot\boldsymbol{\nabla})\boldsymbol{E}''+(\boldsymbol{\nabla}\times\boldsymbol{E}'')\times(\boldsymbol{\nabla}\times\boldsymbol{E}'')\right]\cdot\boldsymbol{j}\end{aligned} \tag{7.25}$$

7.9 Ideal field geometry and sizes

There are several possible field configurations that will produce a PNC vector shift; they are derived in Section 7.10.1. One such geometry is given by

$$\begin{aligned}\boldsymbol{E}' &= E'_x\cos kz\\ \boldsymbol{E}'' &= iE''_z\sin kx,\end{aligned} \tag{7.26}$$

with notation $E'_x = E'\boldsymbol{e}_x$. With these fields Eq.(7.23) becomes

$$2\mathrm{Re}(\Omega'^{\dagger}\Omega'')_{mm} = \Theta_z j_z = \frac{\langle E1^{\mathrm{PNC}}\rangle\langle E2\rangle}{\sqrt{10}\hbar^2} \times kE'_0 E''_0 j_z \tag{7.27}$$

which is a vector shift along the quantization axis. The phase factor i between the two fields is necessary to offset the imaginary PNC matrix element $\langle D\rangle$ and to make $(\boldsymbol{\Omega}'^{\dagger}\boldsymbol{\Omega}'')_{mm}$ real, as required to produce a PNC shift.

The quadrupole term yields, with the ideal geometry of Eq.(7.26), no vector shift; the scalar shift becomes

$$(\Omega''^{\dagger}\Omega'')_{mm} = \Theta\,\mathbb{I}_{2\times 2} = \frac{\langle E2\rangle\langle E2\rangle}{20\hbar^2} \times k^2 E''^2_0\,\mathbb{I}_{2\times 2} \tag{7.28}$$

Finally, with Eq.(7.22) the PNC light shift becomes

$$\Delta_d^{\mathrm{PNC}} \simeq \frac{\Theta_z}{4\sqrt{\Theta}} = \frac{1}{2\sqrt{2}\hbar} E'_0 \langle E1^{\mathrm{PNC}}\rangle \tag{7.29}$$

while the scalar shift is given by

$$\Delta_s^{\mathrm{Q}} = \frac{1}{2}\sqrt{\Theta} = \frac{1}{4\sqrt{5}\hbar} kE''_0 \langle E2\rangle \tag{7.30}$$

The PNC matrix element typically given in the literature is

$$\mathcal{E}_{\mathrm{pnc}} = \langle \gamma' j' \tfrac{1}{2} | ez, H_{\mathrm{pnc}} | \gamma j \tfrac{1}{2}\rangle \tag{7.31}$$

and it can be related to the reduced matrix element $\langle E1^{\mathrm{PNC}}\rangle$ in the even isotopes by

$$\mathcal{E}_{\mathrm{pnc}} = \frac{(\frac{1}{2}\frac{1}{2}; 1, 0|\frac{3}{2}\frac{1}{2})}{\sqrt{2\frac{3}{2}+1}} \langle E1^{\mathrm{PNC}}\rangle = \frac{1}{\sqrt{6}}\langle E1^{\mathrm{PNC}}\rangle \tag{7.32}$$

$\mathcal{E}_{\mathrm{pnc}}$ was recently calculated [19] to be

$$\mathcal{E}_{\mathrm{pnc}}^{\mathrm{Ba}} = 2.34 \times 10^{-11}\, \mathrm{i e a_0 (-Q_W/N)} \tag{7.33}$$

$$\mathcal{E}_{\mathrm{pnc}}^{\mathrm{Ra}} = 45.9 \times 10^{-11}\, \mathrm{i e a_0 (-Q_W/N)} \tag{7.34}$$

where Q_W is the weak nuclear charge and N is the neutron number. For a weak mixing angle $\theta_W = 0.25$, which is close to the presently accepted value of $\theta_W = 0.231$, the

factor $(-Q_W/N) = 1$, as assumed in the following. The parity-violating Hamiltonian increases faster than Z^3 [7], which explains the 20fold increase of PNC effects in radium.

We now have all the pieces to calculate the expected light shifts for a PNC experiment. In Section 7.11 we will show what the maximal useful size of the electric field $E'_{\max}$ is. Using these fields, we arrive at the following PNC-induced shifts:

$$\mathrm{Ba}^+ \quad : \quad \Delta_d^{\mathrm{PNC}}/2\pi = 0.37\,\mathrm{Hz} \;\; (E'_0 = 14900\,\mathrm{V/cm}) \tag{7.35}$$

$$\mathrm{Ra}^+ \quad : \quad \Delta_d^{\mathrm{PNC}}/2\pi = 3.7\,\mathrm{Hz} \;\; (E'_0 = 6800\,\mathrm{V/cm}) \tag{7.36}$$

7.10 Systematic effects and Sensitivity

The currently known systematic effects can be enumerated as follows:

1. resonant shifts due to misalignment of the ideal geometry
   (a) shifts due to individual beams
   (b) shifts due to cross-terms involving E' and E''
2. off-resonant shifts from RF fields
3. Parity mixing from stray electric fields
   (a) ac fields
   (b) dc fields

and will be briefly assessed here, followed by an experimental scenario that would enable a competitive PNC measurement. Many of these effects have already been discussed in detail in [55], and are summarized here or presented in an alternative form.

7.10.1 Resonant shifts due to misalignment of the ideal geometry

With the beams given in Eq.(7.26) there can be no vector shift except for the PNC shift. If the beams deviate from this ideal geometry, as they must at some level, there can be additional mechanisms of creating a vector shift that don't include the PNC interaction, but rather derive their vector nature from the chirality of the fields. Such competing shifts are potential systematic problems and must be carefully identified. It is helpful that the PNC light shift is not the largest vector in the problem; the magnetic field will be 2 to 3 orders of magnitude larger. Therefore vector shifts that are perpendicular will be suppressed by the ratio of shift to B-field. In the following we will only consider shifts along B, and the m-indices: $(\Omega^\dagger\Omega)_{mm} \equiv \Omega^\dagger\Omega$.

Most problems start with the strong PNC field E' being misplaced from the antinode of the standing wave by a fraction δ of its wavelength. Then E' acquires a spatial gradient, which will produce an additional E2 or quadrupole coupling Ω'_Q, which, for the same electric field, is a factor of 10^7 stronger than the PNC coupling. Its ability to produce PNC-like shifts therefore has to be suppressed by at least a factor of 10^{-10} to produce a 0.1% systematic error. Typically small misalignment factor like δ cannot reliably be made much smaller than 10^{-3}; therefore at least three small factors are needed for each systematic problem.

If we write the complete coupling $\Omega^\dagger\Omega$ for $\Omega{=}\Omega'{+}\delta\Omega'_Q{+}\Omega''$ and neglect terms that are small corrections to the parity term or quadratic in Ω', we get the following terms:

$$\Omega^\dagger\Omega = \underbrace{\Omega''^\dagger\Omega'' + \delta^2\Omega'^\dagger_Q\Omega'_Q}_{\text{Q-Q terms from single field}} + \underbrace{2\mathrm{Re}(\delta\Omega'^\dagger_Q\Omega'')}_{\text{Q-Q cross-term}} + \underbrace{2\mathrm{Re}(\Omega'^\dagger\Omega'')}_{\text{PNC term}} \tag{7.37}$$

Cross-term

Since the most challenging systematic shifts come from the cross-term $\mathrm{Re}(\Omega'^\dagger_Q\Omega'')$, it is instructive to understand in detail under which conditions a vector shift can arise from this term.

In general, the light shifts due to a cross-term in a relatively large magnetic field (by which we let the z-axis be defined) have the form

$$\Delta_{(m)} \propto \mathrm{Re}(\Omega_1^\dagger \Omega_2)_{mm} \tag{7.38}$$

Instead of speaking about a vector shift, we can also speak about a shift that is proportional to m. For the spin-1/2 state under consideration ($6S_{1/2}$) it is sufficient to say that there is a *spin-dependent* shift present.

Three conditions must be fulfilled by $\Omega_1^\dagger \Omega_2$ in order to produce a spin-dependent, and therefore measurable effect:

1. *Direction:* Only the diagonal elements of the product $\Omega_1^\dagger \Omega_2$ are relevant, since only those are picked out by the external B-field (to first order). This means that the product must connect spin-states to themselves. Connecting to the respectively other spin state corresponds to a vector shift in a direction orthogonal to B, and is caused by off-diagonal elements. For the individual interactions $\Omega_1^\dagger$ and Ω_2 this means that their Δm selection rules must add to an even number. The combinations $\{\Delta m = \pm 1,\ \Delta m = \pm 1\}$,$\{\Delta m = 0,\ \Delta m = \pm 2\}$ are examples that produce a shift in the z-direction. Helpful sometimes is a graphical representation that shows this behavior. For example, $\{\Delta m = \pm 1,\ \Delta m = \pm 1\}$ can be represented as

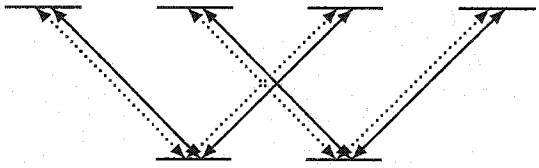

On the other hand, $\{\Delta m = \pm 1,\ \Delta m = \pm 2\}$ or $\{\Delta m = 0,\ \Delta m = \pm 1\}$ do not connect levels back to themselves. For example, $\{\Delta m = 0,\ \Delta m = \pm 1\}$ looks like

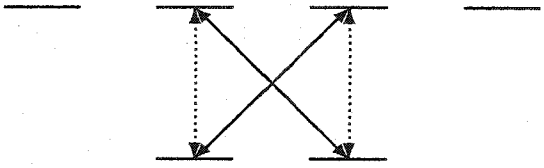

2. *Phase:* The total phase of the product has to be real. Symbolically we can write the phase of the product as

$$P[\Omega_1^\dagger \Omega_2] = P[\Omega_1]P[\Omega_2] \tag{7.39}$$

For this analysis it is most convenient to write each interaction in terms of reduced matrix elements, but with the spherical field components expressed in cartesian components. The geometrical convolution of the field with Clebsch-Gordan coefficients is symbolically represented by $\boldsymbol{f}(\boldsymbol{E})$ for a field in a dipole interaction[3].

$$\Omega = \langle M \rangle \boldsymbol{f}(\boldsymbol{E}) \tag{7.40}$$

The phase of each interaction consists of the phase of the matrix element, the phase of the geometrical function $\boldsymbol{f}(\boldsymbol{E})$, and the phase of the field amplitude $\boldsymbol{E}$ itself:

$$P[\Omega] = P[\langle M \rangle]P[\boldsymbol{f}(\boldsymbol{E})]P[\boldsymbol{E}] \tag{7.41}$$

Usually reduced matrix elements are real, but the PNC dipole elements are purely imaginary. The geometrical phase is only definite for specific choices of $\boldsymbol{E}$, which will be given below.

3. *Symmetry:* The product of the two interactions must be antisymmetric with respect to m, i.e. change sign with m. Otherwise both m-levels will be shifted

[3]For fields in a quadrupole interaction $\boldsymbol{f}$ depends on both derivatives and fields, which we write symbolically as $\boldsymbol{f}(\nabla \boldsymbol{E})$.

in the same direction, which would correspond only to a scalar shift. Again, symbolically we can write

$$S[\Omega_1^\dagger \Omega_2] = S[\Omega_1]\ S[\Omega_2] \tag{7.42}$$

and

$$S[\Omega] = S[\langle M \rangle]\ S[\boldsymbol{f}(\boldsymbol{E})] \tag{7.43}$$

Flipping the sign of m corresponds to a parity transformation. Therefore, if $\langle M \rangle$ is a pseudoscalar, it will reverse sign with m, as is the case with a PNC matrix element. The geometrical symmetry S$[\boldsymbol{f}(\boldsymbol{E})]$ indicates whether $\boldsymbol{f}(\boldsymbol{E})$ changes sign when comparing a $\Delta m = +1(\text{or} + 2)$ transition with a $\Delta m = -1(\text{or} - 2)$ transition.

To obtain the geometrical phases and symmetries for various cartesian fields, we write the spherical dipole and quadrupole fields in terms of their cartesian components (see App.A.3):

$$E^{(1)} = \left[\frac{1}{\sqrt{2}}(E_x - iE_y), E_z, \frac{1}{\sqrt{2}}(-E_x - iE_y)\right] \tag{7.44}$$

$$E^{(2)} = [\frac{1}{2}(\partial_x - i\partial_y)(E_x - iE_y), \frac{1}{2}(\partial_z(E_x - iE_y) + (\partial_x - i\partial_y)E_z), \sqrt{\frac{3}{2}}\partial_z E_z, \tag{7.45}$$

$$\frac{1}{2}(-\partial_x - i\partial_y)(-E_x - iE_y), \frac{1}{2}(\partial_z(-E_x - iE_y) + (-\partial_x - i\partial_y)E_z)] \tag{7.46}$$

Table 7.2 shows the resulting properties, found by substituting the individual cartesian components. First we use these three conditions to derive all possible field configurations that can give a PNC-shift in the first place: The interaction is $\Omega'^\dagger \Omega''$, which is a dipole-quadrupole product. The symmetry of the matrix elements is S$[\langle E1^{\text{PNC}} \rangle \langle E2 \rangle]$=-1, because $\langle E1^{\text{PNC}} \rangle$ is a pseudoscalar. This means that the product of the geometrical symmetries, $S[\boldsymbol{f}(\boldsymbol{E}')]S[\boldsymbol{f}(\boldsymbol{\nabla E}'')]$, must be symmetric, or 1, to obtain an overall antisymmetry. Together with the directional constraints only the following two combinations survive: $(E_y, \partial_z E_y + \partial_y E_z)$ and $(E_x, \partial_z E_x + \partial_x E_z)$. These

Table 7.2: Phase and symmetries of dipole and quadrupole interactions for cartesian components.

interaction	field $\boldsymbol{E}$	P[$\boldsymbol{f}(\boldsymbol{E})$]	S[$\boldsymbol{f}(\boldsymbol{E})$]	Δm
dipole	E_z	1	1	0
	E_y	i	1	± 1
	E_x	1	-1	± 1
interaction	field $\boldsymbol{\nabla E}$	P[$\boldsymbol{f}(\boldsymbol{\nabla E})$]	S[$\boldsymbol{f}(\boldsymbol{\nabla E})$]	Δm
quadrupole	$\partial_z E_z$	1	1	0
	$\partial_z E_x + \partial_x E_z$	1	-1	± 1
	$\partial_z E_y + \partial_y E_z$	i	1	± 1
	$\partial_x E_x + \partial_y E_y$	1	1	± 2
	$\partial_x E_y + \partial_y E_x$	i	-1	± 2

are equivalent configurations, with only the x and y axis exchanged, and without loss of generality we pick $(E_x, \partial_z E_x + \partial_x E_z)$. The phase of this product is given by

$$\begin{aligned} P[\boldsymbol{\Omega}'^{\dagger}\boldsymbol{\Omega}''] =& P[\langle E1^{\mathrm{PNC}}\rangle] \times P[\langle E2\rangle] \times P[\boldsymbol{f}(\boldsymbol{E}')] \times P[\boldsymbol{f}(\boldsymbol{\nabla E}'')] \times P[\boldsymbol{E}'] \times P[\boldsymbol{\nabla E}''] \\ =& i \times 1 \times 1 \times 1 \times P[\boldsymbol{E}'] \times P[\boldsymbol{\nabla E}''] \end{aligned} \tag{7.47}$$

Thus, in order to obtain an overall real phase, we have to make $P[\boldsymbol{E}'] \times P[\boldsymbol{\nabla E}''] = i$ by requiring a phase i between the fields. Because $\boldsymbol{E}'$ is along x, the k-vector $\boldsymbol{k}'$ is confined to the z-y plane. We therefore have the following choices for PNC fields:

$$\boldsymbol{E}' = E'_x \cos k'_z \boldsymbol{e}_z \quad \text{or} \quad E'_x \sin k'_y \boldsymbol{e}_y \tag{7.48}$$

$$\boldsymbol{E}'' = iE''_z \sin k''_x \boldsymbol{e}_x \quad \text{or} \quad iE''_x \sin k''_z \boldsymbol{e}_z \tag{7.49}$$

Now we repeat this selection procedure to identify possible combinations that give a shift through a spurious cross-term $\delta\boldsymbol{\Omega}'^{\dagger}_Q\boldsymbol{\Omega}''$. This is a product of two quadrupole terms. The symmetry of the matrix elements is S[$\langle E2\rangle\langle E2\rangle$]=1. This means that the

Table 7.3: Perturbations from ideal fields that will produce a systematic shift, with the abbreviation $E'_i \equiv E'\boldsymbol{e}_i$. The meaning of the various α is the following: Starting from an ideal field E_i, the misalignment of polarization by an angle α produces a small spurious field αE_j. Likewise, starting from an ideal propagation direction k_i, the misalignment of k_i by an angle α causes a small αk_j to exist.

Systematic-shift combination	ideal field geometries $(k'_z E'_x, k''_x E''_z)$	$(k'_y E'_x, k''_x E''_z)$
$\text{comb}_1 = (\partial_z E_x + \partial_x E_z, \partial_z E_y + \partial_y E_z)$	$i\alpha' E'_y$	$i\alpha' E'_z$
$\text{comb}_2 = (\partial_x E_x + \partial_y E_y, \partial_x E_y + \partial_y E_x)$	$i\alpha'' E''_y \alpha' k'_x + i\alpha'' E''_x \alpha' k'_y$	$i\alpha'' E''_x$

product of the geometrical symmetries, $S[\boldsymbol{f}(\boldsymbol{\nabla E'})]S[\boldsymbol{f}(\boldsymbol{\nabla E''})]$, must be antisymmetric. For the phases,

$$\begin{aligned} P[\Omega'^{\dagger}_Q \Omega''] = \; & P[\langle E2\rangle\langle E2\rangle]P[\boldsymbol{\nabla E'}\boldsymbol{\nabla E''}]P[\boldsymbol{f}(\boldsymbol{\nabla E'})]P[\boldsymbol{f}(\boldsymbol{\nabla E''})] \\ = \; & 1 \times 1 \times P[\boldsymbol{f}(\boldsymbol{\nabla E'})]P[\boldsymbol{f}(\boldsymbol{\nabla E''})] \end{aligned} \tag{7.50}$$

This means the product of geometrical phases $\text{P}[\boldsymbol{f}(\boldsymbol{\nabla E'})]\text{P}[\boldsymbol{f}(\boldsymbol{\nabla E''})]]$ must be real[4].

From these constraints, and the directionality of the shift, the following combinations will give PNC-like shifts:

$$\begin{aligned} \text{comb}_1 &= (\partial_z E_x + \partial_x E_z, \partial_z E_y + \partial_y E_z) \quad \text{(both are } \Delta m = \pm 1 \text{ terms)} \\ \text{comb}_2 &= (\partial_x E_x + \partial_y E_y, \partial_x E_y + \partial_y E_x) \quad \text{(both are } \Delta m = \pm 2 \text{ terms)} \end{aligned}$$

Starting from the two field geometries for $\boldsymbol{E'}$, where $\boldsymbol{k'}$ is either along y or z, we can identify the perturbations that will produce one of these combinations; they are listed in Table 7.3. We can see that for $\boldsymbol{k'} = k'_y$, the perturbations come as a result of only one misalignment angle α, which means that this geometry is inferior to the one where $\boldsymbol{k'} = k'_z$. Here only comb_1 leads to a perturbation with one misalignment

[4] $\text{P}[\boldsymbol{\nabla E'}\boldsymbol{\nabla E''}]$ is 1 here because externally we have chosen a factor of i, and $\boldsymbol{\nabla E'}$ carries another factor of i from the derivative as it now acts in a quadrupole interaction.

angle. Together with the initial misplacement δ of the ion from the antinode of $\boldsymbol{E}$', this would give two small parameters if δ and α' are experimentally independent, but would still lead to an intolerable systematic effect.

Fortunately, there is a piece of this puzzle that we have not analyzed yet and that will provide the additional suppression factor. As we will have mentioned before, $\boldsymbol{E}'$ also causes large off-resonant light shifts. They differ for $m = \pm 1/2$ relative to $m = \pm 3/2$ by $\sim 300\,\mathrm{kHz}$ (see Table 7.4), which is much larger than the laser line width. Thus, if we tune the PNC laser so that it is resonant with the transition $m = \pm 1/2$ states, the $m = \pm 3/2$ levels are barred from producing resonant shifts; instead, they will produce off-resonant light shifts that are suppressed in general by the ratio of Rabi frequency to detuning.

To see how this is relevant in the present analysis, we examine the shift $\delta\Omega_Q'^{\dagger}\Omega''$ in a coordinate system where $\boldsymbol{E}'$ defines the z axis. The resulting m-levels then experience the differential shift mentioned above. We reexamine the important terms $(\partial_x E_z, \partial_z E_y)$ from comb_1 that cause the shift $i\alpha' E_y'$. In the new coordinate system they become $(\partial_z E_y, \partial_y E_x)$. The term $\partial_y E_x$ causes only $\Delta m = \pm 2$ transitions, and this combination can be symbolized as

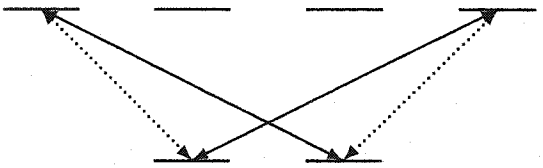

We can see that this interaction depends on the $m = \pm 3/2$ levels. But these levels are now off-resonant, and the corresponding shift is suppressed by

$$R = \frac{\Omega''}{\delta_{3/2,1/2}}, \tag{7.51}$$

where Ω'' is the characteristic size of the quadrupole light shift due to E''. We can see that this creates a trade-off between laser frequency stability and systematic shifts: off-resonant shifts are reduced if we decrease the size of E''. On the other hand, then

the resonant shifts also decrease, and the laser has to be more stable to let the PNC measurement remain to be independent of its frequency.

Terms from single field

The first two terms from Eq.(7.37), $\Omega''^{\dagger}\Omega''$ and $\delta^2\Omega_Q'^{\dagger}\Omega_Q'$, represent interactions that come from the quadrupole couplings of either E' or E'' alone. With purely linearly polarized fields and no misalignment they cannot produce spin-dependent shifts because there are no antisymmetric combinations. They can produce spin-dependent shifts if there is circular polarization, however. We can write these shifts as $\sigma''\Omega''$ and $\delta^2\sigma'\Omega_Q'$ if the fields have residual circular polarization σ. These shifts are easily distinguishable from PNC shifts because we can turn one field off and observe the shift due to the other field, and also use this procedure to null the shifts. However, these shifts are still problematic since any noise in polarization and laser intensity will cause line broadening of the Zeeman resonance and can limit the sensitivity of the experiment. The shift $\sigma''\Omega''$ will be the dominating one and can be made smaller by reducing E''.

7.10.2 Off-resonant shifts

The off-resonant light shifts that help us out in reducing *resonant* shifts also have a drawback: They also produce sub-MHz shifts in the $6S_{1/2}$ state, and any circular polarization will lead to differential shifts. In order for these shifts not to broaden the RF resonances, the polarization of E' must be stable to about 10^{-7} over a time large compared to a spin-resonance trial. As long as these shifts only come from E', they can be distinguished from PNC shifts in the same way as the resonant shifts from single fields, simply by turning E'' off. However, there will also be a cross-term that involves both fields, if the node of E'' is shifted by δ''. Then there will be an additional dipole coupling $\Omega'^{\dagger}\Omega_D''$ that causes systematic shifts. For the field

geometries that minimize resonant shifts, there are only two small parameters that discriminate against this systematic. A detailed analysis should be done.

7.10.3 Parity mixing from stray electric fields

Static electric fields might be thought to pose a great potential hazard for this PNC measurement, since it turns out that a 10 mV/cm field mixes states of opposite parity in the ion to the same extent as the weak interaction. Stray DC fields are indeed a major systematic problem in many current PNC experiments [7]. It is also true, however, no net DC electric fields can exist at the equilibrium position of an ion in the absence of non-electric forces – otherwise the ion would experience a net acceleration. In fact, gravitational effects will cause the ion to find equilibrium in a 1 mV/cm field. This may lead to a gravity-induced shift of 10% of the PNC shift. However, this shift is constant and drops out when, for example, the temporal phases of the light fields are reversed. Also, because of the vector nature of this electric field state-mixing the resulting shift should have a different structure than the PNC shift with its scalar nature of the internal PNC interaction. This has not been studied in detail, though. Other non-electric forces could include forces on the ion due to light-pressure. They should be negligible because the ion is located where the *intensity* of each standing-wave field (E' and E'') has nearly zero spatial gradient. Likewise, magnetic forces should be negligible.

Oscillating electric fields at the ion's location will indeed exist, from the trap field and also from stray fields that are modulated by the ion's motion. These ac fields cause Stark mixing amplitudes that oscillate at the secular and trap frequencies ν_{trap} and ν_{rf}, which are on the order of MHz. These make the resonance for these amplitudes appear shifted by these frequencies, effectively making them off-resonant for a laser tuned to the dc resonance. There still exists, however, a resonant effect: The ion motion adds Lamb-Dicke sidebands to the laser spectrum, and these sidebands could then be resonant with the shifted amplitudes. For a tightly confined ion these

resonant effects should be negligibly small.

7.10.4 M1 transitions

So far the effect of the M1 amplitude between $6S_{1/2}$ and $5D_{5/2}$ has not been included in the analysis of systematic problems. Any misaligned field E' that causes an E2 interaction, will also cause an M1 interaction. Just like the E2 amplitude, the M1 amplitude can then interfere with E2 from E'' to produce a PNC-like effect. While the M1 amplitude is weaker than the E2 amplitude by a factor 1000-10000, interference terms may not be suppressed by additional factors in the geometries considered so far. The M1 amplitude will be discussed later in connection with odd-isotope PNC, but more analysis of M1 systematics needs to be done for both odd and even isotopes.

7.11 Off-resonant effects in detail

As we have seen, off-resonant effects play a large role in this experiment, even though the primary interaction is a resonant one. Here we examine these effects in greater detail.

Since the PNC observable grows with the intensity of the applied PNC field, one might think that the larger this field, the better. Unfortunately there is a natural limit to its size beyond which the PNC shift will continue to rise along with the achievable RF-line widths, yielding no gain in signal-to-noise of the experiment. This limit comes from off-resonant quenching of both the D and the S state that unavoidably takes place as a result of the PNC light field. The other off-resonant effects are light shifts due to E1 couplings in the atom. We will examine the two effects in more detail.

7.11.1 Quenching

Quenching takes place because of a slight mixing of P states (collectively called excited state here) into S and D states, in the following collectively called ground states. This

mixing causes the existence of an E1 transition amplitude between a ground state and its corresponding virtual level, the one that has an identical (now slightly mixed) atomic state, but one fewer photon in the light field.

The transition amplitude now leads to the dipole spontaneous transition rate

$$\Gamma(\omega) = \frac{4\alpha}{3c^2} \frac{|\langle f||d^{(1)}||i\rangle|^2}{2j_i+1} \omega^3 \tag{7.52}$$

Because the energy difference between the two states simply corresponds to the frequency of the applied light (see levels $|a1\rangle$ and $|b2\rangle$ in Figure 2.4), we have to use ω_L in Eq.(7.52). For $\omega_L = \omega_0$ this would simply be the spontaneous transition rate $\Gamma = 1/\tau$, so that we can write

$$\Gamma(\omega_L) = \frac{\omega_L^3}{\omega_0^3}\Gamma \tag{7.53}$$

Such a spontaneous process changes the phase, or/and the m-level, in an unpredictable way. The ground state now has a mechanism for loss of its "phase memory", limiting the time during which one can maintain control over the quantum state of the system. Since a PNC measurement relies on maintaining a coherent state for the time of an RF measurement, this "quenching" process limits the measurement time and therefore the achievable line widths.

The quenching rate is equal to the probability p of finding the atom in the excited-state admixture of the ground state, times the decay rate $\Gamma(\omega_L)$. This probability p was derived in Eq.(2.29) for a two-state system to be $p = \frac{\Omega^2}{4\delta^2}$. Writing this in terms of the associated light shift $\Delta = \frac{\Omega^2}{4\delta}$, and multiplying with the decay rate of the upper state, we get for the quenching rate

$$\Upsilon = \frac{\Delta}{\delta}\Gamma(\omega_L). \tag{7.54}$$

Generalizing this to the situation in an atom, we can write for the off-resonant quenching rate:

$$\Upsilon_{jm} = \frac{e^2E^2}{4\hbar^2} \sum_{\gamma',m',\pm\omega_L} \frac{|\langle\gamma' j' m'||r^{(0)}||\gamma jm\rangle|^2}{(\omega_\gamma - \omega_{\gamma'} \pm \omega_L)^2} \frac{\sum_q |(jm,1q|j'm')\epsilon_q|^2}{2j'+1} \frac{\omega_L^3}{\omega_\gamma - \omega_{\gamma'}^3}\Gamma'_j \tag{7.55}$$

where ϵ_q are the spherical components of the polarization. Since the light shift dominates the magnetic shift in the PNC experiment, *it* defines the quantization axis and, as long as the light is linearly polarized, only $\Delta m = 0$ transitions are driven, which corresponds to $\epsilon = (0, 1, 0)$. Table 7.4 shows the quenching of D and S states due to coupling with the lowest two $P_{1/2}$ and $P_{3/2}$ levels, for Ba^+ and Ra^+. For Ba^+ the $4F_{5/2}$ level was also included.

This quenching will start to shorten the lifetime of the coherent S/D state when its quenching rate becomes comparable to its natural lifetime. Solving for E' when setting

$$\frac{1}{2}(\Upsilon_{6S_{1/2}} + \Upsilon_{5D_{3/2}}) = \frac{1}{2\tau_{5D_{3/2}}} \tag{7.56}$$

gives the field E'_{max} when that starts to happen, and therefore the maximal "useful" PNC field. Later we will see that there may be a reason to increase the size of the field nonetheless. Table 7.5 shows this maximal PNC field for Ba^+ and for Ra^+.

7.11.2 Light shifts

In addition to state quenching there are also off-resonant light shifts due to strong dipole matrix elements. These will alter the resonance frequencies collectively and, if the PNC light field has some circular polarization, will produce a vector shift that is potentially large, and will vary with light intensity. For the D-state there is also a quadrupole shift that produces a shift between the outermost m-levels and the innermost levels, which enables us to essentially choose which pair will be resonant with the PNC light. This turns out to be an advantage in the quest to suppress systematic errors. The light shifts can be calculated as in Section 6.1.3 according to Eq.(6.7):

$$\Delta_{jm} = \frac{e^2E^2}{4\hbar^2} \sum_{\gamma',m',\pm\omega_L} \frac{|\langle\gamma' j' m'||r^{(0)}||\gamma jm\rangle|^2}{\omega_\gamma - \omega_{\gamma'} \pm \omega_L} \frac{|(jm; 10|j'm')|^2}{2j'+1}, \tag{7.57}$$

where $\Delta_{jm}/(2\pi)$ is the light shift of state $|\gamma, jm\rangle$ in units of s^{-1}.

Table 7.4: Comparative calculation of quenching rates and light shifts. The light shifts are due to coupling of the 6P, 7P, and 4F states for Ba^+, and of the 7P and 8P states for Ra^+. The 5F state in Ra^+ should contribute a significant amount to the values, but matrix elements were not available. The quenching rates only include the 6P state in Ba^+ and the 7P state in Ra^+.

state	quenching rates		lightshifts	
	Ba^+	Ra^+	Ba^+	Ra^+
even isotopes (I=0)				
$D_{3/2}$,m=$\frac{1}{2}$	0.0033 Hz	3.36 Hz	-0.48 MHz	0.85 MHz
$D_{3/2}$,m=$\frac{3}{2}$	0.0004 Hz	0.48 Hz	-0.16 MHz	-0.24 MHz
$S_{1/2}$,m=$\frac{1}{2}$	0.002 Hz	0.04 Hz	-0.73 MHz	-0.76 MHz
odd isotopes (I=$\frac{3}{2}$)				
$D_{3/2}$,F=0	0.0018 Hz	1.93 Hz	-0.32 MHz	0.31 MHz
$S_{1/2}$,F=1	0.0022 Hz	0.04 Hz	-0.737 MHz	-0.767 MHz
odd isotopes (I=$\frac{1}{2}$)				
$D_{3/2}$,F=1,m_f=0	0.0033 Hz	3.37 Hz	-0.488 MHz	0.856 MHz
$D_{3/2}$,F=1,m_f=1	0.0011 Hz	1.21 Hz	-0.245 MHz	0.303 MHz
$S_{1/2}$,F=0	0.0022 Hz	0.040 Hz	-0.737 MHz	-0.767 MHz

The light shifts, as well, have been calculated for Ba^+ and Ra^+ and are shown in Table 7.4.

7.12 Experimental requirements with Ba^+ and Ra^+

All aspects of the PNC measurement described so far can not only be applied to Ba^+, but also to Ra^+, the heaviest of the earth-alkalis and isoelectronic to Ba^+. A comparison of some atomic properties of the two species are shown in Table 7.6.

In the following we find some experimental requirements for a competitive PNC

Table 7.5: PNC wavelength and maximal PNC E-field (where the sum of S and D quenching rates becomes equal to the natural decay rate) for Ba^+ and Ra^+.

	Ba^+	Ra^+
Wavelength	2050 nm	828 nm
maximal E-field	14900 V/cm	6800 V/cm

Table 7.6: Comparison of some relevant atomic properties of Ba^+ and Ra^+.

	Ba^+	Ra^+
Isotope	^{138}Ba	^{226}Ra, $t_{1/2} = 1600$ yrs
$S_{1/2}$-$P_{1/2}$	493 nm	468 nm
$S_{1/2}$-$D_{3/2}$	2051 nm	828 nm
$S_{1/2}$-$D_{5/2}$	1760 nm	728 nm
Lifetime of $P_{1/2}$ and $P_{3/2}$	7.8 ns , 6.3 ns	8.8 ns , 4.7 ns
Lifetime of $D_{3/2}$ and $D_{5/2}$	81 s , 30 s	0.6 s , 0.3 s
$\mathcal{E}^{\mathcal{PNC}}$ [19]	$2.09 \cdot 10^{-11}\ iea_B$	$40.8 \cdot 10^{-11}\ iea_B$

experiment with about 0.2 % precision and accuracy, both for Ba^+ and for Ra^+.

7.12.1 Precision

If measurement cycles are repeated at the rate $1/t$, where t is the coherence time, the frequency uncertainty of the Zeeman transitions will be $\sim 1/t$, and the statistical signal-to-noise of the PNC measurement is given by

$$(S/N)_{\text{stat}} = \frac{\Delta_d^{\text{PNC}}}{\delta\Delta_d^{\text{PNC}}} \cong \Delta_d^{\text{PNC}} f\sqrt{tT} \tag{7.58}$$

where f is an efficiency factor given by shelving efficiencies, very important since it appears linearly in Eq. (7.58). In present measurements $f \sim 0.25$ for the S-state, but with direct shelving f could be made much larger.

For the maximal field E'_{max} calculated in Section 7.11, the coherence time t is exactly equal to the lifetime τ_D of the excited state (without quenching the coherence time would be $2\tau_D$). Eq. (7.58) shows that a further increase in E' will not lead to a gain in $(S/N)_{\rm stat}$ because the increase in $\Delta_d^{\rm PNC} \propto E'$ is cancelled by the decrease of $t \propto 1/E'^2$.

According to Eq. (7.58) and with the numbers for Ba^+ and Ra^+, and for an efficiency factor $f \sim 0.5$ (somewhat arbitrary number), the measurement time needed for a 0.2% measurement is about 1.1 days for Ba^+ and 1.4 days for Ra^+. This seems surprising at first because of the larger PNC effect in Ra^+; but the quenching rates in the D-state in Ra^+ are factor of 1000 larger than in Ba^+ for the same field (mainly because of the smaller detuning of the PNC field from other atomic resonances, and the larger frequency between S and D states in Ra^+). This leads to a smaller E'_{max} than in Ba^+, which together with the smaller coherence time in Ra^+ explains why Ra^+ is worse than Ba^+ when it comes to signal-to-noise of the measurement.

However, all experimental conditions are much easier to fulfill with Ra^+. In order to achieve the signal-to-noise given above, all mechanisms for line broadening have to be smaller than $1/\tau$, which is 2 mHz for Ba^+, and 0.25 Hz for Ra^+. Broadening happens through magnetic field fluctuations, fluctuations in laser polarization and intensity, as well as frequency fluctuations of the PNC laser.

7.12.2 Accuracy

In order for all systematic shifts to remain below a small fraction of the PNC shift, misalignment of phases and geometry need to be controlled to about 1 part in 1000 over a time much longer than one measurement cycle. In the experiment, the ion itself would be used to set and check the spatial phases and field geometry. Both measurement of absolute E2 transition rates and purposeful misalignment of phases will be useful tools for alignment and for assessment of drift rates. Indeed, the initial experimental goal for a PNC experiment could consist of a procedure to systemat-

ically remove all shifts and misalignments. For example, with only the E' field on, continuous monitoring of the E2 transition rate will allow standing wave optimization and antinode positioning.

A key issue here is the stability of the ion position, as any drift will produce a systematic error through $\Omega_Q'^{\dagger}\Omega''$. It must remain stable to better than 10^{-9} m for considerably longer than the time period of each measurement cycle. This is likely the hardest experimental requirement, and a main motivating factor to switch to odd isotopes where this systematic is greatly diminished. Electrode surface patch effects produce DC potentials that affect the location of the ion orbit, and it is not clear how quickly these effects change in high vacuum at nominally constant temperature. Presently, cavity-QED experiments are being carried out that may help answer this question [46, 29]. In addition, the trap electrode position relative to the standing-wave reflector must be monitored and locked by a stable laser beam to $\Delta L/L < 10^{-8}$.

All of the resonant systematic effects are relatively smaller in Ra^+ by about a factor of 20. From a comparison of light shifts (Table 7.4) we might expect that the absolute size of off-resonant systematic shifts is comparable in Ba^+ and Ra^+, which makes them relatively smaller in Ra^+ by a factore of 20 also. But the off-resonant effects depend on complicated sums like Eq.(6.4) and haven't been studied in detail yet.

7.12.3 Calibration

An essential aspect in the final PNC measurement will be calibration of the absolute optical field strengths at the ion location. Two independent methods can be used to determine this. Both involve purposeful misalignments of the field geometry, in this case by well-known, reproducible amounts. Most directly, we could purposefully induce the systematic shift $\Omega_Q'^{\dagger}\Omega''$. The ratio of the PNC shift to this quantity then can be related directly to the weak interaction mixing in the ion. This technique requires accurate knowledge of the E2 matrix element, a quantity that in principle

can be calculated as accurately as PNC itself. A second, and independent, calibration technique involves the production of a vector shift of the ground state due only to the off-resonant E1 dipole mixing $\Omega'^{\dagger}\Omega''_D$ discussed above. This can easily be achieved since the relative temporal phasing of the two fields, E' and E'', is such as to produce what is effectively circularly polarized light at the ion location. By shifting E'', by a known phase and misaligning $\boldsymbol{k}''$ by a known angle, a shift is produced that can be measured easily. Calibration by this method then requires knowledge of the sum over dipole matrix elements, a significantly different quantity from the E2 matrix element required in the first method, but one which should also be available to similar accuracy. The E2 and E1 shifts are easily distinguishable due to the off-resonant nature of the dipole shift. The E1 shift would be insensitive to small changes in the laser frequency, whereas the E2 shift would trace out the characteristic dispersive shape as it passes through resonance.

Chapter 8

PNC WITH ODD ISOTOPES

As we have seen in the previous chapter, the dominant electromagnetically allowed amplitude between the states $6S_{1/2}$ and $5D_{3/2}$ used for a PNC measurement is an E2 amplitude. This amplitude is used to produce an interference with the PNC E1 amplitude between the same two states, using two independent standing-wave fields E'' and E'. The E2 amplitude is about 10^7 times stronger than the PNC amplitude. This gives rise to challenging systematic effects as small misalignments cause the E1 field to drive the E2 amplitude and produce shifts that can look like the genuine PNC effect. The geometry is chosen to suppress these shifts by small misalignment factors, but stringent control over parameters like the standing-wave position is necessary, which might be hard to realize. Besides the E2 amplitude, there is also a much smaller, relativistically allowed M1 transition between the same states. It is expected to be a factor $f = 10^3 - 10^4$ smaller than E2, but may also contribute to systematic effects as the geometry may not be optimal to further suppress these shifts. Much simplification would be gained by the complete absence of the strong E2 transition. Then a field geometry can be chosen to discriminate optimally against M1 systematic effects, and the amplitudes causing such effects are much smaller to begin with by the factor f.

It is indeed possible to "turn off" the E2 amplitude by working with an ion that exhibits hyperfine structure. For both Ra and Ba there are isotopes with $I = 1/2$ and $I = 3/2$. Both isotopes feature $F = 0 \leftrightarrow F' = 1$ transitions between $6S_{1/2}$ and $5D_{3/2}$ (more complete level structures can be found in Figure B.1 and B.2). Quadrupole transitions require the triangularity condition $F + F' \geq 2$ and are therefore absent on

that transition.

The price to pay for this simplification is the considerable complication in trapping isotopes with hyperfine structure. Additional optical frequencies are needed to prevent hyperfine pumping, and isotopes may not be abundant and therefore are harder to trap. Also, for the same field E'' the resulting light shifts are smaller by the factor f, making them only about 100s to 1000s of Hz large. The frequency stability of the PNC laser must be much better than the size of these shifts, which calls for a very stable PNC laser.

The odd isotopes offer more options and possible measurement schemes than the even isotopes. First, when doing RF spectroscopy in an $F = 1$ level, there is additional quadrupole spin structure to consider. This still allows us to look for a vector light shift as with the even isotopes, but we can now also consider field configurations that produce a PNC (spin) quadrupole shift. These alternatives lead to quite different experimental scenarios. The quadrupole alternative may prove to be the superior scheme since it is insensitive to systematic effects that can only produce vector shifts (in particular off-resonant effects). Also, one could abandon the M1 amplitude completely and instead use a two-photon transition between S and D state as an interference partner. This again would lead to very different possible realizations for a PNC experiment. Lastly, off-resonant couplings to other *hyperfine states* will in all cases still involve E2 transitions, and must be carefully analyzed.

This initial study calculates the vector structure of the resulting light shifts and discusses some possibilities for field geometries when looking for a PNC vector shift. We propose ideas regarding RF spectroscopy in the $F = 1$ state, including spin-state preparation and detection, in case a light shift approach is chosen; an alternative would be a direct measurement of transition rates. Finally, we give a first survey of some systematic effects.

8.1 *Interaction and vector structure*

The same field $\boldsymbol{E}''$ that would cause an E2 coupling in the even isotopes also creates a magnetic field according to

$$\nabla \times \boldsymbol{E}''(\boldsymbol{r}) = -\frac{\partial \boldsymbol{B}''(\boldsymbol{r})}{\partial t}, \tag{8.1}$$

which in turn causes a magnetic dipole transition

$$\Omega^{M1}_{m'm} = \frac{1}{\hbar}\langle \gamma' j' || \mu^{(1)} || \gamma j \rangle \times \sum_q \frac{(j' m'_j | 1q; j m_j) B^{(1)}_q}{\sqrt{2j'+1}}, \tag{8.2}$$

which acts as the interference partner in the odd isotopes. We label the magnetic dipole coupling between F=1 and F=0 of the states $6S_{1/2}$ and $5D_{3/2}$, in analogy with the E2 term for the even isotopes:

$$\boldsymbol{\Omega}'' = \frac{1}{\hbar}\langle M1 \rangle \boldsymbol{f}(\boldsymbol{B}'') \tag{8.3}$$

This means in the odd isotopes there are no resonant quadrupole interactions at all; instead both the PNC and the interfering coupling are dipole transitions, and the PNC term is given by $2\mathrm{Re}(\boldsymbol{\Omega}'^{\dagger}\boldsymbol{\Omega}'')$, where $\boldsymbol{\Omega}''$ is now the magnetic *dipole* transition due to B''.

Again, the two interactions $\boldsymbol{\Omega}'$ and $\boldsymbol{\Omega}''$ add coherently, and we can write

$$\boldsymbol{\Omega} = \boldsymbol{\Omega}' + \boldsymbol{\Omega}''. \tag{8.4}$$

We then write $\boldsymbol{\Omega}^{\dagger}\boldsymbol{\Omega}$ in terms of $\boldsymbol{\Omega}'$ and $\boldsymbol{\Omega}''$ as

$$\begin{aligned} \boldsymbol{\Omega}^{\dagger}\boldsymbol{\Omega} &= (\boldsymbol{\Omega}'^{\dagger} + \boldsymbol{\Omega}''^{\dagger})(\boldsymbol{\Omega}' + \boldsymbol{\Omega}'') \\ &\simeq \boldsymbol{\Omega}''^{\dagger}\boldsymbol{\Omega}'' + (\boldsymbol{\Omega}'^{\dagger}\boldsymbol{\Omega}'' + \boldsymbol{\Omega}''^{\dagger}\boldsymbol{\Omega}'), \end{aligned} \tag{8.5}$$

as before. Different from the E2 case, now all terms have the *same* structure: All are products of two dipole couplings; for the structure it doesn't matter, of course, whether we are dealing with electric or magnetic fields. Thus, by writing the vector

structure for two dipole couplings, we have already accounted for all terms, including any additional terms due to systematic effects. Note that an exception are off-resonant couplings involving E2 amplitudes.

We can write the general form of the product of two dipole interactions $\mathbf{\Omega}_1$ and $\mathbf{\Omega}_2$ with fields $\boldsymbol{E_1}$ and $\boldsymbol{E_2}$, in an analogous way to Eq.(6.4), as

$$\mathbf{\Omega}_1^\dagger \mathbf{\Omega}_2 = C\left(s(j_1,j_2)\boldsymbol{E_1}^* \cdot \boldsymbol{E_2} + id(j_1,j_2)(\boldsymbol{E_1}^* \times \boldsymbol{E_2}) \cdot \hat{\boldsymbol{j}} + q(j_1,j_2)(E_{1,i}^* E_{2,k})\hat{j}_{ik}\right), \tag{8.6}$$

because this exhausts all possible combinations to form scalar, vector, and tensor products from the two fields. $s(j,j'), d(j,j'), q(j,j')$ are the coefficients for the scalar, vector (dipole), and tensor (quadrupole) parts of the effective Hamiltonian. A quadrupole part now occurs because we are dealing with a spin-1 system rather than with a spin-1/2 system, as was the case for the even isotopes. The factors are calculated explicitly or with the aid of generalized Pauli matrices, and for $j=1, j=0$ are found to be $s=\frac{1}{9}, d=-\frac{1}{6}, q=-\frac{1}{3}$, so that we can write for the vector structure for odd isotopes

$$\mathbf{\Omega}_1^\dagger \mathbf{\Omega}_2 = C\left(\frac{1}{9}\boldsymbol{E_1}^* \cdot \boldsymbol{E_2} - \frac{i}{6}(\boldsymbol{E_1}^* \times \boldsymbol{E_2}) \cdot \hat{\boldsymbol{j}} - \frac{1}{3}(E_{1,i}^* E_{2,k})\hat{j}_{ik}\right), \tag{8.7}$$

or

$$\mathbf{\Omega}_1^\dagger \mathbf{\Omega}_2 = \Theta_s + \mathbf{\Theta} \cdot \hat{\boldsymbol{j}} + \sum_{ik} \Theta_{ik}\hat{j}_{ik} \tag{8.8}$$

with

$$\Theta_s = \frac{C}{9}\boldsymbol{E_1}^* \cdot \boldsymbol{E_2} \tag{8.9}$$

$$\mathbf{\Theta} = -\frac{iC}{6}(\boldsymbol{E_1}^* \times \boldsymbol{E_2}) \tag{8.10}$$

$$\Theta_{ik} = -\frac{C}{3}(E_{1,i}^* E_{2,k}) \tag{8.11}$$

If we, again, assume that the magnetic field is much larger than the non-scalar shifts, only the diagonal matrix elements of $\mathbf{\Omega}^\dagger\mathbf{\Omega}$ will contribute, and we can write

Eq.(8.5) as

$$\Omega^\dagger\Omega = (\Omega'^\dagger + \Omega''^\dagger)(\Omega' + \Omega'') \tag{8.12}$$

$$\simeq \Omega''^\dagger\Omega'' + 2\mathrm{Re}(\Omega'\Omega'') \tag{8.13}$$

Then, for the two fields $\boldsymbol{E}' \equiv \boldsymbol{E}$ and $\boldsymbol{B}'' \equiv \boldsymbol{B}$ and the M1 and E1(PNC) couplings, Eqs.8.9 become

$$\Theta_s = \frac{C_2}{9}\boldsymbol{B}^* \cdot \boldsymbol{B} + \mathrm{Re}(\frac{2C_1}{9}\boldsymbol{E}^* \cdot \boldsymbol{B}) \tag{8.14}$$

$$\boldsymbol{\Theta} = -\frac{iC_2}{6}(\boldsymbol{B}^* \times \boldsymbol{B}) + \mathrm{Re}(\frac{iC_1}{3}(\boldsymbol{E}^* \times \boldsymbol{B})) \tag{8.15}$$

$$\Theta_{ik} = -\frac{C_2}{3}(B_i^* B_k) + \mathrm{Re}(\frac{2C_1}{3}(E_i^* B_k)) \tag{8.16}$$

with

$$C_1 = \frac{1}{\hbar^2}\langle M1\rangle\langle E1^{\mathrm{PNC}}\rangle \qquad \text{pseudoscalar, imaginary} \tag{8.17}$$

$$C_2 = \frac{1}{\hbar^2}\langle M1\rangle\langle M1\rangle \qquad \text{scalar, real} \tag{8.18}$$

If we further assume that the largest light shifts are still much larger than the magnetic field, then we can write for the on-resonance light shift

$$\Delta_{(m)} = \frac{1}{2}\sqrt{(\Omega^\dagger\Omega)_{mm}} \tag{8.19}$$

$$= \frac{1}{2}\sqrt{\Theta_{\mathrm{sc}} + (\boldsymbol{\Theta}\cdot\boldsymbol{j})_{mm} + (\sum_{ik}\Theta_{ik}\hat{j}_{ik})_{mm}} \tag{8.20}$$

$$= \frac{1}{2}\sqrt{\Theta_{\mathrm{sc}} + (\Theta_z j_z)_{mm} + (\sum_{i}\Theta_{ii}\hat{j}_{ii})_{mm}} \tag{8.21}$$

$$= \frac{1}{2}\sqrt{\Theta_{\mathrm{sc}} + m\Theta_z + q_0 + m^2(q_1 - q_0)} \tag{8.22}$$

with

$$q_0 = \left(\sum_i \Theta_{ii}\hat{j}_{ii}\right)_{m=0,m=0} \tag{8.23}$$

$$q_1 = \left(\sum_i \Theta_{ii}\hat{j}_{ii}\right)_{m=\pm1,m=\pm1} \tag{8.24}$$

The difference in light shifts between $m = +1$ and $m = -1$ can be written in simpler form if the vector shift Θ_z is much smaller than the sum of scalar and quadrupole shifts:

$$\begin{aligned}\Delta_{(1)} - \Delta_{(-1)} &= \frac{1}{2}\sqrt{\Theta_{\rm sc} + q_1 + \Theta_z} - \frac{1}{2}\sqrt{\Theta_{\rm sc} + q_1 - \Theta_z} \\ &= \frac{\Theta_z}{2\sqrt{\Theta_s + q_1}} + O\left(\frac{\Theta_z^3}{(\Theta_{\rm s} + q_1)^{5/2}}\right)\end{aligned} \tag{8.25}$$

On the other hand, the difference

$$\Delta_{(1)} - \Delta_{(0)} = \frac{1}{2}\sqrt{\Theta_{\rm sc} + q_1 + \Theta_z} - \frac{1}{2}\sqrt{\Theta_{\rm sc} + q_0} \tag{8.26}$$

has, in general, no such simple form. As expected, the presence of a quadrupole term makes the calculations of light shifts more complicated. If the PNC effect manifests itself in Θ_z, and we measure the difference $\Delta_{(1)} - \Delta_{(0)}$, the quadrupole terms q_1 and q_0 enter directly; if they are produced by the strong $\Omega''^{\dagger}\Omega''$ term, any changes in intensity or polarization will directly affect the PNC measurement. If we measure the difference $\Delta_{(1)} - \Delta_{(-1)}$, the quadrupole term q_1 still enters in through the denominator of Eq.(8.25). However, as long as q_1 is much smaller than the scalar term Θ_s, it will not affect the measurement significantly.

8.2 A possible field geometry

To start, we choose the simplest geometry that would give a vector shift along z,

$$E' = E\cos kz\boldsymbol{e}_y \tag{8.27}$$

$$B'' = B\cos kz\boldsymbol{e}_x \tag{8.28}$$

With these fields we can calculate the various structural factors

$$\Theta_s = \frac{C_2}{9}B^2 \tag{8.29}$$

$$\Theta_z = \frac{1}{3}EB\mathrm{Im}(C_1) \tag{8.30}$$

$$q_1 = \frac{1}{18}B^2C_2 \tag{8.31}$$

$$q_0 = -\frac{1}{9}B^2C_2. \tag{8.32}$$

This shows that there is a vector shift due to the PNC interference term, and a scalar and quadrupole shift due to the pure M1-M1 dipole coupling. The resulting light shift $\Delta_{(1)} - \Delta_{(-1)}$ is, according to Eq.(8.25):

$$\Delta_{(1)} - \Delta_{(-1)} = \sqrt{\frac{1}{6}}\mathrm{Im}\langle E1^{\mathrm{PNC}}\rangle E \tag{8.33}$$

$\Delta_{(1)} - \Delta_{(-1)}$ can be measured with RF spectroscopy, as we will see, as the sum of the two frequencies corresponding to $\Delta_{(1)} - \Delta_{(0)}$ and $\Delta_{(0)} - \Delta_{(-1)}$. These two frequencies directly depend on the quadrupole shifts q_0 and q_1, which would produce large signal/noise issues due to fluctuations in the laser intensity etc.

We can suppress this shift by aligning B' so that the quadrupole shift j_{zz} vanishes. To see this, we look at the spherical harmonic that corresponds to it: $Y_0^2 \propto 3\cos^2\theta - 1$. This expression vanishes as $3\cos^2\theta - 1 = 0$, which is then the condition on the orientation of the magnetic field that produces j_{zz}. Since for the diagonal elements $j_{zz} \propto j_{yy} \propto j_{xx}$ (see representations of angular momentum operators, App.A.2), all diagonal elements become zero at this "magical angle" θ_c, and we are left with no quadrupole contribution from the pure M1 interaction. Any residual quadrupole shifts are then suppressed by deviations of the alignment from angle θ_c. The fields of this improved geometry are

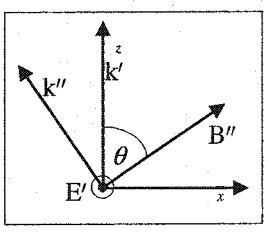

$$E' = \boldsymbol{e}_y E \cos k' z \tag{8.34}$$

$$B'' = (\sin\theta_c \boldsymbol{e}_x + \cos\theta_c \boldsymbol{e}_z) B \cos \boldsymbol{k}'' \cdot \boldsymbol{x} \tag{8.35}$$

with a propagation direction like $\boldsymbol{k}'' = k''(\cos\theta_c \boldsymbol{e}_x - \sin\theta_c \boldsymbol{e}_z)$. For the This additional B-field in the z-direction does not affect the size of the light shift $\Delta_{(1)} - \Delta_{(-1)} = \frac{\Theta_z}{2\sqrt{\Theta_s + q_1}}$, because the sum $\theta_s + q_1$ is not dependent on B fields in the z-direction (see A.2). Explicitly, we have

$$\Theta_s = \frac{C_2}{9} B^2 \tag{8.36}$$

$$\Theta_z = \sqrt{\frac{2}{9}} E B \mathrm{Im}(C_1) \tag{8.37}$$

$$q_1 = 0 \tag{8.38}$$

$$q_0 = 0, \tag{8.39}$$

and still

$$\Delta_{(1)} - \Delta_{(-1)} = \sqrt{\frac{1}{6}} \mathrm{Im}\langle E1^{\mathrm{PNC}} \rangle E. \tag{8.40}$$

8.3 Systematics

8.3.1 Resonant shifts

The systematics for this experiment are largely unexplored, and will depend on the specific geometry and size of fields. As with the even isotopes, we expect that the major systematic comes from misalignments that produce PNC-like shifts through a term $\Omega'^{\dagger}_{M1}\Omega''$, analogous to the E2 term $\Omega'^{\dagger}_{Q}\Omega''$ in the even isotopes. If the ion is slightly misplaced from the antinode of E', there will be a magnetic field $B' = i\nabla \times \boldsymbol{E}'$. If this field now has the correct phase and a component along z due to a misalignment of E' from the z-axis, B' will produce *exactly* the same type of shift in $\Omega'^{\dagger}_{M1}\Omega''$ as E' in the PNC-shift $\Omega'^{\dagger}\Omega''$: *Whatever can interfere with E' will interfere*

with this spurious B' field. This shift is, similarly to the E2 case, only suppressed by two small parameters[1]: One is the misplacement of the antinode from the ion position, which will, in general cause spurious light of an unknown phase; the other is a misalignment from its original direction of polarization. Worse than for E2, where the different structure of this shift allowed further reduction by off-resonant light shifts (see Section 7.10.1), here the vector structures of PNC-signal and fake signal are identical (both have dipole-dipole structure). On the other hand, compared to the even isotopes, these types of systematics are suppressed by the factor f, which brings them down to a level comparable to that of the E2 term in the even isotopes, depending on the actual size of f. Much will therefore depend on the precise size of the M1 amplitude, which will hopefully be calculated in the near future.

8.3.2 Off-resonant shifts

Even though the $F = 0 \leftrightarrow F = 1$ transition is E2-forbidden, all other combinations ($F = 0 \leftrightarrow F = 2, 3$) of transitions between hyperfine levels are E2-allowed. These couplings are off-resonantly driven by E'' and can produce corresponding light shifts. Also, if E' has an imperfect spatial phase, it can produce an E2 amplitude and there will be a spurious interference term. We can estimate the characteristic size of these off-resonant shifts:

$$\frac{\Omega''^{\dagger}_{E2}\Omega''_{E2}}{\delta_L} \simeq \left(\frac{E''}{E'}\right)^2 \eta^2 \frac{\Omega'^2}{\delta_L} \tag{8.41}$$

$$\frac{\Omega'^{\dagger}_{E2}\Omega''_{E2}}{\delta_L} \simeq \alpha'\delta\frac{E''}{E'}\eta^2\frac{\Omega'^2}{\delta_L}, \tag{8.42}$$

where, δ_L is the detuning from the nearest hyperfine level, $\eta = \langle E2\rangle/\langle E1^{\mathrm{PNC}}\rangle$ is a ratio of matrix elements, and Ω' gives the characteristic size of the PNC light shift. δ is the spatial phase error that causes E' to produce an E2 amplitude, and α' is the misalignment of polarization of E', which is required to give a shift along z, as shown

[1] Again, assuming the two parameters are experimentally independent

below.

Thus, the most worrisome E2 shift for the odd isotopes, Eq.8.42, looks much like the off-resonant E2 shift on Page 159. However, because presently the detuning is given by the large hyperfine splitting ($\sim$100 MHz) rather than the light-induced shift, the reduction factor Eq.7.51 that applies here is larger by more than two orders of magnitude. Also, the same trade-off between laser frequency stability and systematic shifts applies: off-resonant shifts are reduced if we decrease the size of E''. On the other hand, then the resonant shifts also decrease, and the laser has to be more stable to let the PNC measurement remain to be independent of its frequency.

For concreteness, let us assume that $\frac{E''}{E'} \simeq \frac{1}{1000}$, $\eta \simeq 10^7$, $\delta_L \simeq 100\,\mathrm{MHz}$, and $\Omega' \simeq 1\,\mathrm{Hz}$. We then find that the interference term is on the order of $\frac{\Omega'^{\dagger}_{E2}\Omega''_{E2}}{\delta_L} \simeq \alpha'\,\delta \times 1000\,\mathrm{Hz}$. Thus $\alpha'\,\delta$ must be $< 10^{-5}$ for a 1% PNC measurement. The misalignment factor α' appears because the vector part of this shift will be proportional to $c_1(\boldsymbol{\nabla} \times \boldsymbol{E'}) \times \boldsymbol{B''} + c_2((\boldsymbol{\nabla} \times \boldsymbol{E'}) \cdot \boldsymbol{\nabla})\boldsymbol{E''}$, which points in the y-direction for the field geometry considered above, making it orthogonal to the PNC shift.

8.4 RF spectroscopy

In this section we explore some initial ideas as to the possibilities of RF-spectroscopy in a three-level system like $F = 1$, focusing on the $I = 3/2$ isotopes where $F = 1$ is the ground state. Mainly, we explain a variation of spin-pumping, RF-spin flips and spin-detection that should yield the vector and spin quadrupole shift in the $S_{1/2}, F = 1$ state simultaneously. For the following section we will label these two shifts v and q as explained in Figure 8.1.

To cool and observe a single odd isotope ion we now need to consider the hyperfine structure. For the S-P transition both ground state levels have to be connected to $\mathrm{P}_{1/2}, F = 1$ (we could also choose $F = 2$). The groundstates have a splitting of about 8 GHz, which can be bridged by a resonant EOM modulator at either 4 or 8 GHz.

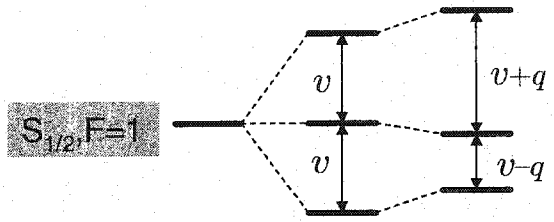

Figure 8.1: Vector and quadrupole spin shifts in $F = 1$.

From $P_{1/2}, F = 1$ decays to $D_{3/2}, F = 0, 1, 2$ are possible; however, off-resonant excitations to $P_{1/2}, F = 2$ can result in decay into $D_{3/2}, F = 3$. Below saturation the off-resonant transition rate is smaller than the resonant transition rate by a factor of $\frac{\Gamma^2}{\delta^2}$, where δ is the hyperfine splitting of the $P_{1/2}$ state with line width Γ. This rate is still in the kHz range so that the ion would get pumped very quickly into the $F = 3$ state. Thus, repumping from all four $D_{3/2}$ levels is necessary. First we prepare the ion in the $F = 1, m_F = 0$ state. This can be done by using linearly polarized blue light driving only $\Delta m = 0$ transitions, connecting both ground state hyperfine levels to the $P_{1/2}, F = 1$ level. Because of the Clebsch-Gordan relation

$$(j0; 10|j0) = 0 \tag{8.43}$$

the $F = 1, m_F = 0$ ground state will be the uncoupled. Unfortunately, so are the $F = 2, m_F = \pm 2$ ground states. A way has to be found to destabilize these unwanted dark states such that $F = 1, m_F = 0$ is the only uncoupled state. This could be done, for example, by connecting them to the $P_{1/2}, F = 2$ state, or with an RF field resonant with the Zeeman splitting in the $F = 2$ ground states, acting to cause spin transitions. The latter method relies on the fact that the two hyperfine ground states have slightly different Zeeman splittings so that the $F = 1$ ground state won't be affected by the RF field. Of course the ion can still decay into the D hyperfine levels, so that repumping light has to be present.

With the ion in a definite spin state (given by population vector $p_i = (0, 1, 0)$)

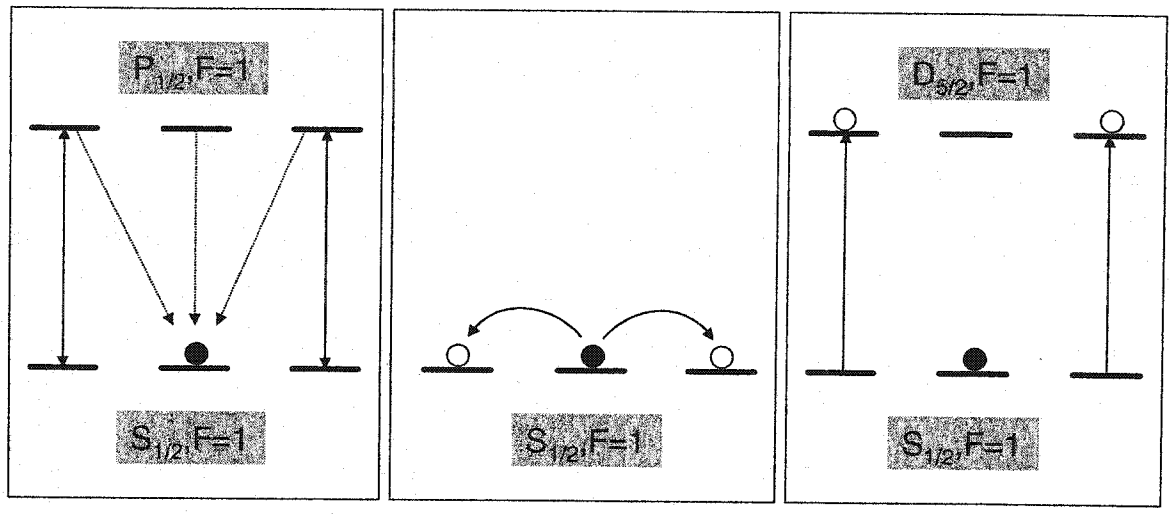

Figure 8.2: Possible scheme for RF spectroscopy in $I = 3/2$ isotopes. Left figure shows pumping into the $m_F = 0$ state. Middle figure shows RF interaction that will, on resonance, transfer the population to the outer levels. Right figure shows direct shelving to the $D_{5/2}$ state with an optical π-pulse, exploiting the fact that the $m_F = 0 \leftrightarrow m_F = 0$ amplitude vanishes.

we can now apply RF pulses, with the goal of measuring the quadrupole shift q and the vector splitting ω. If there is no quadrupole, the system behaves like a classical rotating spin, and the solutions to its time evolution are given by the Wigner formula (see Section 3.5). On resonance at ω, a $\pi/2$ pulse will produce the population vector $p_f = (1/2, 0, 1/2)$. Moving away from resonance, the population of $m_F = 0$ will increase, forming a resonance line shape that looks similar to that of a two-state system (see Figure 8.3). The simplest though not necessarily easiest way to observe this resonance line is by direct shelving to the $D_{5/2}, F = 1$ state. If we tune a laser to this frequency that drives only $\Delta m = 0$ transitions, only the outer spin levels will be connected and, with an optical π pulse, driven up into the shelving state. In this case there is an almost perfect detection efficiency of the $m_F = 0$ state by shelving. Even if the technical requirements for driving optical π pulses are not all fulfilled, one can still get a 50% correlation as long as the laser can be tuned reliably to this transition.

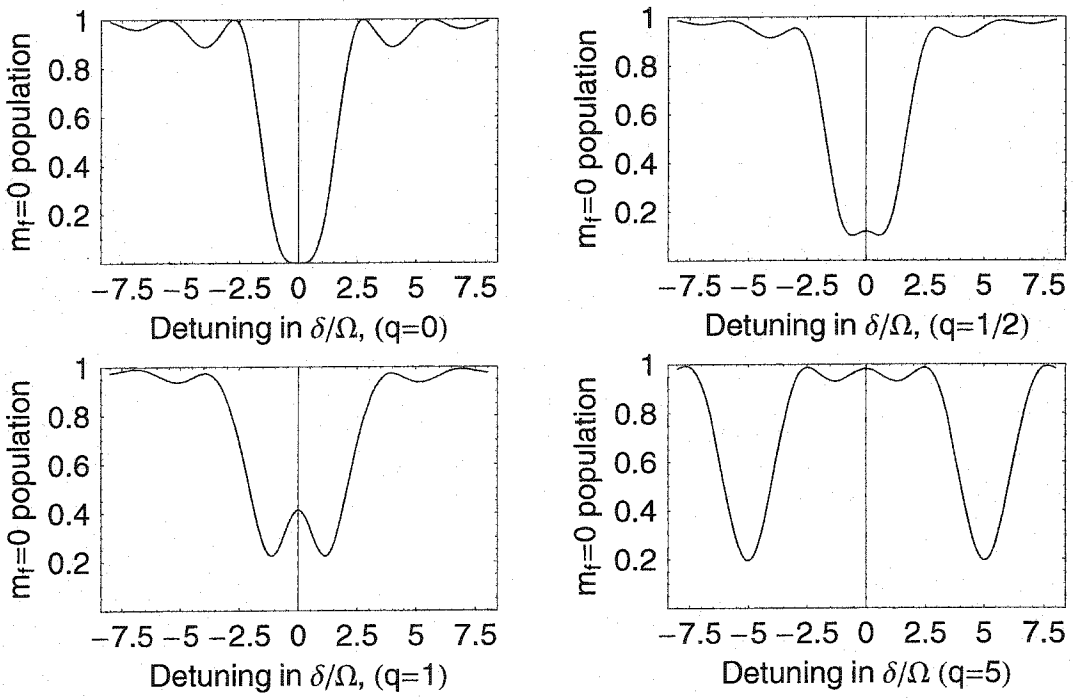

Figure 8.3: Three-level resonances with various quadrupole shifts ($q = 0, 1/2, 1, 5\,\Omega$).

If a quadrupole shift is present, solutions to the equations of motion can be obtained numerically. If the quadrupole shift is much larger than the Rabi frequency, instead of the central resonance dip two separate dips appear. In this limit, the three-state system splits into two disjoint two-state systems with Rabi frequencies $\Omega_{01} = \sqrt{2}\Omega$ and resonance frequencies $\omega \pm q$. Thus from the location of the two peaks both ω and q can be determined. Off-resonant effects will alter the location of the two peaks from $\omega \pm q$ and lead to a systematic under-estimation of q. This problem can be corrected for by comparison with the numerical solution in analogy to Section 6.2.1.

In the opposite limit, the single resonance at ω gains an altered line shape in which the peak begins to split. The alteration is symmetrical about ω so that any symmetric fit to this resonance should still just give the vector shift ω.

8.5 Measurement of the M1 transition

It will be important to measure the M1 amplitude between $6S_{1/2}$ and $5D_{3/2}$. One way to do this is to use an interference method, much like doing an actual PNC experiment: For example, one could use the even isotope where both E2 and M1 are allowed between $6S_{1/2}$ and $5D_{3/2}$. Then, in the presence of an optical magnetic field $\boldsymbol{B'}$, there will be a vector shift that has the same structure as Eq.(7.23):

$$\Omega_{M1}'^{\dagger}\Omega'' = \frac{1}{2\sqrt{10}}\frac{1}{\hbar^2}\langle M1\rangle\langle E2\rangle\,(2(\boldsymbol{B'}\cdot\boldsymbol{\nabla})\boldsymbol{E''} + \boldsymbol{B'}\times(\boldsymbol{\nabla}\times\boldsymbol{E''}))\cdot\boldsymbol{j} \qquad (8.44)$$

With the M1 transition 1000-10000 times larger than the PNC amplitude, this would give kHz-sized vector shifts that are easily measurable to a few percent even with the current precision of RF spectroscopy. However, there is in general a much larger E2 vector shift due to $\Omega_{E2}'^{\dagger}\Omega''$. Using larger static B fields or the tensor shift discussed in Section 8.6 provide ways of discriminating against such pure E2 shifts.

One would still have to calibrate the M1 measurement. This could be done by simultaneously measuring off-resonant light shifts and using known matrix elements

to obtain the size of $\boldsymbol{B'}$ at the site of the ion. Alternatively, the ratio of M1 and E2 shifts would calibrate M1 in terms of the more reliably known E2 matrix elements.

8.6 Using the tensor spin shift for a PNC measurement

The PNC interference term does not only produce a vector shift, but also a tensor (quadrupole) spin shift q, as can be seen from Eq.(8.7). We therefore have an alternative PNC observable, provided there is a good way to measure the spin quadrupole shift in the F=1 ground state. Such an experiment looks very promising, because it discriminates against all systematic vector shifts. For example, the spin quadrupole shift is not altered by magnetic field changes as magnetic fields can only produce spin *vector* shifts. More importantly, all off-resonant shifts have highly suppressed tensor shifts. The argument is the same argument as in Section 6.1.3. The underlying spin structure of the off-resonant shifts is given by the $j = 1/2$ ground state, which doesn't have quadrupole structure. Because an off-resonant coupling to state P sums over all of P's hyperfine components, no higher multipole spin shifts can be introduced. This is strictly true only if the hyperfine components are degenerate. In reality small quadrupole shifts exist, but they are suppressed by a factor $\omega_{\text{hfs}}/\omega_{\text{optical}}$, where ω_{hfs} is the hyperfine splitting and ω_{optical} is the frequency of the off-resonant light. Furthermore, preliminary studies indicate that the shifts discussed in Section 8.3.2have no quadrupole (tensor) part.

An interesting, simplified experiment to consider would be to combine E' and B'' into a *single* beam having a small degree of circular polarization, in which B'' comes from the small component creating the circular polarization. Reversing the sense of circular polarization reverses the tensor PNC shift, while monitoring the off-resonant vector light shift provides a way of guaranteeing the reversal is exact with high sensitivity.

Chapter 9

FUTURE DIRECTIONS

9.1 Ion Clock

Besides a superior measurement of PNC, an odd barium isotope like $^{137}Ba^{+}$ is a very viable candidate for an accurate single-ion optical clock. The idea of such clocks is to lock a very stable optical laser to a narrow resonance of a single ion. In all cases the transition on the narrow resonance is observed by the absence of fluorescence on a strong transition, in other words by electron shelving.

In general, the precision of a clock is determined by its quality factor $\frac{\nu}{\Delta\nu}$, which is the inverse of the relative frequency uncertainty. When deriving a frequency from atoms, $\Delta\nu$ is given by the line width of the atomic transition, and ν is the resonance frequency. It is therefore natural to try and use very high frequencies in combination with narrow line widths.

If we want to directly read out the laser frequency by counting, we are limited to the microwave regime ($<10^{10}$ Hz) because no faster counting electronics exists. Recently, however [16], femtosecond lasers have been used to create an "optical frequency comb", which allows the accurate conversion of optical frequencies (10^{15} Hz) to the microwave regime. Thus optical clocks have become feasible and are now rivalling the most accurate microwave clocks [5].

Ion traps present an ideal implementation of atomic clocks because of the virtual absence of line broadening mechanisms, like first-order Doppler broadening or line widths given by limited observation time. Furthermore, if we use a single ion, all inter-ion broadening effects are absent. Because of sideband cooling, the ion can be

prepared with very low kinetic energies, which reduces the second-order Doppler effect to negligible values.

Still, a trapped ion is subject to external perturbations that can alter its resonance and limit the clock accuracy. The most problematic perturbations come from magnetic fields which can cause Zeeman shifts, and from static and ac electric quadrupole trap fields causing quadrupole spin shifts. For example, the currently most precise ion clock is based on $^{199}Hg^+$, which suffers from both of these shifts [5], though in principle not the Zeeman shift.

The $6S_{1/2}$ to $5D_{3/2}$ transition in $^{137}Ba^+$ is very narrow with a line width of only 2 mHz. Furthermore, the $F = 2, m_F = 0 \Leftrightarrow F' = 0, m_{F'} = 0$ transition is not affected by electric quadrupole shifts nor by linear Zeeman effects. Quadratic Zeeman shifts are still present, but can be made negligible in small fields.

In addition, a recent paper [18] shows that the $6S_{1/2}$ to $5D_{3/2}$ transition in Ba^+ has a very large dependence on the fine structure constant α. This makes a clock based on Ba^+ a useful tool for an $\dot{\alpha}/\alpha$ experiment where one determines whether α is changing with time. In such an experiment one compares two clocks based on atomic resonances that have a different dependence on α. Motivation for an $\dot{\alpha}$ search comes from the fact that time variation of fundamental constants is suggested by several contemporary cosmological theories, such as the Inflationary Model. Also, a recent analysis of astrophysical spectral data [65] indeed suggests that α was different in the past, even though geophysical data disagrees [24].

9.2 Measurement of the quadrupole moment of $5D_{3/2}$

As mentioned in the previous section, one of the major problems of ion-based optical clocks is the presence of quadrupole spin shifts, which can occur if levels have an electronic quadrupole moment that interacts with electric quadrupole fields created by the trap. Electronic quadrupole moments can be calculated approximately, but

have never been measured directly. This section presents a scheme that enables the direct measurement of such quadrupole moments by using RF spectroscopy.

9.2.1 Idea and measurement

The quadrupole moment of the $5D_{3/2}$ state interacts with any applied field gradients the ion sees, even though ac gradients will always average out in a measurement. Dc gradients can be introduced simply by applying a common dc voltage to the trap. The resulting spin shifts have quadrupole structure, as shown explicitly later. This means that the shifts are independent of the sign of m, and observable shifts of resonances occur only between the $m = \pm 1/2 \Leftrightarrow m = \pm 3/2$ states. This means that our current setup, sensitive only to the transition between the innermost m-levels, needs to be altered to look much like the setup of the first observations of RF resonances [55]. Briefly, we need to prepare the ion in the outermost spin states with a red laser that drives only $\Delta m = 0$ transitions. RF transitions then populate the innermost m-levels and with a $\Delta m = 0$ probe pulse and subsequent shelving these transitions can be detected.

In order to measure the quadrupole moment we also have to know the size of the electric field gradients at the site of the ion. This information can be extracted by measuring the change in the secular frequencies of the ion motion as the dc field is turned on. This in turn can be done by trying to parametrically excite the secular motion of the ion by RF fields. When the RF frequency matches a secular frequency, enormous ion heating takes place and a drop in the ion fluorescence can be observed. In order to relate the field gradients obtained in this way to the field gradient in the coordinate system of the magnetic field, one also has to know the relative orientation between these two coordinate systems. In our current ring trap the principal axes are not well-known because of unknown trap tilt angles and asymmetries. A better trap for such a measurement would probably be an endcap trap as shown in Figure 9.1. Here one of the principal axes, z', is well-defined by the position of the two endcaps,

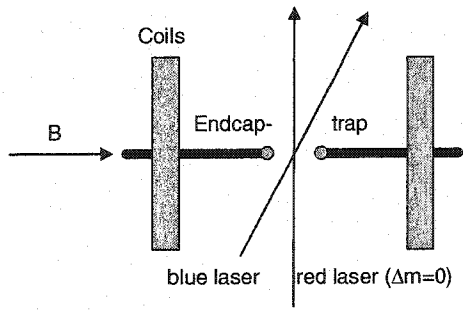

Figure 9.1: Possible setup for a quadrupole measurement.

and the other two can be arbitrarily defined as long as they are perpendicular to each other and to z'.

9.2.2 Size of the quadrupole shift

For this experiment it is crucial to know the relative orientation of the principal axes of the trap (coordinate system Σ') to the orientation of the magnetic field (coordinate system Σ). z' is well-defined by the position of the two endcaps, and x' and y' can be arbitrarily chosen to the extend the system is azimuthally symmetric. We choose x' to coincide with x, and define α as the angle between z' and z. If we then measure a quadrupole shift in Σ' of

$$(\nabla \boldsymbol{E})' = \begin{pmatrix} E_g & 0 & 0 \\ 0 & E_g & 0 \\ 0 & 0 & -2E_g \end{pmatrix}, \tag{9.1}$$

where $E_g = \partial_{x'} E_{x'} = \partial_{y'} E_{y'} = -1/2 \partial_{z'} E_{z'}$, then in Σ the gradient field is given by a rotation about the x-axis by

$$(\nabla \boldsymbol{E}) = \begin{pmatrix} E_g & 0 & 0 \\ 0 & E_g \cos(\alpha)^2 - 2E_g \sin(\alpha)^2 & 3E_g \cos(\alpha)\sin(\alpha) \\ 0 & 3E_g \cos(\alpha)\sin(\alpha) & -2E_g \cos(\alpha)^2 + E_g \sin(\alpha)^2 \end{pmatrix} \tag{9.2}$$

The quadrupole shift of the $5D_{3/2}$ levels is given by

$$\Delta_m = \langle 5D_{3/2}, m|W|5D_{3/2}, m\rangle \tag{9.3}$$

with

$$W = \frac{e}{6}\sum_{ij} Q_{ij}(\nabla \boldsymbol{E})_{ij}, \tag{9.4}$$

$$Q_{ij} = 3x_i x_j - \delta_{ij}x^2 \tag{9.5}$$

where Q_{ij} is the quadrupole moment cartesian tensor and $(\nabla \boldsymbol{E})_{ij}$ a component of the electric field derivative tensor in Σ. When rewriting W in spherical coordinates and plugging in the expression for $\nabla \boldsymbol{E}$, the problem can be split into an angular and radial part:

$$W = \frac{eE_g}{6}r^2 * W_{\text{ang}} \tag{9.6}$$

The matrix element $\frac{eE_g}{6}\langle 5D_{3/2}|r^2|5D_{3/2}\rangle$ is an m-independent factor and hard to calculate accurately; it determines the overall size of the quadrupole shift and will be estimated below. W_{ang} contains the quadrupole structure of the shifts and can its matrix elements can be evaluated, for example, by decomposing the state $|j, m\rangle$ into it's $|l, m\rangle$ components and then performing the angular integral over the corresponding spherical harmonics. For the two upper levels we have (omitting the spin states)

$$|j = 3/2, m = 3/2\rangle = -\frac{1}{\sqrt{5}}|l = 2, m = 1\rangle + \frac{2}{\sqrt{5}}|l = 2, m = 2\rangle \tag{9.7}$$

$$|j = 3/2, m = 1/2\rangle = -\sqrt{\frac{2}{5}}|l = 2, m = 0\rangle + \sqrt{\frac{3}{5}}|l = 2, m = 1\rangle \tag{9.8}$$

and for $\Delta_m^{\text{ang}} = \langle j = 3/2, m|W_{\text{ang}}|j = 3/2, m\rangle$ we find

$$\Delta_{\pm 3/2}^{\text{ang}} = -\frac{3}{5}(1 - 3\cos^2\alpha) \tag{9.9}$$

$$\Delta_{\pm 1/2}^{\text{ang}} = +\frac{3}{5}(1 - 3\cos^2\alpha) \tag{9.10}$$

The shifts are independent of the sign of m, as expected from a quadrupole shift, and move the $\pm 1/2$ levels relative to the $\pm 3/2$ levels. As a result, the resonance

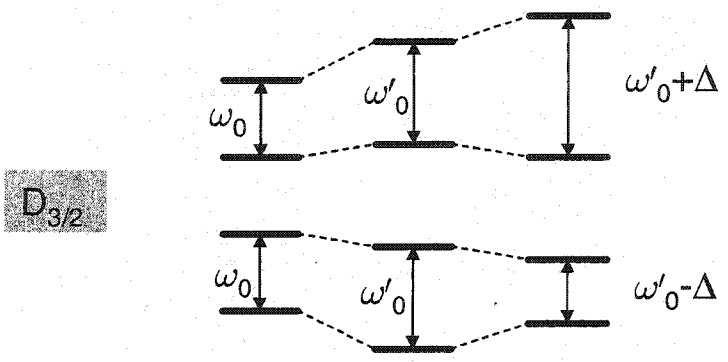

Figure 9.2: Level shifts in the quadrupole measurement.

$\omega_1 = (m = +3/2 \leftrightarrow m = +1/2)$ will be reduced by $\Delta = \frac{6}{5}(1 - 3\cos^2\alpha)$ and the resonance $\omega_2 = (m = -3/2 \leftrightarrow m = -1/2)$ will be decreased by Δ. Suppose now that we have an initial Zeeman splitting ω_0. When turning on the quadrupole field, the magnetic field may systematically change to give a new splitting ω_0' (see Figure 9.2). The quadrupole measurement then requires measuring $\omega_1 = \omega_0' - \Delta$ and $\omega_2 = \omega_0' + \Delta$ simultaneously. ω_0' drops out in the difference $\omega_1 - \omega_2$ of the two new resonances and one has a measurement that is not sensitive to systematic magnetic field changes. It is merely necessary to keep the field stable enough so that it doesn't broaden the resonances intolerably. By comparing $\omega_1 + \omega_2$ to $2\omega_0$ one can evaluate any systematic field shift.

It is also obvious that a design would be preferable where $\alpha = 0$, i.e. the magnetic field along the endcaps, since then Δ is, to first order, independent of α.

The radial part $\Delta^{\text{rad}} = \frac{eE_g}{6}\langle 5D_{3/2}|r^2|5D_{3/2}\rangle$ can be approximately evaluated by using the effective quantum number for $5D_{3/2}$ in Ba^+, $n^* = 2.41$, and using hydrogen radial wavefunctions. This results in $\Delta^{\text{rad}} \simeq \frac{eE_g}{6} \times 9a_0^2$, where a_0 is the Bohr radius. $E_g = 2f * Ur_0^{-2}$, where f is a geometric voltage reduction factor and r_0 is the distance between the endcaps. For $f = 1/8$, $r_0 = 0.5$ mm, and together with the maximal angular factor $\Delta^{\text{ang}} \simeq 2$ we get a shift of about $\Delta = 2$Hz/Volt. When

the same calculation is performed with radial wavefunctions derived from the Baates-Damgaard approximation [57, p.236f], we get about twice the result as compared with the hydrogenic radial functions.

9.2.3 Calibration of the electric field

One can determine the field gradient in an RF trap from measuring the corresponding secular frequency: The secular frequencies are given by

$$\omega_r = \beta_r \frac{\Omega}{2}, \omega_z = \beta_z \frac{\Omega}{2}, \tag{9.11}$$

where Ω is the trap drive frequency, and β_r, β_z are the characteristic exponents of the solution of Mathieu's equations. From the pseudopotential approximation, we find

$$\beta = a + \frac{q^2}{2} \tag{9.12}$$

(with indices z or r), where

$$a_z = -2a_r = \frac{-8efU}{mr_0\Omega^2}, q_z = -2q_r = \frac{-4efV}{mr_0\Omega^2} \tag{9.13}$$

Here, V is the ac voltage, and U the applied dc part that produces the quadrupole shift.

One would measure the difference between two secular frequencies, one with U on and one without U. Choosing the axial direction, we can write $\beta_z'^2 = a_z + q_z^2/2$ when U is on and $\beta_z^2 = q_z^2/2$ when U is off. Then the difference in the corresponding secular frequencies is

$$\omega_z'^2 - \omega_z^2 = \frac{\Omega^2}{4}(\beta_z'^2 - \beta_z^2) = a_z \frac{\Omega^2}{4} = \frac{2eU}{mr_0^2} \tag{9.14}$$

On the other hand, the same voltage U gives rise to a quadrupole potential

$$\phi = \frac{U}{r_0^2}(r^2 - 2z^2) \tag{9.15}$$

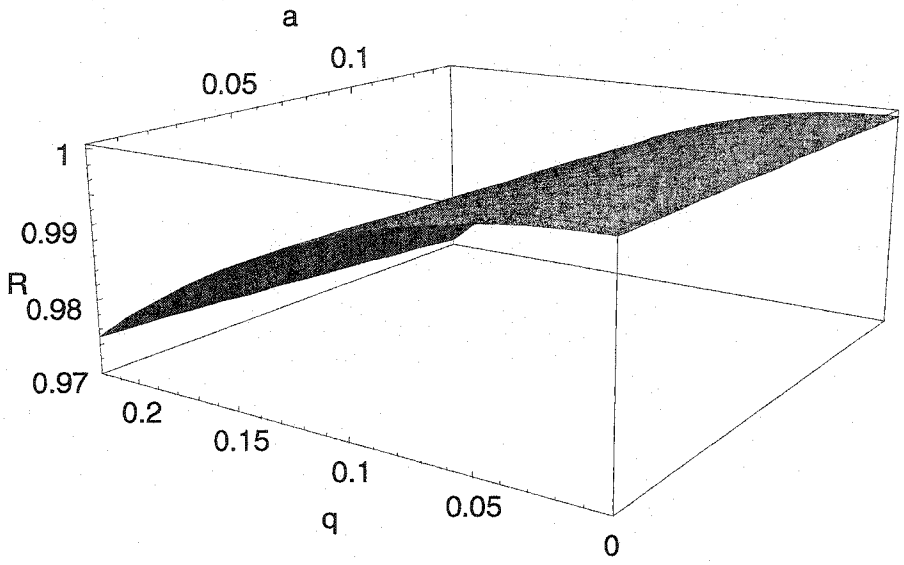

Figure 9.3: Calculated relative correction of electric field calibration due to deviations from the pseudopotential approximation.

and a field gradient

$$\nabla \boldsymbol{E} = E_g \begin{pmatrix} 1 & 0 & 0 \\ 0 & 1 & 0 \\ 0 & 0 & -2 \end{pmatrix}, E_g = \frac{2U}{r_0^2} \tag{9.16}$$

Finally, by combining this with (9.14), E_g can be expressed in terms of the difference in the squares of the secular frequencies:

$$E_g = \frac{m}{e}(\omega_z'^2 - \omega_z^2) \tag{9.17}$$

One complication arises from the fact that Eq.(9.12) is only approximately true. To be exact, we can write

$$\beta_z'^2 = a_z + q_2^2/2 + C_1(a,q) \text{ for U on} \tag{9.18}$$

$$\beta_z^2 = q_2^2/2 + C_2(a,q) \text{ for U off} \tag{9.19}$$

where C_1 and C_2 are correction factors to the pseudopotential approximation. Then

$$E_g = R(a,q)\frac{m}{e}(\omega_z'^2 - \omega_z^2) \tag{9.20}$$

with reduction factor

$$R(a,q) = \frac{a}{a + C_1(a,q) - C_2(a,q)} \tag{9.21}$$

$R(a,q)$ can be calculated using the recursion relations Eq.(3.11) that come from solving Mathieu's equation (see Figure 9.3). To apply this correction in the experiment, one has to determine a and q from (9.12) and (9.11).

Appendix A

THEORETICAL SUPPLEMENT

A.1 Calculation of reduced matrix elements from radial integrals

Sometimes in the literature the radial integral between two atomic states is given; one needs, however, the reduced dipole matrix element between the corresponding two states. The conversion can be done with the help of an important result from angular momentum theory [57, 4.175]. If an operator T^k commutes with $\boldsymbol{J}_2$ in the representation $|J_1 J_2 J M\rangle$, we can write for the reduced matrix elements:

$$\langle \gamma J_1 J_2 J || T^k || \gamma' J_1' J_2 J' \rangle =$$
$$(-1)^{J_1+J_2+J'+k} \langle \gamma J_1 || T^k || \gamma' J_1' \rangle \sqrt{(2J+1)(2J'+1)} \begin{Bmatrix} J_1 & J & J_2 \\ J' & J_1' & k \end{Bmatrix} \tag{A.1}$$

where the expression in curly brackets is a $6j$-symbol.

Since the dipole operator $D = -er^{(1)}$ commutes with the spin of the nucleus, we can apply this identity to expressing reduced hyperfine matrix elements in terms of their underlying reduced matrix elements $\langle \gamma LSJ || D || \gamma' L' S J' \rangle$:

$$\langle \gamma JIF || D || \gamma' J' I F' \rangle =$$
$$(-1)^{J+I+F'+1} \langle \gamma LSJ || D || \gamma' L' S J' \rangle \sqrt{(2F+1)(2F'+1)} \begin{Bmatrix} J & F & I \\ F' & J' & 1 \end{Bmatrix} \tag{A.2}$$

$D = er^{(1)}$ also commutes with the spin of the electron, so we can continue to write

$$\langle \gamma LSJ || D || \gamma' L' S J' \rangle =$$
$$(-1)^{L+S+J'+1} \langle \gamma L || D || \gamma' L \rangle \sqrt{(2J+1)(2J'+1)} \begin{Bmatrix} L & J & S \\ J' & L' & 1 \end{Bmatrix} \tag{A.3}$$

Table A.1: Factors to convert radial integrals to reduced dipole matrix elements in the $|lsjm\rangle$ basis.

final state	$S_{1/2}$	$D_{3/2}$
$P_{1/2}$	$-\sqrt{\frac{2}{3}}$	$-\frac{2}{\sqrt{3}}$
$P_{3/2}$	$-\frac{2}{\sqrt{3}}$	$-\frac{2}{\sqrt{15}}$
$F_{5/2}$	0	$\sqrt{\frac{3}{5}}$

Finally, the reduced matrix elements of orbital angular momentum can be written as

$$\langle \gamma L||D||\gamma' L\rangle = -eR^{\gamma L}_{\gamma' L'}\langle L||n||L'\rangle, \tag{A.4}$$

where the radial integral is defined as

$$R^{\gamma L}_{\gamma' L'} = \int R_{\gamma L} R_{\gamma' L'} r r^2 dr \tag{A.5}$$

and $\langle L||n||L'\rangle$ is the reduced matrix element of the unit vector,

$$\langle L||n||L'\rangle = (-1)^{\frac{1}{2}(3L+L'+1)}\sqrt{L_{\max}}, L' = L \pm 1 \tag{A.6}$$

In Table A.1 we use these identities to calculate the factors for the relevant states in the even isotopes.

A.2 Representations of j and j_{ik}

A.2.1 j=1

The vector and tensor representations of j are given by

$$\boldsymbol{j} = \left(\begin{pmatrix} 0 & \frac{1}{\sqrt{2}} & 0 \\ \frac{1}{\sqrt{2}} & 0 & \frac{1}{\sqrt{2}} \\ 0 & \frac{1}{\sqrt{2}} & 0 \end{pmatrix} \begin{pmatrix} 0 & \frac{-i}{\sqrt{2}} & 0 \\ \frac{i}{\sqrt{2}} & 0 & \frac{-i}{\sqrt{2}} \\ 0 & \frac{i}{\sqrt{2}} & 0 \end{pmatrix} \begin{pmatrix} -1 & 0 & 0 \\ 0 & 0 & 0 \\ 0 & 0 & 1 \end{pmatrix} \right) \tag{A.7}$$

$$j_{ik} = \begin{pmatrix} \begin{pmatrix} -\frac{1}{6} & 0 & \frac{1}{2} \\ 0 & \frac{1}{3} & 0 \\ \frac{1}{2} & 0 & -\frac{1}{6} \end{pmatrix} & \begin{pmatrix} 0 & 0 & \frac{-i}{2} \\ 0 & 0 & 0 \\ \frac{i}{2} & 0 & 0 \end{pmatrix} & \begin{pmatrix} 0 & \frac{-1}{2\sqrt{2}} & 0 \\ \frac{-1}{2\sqrt{2}} & 0 & \frac{1}{2\sqrt{2}} \\ 0 & \frac{1}{2\sqrt{2}} & 0 \end{pmatrix} \\ \begin{pmatrix} 0 & 0 & \frac{-i}{2} \\ 0 & 0 & 0 \\ \frac{i}{2} & 0 & 0 \end{pmatrix} & \begin{pmatrix} -\frac{1}{6} & 0 & -\frac{1}{2} \\ 0 & \frac{1}{3} & 0 \\ -\frac{1}{2} & 0 & -\frac{1}{6} \end{pmatrix} & \begin{pmatrix} 0 & \frac{i}{2\sqrt{2}} & 0 \\ \frac{-i}{2\sqrt{2}} & 0 & \frac{-i}{2\sqrt{2}} \\ 0 & \frac{i}{2\sqrt{2}} & 0 \end{pmatrix} \\ \begin{pmatrix} 0 & \frac{-1}{2\sqrt{2}} & 0 \\ \frac{-1}{2\sqrt{2}} & 0 & \frac{1}{2\sqrt{2}} \\ 0 & \frac{1}{2\sqrt{2}} & 0 \end{pmatrix} & \begin{pmatrix} 0 & \frac{i}{2\sqrt{2}} & 0 \\ \frac{-i}{2\sqrt{2}} & 0 & \frac{-i}{2\sqrt{2}} \\ 0 & \frac{i}{2\sqrt{2}} & 0 \end{pmatrix} & \begin{pmatrix} \frac{1}{3} & 0 & 0 \\ 0 & -\frac{2}{3} & 0 \\ 0 & 0 & \frac{1}{3} \end{pmatrix} \end{pmatrix} \tag{A.8}$$

A.3 Conversion between spherical and cartesian tensors

In this thesis we are concerned with matrix elements that contain the interaction energy between the potential due to the field and the charge density of the outer electron. Classically this could be written as

$$W = \int \rho(\boldsymbol{x})\Phi(\boldsymbol{x})d^3x \tag{A.9}$$

For optical transitions the wavelength of the field is large compared to the size of the electron's wave function, and therefore the spatial variations of the potential are small. We can therefore expand the interaction around $\boldsymbol{x} = 0$ in terms of the field and the potential, yielding the Taylor expansion

$$W = q\Phi(0) - \boldsymbol{d}\cdot\boldsymbol{E}(0) - \frac{1}{2}\sum_{ij} Q_{ij}\,\partial_i E_j(\boldsymbol{r})|_{\boldsymbol{r}=0} + \ldots \tag{A.10}$$

This sum is made of scalar products of two cartesian tensors, with growing rank. Because $|\frac{1}{E}\frac{dE}{dx}|a_0 \ll 1$, the terms get progressively smaller. In an atom (or ion) the first term averages to zero, and the second term is the electric dipole term, corresponding to an E1 transition. The third term corresponds to an electric quadrupole (E2) transition.

We can write the first three terms using irreducible tensors (i.e., tensors that can't be broken down into terms with different properties under rotation). The scalar and vector part are trivially irreducible. The second-rank tensors in the third term are, in general, reducible; the conditions for its irreducibility are that it is symmetric and traceless. However, in our case the condition $\boldsymbol{\nabla} \cdot \boldsymbol{E} = 0$ makes the tensor $\partial_i E_j$ naturally irreducible. Also, the reducible tensor $x_i x_j$ can be replaced by its irreducible form $x_i x_j - \delta_{ij} \frac{1}{3} r^2$ without changing the sum in Eq.(A.10) because $\sum_{ij} \delta_{ij} \partial_i E_j = 0$. Thus we end up with the multipole expansion (see [33])

$$W = q\Phi(0) - \boldsymbol{d} \cdot \boldsymbol{E}(0) - \frac{1}{2} \sum_{ij} Q_{ij} \partial_i E_j(0) + ... \tag{A.11}$$

with

$$d_i = e x_i \tag{A.12}$$

$$Q_{ij} = e(x_i x_j - \frac{1}{3} r^2 \delta_{ij}) \tag{A.13}$$

The advantage of writing the series with irreducible terms is that then for each cartesian tensor there is a spherical counterpart, and many processes can be understood more easily in terms of spherical tensors. In the following we therefore show how to do this translation in a consistent way.

The spherical tensor corresponding to the cartesian unit vector $\boldsymbol{n}$ has to transform like a spherical harmonic with $l = 1$:

$$n_q^{(1)} \propto Y_l^q(\boldsymbol{n}) = \sqrt{\frac{3}{4\pi}} \begin{cases} e^{-i\phi} \sin\theta \\ \cos\theta \\ -e^{i\phi} \sin\theta \end{cases} \tag{A.14}$$

Substituting cartesian coordinates and requiring the normalization $\sum_q |n_q^{(1)}|^2 = 1$ we find

$$n_0^{(1)} = n_z, n_{\pm 1}^{(1)} = \frac{\mp n_x - i n_y}{\sqrt{2}} \tag{A.15}$$

We can now substitute any vector for $\boldsymbol{n}$ to find its spherical components. For the electric field, for example, we have

$$\begin{aligned} E^{(1)}_{\pm 1} &= \frac{1}{\sqrt{2}}(\mp E_x - iE_y) \\ E^{(1)}_{0} &= E_z \end{aligned} \tag{A.16}$$

We can rewrite the dipole moment $\boldsymbol{d} = e\boldsymbol{x}$ and the nabla operator $\boldsymbol{\nabla}$ in the same way.

The interaction terms then involve various products of these tensors. While a cartesian tensor product simply involves a combination of scalar and direct products, spherical tensors products have to be constructed using the transformation properties of spherical harmonics. In general, the product for two spherical tensors $A^{(k1)}_{q1}$ and $B^{(k2)}_{q2}$ is given by [57]:

$$T^{(k)}_q \equiv [A^{(k1)} \otimes B^{(k2)}]^k_q = C \sum_{q1,q2} (k1, q1; k2, q2|kq) A^{(k1)}_{q1} B^{(k2)}_{q2} \tag{A.17}$$

where C is a constant usually defined by a normalization condition. If the two tensors have equal rank, we can construct a scalar by choosing $k = 0$. This scalar product of the tensor operators $A^{(k)}$ and $B^{(k)}$ is defined by

$$[A^{(k)} B^{(k)}]^0_0 = \sum_q (-1)^q A^{(k)}_q B^{(k)}_q \tag{A.18}$$

up to a constant that is chosen to be 1 here. With these definitions it is then true that

$$[d^{(1)} \otimes E^{(1)}]^0_0 = \boldsymbol{d} \cdot \boldsymbol{E} \tag{A.19}$$

Now let's do the conversion for the quadrupole term. Here we have the quadrupole moment $x_i x_j$, which is a direct product of two vectors $\boldsymbol{x}$, forming a cartesian tensor of rank 2. The same can be achieved by forming the product $x^{(2)}_q = [x^{(1)} \otimes x^{(1)}]^2_q$ with

$C = 1$, which yields

$$x^{(2)}_{\pm 2} = \frac{1}{2}(x \pm iy)^2 \tag{A.20}$$

$$x^{(2)}_{\pm 1} = (x \pm iy)z \tag{A.21}$$

$$x^{(2)}_{0} = \sqrt{\frac{3}{2}}z^2 \tag{A.22}$$

In the same way the second-rank tensor $\partial_i E_j$ can be rewritten as $\nabla E^{(2)}_q = [\nabla^{(1)} \otimes E^{(1)}]^2_q$, which yields

$$\nabla E^{(2)}_{\pm 2} = \frac{1}{2}(\partial_x \pm i\partial_y)(E_x \pm iE_y) \tag{A.23}$$

$$\nabla E^{(2)}_{\pm 1} = \frac{1}{2}[\partial_z(\mp E_x - iE_y) + (\mp\partial_x - i\partial_y)E_z] \tag{A.24}$$

$$\nabla E^{(2)}_{0} = \sqrt{\frac{3}{2}}\partial_z E_z \tag{A.25}$$

Again, with these definitions it is true that

$$[d^{(1)} \otimes \nabla E^{(2)}]^0_0 = \sum_{ij} Q_{ij}\partial_i E_j(0) \tag{A.26}$$

A.4 Two different forms for vector structures

Vector structures for the PNC experiment have been written in two different ways: In terms of time averages with explicitly time-dependent fields, and in terms of time-independent field amplitudes. Here we show how the two formulations are equivalent. As an example we pick the vector structure for the PNC observable in $^{138}Ba^+$. In the original paper [23] it is given by

$$\left\langle (\boldsymbol{E}' \cdot \boldsymbol{\nabla})\dot{\boldsymbol{E}}'' + \boldsymbol{\nabla}(\boldsymbol{E}' \cdot \dot{\boldsymbol{E}}'') \right\rangle_t \tag{A.27}$$

This implies the following definitions for the electric fields:

$$\boldsymbol{E}' \equiv \boldsymbol{E}'(\boldsymbol{r}, t) = \boldsymbol{E}'(\boldsymbol{r})\cos(\omega t) \tag{A.28}$$

$$\boldsymbol{E}'' \equiv \boldsymbol{E}''(\boldsymbol{r}, t) = \boldsymbol{E}''(\boldsymbol{r})\cos(\omega t + \phi) \tag{A.29}$$

Plugging these definitions into Eq(A.27) and taking the time derivatives gives

$$-\omega \left\langle (\boldsymbol{E}'(\boldsymbol{r})\cos(\omega t)\cdot\boldsymbol{\nabla})\boldsymbol{E}''(\boldsymbol{r})\sin(\omega t+\phi)+\boldsymbol{\nabla}(\boldsymbol{E}'(\boldsymbol{r})\cos(\omega t)\cdot\boldsymbol{E}''(\boldsymbol{r})\sin(\omega t+\phi))\right\rangle_t \tag{A.30}$$

Next we use the definition of the time average to write

$$\langle\cos(\omega t)\sin(\omega t+\phi)\rangle_t = \frac{\omega}{2\pi}\int_0^{2\pi/\omega}\cos(\omega t)\sin(\omega t+\phi)dt = \frac{\sin\phi}{2} \tag{A.31}$$

With this we can write Eq.(A.30) as

$$= -\tfrac{\omega}{2}\sin\phi\left[(\boldsymbol{E}'(\boldsymbol{r})\cdot\boldsymbol{\nabla})\boldsymbol{E}''(\boldsymbol{r})+\boldsymbol{\nabla}(\boldsymbol{E}'(\boldsymbol{r})\cdot\boldsymbol{E}''(\boldsymbol{r}))\right] \tag{A.32}$$

$$= \tfrac{\omega}{2}\mathrm{Re}\left[(\boldsymbol{E}'(\boldsymbol{r})\cdot\boldsymbol{\nabla})\boldsymbol{E}''^{*}(\boldsymbol{r})+\boldsymbol{\nabla}(\boldsymbol{E}'(\boldsymbol{r})\cdot\boldsymbol{E}''^{*}(\boldsymbol{r}))\right] \tag{A.33}$$

with the electric fields as defined in Eq.(2.9):

$$\boldsymbol{E}'(\boldsymbol{r}) = \boldsymbol{E}'e^{-i\boldsymbol{k}'\cdot\boldsymbol{r}} \tag{A.34}$$

$$\boldsymbol{E}''(\boldsymbol{r}) = \boldsymbol{E}''e^{-i\boldsymbol{k}''\cdot\boldsymbol{r}-i\phi}, \tag{A.35}$$

which is the alternative way of writing vector structures found in M. Schacht's thesis [55].

A.5 Circular polarization

A.5.1 Definitions

Various parts of the experiment depend on circularly polarized light. Here we give some working definitions of circular polarization, as well as describe a measurement of the quality of circular polarization.

We first consider electric fields that propagate along the z axis. We define the circular polarization σ by

$$\sigma = \frac{E_+ - E_-}{E_+ + E_-}, \tag{A.36}$$

where E_+ and E_- are the components of the electric field written in terms of circular basis vectors,

$$\boldsymbol{E} = E_+\boldsymbol{e}_+ + E_-\boldsymbol{e}_- \tag{A.37}$$

$$\boldsymbol{e}_\pm = \frac{1}{\sqrt{2}}(\boldsymbol{e}_x \pm i\boldsymbol{e}_y). \tag{A.38}$$

For $\sigma = \pm 1$ we have completely circularly polarized light ($\sigma_\pm$-light), and for $\sigma = 0$ the light is plane polarized

With the further definition $E_0^2 = E_+^2 + E_-^2$ we can write the electric field in terms of σ:

$$\boldsymbol{E} = \frac{E_0}{\sqrt{2}\sqrt{1+\sigma^2}}[(1-\sigma)\boldsymbol{e}_+ + (1+\sigma)\boldsymbol{e}_-] \tag{A.39}$$

Often the spherical components of the field are needed. In terms of σ they read:

$$E_0^{(1)} = 0 \tag{A.40}$$

$$E_{\pm 1}^{(1)} = E_0\frac{1 \pm \sigma}{\sqrt{2}\sqrt{1+\sigma^2}} \tag{A.41}$$

If we now include a rotation of θ of the k vector in the x-z plane, we arrive at a general field expression that is used in misalignment analyses:

$$E_0^{(1)} = E_0\frac{\sin\theta}{\sqrt{1+\sigma^2}} \tag{A.42}$$

$$E_{\pm 1}^{(1)} = E_0\frac{\cos\theta \pm \sigma}{\sqrt{2}\sqrt{1+\sigma^2}} \tag{A.43}$$

A.5.2 Measurement

A common way of measuring σ is by measuring its intensity through a polarizer. By rotating the polarizer we can measure the maximum and minimum, and the degree of circular polarization is assessed by the normalized difference between minimum and maximum. Ideally, they are the same, since for circularly polarized light, there can be no preferred axis. More quantitatively, the "quality factor" Q that we measure is given by

$$Q = \frac{E_x^2 - E_y^2}{E_x^2 + E_y^2} \tag{A.44}$$

where the field is $\boldsymbol{E} = E_x \boldsymbol{e}_x + iE_y \boldsymbol{e}_y$. Here $\boldsymbol{e}_x$ is defined by the direction where the transmitted intensity becomes maximal. All other field components E_y then have to be phase-shifted by i.

We can now express the polarization σ in terms of Q and have a convenient method of experimentally finding σ:

$$\sigma = \frac{\sqrt{1-Q}}{\sqrt{1+Q}} \tag{A.45}$$

Appendix B

ATOMIC PROPERTIES OF RA^+ AND BA^+

Table B.1: Ba and Ra isotopes, with half-life and nuclear spin.

isotope	half-life	nuclear spin
Ra 223	11.4 d	I=3/2
Ra 224	3.6 d	I=0
Ra 225	14.8 d	I=1/2
Ra 226	1600 yrs	I=0
Ra 227	42.2 m	I=3/2
Ba 131	11.5 d	I=1/2
Ba 132	stable(0.1%)	I=0
Ba 133	10.5 yrs	I=1/2
Ba 134	stable(2.4%)	I=0
Ba 135	stable(6.6%)	I=3/2
Ba 136	stable(7.8%)	I=0
Ba 137	stable(11.2%)	I=3/2
Ba 138	stable(71.7%)	I=0

Table B.2: Experimental energy levels in Ra^+ and Ba^+ [44]. For correct Ra^+ state designations, increase principal quantum number N by one.

State	$Ba^+(cm^{-1})$	Ra^+ (cm^{-1})
$6S_{1/2}$	0	0
$5D_{3/2}$	4873.850	12084.38
$5D_{5/2}$	5674.824	13743.11
$6P_{1/2}$	20261.562	21351.20
$6P_{3/2}$	21952.422	26208.86
$7S_{1/2}$	42355.182	43405.01
$6D_{3/2}$	45949.496	48744.04
$6D_{5/2}$	46154.89	49240.48
$4F_{5/2}$	48258.59	48987.98
$4F_{7/2}$	48483.29	49272.31
$7P_{1/2}$	49390.05	50606.01
$7P_{3/2}$	50011.22	52392.05
$5F_{5/2}$	57390.93	59515.48
$5F_{7/2}$	57631.64	59815.59
$8S_{1/2}$	58025.18	59165.23
⋮	⋮	⋮
ionization	80686.87	81842.31

Table B.3: Relevant transition wavelengths in Ba^+ and Ra^+.

	Ba^+	Ra^+
S1/2↔P1/2	493.545 nm	468.358 nm
D3/2↔P1/2	649.869 nm	1079.12 nm
S1/2↔P3/2	585.529 nm	707.99 nm
S1/2↔D3/2	2051.77 nm	827.515 nm
S1/2↔D5/2	1762.17 nm	727.637 nm

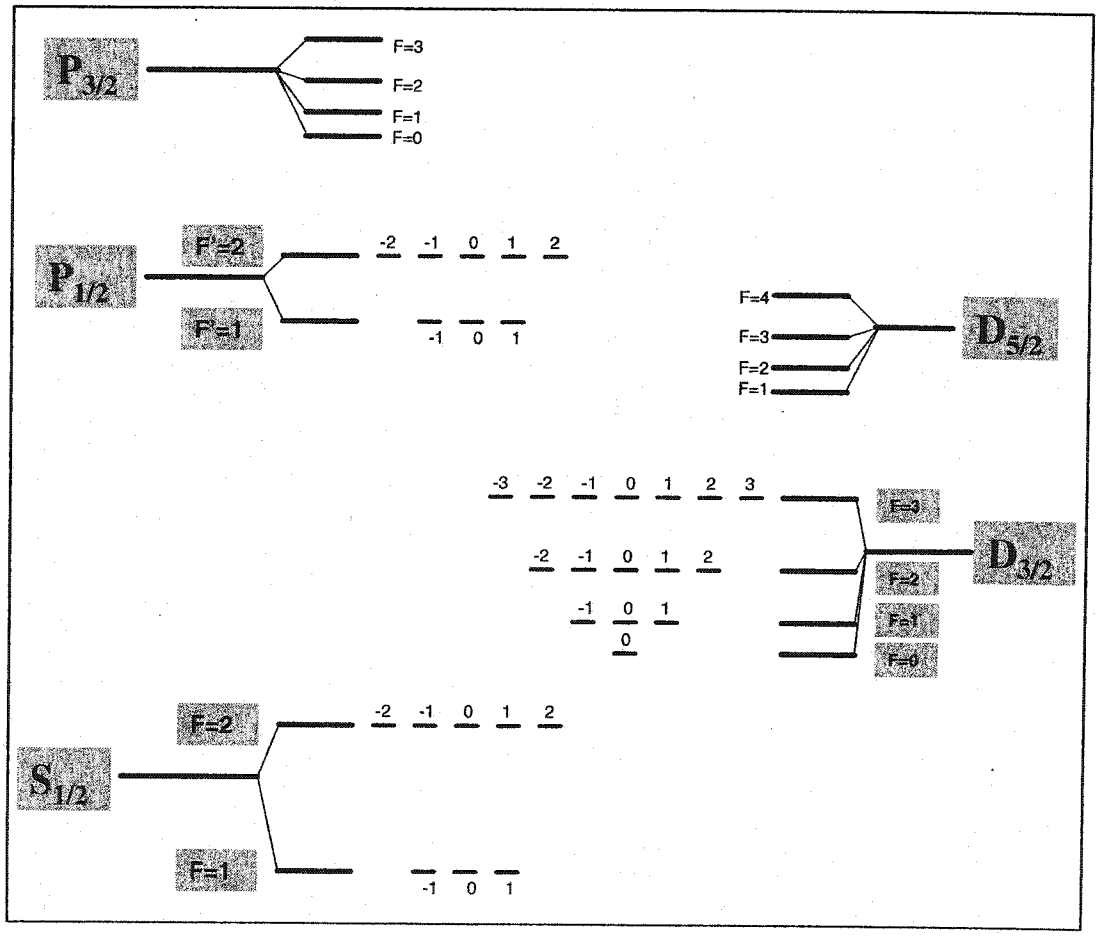

Figure B.1: Hyperfine structure for I=3/2.

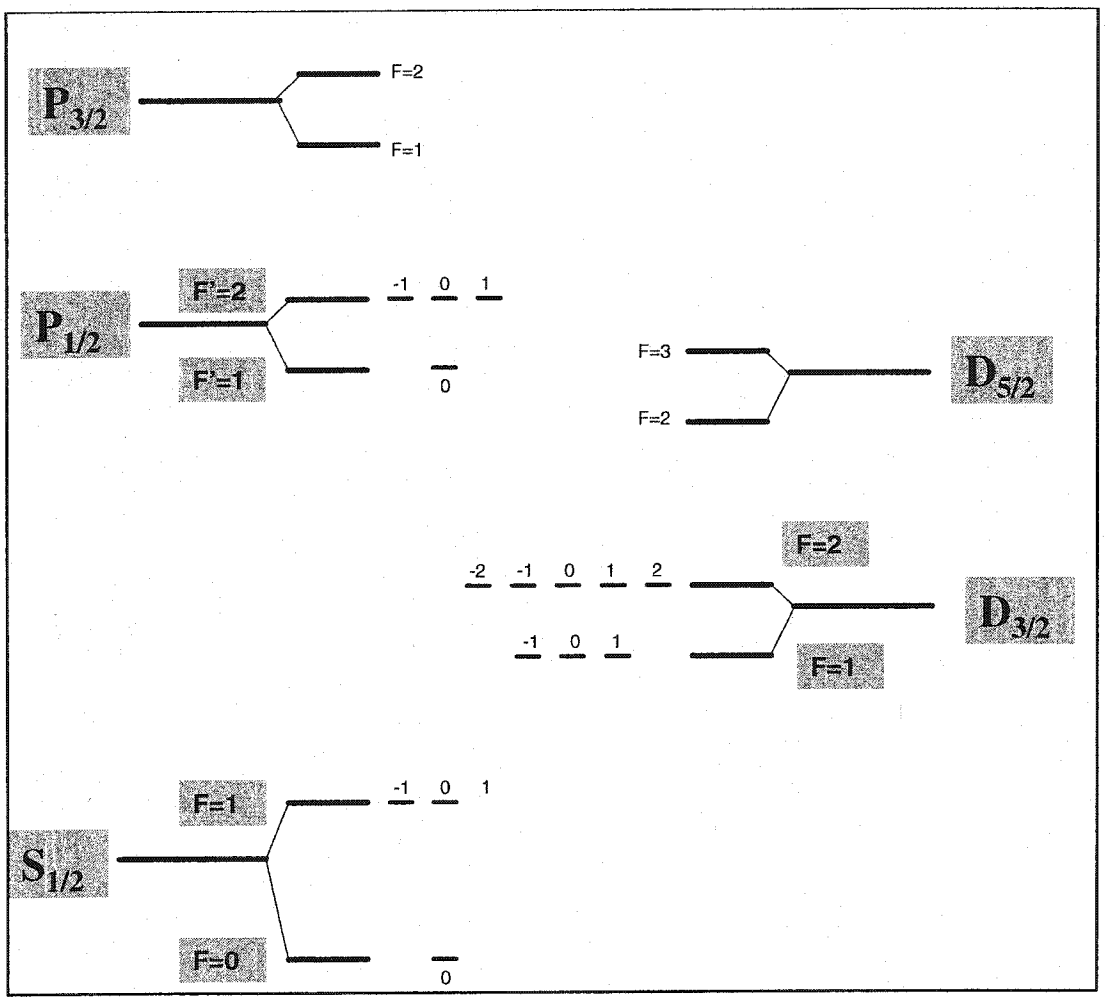

Figure B.2: Hyperfine structure for I=1/2.

Table B.4: Summary of relevant reduced dipole transition matrix elements for Ba^+, some of which have been calculated from radial integrals. The matrix elements are given in atomic units (ea_0).

States		Dzuba[a]	Gopakumar[b]	Guet[c]	Kastberg(exp.)[d]
$6S_{1/2}$	$6P_{1/2}$	3.31	3.33	3.30	3.36
	$6P_{3/2}$	-4.67	-4.70	-4.66	(-)4.67
	$7P_{1/2}$	-0.098	0.12	-	-
	$7P_{3/2}$	-0.034	-0.36	-	-
$5D_{3/2}$	$6P_{1/2}$	-3.05	-2.94	3.01	3.02
	$6P_{3/2}$	-1.33	-1.28	-1.31	(-)1.36
	$7P_{1/2}$	-0.26	-0.31	-	-
	$7P_{3/2}$	-0.15	-0.16	-	-
	$4F_{5/2}$	5.2[e]	-	-	-
	$5F_{5/2}$	1.3[e]	-	-	-
$5D_{5/2}$	$6P_{3/2}$	-	3.98	4.06	4.15

[a][19], calculated from radial integrals

[b][27]

[c][28]

[d][35], from transition rate measurements using optical nutation. This reference implies a 1-σ error of about 3%. Also in this reference are previously published transition rates.

[e]M. Schacht (unpublished), calculated from radial integral

BIBLIOGRAPHY

[1] C. S. Bennett and C. E. Wieman, *Measurement of the 6S-7S transition polarizability in atomic cesium and an improved test of the standard model*, Phys. Rev. Lett. **82** (1999), 2484.

[2] J. C. Bergquist, R. G. Hulet, W. M. Itano, and D. J. Wineland, *Observation of quantum jumps in a single atom*, Phys. Rev. Lett. **57** (1986), no. 14, 1699.

[3] J. C. Bergquist, W. M. Itano, and D. J. Wineland, *Recoilless optical absorption and Doppler sidebands of a single trapped ion*, Phys. Rev. A **36** (1987), no. 1, 428.

[4] D.J. Berkeland and M.G. Boshier, *Destabilization of dark states and optical spectroscopy in Zeeman-degenerate atomic systems*, Phys. Rev. A **65** (2002), 033413.

[5] S. Bize, S.A. Diddams, U. Tanaka, C.E. Tanner, W.H. Oskay, R.E. Drullinger, T.E. Parker, T.P. Heavner, S.R. Jefferts, L. Hollberg, W.M. Itano, and J.C. Bergquist, *Testing the stability of fundamental constants with the $^{199}Hg^{+}$ single-ion optical clock*, Phys. Rev. Lett. **90** (2003), no. 15, 150802.

[6] R. Blatt, G. Lafyatis, W. D. Phillips, S. Stenholm, and D. J. Wineland, *Cooling in traps*, Phys. Scri. **T** (1988), 216.

[7] M. A. Bouchiat and C. C. Bouchiat, *The quantum-jump approach to dissipative dynamics in quantum optics*, Rev. Mod. Phys. **70** (1998), no. 1, 101.

[8] M. B. Bouchiat, *Parity violation in atoms*, Rep. Prog. Phys. **60** (1997), 1351.

[9] M.A. Bouchiat, J. Guena, L. Pottier, and L. Hunter, *New observation of a parity violation in cesium*, Phys. Lett. B **134** (1984), 463.

[10] J.I. Cirac and P. Zoller, *Quantum computations with cold trapped ions*, Phys. Rev. Lett. **74** (1995), no. 20, 4091.

[11] C. Cohen-Tannoudji, J. Dupont-Roc, and G. Grynberg, *Atom-Photon Interactions*, Wiley-Interscience.

[12] CDF collaboration, *Search for New Gauge Bosons Decaying into Dileptons in $\bar{p}$-p Collisions at $\sqrt{s}$ =1.8 TeV*, Phys. Rev. Lett. **79** (1997), 2192.

[13] A.D. Cronin, *New techniques for measuring atomic parity violation*, Ph.D. thesis, University of Washington, 1999.

[14] H.G. Dehmelt, *Proposed 10^{14} $\Delta\nu < \nu$ Laser Fluorescence Spectroscopy on Tl+ Mono-Ion Oscillator II (spontaneous quantum jumps)*, Bull. Am. Phys. Soc. **20** (1975), 60.

[15] R.H. Dicke, *The effect of collisions upon the Doppler width of spectral lines*, Phys. Rev. **89** (1953), no. 2, 472.

[16] S. Diddams, D. Jones, J. Ye, T. Cundiff, J. Hall, J. Ranka, R. Windeler, R. Holzwarth, T. Udem, and T. Hansch, *Direct link between microwave and optical frequencies with a 300 THz femtosecond laser comb*, Phys. Rev. Lett. **84** (2000), no. 22, 5102.

[17] P.S. Drell and E.D. Commins, *Parity nonconservation in atomic thallium*, Phys. Rev. A **32** (1985), 2196.

[18] V. Dzuba and V. Flambaum, *Atomic optical clocks and search for variation of the fine-structure constant*, Phys. Rev. A **61** (2000), no. 3, 034502.

[19] V.A. Dzuba, V.V. Flambaum, and J.S. Ginges, *Calculations of parity-nonconserving s-d amplitudes in Cs, Fr, Ba^+, and Ra^+*, Phys. Rev. A **63** (2001), no. 6, 062101.

[20] V.A. Dzuba, V.V. Flambaum, P.G. Silvestrov, and O.P. Sushkov, *Calculation of parity nonconservation in thallium*, J. Phys. B **20** (1987), 3297.

[21] V.A. Dzuba, C. Harabati, W.R. Johnson, and M.S. Safronova, *Breit correction to the parity-nonconservation amplitude in cesium*, Phys. Rev. A **63** (2001), no. 4, 044103.

[22] N.H. Edwards, S.J. Phipp, P.E.G. Baird, and S. Nakayama, *Precise measurement of parity nonconserving optical rotation in atomic thallium*, Phys. Rev. Lett. **74** (1995), 2654.

[23] E.N. Fortson, *Possibility of measuring parity nonconservation with a single trapped atomic ion*, Phys. Rev. Lett. **70** (1993), no. 16, 2383.

[24] Y. Fujii, A. Iwamoto, T. Fukahori, T. Ohnuki, M. Nakagawa, H. Hidaka, Y. Oura, and P. Möller, *The nuclear interaction at Oklo 2 billion years ago*, Nucl. Phys **B573** (2000), 377.

[25] K.P. Geetha, A.D. Singh, and B.P. Das, *Nuclear-spin-dependent parity-nonconserving transitions in Ba^+ and Ra^+*, Phys. Rev. A **58** (1998), no. 1, R16.

[26] P. Ghosh, *Ion traps*, Oxford Univerity Press.

[27] G. Gopakumar, H. Merlitz, R.K. Chaudhuri, B.P. Das, U.S. Mahapatra, and D. Mukherjee, *Electric dipole and quadrupole transition amplitudes for Ba^+ using the relativistic coupled-cluster method*, Phys. Rev. A **66** (2002), no. 3, 32505.

[28] C. Guet and W.R. Johnson, *Relativistic many-body calculations of transition rates for Ca^+, Sr^+, and Ba^+*, Phys. Rev. A **44** (1991), no. 3, 1531.

[29] G. R. Guthohrlein, M. Keller, K. Hayasaka, W. Lange, and H. Walther, *A single ion as a nanoscopic probe of an optical field*, Nature **414** (2001), 49.

[30] W. Happer, *Optical Pumping*, Rev. Mod. Phys. **44** (1972), 169.

[31] K.R. Hendrickson, *Toward a Measurement of Atomic Parity Nonconservation Using a Single and Trapped Barium Ion*, Ph.D. thesis, University of Washington, 1999.

[32] W.M. Itano, D.J. Heinzen, J.J. Bollinger, and D.J. Wineland, *Quantum Zeno effect*, Phys. Rev. A **41** (1990), no. 5, 2295.

[33] J.D. Jackson, *Classical Electrodynamics*, Wiley Publishing, 1999.

[34] W.R. Johnson, *Weak Interactions in Atoms*, 1999 (unpublished, available at http://www.nd.edu/ johnson).

[35] A. Kastberg, P. Villemoes, A. Arnesen, F. Heijenskjoeld, and A. Langereis, *Measurements of absolute transition probabilities in Ba II through optical nutation*, J. Opt. Soc. Am. B **10** (1993), no. 8, 1330.

[36] D. Kielpinski, C. Monroe, and D.J. Wineland, *Architecture for a large-scale ion-trap quantum computer*, Nature **417** (2002), 709.

[37] K.H. Knoll, G. Marx, K. Hubner, F. Schweikert, S. Stahl, C. Weber, and G. Werth, *Experimental g_J factor in the metastable $5D_{3/2}$ level of Ba^+*, Phys. Rev. A **54** (1996), no. 2, 1199.

[38] T.W. Koerber, M. Schacht, W. Nagourney, and E.N. Fortson, *Radio frequency spectroscopy with a trapped Ba^+ ion: recent progress and prospects for measuring parity nonconservation*, J. Phys. B **36** (2003), 637.

[39] T.D. Lee, *Question of parity conservation in weak interactions*, Phys. Rev. **104** (1956), 254.

[40] D. Leibfried, R.Blatt, C. Monroe, and D. Wineland, *Quantum dynamics of single trapped ions*, Rev. Mod. Phys. **75** (2003), 281.

[41] D.M. Meekhof, P.V. Vetter, P.K. Majumder, S.K. Kamoreauz, and E.N. Fortson, *High-precision measurement of parity nonconserving optical rotation in atomic lead*, Phys. Rev. Lett. **71** (1993), 3442.

[42] H.J. Metcalf and P. van der Straten, *Laser Cooling and Trapping*, 1999.

[43] B.R. Mollow, *Power spectrum of light scattered by two-level systems*, Phys. Rev. **188** (1969), no. 5.

[44] C.E. Moore, *Atomic energy levels*, NSRDS-NBS **III** (1971).

[45] G. Morigi, J.Eschner, J.I. Cirac, and P. Zoller, *Laser cooling of two trapped ions: Sideband cooling beyond the Lamb-Dicke limit*, Phys. Rev. A **59** (1999), no. 5, 3797.

[46] A.B. Mundt, A. Kreuter, C. Becher, D. Leibfried, J. Eschner, F. Schmidt-Kaler, and R. Blatt, *Coupling a single atomic quantum bit to a high finesse optical cavity*, Phys. Rev. Lett. **89** (2002), 103001.

[47] W. Nagourney, H. Dehmelt, and G. Janik, *Optical Lamb-Dicke confinement of a Ba^+ mono-ion oscillator*, Advances in Laser Science - I. Proceedings of the First

International Laser Science Conference. 18-22 Nov. 1985; Dallas and TX, USA, 1986, p. 401.

[48] W. Neuhauser, M. Hohenstatt, P.E. Toschek, and H. Dehmelt, *Localized visible Ba^+ mono-ion oscillator*, Phys. Rev. A **22** (1980), no. 3, 1137.

[49] M. Peskin and T. Takeuchi, *Estimation of oblique electroweak corrections*, Phys. Rev. D **46** (1992), no. 1.

[50] M.B. Plenio and P.L. Knight, *The quantum-jump approach to dissipative dynamics in quantum optics*, Rev. Mod. Phys. **70** (1998), no. 1, 101.

[51] P. M. Radmore and P. L. Knight, *Population trapping and dispersion in a three-level system*, J. Phys. B **15** (1982), 561.

[52] R.J. Rafac, B.C. Young, J.A. Beall, W.M. Itano, D.J. Wineland, and J.C. Bergquist, *Sub-dekahertz ultraviolet spectroscopy of $^{199}Hg^+$*, Phys. Rev. Lett. **85** (2000), no. 12, 2462.

[53] J.J. Sakurai, *Modern Quantum Mechanics*, Addison-Wesley, 1994.

[54] T.H. Sauter, R. Blatt, W. Neuhauser, and P.E. Toschek, *'Quantum jumps' observed in the fluorescence of a single ion*, Optics-Communications **60** (1986), no. 5, 287.

[55] M. Schacht, *Spin State Detection and Manipulation and Parity Violation in a Single Trapped Ion*, Ph.D. thesis, University of Washington, 2000.

[56] B. W. Shore and J. Ackerhalt, *Dynamics of multilevel laser excitation: three-level atoms*, Phys. Rev. A **15** (1977), no. 4, 1640.

[57] I.I. Sobelman, *Atomic spectra and radiative transitions*, Springer, 1992.

[58] S. Stenholm, *The semiclassical theory of laser cooling*, Rev. Mod. Phys. **58** (1986), no. 3, 699.

[59] T.J. Sumner, J.M. Pendlebury, and K.F. Smith, *Convectional magnetic shielding*, J. Phys. D **20** (1987), no. 9, 1095.

[60] S. Swain, *Conditions for population trapping in a three-level system*, J. Phys. B **15** (1982), 3405.

[61] Q.A. Turchette, C.J. Myatt, B.E. King, C.A. Sackett, D. Kielpinski, W.M. Itano, C. Monroe, and D.J. Wineland, *Decoherence and decay of motional quantum states of a trapped atom coupled to engineered reservoirs*, Phys. Rev. A **62** (2000), no. 5, 053807.

[62] R.S. van Dyck, S.L. Zafonte, and P.B. Schwinberg, *Ultra-Precise mass measurements using the UW-PTMS*, Hyperfine Interactions **132** (2001), 163.

[63] P.A. Vetter, D.M. Meekhof, P.K. Majumder, S.K. Lamoreaux, and E.N. Fortson, *Precise test of electroweak theory from a new measurement of parity nonconservation in atomic thallium*, Phys. Rev. Lett. **74** (1995), 2658.

[64] J. Von Zanthier, J. Abel, T. Becker, M. Fries, E. Peik, H. Walther, R. Holzwarth, J. Reichert, T. Udem, T.W. Hansch, A.Y. Nevsky, M.N. Skvortsov, and S.N. Bagayev, *Absolute frequency measurement of the* $^{115}In^{+}5s^{2}\ {}^{1}S_{0}$-$5s5p\ {}^{3}P_{0}$ *transition*, Opt. Comm **166** (1999), 57.

[65] J. K. Webb, M.T. Murphy, V. V. Flambaum, V. A. Dzuba, J. D. Barrow, C. W. Churchhill, J. X. Prochaska, and A. M. Wolfe, *Further Evidence for Cosmological Evolution of the Fine Structure Constant*, Phys. Rev. Lett **87** (2001), 091301.

[66] S.C. Wieman and S.C., *Measurement of the $6S \rightarrow 7S$ transition polarizability in atomic cesium and an improved test of the standard model*, Phys. Rev. Lett. **82** (1999), 2484.

[67] D.J. Wineland, D.A. Howe, M.B. Mohler, and H.W. Hellwig, *Special purpose ammonia frequency standard-a feasibility study*, IEEE **IM-28** (1979), no. 2, 122.

[68] D.J. Wineland and W.M. Itano, *Spectroscopy of a single Mg^+ ion*, Phys. Rev. A **82** (1981), no. 2, 75.

[69] C. S. Wood, S. C. Bennet, D. Cho, B. P. Masterson, J. L. Roberts, C. E. Tanner, and C. E. Wieman, *Measurement of parity nonconservation and anapole moment in cesium*, Science **275** (1997), 1759.

[70] C.S. Wu, E. Ambler, R.W. Hayward, D.D. Hoppes, and R.P. Hudson, *Experimental Test of Parity Conservation in Beta Decay*, Phys. Rev. **105** (1957), 1413.

[71] N. Yu, H. Dehmelt, and W. Nagourney, *Demonstration of new Paul-Straubel trap for trapping single ions*, J. App. Phys. **69** (1991), no. 6, 3779.

[72] N. Yu and W. Nagourney, *Analysis of Paul-Straubel trap and its variations*, J. App. Phys. **77** (1995), no. 8, 3623.

[73] N. Yu, W. Nagourney, and H. Dehmelt, *Radiative lifetime measurement of the Ba^+ metastable $D_{3/2}$ state*, Phys. Rev. Lett. **78** (1997), no. 26, 4898.

VITA

Timo W. Koerber was born on July 3, 1973 in Karlsruhe, Germany, to Helmut and Waltraud Körber. He spent most of his undergraduate years at the Gutenberg university of Mainz, Germany, studying physics and theology. He entered the physics graduate program at the University of Washington in 1998, earning a Master of Science degree in 1999. In 2000 he also earned a Physik-Diplom from the University of Mainz. He has been working in Prof. N. Fortsons group since 1999 and completed his Ph.D. in 2003.